

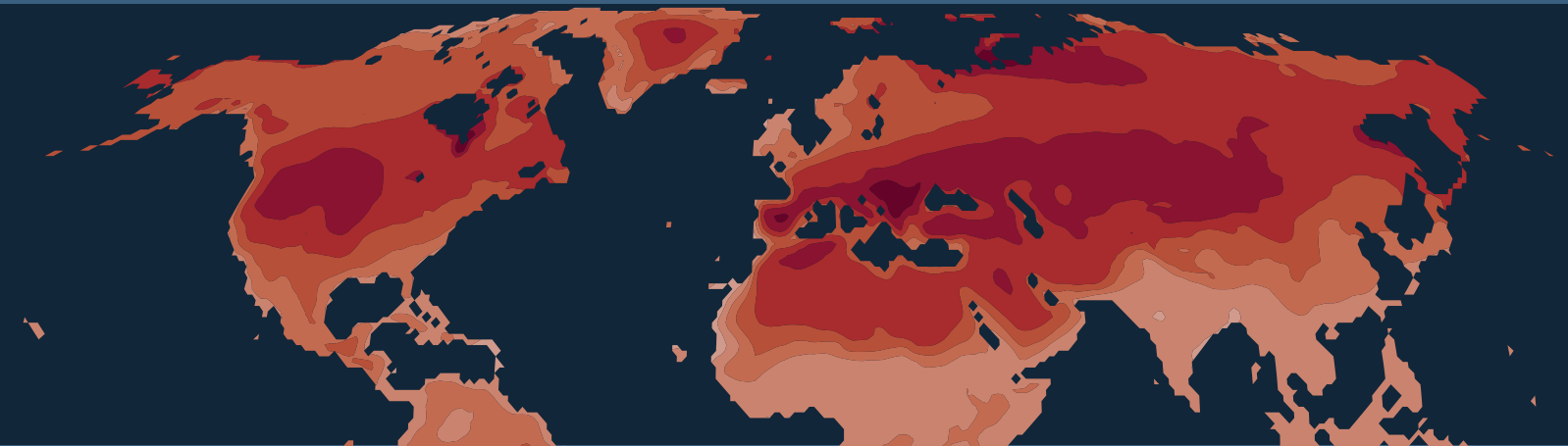


Universität  
Bremen

Department I  
Physics/Electrical Engineering



Alfred Wegener Institute  
Paleoclimate Dynamics



# A PAST, PRESENT AND FUTURE PERSPECTIVE ON THE EUROPEAN SUMMER CLIMATE

A study based on climate proxies,  
climate observations and climate models

DANIEL F. BALTING

# A PAST, PRESENT AND FUTURE PERSPECTIVE ON THE EUROPEAN SUMMER CLIMATE

A STUDY BASED ON CLIMATE PROXIES, CLIMATE OBSERVATIONS AND  
CLIMATE MODELS

DISSERTATION

for the award of the academic degree  
doctor rerum naturalium (Dr. rer. nat.)  
in Faculty 1 - Physics/Electrical Engineering

submitted to the  
University of Bremen  
from  
M. Sc. Daniel F. Balting

Rector of the University of Bremen  
Prof. Dr.-Ing. Bernd Scholz-Reiter

Dean of Faculty 1 - Physics/Electrical Engineering  
Prof. Dr. rer. nat. Jens Falta

Reviewers:

1. Prof. Dr. rer. nat. Gerrit Lohmann
2. Prof. Dr. rer. nat. Jan Esper

Date of PhD defense: 23.02.2022

---

**PUBLICATIONS**

---

---

**PEER REVIEWED**

**Balting, D. F.**, Ionita, M., Wegmann, M., Helle, G., Schleser, G. H., Rimbu, N., Freund, M. B., Heinrich, I., Caldarescu, D., and Lohmann, G.: Large-scale climate signals of a European oxygen isotope network from tree rings, *Clim. Past*, 17, 1005–1023, <https://doi.org/10.5194/cp-17-1005-2021>, 2021a.

**Balting, D. F.**, AghaKouchak, A., Lohmann, G., and Ionita, M.: Northern Hemisphere drought risk in a warming climate, *npj Climate and Atmospheric Science*, 4, 1–13, <https://doi.org/10.1038/s41612-021-00218-2>, 2021b.

Pauly, M., Helle, G., Büntgen, U., Wacker, L., Treydte, K., Reinig, F., Turney, C., Nievergelt, D., Kromer, B., Friedrich, M., Sookdeo, A., Heinrich, I., Riedel, F., **Balting, D. F.**, and Brauer, A.: An annual-resolution stable isotope record from Swiss subfossil pine trees growing in the late Glacial, *Quaternary Science Reviews*, 247, 1–12, <https://doi.org/10.1016/j.quascirev.2020.106550>, 2020.

Sokolova, N., Butzin, M., Dahlke, F., Werner, K. M., **Balting, D. F.**, Lohmann, G., and Pörtner, H.-O.: Exploring the role of temperature in observed inter-population differences of Atlantic cod (*Gadus morhua*) growth with a 4-dimensional modelling approach, *ICES Journal of Marine Science*, 78, 1519–1529, <https://doi.org/10.1093/icesjms/fsab043>, 2021.

---

**UNDER REVIEW**

Freund, M. B., Helle, G., **Balting, D. F.**, Ballis, N., Cubasch, U., and Schleser, G. H.: European hydroclimate of the past 400 years indicates unusual recent summer drought, *Nat Commun*, in review.

Nixdorf, J., Lohmann, G., Ionita, M., Werner, M., and **Balting, D. F.**: Climate signature of stable isotopic composition of Danube River water, *Theoretical and Applied Climatology*, in review.

---

**IN PREPARATION**

**Balting, D. F.**, Michel, S., Nagavciuc, V., Helle, G., Schleser, G. H., Steger, D., Lohmann, G., and Ionita, M.: A past, present and future perspective on the European summer vapour pressure deficit, *Nature Scientific Data*, in preparation.

Rimbu, N., **Balting, D. F.**, Michel, S., and Ionita, M.: Extreme temperature and precipitation variability in Europe during the last four centuries inferred from oxygen isotope tree rings, in preparation.

Sokolova, N., Ackermann, L., **Balting, D. F.**, Lohmann, G., Pörtner, H.-O., and Dahlke, F.: Atlantic cod (*Gadus morhua*) growth and reproduction under future warming, in preparation.

Steger, D., Peters, R. L., Blume, T., Hurley, A., Balanzategui, D., **Balting, D. F.**, and Heinrich, I.: Relevance of internal water status when assessing inter- and intraspecific variability in crown conductance regulation, *New Phytologist*, in preparation.

## ABSTRACT

The climate in the summer months is essential for ecosystems and society. However, climate change is causing lasting changes in the characteristics of the summer climate. In order to better understand the summer climate, to capture changes in a statistically meaningful way and to develop climate scenarios for the future, long-term climate observations and reliable climate models are needed. These three points are addressed in this thesis with the help of three main research questions.

The first question examines the prevailing large-scale climate patterns which are elaborated using the climate signature of the oxygen isotope ratio in tree ring cellulose ( $\delta^{18}\text{O}_{\text{cel}}$ ) over the past 400 years. An empirical orthogonal function analysis reveals two different modes of variability. The first mode is related to multi-seasonal anomaly patterns associated with the El Niño-Southern Oscillation. The second mode of  $\delta^{18}\text{O}_{\text{cel}}$  variability, which captures a north-south dipole, is associated with a regional summer atmospheric circulation pattern that has a distinct centre over the North Sea.

To further exploit the climate sensitivity of  $\delta^{18}\text{O}_{\text{cel}}$  tree-ring records, the first grid-based reconstruction of the European summer vapour pressure deficit (VPD) for the last four centuries is presented. This reconstruction is used to answer the second question of what trends in VPD have occurred in Europe over the last 400 years. The simultaneous increase in temperature and decrease in precipitation starts from mid-17<sup>th</sup> century in Central Europe and the Mediterranean region and relates to a positive VPD trend. This trend towards higher VPD continues throughout the observation period.

In addition to studying the past summer climate with the help of a tree ring network, climate models provide valuable information on future scenarios which are highly relevant for society and ecosystems. Therefore, this thesis addresses the question of whether simulations with different climate models from a climate model comparison project are suitable for making reliable statements about future drought conditions and what influence the amount of greenhouse gases has on drought occurrence. Based on a comparison between simulated and observed drought conditions for the period 1971-2000, reasonable agreement can be found between climate model simulations and the observations. However, climate models cannot reproduce drought trends in observations for recent decades for large parts of the Northern Hemisphere. Furthermore, it is shown that drought occurrence is projected to increase significantly in arid regions under three different future scenarios, with the severity of droughts depending on greenhouse gas emissions. For regions currently less affected by prolonged droughts, such as the European continent, the climate models show that the probability of drought occurrence increases significantly under the warmest future scenario. Thus, this thesis presents new perspectives on past, present and future European summer climate using a  $\delta^{18}\text{O}_{\text{cel}}$  tree ring network, climate observations and climate model simulations.

## TABLE OF CONTENTS

Publications .....	II
Abstract.....	III
Table of Contents.....	IV
List of figures.....	VII
List of tables .....	VIII

# 01

INTRODUCTION .....	1
1.1 Motivation.....	2
1.2 Structure & objectives of the thesis.....	4

# 02

THE CLIMATE SYSTEM AND CLIMATE PROXIES.....	7
2.1 Climate system.....	8
2.2 Climate Models.....	9
2.2.1 Coupled Model Intercomparison Project.....	11
2.2.2 The Scenario Model Intercomparison Project.....	13
2.3 Climate Proxies.....	15
2.3.1 Photosynthesis and endo- genous & exogenous factors ...	15
2.3.2 Structure of a tree trunk .....	16
2.3.3 Stable Isotopes from tree rings.....	17

2.3.4 The isotope effect .....	18
2.3.5 Isotopes of oxygen.....	19
2.3.6 Environmental influences on the oxygen isotope.....	19

# 03

## CLIMATE SIGNALS OF A EUROPEAN OXYGEN ISOTOPE NETWORK .....

21

3.1 Large-scale climate signals & $\delta^{18}\text{O}_{\text{cel}}$ .....	22
3.2 Isotope Network & Method.....	24
3.2.1 The isotope network.....	24
3.2.2 Climate data.....	25
3.2.3 Modelled $\delta^{18}\text{O}_{\text{cel}}$ in preci- pitation and soil water.....	26
3.2.4 Data analysis.....	27
3.3 Results of the $\delta^{18}\text{O}_{\text{cel}}$ network analysis .....	29
3.3.1 Characteristics of the $\delta^{18}\text{O}_{\text{cel}}$ network .....	29
3.3.2 Characteristics of the principal components.....	30
3.3.3 Climate signals of PC1.....	32
3.3.4 Comparison with modelled $\delta^{18}\text{O}_{\text{cel}}$ in precipitation & soil water .....	36
3.3.5 Further climate signals in $\delta^{18}\text{O}_{\text{cel}}$ .....	36
3.4 Discussion of the $\delta^{18}\text{O}_{\text{cel}}$ network analysis .....	37
3.4.1 Latitudinal and altitudinal dependence of the $\delta^{18}\text{O}_{\text{cel}}$ network.....	37

3.4.2 Links between ENSO and PC1 .....	38	4.3.4 Comparison of the time series with other reconstructions .....	55
3.4.3 The stability of the ENSO signal in the isotope network .	39	4.3.5 Spatial variability of the VPD reconstruction .....	58
3.4.4 The winter climate signal in $\delta^{18}\text{O}_{\text{cel}}$ .....	40	4.3.6 Comparison of past/histo- rical spatial variability .....	59
3.4.5 Links between PC2 and large-scale atmospheric modes.....	41	4.3.7 Historical and future Euro- pean VPD in CMIP6.....	61
<b>3.5 Conclusion of the <math>\delta^{18}\text{O}_{\text{cel}}</math> network study .....</b>	<b>42</b>	<b>4.4. Limitations of the VPD reconstruction.....</b>	<b>64</b>
		<b>4.5 Conclusion of the long-term VPD variability .....</b>	<b>65</b>

# 04

## A RECONSTRUCTION OF THE EUROPEAN SUMMER VPD .....

### 4.1 Motivation for a reconstruction ...

### 4.2 Data & reconstruction technique .....

4.2.1 The stable isotope network....

4.2.2 Observational data.....

4.2.3 General procedure of the  
European VPD  
reconstruction.....

4.2.4 VPD computation and  
further pre-processing.....

4.2.5 Future scenarios.....

### 4.3 Results of the VPD reconstruction.....

4.3.1 Climate sensitivity.....

4.3.2 Validation statistics.....

4.3.3 Temporal variability of the  
European VPD  
reconstruction.....

# 05

## NORTHERN HEMISPHERE DROUGHT RISK IN A WARMING CLIMATE .....

### 5.1 Future drought projections .....

### 5.2 Risk statistics & the used climate model ensemble.....

5.2.1 Climate model ensemble .....

5.2.2 Computation of the SPEI  
drought index .....

5.2.3 Model evaluation .....

5.2.4 Occurrence rate statistics .....

### 5.3 Future Summer Warming & drought risk.....

5.3.1 Model evaluation .....

5.3.2 Projected summer tempera-  
ture changes .....

5.3.3 Projected precipitation and  
potential evapotranspiration...

5.3.4 Drought conditions by the end of 21 <sup>st</sup> century .....	79
5.3.5 Occurrence of dry periods at the end of 21 <sup>st</sup> century .....	80
<b>5.4 Discussion &amp; Conclusion of drought projections .....</b>	<b>84</b>

# 06

FINAL CONSIDERATION OF THE RESEARCH QUESTIONS ....	87
<b>6.1 Conclusion .....</b>	<b>88</b>
<b>6.2 Outlook .....</b>	<b>90</b>
References.....	91
Appendix A.....	112
1 Random Forest Reconstruction.....	112
Appendix B.....	116
Acknowledgment.....	132

## LIST OF FIGURES

Figure 2.1: The six spheres of the Earth that influence the climate system. ....	9
Figure 2.2: The anatomy of a tree stem. ....	17
Figure 3.1: Spatial distribution of sample sites combined with the corresponding altitude. ....	24
Figure 3.2: The characteristics of the European $\delta^{18}\text{O}_{\text{cel}}$ time series. ....	30
Figure 3.3: Spatial and temporal variability of the first two $\delta^{18}\text{O}_{\text{cel}}$ components and EOFs. ....	31
Figure 3.4: Composite maps (high and low) of SSTs related to the first $\delta^{18}\text{O}_{\text{cel}}$ component for the DJF, MAM, and JJA seasons. ....	33
Figure 3.5: Composite maps (high and low) for Z500 related to the first $\delta^{18}\text{O}_{\text{cel}}$ component for the DJF, MAM, and JJA seasons. ....	34
Figure 3.6: Composite maps (high–low) for precipitation and air temperature related to the first $\delta^{18}\text{O}_{\text{cel}}$ component for the DJF, MAM, and JJA seasons. ....	35
Figure 3.7: Links between the first $\delta^{18}\text{O}_{\text{cel}}$ component and the modelled $\delta^{18}\text{O}$ in soil water and precipitation from nudged climate simulations with ECHAM5-wiso. ....	35
Figure 3.8: Composite maps (high–low) for the boreal summer related to the second $\delta^{18}\text{O}_{\text{cel}}$ component. ....	36
Figure 3.9: Composite map (high–low) for Z500 related to the second $\delta^{18}\text{O}_{\text{cel}}$ component (PC2) for the boreal summer. ....	37
Figure 4.1: The site distribution of the used $\delta^{18}\text{O}_{\text{cel}}$ network combined with the corresponding tree species. ....	47
Figure 4.2: The number of available $\delta^{18}\text{O}_{\text{cel}}$ time series within the network. ....	48
Figure 4.3: Correlation of the $\delta^{18}\text{O}_{\text{cel}}$ time series with the European VPD for the period 1900 to 1994. ....	51
Figure 4.4: The Nash–Sutcliffe CE for four different time slices. ....	52
Figure 4.5: Temporal variability of the VPD reconstruction. ....	54
Figure 4.6: The reconstructed summer VPD for Northern Europe in comparison with reconstructed summer temperature, precipitation and PDSI. ....	55
Figure 4.7: Same as Figure 4.6, but for Central Europe. ....	56
Figure 4.8: Same as Figure 4.6, but for the Mediterranean region. ....	57
Figure 4.9: Spatial pattern of VPD anomalies for selected years. ....	59
Figure 4.10: Five centuries of VPD variability for three different regions in Europe. ....	62

Figure 4.11: Spatial distribution of the summer VPD anomalies in Europe based on the projected changes (2071-2100) for SSP1-2.6 (A), SSP2-4.5 (B) and SSP5-8.5 (C) scenarios relative to the historical summer VPD during the 1971–2000 reference period. ....	64
Figure 5.1: Comparison of the modelled and observed climate for the period 1971-2000. ....	73
Figure 5.2: Differences in trends in climate model simulations and observations. ....	74
Figure 5.3: Projected changes to the Northern Hemisphere summer temperature. ....	76
Figure 5.4: Changes to summer precipitation under SSP1-2.6, SSP2-4.5 and SSP5-8.5. ....	77
Figure 5.5: Changes to summer potential evapotranspiration under SSP1-2.6, SSP2-4.5 and SSP5-8.5. ....	78
Figure 5.6: Changes to summer drought conditions under SSP1-2.6, SSP2-4.5 and SSP5-8.5. ....	80
Figure 5.7: Projected drought conditions for selected AR6 regions in Europe and Asia. ....	82
Figure 5.8: Projected drought conditions for selected AR6 regions in North America. ....	83
Figure 5.9: Averaged anomalies of summer soil moisture (entire column) under SSP1-2.6, SSP2-4.5, and SSP5-8.5. ....	85

## LIST OF TABLES

Table 2-1: Tier 1 experiments of ScenarioMIP described by the radiative forcing and the SSP. ....	14
Table 4-1: Characteristics of each sample site. ....	48
Table 4-2: Characteristics of the linear trend of three different future scenarios for Northern Europe, Central Europe and Mediterranean. ....	63
Table 5-1: Description of the used climate model ensemble for the historical run and three future scenarios. ....	69

# 01

## INTRODUCTION

## 1.1 MOTIVATION

Summer 2021 was extreme in many respects: numerous new temperature and precipitation records were set worldwide. For example, a heat wave occurred in western North America in June and July, which, in addition to setting a new Canadian temperature record of 49.6 °C, also set a new record for the measured temperature north of 50°N (e.g. Philip et al., 2021; WMO, 2021). Almost in parallel, several cities and communities in western Europe, centred on western Germany and eastern Belgium, experienced some of the most severe flooding since records began, killing over 200 people (e.g. Fekete and Sandholz, 2021). This included large-scale rainfalls of 100 to 150 mm on 14 and 15 July on already very wet soils. A few days later, from 17 to 21 July, the Chinese city of Zhengzhou was flooded. During these days, 720 mm of rain fell and the highest measured precipitation in one hour in China was recorded with 201.9 mm (WMO, 2021). Shortly afterwards, temperatures rose sharply in the Mediterranean region, with a new European temperature record of 48.8 °C being recorded in Italy in mid-August (Keith et al., 2021). In addition to these selected examples, there were numerous other global extreme events in the summer of 2021, such as a tornado in the Czech Republic or forest fires in Greece. But also throughout the year, e.g. temperature or precipitation anomalies could be observed that exceeded records from the past and demonstrably had a major impact on society (e.g. Fekete and Sandholz, 2021).

The changing climate on planet Earth is not only causing temperatures to rise globally but also causing the characteristics of climate extremes, such as frequency and magnitude, to change. The causes of this can be very diverse and are often indirectly or directly related to the rise in the global mean temperature (e.g. IPCC, 2021). As the highest temperatures are reached in the summer months, several of these climate extremes, such as heat waves, floods and droughts, occur mainly in the summer (IPCC, 2021). Precise knowledge of how climate extremes and their spatial and temporal characteristics develop in the summer is accordingly highly relevant for society to adapt or prepare for the impacts of climate extremes. For example, early warning mechanisms can be developed to prepare for large economic losses, or disaster management in case of floods can be optimised.

The World Climate Research Programme's (WCRP) international climate science research strategy addresses the high societal relevance and incomplete scientific understanding of climate extremes. The WCRP is a WMO-based international climate science coordinating organisation that works to develop, share, and apply climate knowledge for the benefit of society (Brasseur and Carlson, 2015). In order to answer the questions with the highest societal relevance, to combine capacities and efforts, to minimize uncertainties and to deepen knowledge about climate, seven Grand Science Challenges (GCs) have been developed by the WCRP (Brasseur and Carlson, 2015). One of these GCs deals with the assessment of climate extremes. The aim is to work out what controls them, how they have

changed in the past, and how they might change in the future (Zhang et al., 2014; Alexander et al., 2016). Therefore, this research field is currently a key topic for climate science.

The major challenge begins with the definition of climate extremes. There is a multitude of definitions, different international standards, different temporal durations of climate extremes, and different spatial conditions that are often not taken into account (e.g. Sillmann et al., 2017). In addition, the definition is often based on a threshold or distribution of historical observations that, when applied in recent decades or for future projections, cannot draw on the same stationary processes as once existed in the historical periods. Therefore, stationarity and linearity cannot be assumed when comparing climate extremes. However, one of the greatest challenges is the availability of observational records. Climate extremes are rare in themselves. Therefore, long-term observations are needed to compare several climate extremes of the same type and under the same initial spatial and climatic conditions. This is challenging as weather records are very inhomogeneous in spatial distribution as well as in quality (e.g. Schneider et al., 2018). While in densely populated and industrialised areas, such as Western Europe, one can draw on many time series covering the last 100 to 150 years, records from unpopulated or non-industrialised areas often cover only 40 to 70 years. When analysing climate extremes that occur only a few times a century, their large-scale drivers and the influence of climate change on their frequency, there is often a lack of statistical significance for many parts of the world due to the data situation described. Thus, it is a challenge for climate science to quantify changes in the spatial and temporal characteristics or underlying mechanisms of climate extremes (e.g. Sillmann et al., 2017). In addition, it is challenging to check future developments of climate extremes in future scenarios for plausibility and consistency in comparison with historical observations (Sillmann et al., 2017).

It is precisely these challenges that this thesis addresses. The analyses and results presented in this thesis are based on four defined strategy points of the WCRP for this GC (Alexander et al., 2016) and focus in particular on the summer climate. The first task of the topic climate extremes is to document them. In this thesis, past climate conditions outside the instrumental observation period are reconstructed in order to be able to make more reliable statements about climate change and current climate extremes. The second point of the WCRP is the understanding of the effect of large-scale, regional and local climate-affecting activities and processes and their impact on the occurrence of climate extremes, which can be enabled by reconstructed climate data. For this purpose, reconstructed climate states are compared and visualised in this thesis with large-scale climatic processes, such as large-scale atmospheric and oceanic circulation. Thirdly, climate extremes are to be successfully modelled and their changes simulated. Therefore, this thesis makes use of existing climate models, which are evaluated with a focus on drought extremes and verified with historical observations. Furthermore, these models can also be used to determine the decisive factors for climate extremes, and to predict their propagation and frequency, which is the subject of point four of the GC strategy.

In this thesis, future climate scenarios are used to investigate the influence of increasing greenhouse gas emissions on drought extremes.

## 1.2 STRUCTURE & OBJECTIVES OF THE THESIS

Besides the introduction, the thesis is divided into 5 main chapters. Chapter 2 provides the necessary basics about the climate system, climate models and climate proxies. Based on this, Chapters 3 to 5 present the main findings of this thesis and are oriented towards the research questions explained below. Chapter 3 is published in Balting et al. (2021a) in *Climate of the Past*. The results shown in Chapter 4 are prepared for the submission at *Nature Scientific Data* (Balting et al., in preparation), while Chapter 5 is published in Balting et al. (2021b) in *npj Climate and Atmospheric Science*. Thus, each of the chapters represents a separate study, with a separate introduction, methodology and presentation of results, as well as a separate discussion. Finally, Chapter 6 summarises the main findings and presents an outlook.

The aim of this thesis is to address three research questions. These questions and a brief explanation of them are presented in the following:

1. What large-scale patterns can be captured by a  $\delta^{18}\text{O}_{\text{cel}}$  tree-ring network and is there a link to the El Niño-Southern Oscillation (ENSO)?

The analysis of time series of oxygen isotope ratio in tree ring cellulose ( $\delta^{18}\text{O}_{\text{cel}}$ ) from individual sample sites has so far been used to establish local or regional links to climate parameters (e.g. Etien et al., 2008). The aim is to present a comprehensive spatial-temporal analysis of a European large-scale  $\delta^{18}\text{O}_{\text{cel}}$  network and to determine the dominant modes of the network for the last 400 years. Furthermore, the influence of external and internal factors on the summer climate will be investigated, e.g. ENSO, and the composition of the  $\delta^{18}\text{O}_{\text{cel}}$  can be better understood.

2. What trends in the summer water vapour pressure deficit (VPD) have occurred in Europe over the last 400 years and how do they look in future scenarios?

The topic of VPD is still relatively new and unexplored. VPD has received particular attention as studies have found that VPD is an important factor for plant growth (Restaino et al., 2016), forest mortality (Park Williams et al., 2013), drought occurrence (Dai, 2013), crop production (Zhao et al., 2017) and wildfire occurrence (Seager et al., 2015). Long-term observations and large-scale evaluation of VPD variability are scarce. Therefore, gridded fields of European summer VPD from 1600 to 1994 are reconstructed to answer this question using a European  $\delta^{18}\text{O}_{\text{cel}}$  network from tree rings. The goal is to provide the first large-scale and long-term perspective on the past VPD variability and trends in Europe. Furthermore, the reconstructed and observed VPD conditions in Europe are compared with the VPD evolution in different future climate scenarios.

3. Can historical simulations of a climate model reproduce historical summer drought observations, and how do the greenhouse gas concentration affect the probability of summer droughts?

Reliably determining drought conditions for the coming century can help to develop adaptation strategies or provide information on how greenhouse gas emissions effect drought probability. To make this possible, the current ability of climate models from a coupled model intercomparison project is evaluated in the context of reproducing historical observed drought conditions. Depending on this, the ability to determine future drought probabilities of three climate scenarios can be assessed. Furthermore, with the help of the climate model experiments for a future climate, it is also possible to predict the influence of greenhouse gas concentrations on regional drought probabilities, to recognise spatial patterns, and to identify hotspots for future droughts.



# 02

## THE CLIMATE SYSTEM AND CLIMATE PROXIES

## 2.1 CLIMATE SYSTEM

Before the hypotheses can be discussed, it is necessary to explain the climate system and the individual factors in more detail. Basically, the climate system is determined by five spheres (Figure 2.1; Stocker, 2011):

1. The atmosphere is an important part of the climate system, since processes such as the weather, the Earth's radiation budget, the formation of clouds and precipitation, large-scale circulations, and heat transport among others, are co-determined in it. The atmosphere is a mixture of gases and it reacts comparatively fast to changes in the climate system.
2. The hydrosphere comprises all forms of water above and below the Earth's surface: the entire ocean as well as freshwater in rivers, lakes, and groundwater. Important processes that belong to the hydrosphere are, for example, transport processes of oceanic water masses, heat transport, or mass transport.
3. The cryosphere includes all forms of ice in the climate system: ice shelves, sea ice, glaciers, and permafrost. The cryosphere is an important part of the climate system because among others, it has a significant influence on the Earth's albedo. This sphere responds comparatively slowly to changes in the climate system.
4. The lithosphere or land surface describes the properties of the soil and solid earth. This sphere is decisive for the position of the continents, the depth of the oceans, the albedo of the land surface, and the position of the climate zones.
5. The biosphere groups together all the flora and fauna on land masses as well as in the oceans. One well-known influence of the biosphere is the uptake and release of greenhouse gases, although it is also relevant for many other processes in the climate system.

In some cases, a sixth sphere is also attributed to the climate system. This is the so-called anthroposphere, which describes the influence of humans on the climate system. This includes, for example, gas emissions (e.g. IPCC, 2013). However, these five or six spheres that determine the climate system do not stand alone, as all spheres interact with each other on different time and spatial scales. This can be the change in the position of the continents, which significantly alters the properties of the local biosphere, or the comparatively rapid heat exchange between the oceans and the atmosphere. Therefore, a major challenge in climate science is to explore mechanisms and processes in the spheres, as well as to understand the interactions between them.

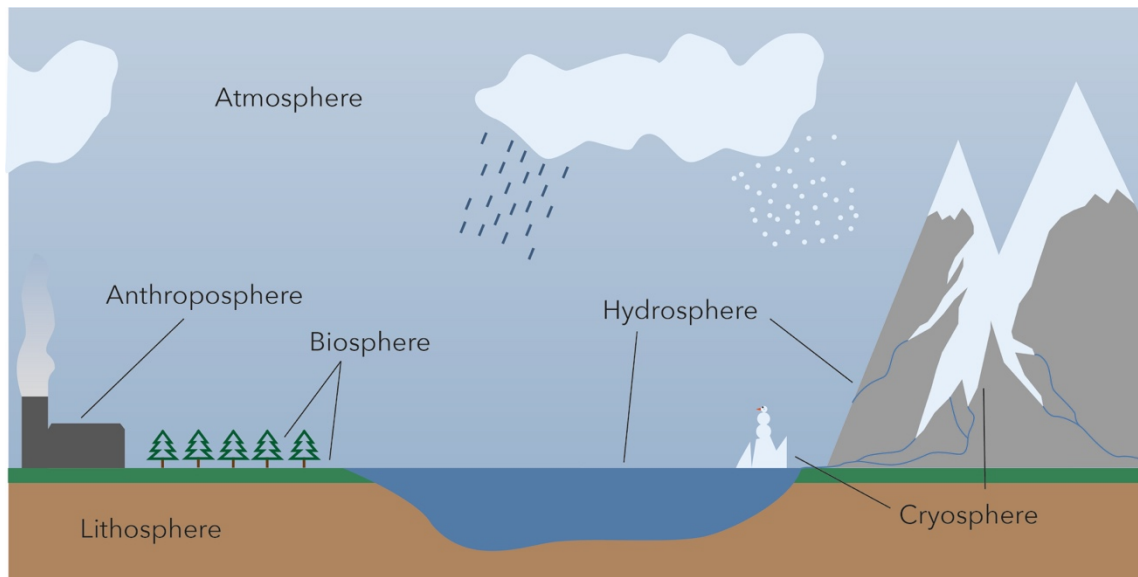


**Figure 2.1:** The six spheres of the Earth that influence the climate system. Note, the representation of the spheres and the climate system is a simplification, as the processes within and interacting with other spheres are more complex.

## 2.2 CLIMATE MODELS

After the brief introduction of the components of the climate system, the question now is how processes that take place within and between spheres can be analysed more precisely. The classical way to better understand processes or to test hypotheses is to collect measurements and to analyse them specifically. However, when it comes to large-scale or complex mechanisms that are difficult to analyse with observations, it can be advantageous to model the processes and mechanisms. The aim of climate modelling is to understand physical and chemical information and data obtained from palaeodata (Stocker, 2011).

Since the processes and mechanisms in the climate system are very diverse, there are models with different sizes of dimensions or spatial resolution. Basically, climate and Earth system models are based on fundamental physical principles and reproduce many important aspects of the observed climate (IPCC, 2021). However, the set-up of the models can differ significantly from climate models with zero dimensions (e.g. simple energy balance models) to complex Earth system models with three spatial dimensions (e.g. Atmosphere–Ocean General Circulation Models (AOGCMs)). Earth system models are so complex because the explicit solution of the energy, momentum and mass conservation equations must be calculated at millions of points on Earth, in the atmosphere and on land (IPCC, 2013).

The final choice of model for a particular application depends directly on the scientific problem (Held, 2005), with the complexity of the models defining the appropriate scope of application (IPCC, 2013). For many research projects, it is not necessary that all global processes are well represented.

Rather, it is important that the processes to be analysed can be represented well enough by the model. Therefore, even supposedly unimportant processes are removed from the model or simply parameterised. In general, parameterizations are included in all model components to incorporate processes that cannot be explicitly resolved or are not understood (IPCC, 2013). This saves additional computing resources, which can play a major role for large and long simulation durations. For this reason, intelligent simplifications and models with reduced complexity are in demand (Stocker, 2011). The ‘standard’ climate models are AOGCMs, which are used to understand the dynamics of the physical components of the climate system (atmosphere, ocean, land, biosphere and sea ice), and for making projections (IPCC, 2013). In case of biogeochemical feedbacks, Earth System Models (ESMs) are the current state-of-the-art models, and they include representation of various biogeochemical cycles (Flato, 2011).

In order to expand the application areas of models, it is possible to couple models with each other. This means that two or more models regularly exchange the relevant boundary conditions with each other. For the coupling of ocean and atmospheric models, this means that, among other things, the heat transfer between oceans and atmosphere must be implemented. As a consequence, a warm atmosphere, for example, gives off energy to a cold ocean. The coupling between models of the spheres has the advantage that processes that depend globally on several spheres can be represented better and more accurately. Furthermore, a more accurate picture of processes can be generated, as further boundary conditions and interfaces can be better modelled. To be able to model the global climate system completely, it is therefore necessary to represent all spheres as a model and to couple them efficiently and meaningfully with each other.

Especially in the climate system, the investigation of different driving forces on the different spheres are highly relevant. So-called radiative forcing (RF) can be used to define which influences act on the observed system, whereby RF is defined as a measure of the net change in the energy balance in response to an external perturbation (IPCC, 2013). An example of a predefined RF is the fluctuation of solar radiation, volcanic eruptions or changes in greenhouse gas emissions. Also anthropogenic activity can perturb the Earth’s radiation budget and can be considered (Flato, 2011). Once a forcing is applied, complex internal feedbacks determine the eventual response of the climate system (e.g. IPCC, 2008). Therefore, changes to the RF allow statements about the reaction of the climate system to certain events or certain conditions and can be used to develop scenarios or to model the climate of the past.

The simplest approach to assessing the quality of climate models is to compare observed and simulated climate variables (e.g. Gleckler et al., 2008). In order to understand the cause of model errors, it is necessary to examine the processes both in the context of the full model as well as to evaluate them in isolation (IPCC, 2013). In addition to looking at the model individually, it is also possible to evaluate the performance of multiple models. So-called multi-model ensemble methods are used to

investigate uncertainty in climate model simulations, including structural uncertainties due to different model formulations (e.g. Tebaldi and Knutti, 2007; IPCC, 2013, 2021). If the results of a model are consistent overall, the model created provides a quantitative interpretation of the development of the climate within a certain time frame based on the physical and chemical replication of reality (Stocker, 2011). Nevertheless, climate models should always be viewed critically, because, like any mathematical model of natural systems, a climate model is a simplification.

---

### 2.2.1 COUPLED MODEL INTERCOMPARISON PROJECT

Over the past decades, a large number of institutes have developed their own General Circulation Models (GCM) or use the GCM from other institutes for their applications. However, it is important to compare the model used with other climate models in order to assess its validity and performance compared to other climate models (IPCC, 2013). This allows the quality of the individual climate models to be assessed and sources of error to be identified (e.g. Tebaldi and Knutti, 2007).

The systematic comparison of several climate models from different institutes is organised within the framework of Model Intercomparison Projects (MIPs). They define experiments in advance, the necessary standardisation of data structure, and output requirements to enable a meaningful comparison. The structure of MIPs is crucial for the reusability of the generated data and the transparency of the calculated results. Because MIPs were not uniformly standardised, relationships between models were difficult to determine, and there was a growing need for systematic multi-model comparison of climate models (Eyring et al., 2016), the Coupled Model Intercomparison Project (CMIP) was first organised by the Working Group on Coupled Modelling more than 20 years ago (Meehl et al., 1997). Since then, it has evolved over six phases into a major international multi-model research activity (Meehl et al., 1997, 2000, 2005, 2007; Taylor et al., 2012; Meehl et al., 2014; Eyring et al., 2016).

The aim of the CMIP is to create a common standardisation for data formats (structure and metadata), data management, data documentation, data collection, and data access to provide a framework that promotes consistency and transparency and serves as a reference system (e.g. Eyring et al., 2016). An important part of CMIP is to make the multi-model results publicly available and to involve the whole community (e.g. Meehl et al., 2014). This framework can also be used by other MIPs that can draw on the data infrastructure and CMIP standards. Thus, the CMIP creates a framework that unites a variety of coordinated modelling activities. According to Eyring et al. (2016), this can reduce duplication of effort, minimise operational and computational burden, and establish common practices in the production and analysis of large volumes of model results. Furthermore, it also gives researchers access to climate model data who do not have the required computing resources.

To increase the relevance of the CMIP, it is now organised under the patronage of the WCRP. Thus, the CMIP not only addresses general questions, such as "How does the Earth system respond to forcing?", but also addresses the WCRP GCs (WCRP, 2016). However, the CMIP has received more

attention in recent years because the IPCC's Fifth Assessment Report (IPCC, 2013) uses the output data of CMIP5 (Taylor et al., 2012). The output of the next phase of CMIP is also used for the IPCC's Sixth Assessment Report (AR6; IPCC, 2021). It should be noted that not only the comparison of CMIP experiments is used, but also the results of the 23 MIPs developed in the framework of CMIP6.

Participation in CMIP and thus in the associated MIPs is conditional on adherence to the common standards, coordination, infrastructure and documentation, as well as the implementation of the DECK (Diagnostic, Evaluation and Characterisation of Climate) and CMIP historical simulations (Meehl et al., 2014). The DECK experiments are designed to (1) provide continuity across past and future CMIP phases, (2) change as little as possible over time, (3) be well-established and include simulations that modelling centres are doing anyway as part of their own development cycle, and (4) be relatively independent of the drivers and scientific goals of any particular CMIP phase (Eyring et al., 2016). According to Eyring et al. (2016), the design of the DECK experiments has proved useful in answering a variety of questions related to recent climate change and in detecting model errors.

The first DECK simulation is the pre-industrial control simulation (piControl). According to Eyring et al. (2016), this simulation is conducted under conditions representative of the period before the onset of large-scale industrialisation, using 1850 as the reference year. The piControl simulation serves as an equilibrium climate experiment, which is defined as an experiment in which the models can fully adapt to a given change in RF (IPCC, 2013). Thus, no change in RF takes place. This experiment can be used to analyse the dynamics of internal processes that are not affected by the variability of the RF. Furthermore, the piControl simulations serve as a starting point for all subsequent historical simulations.

The next two experiments are clearly driven by CO<sub>2</sub> forcing and start with the piControl simulation. In the first, the CO<sub>2</sub> concentration is immediately and abruptly quadrupled (abrupt-4×CO<sub>2</sub>) from the 1850 global annual mean used in piControl (Hansen et al., 1981). In the second, the CO<sub>2</sub> concentration is gradually increased at a rate of 1% per year (1pctCO<sub>2</sub>; Meehl et al., 2014). Both experiments are used to analyse the response of the climate system to greenhouse gas forcing and equilibrium climate sensitivity, comparing non-linear and linear influences.

The final DECK experiment is the Atmospheric Model Intercomparison Project (AMIP; Meehl et al., 2014), where simulations are performed using only atmospheric general circulation models for the period 1979 to 2015.. The idea of AMIP is to analyse and assess the atmospheric and land-based components of the climate system when constrained by observed ocean conditions (Eyring et al., 2016).

In addition to the four DECK experiments, another requirement for participation in CMIP is the simulation of the historical period from 1851 to the end of 2014. The simulation starts from the piControl simulation, and the forcing is based on observations of externally imposed forcing such as

solar variability, optical properties and fractional changes in the effective radius of cloud droplets, volcanic aerosols, global gridded land use datasets, and changes in atmospheric composition caused by human activities (Eyring et al., 2016). This will allow the simulations to be compared with observations of historical climate and determine the ability to represent variability and trend (e.g. Balting et al., 2021b). Therefore, the simulations of the historical climate are also used in later chapters of the thesis.

---

### 2.2.2 THE SCENARIO MODEL INTERCOMPARISON PROJECT

In order to better understand the impacts of climate change and to develop adaptation strategies, it is necessary to investigate scenarios of future climate development. Thus, based on the Special Report on Emissions Scenarios (SRES; Nakićenović et al., 2000) of the IPCC, climate model projections were carried out for the first time in phase 3 of the Coupled Model Intercomparison Project (CMIP3; Meehl et al., 2007). Since then, the primary goal has been a better understanding of the impacts on the climate system and on society with AOGCMs (e.g. Meehl et al., 2007).

Since CMIP3, not only the CMIP framework but also the scenarios have evolved. For example, the scenarios, which used to be an integral part of CMIP (e.g. Taylor et al., 2012), are now a stand-alone MIP based on the CMIP6 framework. In addition, the Scenario Model Intercomparison Project (ScenarioMIP) scenarios are no longer based on the representative concentration pathways (RCPs; van Vuuren et al., 2011) used in CMIP5, but on the Shared Socioeconomic Pathways (SSPs) as described in O'Neill et al. (2016). The advantage of the SSPs is that in addition to the change in greenhouse gas forcing, they also take into account the future development of society independent of climate change impacts (e.g. Kriegler et al., 2012). For this purpose, five SSPs were developed by O'Neill et al. (2017) to describe the societal development trend that are shortly summarized here. The SSPs 1 and 5 assume optimistic development for society, including a growing economy. However, they differ in that SSP 1 describes an increasing turn towards sustainability, while growth in SSP 5 is based on an energy-intensive, fossil-based economy. Also positive is SSP 2, which describes the development of society, with trends similar to historical development trends. In addition to the three SSPs with positive development trends, SSPs 3 and 4 describe a pessimistic trend with exemplary low investment in education and increasing inequality. Based on these five SSPs, integrated assessment models were used to determine the impacts of the different scenarios on energy systems, land use and the associated resulting greenhouse gases (Riahi et al., 2017) which can be used as in input for GCMs.

In order to map the possible development of society and climate change, it is necessary to integrate the designed SSPs into a scenario. For this purpose, all SSPs and model forcing were entered into a matrix as described in van Vuuren et al. (2014). Subsequently, each climate warming pathway was combined with the corresponding SSPs, if it is reasonable to create the social conditions for the SSP emissions to correspond to the pathway (van Vuuren et al., 2014). This results in a combination of

SSP drive pathways that represents an integrated scenario of future climate and societal change as proposed in Moss et al. (2010). Since the former four RCP scenarios from CMIP5 are not sufficient to cover the spectrum, new pathways have been identified based on this matrix or on policy decisions, e.g. the Paris Agreement (O'Neill et al., 2016). The name of the scenarios in ScenarioMIP is constructed to consist of the SSP and the long-term global mean radiative forcing (SSPX-Y) as shown in Table 2-1.

**Table 2-1: Tier 1 experiments of ScenarioMIP described by the radiative forcing and the SSP (O'Neill et al., 2016). Additionally the very likely change of surface temperature for 2081-2100 compared to 1850-1900 is given for each scenario (IPCC, 2021).**

SCENARIO	2100 RADIATIVE FORCING (W M-2)	SSP	WARMING RANGE (°C)
SSP1-2.6	2.6	1	1.3 - 2.4
SSP2-4.5	4.5	2	2.1 - 3.5
SSP3-7.0	7.0	3	2.8 - 4.6
SSP5-8.5	8.0	5	3.3 - 5.7

According to O'Neill et al. (2016), the ScenarioMIP experiments include a total of eight pathways of future emissions for the period 2015 to 2100, one simulation with a minimum number of ensemble members, and three long-term scenarios. All scenarios use the last day of the historical simulation (31 December 2014) as the starting point (1 January 2015) for the simulations. Therefore, the forcing of the scenarios has been harmonised with the historical forcing. Furthermore, all experiments are divided into two priority groups (O'Neill et al., 2016). The highest priority simulations (Tier 1), which must be carried out with at least one simulation per model in order to participate in the ScenarioMIP, comprise four key scenarios (Table 2-1). These are three further developments of the previous CMIP5 RCP scenarios. RCP2.6 became SSP1-2.6, RCP4.5 became SSP2-4.5 (middle part of the spectrum of future warming pathways) and RCP8.5 became SSP5-8.5 (upper end of the spectrum of future pathways; O'Neill et al., 2016). In addition, scenario SSP4-7.0 was developed to fill a gap between the RCP scenarios and to represent a mid to high future greenhouse gas pathway.

In addition to the experiments with the highest priority, there are further Tier 2 simulations as described in O'Neill et al. (2016). These simulations comprise four pathways of future emission, which either close gaps between the Tier 1 experiments or clarify specific forcing issues (SSP4-6.0, SSP4-3.4, SSP5-3.4-OS, SSPa-b). In addition, there is the SSP4-7.0 experiment, which, in contrast to Tier 1, requires at least nine simulations per model to make statements about the variability and uncertainty of the forcing. The Tier 2 simulations are concluded with long-term scenarios covering the period 2015 to 2300 to learn more about long-term feedbacks reversibility (SSP5-8.5-Ext, SSP5-3.4-OS-Ext, SSP1-2.6-Ext). In this thesis, only Tier1 scenarios are examined.

## 2.3 CLIMATE PROXIES

To study past climate conditions, instrumental observations are available for the past 150 years. Beyond this period, direct measurements of various climate variables are not attainable, and other indicators have to be used to obtain information on the evolution of climate. For example, historical records of Japanese cherry blossom dates for the last 1200 years have been used as proxy records for spring temperature (e.g. Aono and Saito, 2010). With the help of such historical information, not only temperatures for the beginning of the growing period can be estimated, but also for the whole growing season. The advantage of such records is that the information is comparatively reliable and that they are often available with a high temporal resolution. However, continuous historical records are relatively scarce and spatially limited.

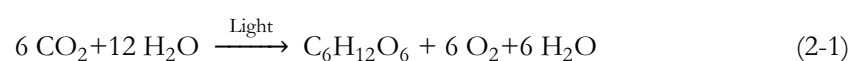
In order to obtain information about the past climate from locations where no human records are available, so-called climate proxies can be used. Climate proxies are indicators that are coupled or strongly correlated with at least one climate variable by a physical, chemical or biological process. Due to the different nature of proxy archives, a distinction is made between terrestrial and maritime climate proxies. An example for a terrestrial proxy is the tree ring width of trees, whereas an example of a maritime proxy is the chemical composition of growth layers of corals. The temporal resolution and the temporal coverage of climate proxies can be different. For example, tree-rings are annual, the growth layers of corals can be resolved bimonthly (e.g. Felis et al., 2018a), whereas marine sediments often have a decadal, multi-decadal or lower resolution (e.g. Nowaczyk et al., 2021).

In this thesis, a high-resolution climate proxy is needed to reconstruct information about the European climate in summer, which is resolved at least annually and is particularly sensitive to the months of June, July and August. The terrestrial climate proxy of stable isotopes in tree rings is suitable for this purpose and will be presented in the following subchapters.

---

### 2.3.1 PHOTOSYNTHESIS AND ENDOGENOUS & EXOGENOUS FACTORS

Trees and climate are linked in a multidirectional way. The number and distribution of trees influences climate, while the climate influences the growth and biochemical composition of a tree. An internal tree process that is strongly dependent on climate conditions and influences climate is photosynthesis. In this process, trees use inorganic carbon ( $\text{CO}_2$ ) from the atmosphere and water from the soil ( $\text{H}_2\text{O}$ ) to build glucose ( $\text{C}_6\text{H}_{12}\text{O}_6$ ) as part of the Calvin cycle. The resulting glucose is used for primary growth at the shoot tip of a tree and for secondary growth in the cambium (see Subchapter 2.3.2), which is essential for wood formation in an annual layer, i.e. tree rings. Furthermore, photosynthesis releases oxygen into the atmosphere ( $6\text{O}_2$ ).



The entire process of photosynthesis depends on various conditions. Endogenous factors result from the genetic and physiological structure of a plant, while exogenous factors are governed by the environment. The latter are defined by the six spheres and are related, for example to climate, soil structure or landscape morphology. Thus, endogenous and exogenous factors fundamentally control the entire growth process (Fritts, 1976; Schweingruber, 1996; Schönwiese, 2013a; Esper et al., 2017). However, the individual factors can vary in time and space and are perceived as stimuli by special sensor organs of the plant. Corresponding stimuli either lead to plant growth or trigger protective functions, such as the closing of the stomata of the leaves (Schönwiese, 2013a).

The influence of all endogenous and exogenous factors is stored annually in a tree ring. The temporal classification is supported by the ring formation, which makes it possible to obtain data with a high temporal resolution. Thus, tree rings are a proxy archive containing information about tree growth and conditions (endogenous, exogenous) at the time of ring formation (Saurer et al., 1997). The formation of a tree ring and the structure of the tree trunk associated with it are explained in the following subchapter.

---

### 2.3.2 STRUCTURE OF A TREE TRUNK

To better understand the importance of the annual ring and the interactions with other components, it is necessary to discuss the structure of a tree trunk in more detail (Figure 2.2). A key role in this is assigned to the so-called cambium which is responsible for the growth of wood and bast (Kaennel and Schweingruber, 1995). The cambium ring, which runs around the entire trunk of the tree, is formed from delicate, juicy, constantly dividing cells and increases the tissues that lie on both sides through an ongoing cell proliferation process (Rathgeber et al., 2016). When the tissue expands inwards, it forms the so-called secondary xylem (wood), which is the main component of a tree ring (Rathgeber et al., 2016). Within the secondary xylem, water and nutrients are transported towards the leaves from the roots. Cambium cells also expand outwards. As a result, new bast cells (phloem) are created every growing season, which constitute the innermost layer of the bark (Rathgeber et al., 2016). The bast cells are likewise important for transport processes, moving the sugar sucrose synthesized during photosynthesis in the crown to all parts of the plant where it is needed. The phloem is protected through the outer lying bark. Latter consists of dead cells from the bast.

With increasing age, the xylem cells in the annual rings "lignify" and finally die forming a solid inner wood area. This strongly lignified heartwood is much darker in colour as the less lignified so-called sapwood which contains alive and active cells close to the cambium.

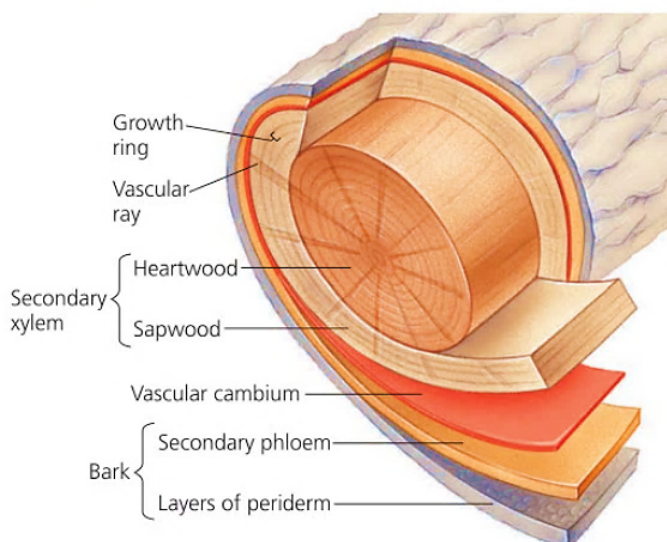


Figure 2.2: The anatomy of a tree stem (Urry et al., 2016).

In general, a tree ring consists of lighter and darker wood colorations. The reason for these effects is driven by different vegetation periods. On the temperate zone of the Northern Hemisphere, the vegetation period roughly reaches from March to October and is divided into three different phases of tree physiological activity: reserve mobilization phase (March to April), a growth phase (tree ring growth or thickness growth, May to July) and a reserve deposition phase (storage phase, August to October; Schweingruber, 1983). The inner element of a tree ring is the early wood. The early wood cells are thin-walled, very large, and they have tracheids (conifers and broad-leaf species) and/or tracheae (wood vessels; broad-leaf species, only), which serve as water pipes and perform mechanical support (Nultsch, 2001; Rathgeber et al., 2016). In contrast, late wood builds up in late summer/autumn when the wood accumulation decreases significantly in favour of reserve substances (starch, fatty acids) stored in woody rays and other woody parenchyma cells for fuelling the sprout in the coming spring (Schweingruber, 1983). Late wood consists of smaller cells that are additionally created which look dark brown. This type of wood is particularly dependent on the late summer/autumnal weather conditions.

### 2.3.3 STABLE ISOTOPES FROM TREE RINGS

To study and reconstruct the climate of the past, structural/physical as well as chemical properties of the tree ring can be used. In this study, the focus is particularly on ratios of stable isotopes. Isotopes are elements that have an equal number of protons and a different number of neutrons in their atoms. In the science of dendrochronology, the isotope ratios of oxygen, carbon and hydrogen in tree-ring cellulose, are often investigated. The advantage of evaluating isotope data from tree rings is the robust model understanding of isotope fractionations during photosynthesis. Besides the general advantage of tree-ring times series providing annual resolution, accurate dating and statistical confidence intervals from calibration and verification against instrumental climate data.

However, in order to measure isotopes in cellulose, a complex procedure is necessary to remove other components of a tree's annual ring, e.g. lignin and resins. The reason to remove them is that the use of the whole wood for stable isotope analysis leads to signal distortions because the mass fractions of the different wood components change and isotope signatures of the individual components differ from each other (Schollaen et al., 2017). To measure the isotopic ratios of the extracted cellulose, cellulose is packed into small silver foils that are subsequently converted to CO measuring gas in a pyrolysis oven (at 1400 °C) (cf. McCarroll and Loader (2004) and Loader et al. (2015) for details). The gas from each sample is passed through capillary tubes to an isotope ratio mass spectrometer (IRMS) where the individual isotopes are attracted to a magnetic field to varying degrees (depending on their neutron number). A detector then records exactly these isotope masses with an error tolerance of  $\pm 0.1\%$  for carbon and  $\pm 0.3\%$  for oxygen in this thesis.

In paleoclimate research, the isotope masses are grouped into element-related ratios (Equation 2-2), where the heavier, much less abundant isotope ( $E^{m+i}$ ) is always divided by the lighter isotope ( $E^m$ ). For instance, the ratio  $^{18}\text{O}/^{16}\text{O}$  is used in oxygen isotope analysis.

$$R_p = \frac{E^{m+i}}{E^m} \quad (2-2)$$

To minimize the error and to calibrate the results, the measured isotope data are calibrated with the standard value  $R_s$ , which leads to the well-known isotope ratio  $\delta$  (Craig, 1957; O'Leary, 1981). It is a helpful indicator, which is widely used in climate science:

$$\delta E^{m+i} = \frac{R_p - R_s}{R_s} \times 10^3 \quad (2-3)$$

---

#### 2.3.4 THE ISOTOPE EFFECT

While the representation of isotope ratios has been described, the question remains as to why and how isotope ratios can change. The answer to this question can be found in the basic differences between two isotope types of an element, e.g.  $^{16}\text{O}$  and  $^{18}\text{O}$ . Even though the number of neutrons has no influence on the gross chemical properties of the element and its compounds, mass differences can cause chemical and physical differences (Sharp, 2007). These differences are called the isotope effect (O'Leary, 1981), whereby the corresponding shift of an isotope ratio is called fractionation.

In the concept of fractionation, a difference is made between kinetic and equilibrium fractionation. Kinetic fractionation describes the effects of the different masses of two isotopes of the same element on their motion. According to Sharp (2007), the average velocity of a light isotope is higher than that of a heavy isotope, since the activation energy for heavy isotopes is higher than for light ones. As a result, lighter isotopes are fundamentally faster and can overcome resistance more easily than their heavier counterparts (O'Leary, 1980). This type of fractionation leads, for example, to the fact that

isotopically light molecules will preferentially diffuse out of a system and leave the reservoir enriched in the heavy isotope. Furthermore, it explains that more  $^{12}\text{CO}_2$  molecules than  $^{13}\text{CO}_2$  molecules strike the surfaces of leaves and enter the stomata (Sharp, 2007). This benefit for lighter isotopes is called fixation advantage (O'Leary, 1980).

In contrast to kinetic fractionation, equilibrium isotope fractionation describes the effects of atomic mass on bond energy and often occurs when a chemical exchange takes place between two molecules (Peterson and Fry, 1987). The energy required to break a bond is higher for a heavy isotope than for a light isotope, resulting in a difference in bond strength (Sharp, 2007). As a result, heavier isotopes concentrate in molecules where the bond strength is higher and lighter isotopes concentrate in molecules where the bond strength is weaker (Peterson and Fry, 1987; Fry, 2007). Moreover, this type of fractionation is dependent on temperature. When temperature increases, fractionation becomes smaller and when temperature decreases, fractionation are greater (Sharp, 2007).

The differences and fractionations form the foundation for the study of stable isotopes in science. With the help of the described fraction mechanisms, for example past temperatures can be reconstructed or entire chemical cycles can be better understood.

---

### 2.3.5 ISOTOPES OF OXYGEN

In this study, the focus is on the stable isotopes of oxygen since the necessary data coverage is given and the relevant processes are among the best researched. In general, oxygen is widely distributed in the climate system, an important part of the photosynthesis process, and the second most common element on Earth. In nature, this element has three stable isotopes. The lightest one, the  $^{16}\text{O}$  isotope, accounts for 99.757%, the heavier isotopes  $^{17}\text{O}$  and  $^{18}\text{O}$  account for 0.038% and 0.205% respectively (Audi et al., 2017). The isotope  $^{16}\text{O}$  (8 protons + 8 neutrons) and  $^{18}\text{O}$  (8 protons + 10 neutrons) are mostly used in paleo-climatological analysis because fractionation effects are more visible at higher mass differences (McCarroll & Loader, 2004). As already indicated in the subchapter before, the oxygen isotope ratio can be written in the conventional delta notation (Equation 2-4):

$$\delta^{18}\text{O} = \frac{\frac{^{18}\text{O}}{^{16}\text{O}}_{\text{sample}} - \frac{^{18}\text{O}}{^{16}\text{O}}_{\text{standard}}}{\frac{^{18}\text{O}}{^{16}\text{O}}_{\text{standard}}} * 1000 \quad (2-4)$$

Nowadays, the international reference standard is normed by the International Atomic Energy Agency and it is called Vienna standard mean ocean water (McCarroll & Loader, 2004).

---

### 2.3.6 ENVIRONMENTAL INFLUENCES ON THE OXYGEN ISOTOPE

For the interpretation of the environmental signature of the oxygen isotope ratio in tree ring cellulose ( $\delta^{18}\text{O}_{\text{cel}}$ ), it is important to know and describe the three main control factors. The first factor is the  $\delta^{18}\text{O}$  of soil water ( $\delta^{18}\text{O}_{\text{SW}}$ ) as it represents the  $\delta^{18}\text{O}$  input into the arboreal system. The  $\delta^{18}\text{O}_{\text{SW}}$

reflects an average or long-term variations of  $\delta^{18}\text{O}$  of precipitation ( $\delta^{18}\text{O}_p$ ) over several precipitation events (e.g. Saurer et al., 2012).  $\delta^{18}\text{O}_p$  at any location is the result of the previous rainout history and origin(s) of the moist air mass(es), which are governed by atmospheric circulation patterns and further fractionations. In middle and higher latitudes a significant positive relationship between  $\delta^{18}\text{O}_p$  values and air temperature, commonly called the temperature effect, is observed (e.g. Rozanski et al., 2013). Therefore, a steady shift of the isotope values from the equator to the poles is visible which is called latitude effect (Dansgaard, 1964; Gat, 2010). The averaged  $\delta^{18}\text{O}_p$  signal in  $\delta^{18}\text{O}_{\text{SW}}$  can be further modified by fractionation due to partial evaporation of isotopically lighter water vapor from the soil (depending on soil texture and porosity; Saurer et al., 2012). Therefore,  $\delta^{18}\text{O}_{\text{SW}}$  in combination with  $\delta^{18}\text{O}_p$  and  $\delta^{18}\text{O}$  of the groundwater (depending on site and tree species) represents the baseline variability.

The second factor is biochemical fractionation including partial isotopic exchange of cellulose precursors with stem water during cellulose biosynthesis (e.g. Saurer et al., 1997; Roden et al., 2000; Barbour, 2007), which can be considered as largely constant at  $27 \pm 4 \text{‰}$  (Sternberg and Deniro, 1983). This involves the proportional depression of water vapor pressure by the heavier  $\text{H}_2^{18}\text{O}$  ( $\epsilon^* = 9\text{‰}$  by  $20 \text{ °C}$ ) and the diffusion of the isotope through stomata ( $\epsilon^k = 16 \text{‰}$ ) (McCarroll and Loader, 2004).

Most important is the third factor: the evaporative  $^{18}\text{O}$  enrichment of leaf or needle water via transpiration of water vapor to the atmosphere (e.g. Saurer et al., 1997; Roden et al., 2000; Barbour, 2007; Kahmen et al., 2011; Treydte et al., 2014 and citations therein). The transpiration process is controlled by the leaf-to-air VPD modified by the aperture of stomata which controls the conductance for water vapor. In general, the stomata opens only as far as it allows to keep the optimal balance between  $\text{CO}_2$  binding and transpiration (Helle and Schleser, 2004). The  $\delta^{18}\text{O}$  values of leaf water are typically enriched in  $^{18}\text{O}$  compared to the plant's parent water because evaporative losses are greater for  $^{16}\text{O}$  than for  $^{18}\text{O}$  (Roden et al., 2000). Therefore, especially the first and the third control factor allow to relate  $\delta^{18}\text{O}_{\text{cel}}$  records to external environmental factors, whereas the biochemical fractionations are considered being rather constant.

# 03

## CLIMATE SIGNALS OF A EUROPEAN OXYGEN ISOTOPE NETWORK

### 3.1 LARGE-SCALE CLIMATE SIGNALS & $\delta^{18}\text{O}_{\text{CEL}}$

Tree growth is irrevocably affected by interactions with the hydrosphere, atmosphere, and pedosphere, and the influence of environmental factors is stored in the physical and chemical properties of each tree ring (Schweingruber, 1996). A major component of a tree ring is cellulose, which consists of the elements carbon, oxygen, and hydrogen. Their stable isotope signatures are determined by varying environmental conditions, influencing a series of fractionation processes during the uptake of  $\text{CO}_2$  and  $\text{H}_2\text{O}$  from the atmosphere and soil as well as the biosynthesis of tree-ring cellulose. For instance, the climate signature of  $\delta^{13}\text{C}$  values of tree-ring cellulose basically originates from fractionations during photosynthesis at the leaf or needle level that generally lower the  $\delta^{13}\text{C}$  of the atmospheric  $\text{CO}_2$  source which contains no direct climatic signal (e.g. Schleser et al., 1995).  $\delta^{18}\text{O}$  of tree-ring cellulose ( $\delta^{18}\text{O}_{\text{cel}}$ ) is of particular interest for paleoclimate studies because it is related to source water, i.e.  $\delta^{18}\text{O}$  of precipitation ( $\delta^{18}\text{O}_{\text{P}}$ ), which is directly affected by climate processes, such as temperature during droplet condensation within air masses, transport distance from ocean source, type of precipitation (e.g. rain or snow), and precipitation amount (e.g. Dansgaard, 1964; Epstein et al., 1977; Rozanski et al., 2013). Within the arboreal system,  $\delta^{18}\text{O}$  of soil water ( $\delta^{18}\text{O}_{\text{SW}}$ ) constitutes the  $\delta^{18}\text{O}$  input and usually represents an average  $\delta^{18}\text{O}_{\text{P}}$  over several precipitation events modified by partial evaporation from the soil (depending on soil texture and porosity) and by a possible time lag (depending on rooting depth) (Saurer et al., 2012). Representing the baseline variability, the oxygen isotope signature of tree-ring cellulose ( $\delta^{18}\text{O}_{\text{cel}}$ ) is invariably tied to  $\delta^{18}\text{O}_{\text{SW}}$ .

However,  $\delta^{18}\text{O}_{\text{cel}}$  is dependent on two more clusters of fractionations that reflect tree internal processes, namely (1) evaporative  $^{18}\text{O}$  enrichment of leaf or needle water via transpiration and (2) biochemical fractionations including partial isotopic exchange of cellulose precursors with trunk water during cellulose biosynthesis (e.g. Saurer et al., 1997; Roden et al., 2000; Barbour, 2007; Kahmen et al., 2011; Treydte et al., 2014; and citations therein). The biochemical fractionation during cellulose biosynthesis can be largely considered as constant at  $27 \pm 4 \text{‰}$  (Sternberg and Deniro, 1983). Nonetheless, varying leaf-to-air vapour pressure deficit and varying air humidity cause corresponding changes in the  $\delta^{18}\text{O}$  signature of leaf or needle water (e.g. Helliker and Griffiths, 2007). Although modified and dampened by physiological processes (e.g. Péclet effect; Farquhar and Lloyd, 1993) and oxygen isotope exchange with stem water during cellulose synthesis (Hill et al., 1995), the variability of the  $^{18}\text{O}$  enrichment of leaf water clearly affects  $\delta^{18}\text{O}_{\text{cel}}$ , as well as the strong signature of  $\delta^{18}\text{O}_{\text{P}}$ . For example,  $\delta^{18}\text{O}_{\text{cel}}$  values are used to reconstruct precipitation (e.g. Rinne et al., 2013), air temperature (e.g. Porter et al., 2014), and drought (e.g. Nagavciuc et al., 2018). As these quantities are largely based on transport processes within the atmosphere, the  $\delta^{18}\text{O}_{\text{cel}}$  values can be used to get detailed

information about large-scale atmospheric circulation patterns (Andreu-Hayles et al., 2017; Brienen et al., 2012; Lavergne et al., 2016; Nagavciuc et al., 2018; Trouet et al., 2018). The resulting long-term perspective on the climate from the use of  $\delta^{18}\text{O}_{\text{cel}}$  as a climate proxy may be the key to identifying the influence of different external forcing on, and the internal variability of, the behaviour of large-scale atmospheric circulation.

One of the most important components for the internal climate variability is the El Niño–Southern Oscillation (ENSO), which influences the atmospheric circulation globally (Allan et al., 1996). As ENSO variability is strongest in winter, multiple studies have identified a significant ENSO impact on the European climate during this season. Observational (e.g. Fraedrich and Müller, 1992; Fraedrich, 1994; Brönnimann et al., 2004; Pozo-Vázquez et al., 2005; Brönnimann et al., 2007) and model studies (e.g. Merkel and Latif, 2002; Mathieu et al., 2004) suggest that an El Niño event leads to a negative phase of the North Atlantic Oscillation (NAO), with cold and dry conditions over northern Europe and wet and warm conditions over south-eastern Europe in winter. Furthermore, it is also possible to identify a significant ENSO influence on European precipitation in spring (Van Oldenborgh et al., 2000; Lloyd-Hughes and Saunders, 2002; Brönnimann et al., 2007; Helama et al., 2009). However, significant impacts of ENSO with respect to European droughts could only be detected for the most extreme El Niño events (King et al., 2020). The extent to which these preconditions influence the climate conditions during summer is not yet known for Europe, but this information could be the key to a better understanding of European climate. Nevertheless, the relatively short period of existing instrumental data (Van Oldenborgh et al., 2000; Brönnimann et al., 2007) makes it difficult to describe the full range of ENSO variability as well as its possible consequences with respect to the climate of the European continent (Domeisen et al., 2019). Furthermore, the response of different climate variables to ENSO variability is either non-stationary (e.g. Fraedrich and Müller, 1992) and/or non-linear. For example, (Wu and Hsieh, 2004) showed that the large-scale atmospheric circulation response to El Niño and La Niña is asymmetrical.

The aim of this chapter is to present a comprehensive spatial-temporal analysis of the large-scale European atmospheric circulation based on the climatological signals of a European  $\delta^{18}\text{O}_{\text{cel}}$  network that extends back  $\sim 400$  years. The climate signal of the isotope network is extracted using an empirical orthogonal function (EOF) analysis. The results of the first two components are compared to climate data and different ENSO reconstructions. The comparison is carried out using a composite analysis and a correlation analysis. To test if  $\delta^{18}\text{O}_{\text{cel}}$  can capture multi-seasonal signals, the first component of the isotope network is correlated with gridded fields of modelled  $\delta^{18}\text{O}_{\text{p}}$  and  $\delta^{18}\text{O}_{\text{sw}}$ . Finally, the major results are critically discussed and compared to other studies.

## 3.2 ISOTOPE NETWORK & METHOD

### 3.2.1 THE ISOTOPE NETWORK

In this chapter, the first two dominant modes of variability of 26  $\delta^{18}\text{O}_{\text{cel}}$  records, distributed over Europe, are investigated and their relationships with regional and large-scale climate anomalies. A total of 22 of the 26  $\delta^{18}\text{O}_{\text{cel}}$  records were generated within the EU ISONET (Annual Reconstructions of European Climate Variability using a High-Resolution Isotopic network) project (Treydte et al., 2007a, b). Furthermore, four additional sites from Bulgaria, Turkey, southwestern Germany, and Slovenia were added to the ISONET network for the current study (Heinrich et al., 2013; Hafner et al., 2014). In total, the isotope network contains eight broadleaf tree sites (*Quercus*) and 18 coniferous tree sites (*Pinus*, *Juniper*, *Larix*, and *Cedrus*) from altitudes varying for each location from 10 m up to 2200 m above sea level (Figure 3.1 and Supplement 2). A total of 24 of the 26 sites are distributed over the European continent, whereas two additional sites are located in the Atlas Mountains of Morocco and in the Taurus Mountains of Turkey.

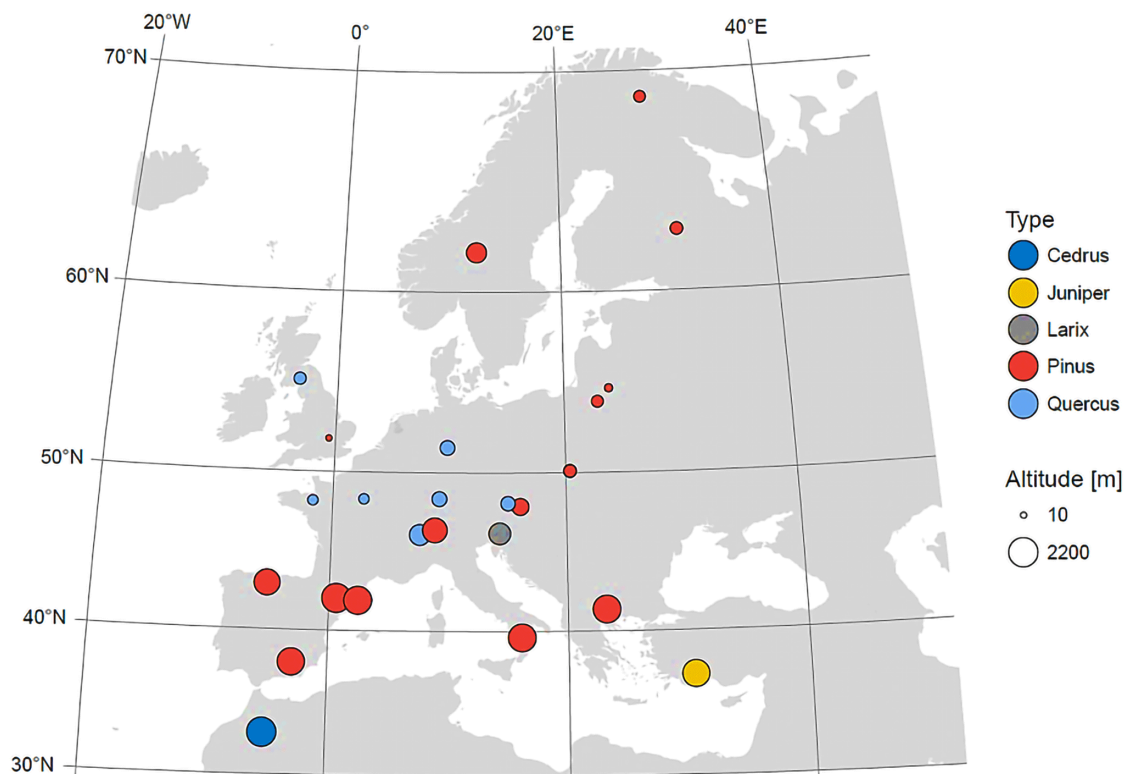


Figure 3.1: Spatial distribution of sample sites combined with the corresponding altitude. The highest density of sample sites exists in central and western Europe. The colour indicates the tree type: *Cedrus* – dark blue, *Juniper* – yellow, *Larix* – grey, *Pinus* – red, and *Quercus* – light blue. The corresponding elevation (10–2200 m) is shown by the size of the circles.

The stable isotopes of oxygen in tree-ring cellulose, reported as  $\delta^{18}\text{O}_{\text{cel}}$  vs. Vienna Standard Mean Ocean Water (Craig, 1957), for each site were determined as described by (Treydte et al., 2007a, b). At least four dominant trees were chosen per site, and two increment cores were taken per tree. After the standard dendrochronological dating following Fritts (1976), the individual tree rings were dissected from the cores. According to Treydte et al. (2007a, b), all tree rings from the same year were pooled prior to cellulose extraction for the majority of sites. For oak, however, only the latewood was used for the analyses. This procedure assumed that climate signals of the current year were predominantly applied, as the early wood of oaks frequently contains climate information of the preceding year. This is based on the fact that the proportion of the reserves of deciduous trees of the isotope network is higher at the beginning of tree-ring formation compared with the conifers of the isotope network (because they are evergreen). The isotope records have an annual temporal resolution.

The first 100 years of data from the network as well as a general description have already been published (Treydte et al., 2007a, b). Data from individual sites or regional groups of sites have also been published elsewhere (Saurer et al., 2008; Vitas, 2008; Etien et al., 2009; Hilasvuori et al., 2009; Haupt et al., 2011; Saurer et al., 2012; Rinne et al., 2013a; Helama et al., 2014; Labuhn et al., 2014; Saurer et al., 2014; Labuhn et al., 2016; Andreu-Hayles et al., 2017). Here, the extended ISONET+ product is used where the longest chronologies cover a period from 1600 to 2005. The highest data density is available for the period from 1850 to 1998: a total of 26 time series available for further analysis. A total of 12 time series covers the entire period of 400 years.

---

### 3.2.2 CLIMATE DATA

For the gridded climate information, the gridded fields of monthly temperature averages and monthly precipitation sums from the Climatic Research Unit (CRU TS) version 4.04 (Harris et al., 2020) are used. Both quantities are derived from the interpolation of monthly climate anomalies from extensive networks of weather station observations. The CRU TS dataset has a spatial resolution of  $0.5^\circ \times 0.5^\circ$  and covers the period from 1901 to 2019.

For the large-scale atmospheric circulation, gridded fields of geopotential height 500 mbar (Z500) from the 20<sup>th</sup> Century Reanalysis Project (20CR) version V2c (Compo et al., 2011) are used. The 20CR reanalysis dataset has a temporal resolution of 6 h and a meridional and zonal resolution of  $2^\circ$ . In this chapter, the ensemble mean of 20CR was used, which was computed from 56 ensemble members. The climate variables are available for the period from 1851 to 2014, and they are provided by NOAA/OAR/ESRL PSL, Boulder, Colorado, USA (downloadable from their website: [https://www.psl.noaa.gov/data/gridded/data.20thC\\_ReanV2c.html](https://www.psl.noaa.gov/data/gridded/data.20thC_ReanV2c.html), last access: 2 March 2020).

As precipitation and temperature are both important for the  $\delta^{18}\text{O}_{\text{cel}}$  ratio, the relation between the isotope ratio and drought conditions at the European scale is tested. For this purpose, the

Standardized Precipitation Evapotranspiration Index dataset from Vicente-Serrano et al. (2010) is used in this chapter with an aggregation time of three months (SPEI3). The SPEI3 index is suitable for this analysis because it considers the climate conditions of the pre-season.

Furthermore, the Extended Reconstructed Sea Surface Temperature version 5 (ERSST5; Huang et al., 2017) is included to investigate the correlation between the global sea surface temperature (SST) and the climate signals of  $\delta^{18}\text{O}_{\text{cel}}$ . The ERSST5 dataset was created by Huang et al. (2017), and it is derived from the International Comprehensive Ocean–Atmosphere Data Set. The monthly SST fields have a spatial resolution of  $2^\circ \times 2^\circ$ , and they are available for the time range from 1854 to present. The gridded fields of the ERSST5 dataset are provided by NOAA/OAR/ESRL PSL, Boulder, Colorado, USA, and they can be downloaded from their website (<https://www1.ncdc.noaa.gov/pub/data/cmb/ersst/v5/netcdf/>, last access: 15 October 2020). All of the above-mentioned climate data were seasonally averaged: DJF (December to February), MAM (March to May), JJA (June to August), and SON (September to November). Furthermore, the linear trend from each grid cell was removed.

As the chapter is focused on the relation between ENSO variability and the  $\delta^{18}\text{O}_{\text{cel}}$  network, anomalies (1981–2010 mean removed) of the December Niño 3.4 index (HadISST1; Rayner, 2003) are used. The index represents the averaged SST from  $5^\circ\text{S}$  to  $5^\circ\text{N}$  and from  $170^\circ$  to  $120^\circ\text{W}$  (downloadable from [https://psl.noaa.gov/gcos\\_wgsp/Timeseries/Nino34/](https://psl.noaa.gov/gcos_wgsp/Timeseries/Nino34/), last access: 3 March 2020). To compare the relation between ENSO variability and the variability of the isotope network (also in the past), three different reconstruction of ENSO activity have been used in this chapter: (i) the Dätwyler et al., (2019) reconstruction of the annual Niño 3.4 index for the last millennium (based on a multiproxy network); (ii) the reconstruction of the NDJ (November–December–January) Niño 3.4 index for the last 700 years by Li et al., (2011) (based on a tree-ring network in the tropics and mid-latitudes), and (iii) an annual reconstruction of ENSO variability based on the North American Drought Atlas (Cook et al., 2004; Li et al., 2013).

---

### 3.2.3 MODELLED $\delta^{18}\text{O}_{\text{CEL}}$ IN PRECIPITATION AND SOIL WATER

In addition to the observational and reanalysis-based climate data, the relation between  $\delta^{18}\text{O}_{\text{cel}}$  and  $\delta^{18}\text{O}_{\text{P}}$  and between  $\delta^{18}\text{O}_{\text{cel}}$  and  $\delta^{18}\text{O}_{\text{SW}}$  is investigated, as simulated by the water-isotope-enabled ECHAM5-wiso model (Werner et al., 2011), in order to gain further insights into the correlation with other seasons and to identify a multi-seasonal climate signal. The  $\delta^{18}\text{O}_{\text{P}}/\delta^{18}\text{O}_{\text{SW}}$  dataset was created by Butzin et al. (2014), who used the isotope-enabled version of the ECHAM5 atmospheric general circulation model (Roeckner et al., 2003; Hagemann et al., 2006; Roeckner et al., 2006) which is called ECHAM5-wiso (Werner et al., 2011). In Butzin et al. (2014), values of present-day insolation and greenhouse gas concentrations (IPCC, 2000) and monthly varying fields of sea surface temperatures and sea ice concentrations according to ERA-40 and ERA-Interim reanalysis data (Uppala et al.,

2005; Berrisford et al., 2011; Dee et al., 2011) are used to force the model. To represent the climate conditions of the period from 1960 to 2010, Butzin et al. (2014) used an implicit nudging technique (Krishnamurti et al., 1991; the implementation in ECHAM is described by Rast et al., 2013). The nudging technique is a part of climate modelling sciences, where modelled fields of climate variables are relaxed to observations or data from reanalyses. In the study of Butzin et al. (2014), the modelled fields of surface pressure, temperature, divergence, and vorticity are coupled to ERA-40 and ERA-Interim reanalysis fields (Uppala et al., 2005; Berrisford et al., 2011; Dee et al., 2011) for the period from 1960 to 2010. The monthly grids of  $\delta^{18}\text{O}_P / \delta^{18}\text{O}_{\text{SW}}$  have a horizontal grid size of approximately  $1.9^\circ \times 1.9^\circ$ . As this chapter is focused on seasonal variability, the seasonal averages are computed for  $\delta^{18}\text{O}_P / \delta^{18}\text{O}_{\text{SW}}$  (DJF, MAM, JJA, and SON).

---

### 3.2.4 DATA ANALYSIS

As a first step, the characteristics of each time series of the  $\delta^{18}\text{O}_{\text{cel}}$  network and their relation to altitude and latitude are investigated. For a better comparison, the linear trend of each  $\delta^{18}\text{O}_{\text{cel}}$  time series is removed and the time series are standardized (*z* values).

To combine the signals of the isotope network, the principal component analysis (PCA) and empirical orthogonal functions (EOFs) are used. These techniques have been described by Pearson (1902) and Hotelling (1935) and were used for the first time by (Lorenz, 1956) for climatological studies (Storch and Zwiers, 1999). By applying PCA, it is possible to extract a common climate signal from the  $\delta^{18}\text{O}_{\text{cel}}$  network that explains the highest part of the variability of the input dataset. This is done by rotating the initial data onto axes that are orthogonal to each other (Schönwiese, 2013b) by the corresponding eigenvectors. Therefore, the eigenvectors are used as a transformation matrix. The corresponding analysis of the eigenvector values is known as empirical orthogonal function (EOF) analysis. The goal of this analysis is to identify the most dominant patterns of the  $\delta^{18}\text{O}_{\text{cel}}$  tree network variability, which explain a significant part of the variance for a specific region. The largest part of the variance can be explained by the pattern of the leading EOF. The temporal perspective on these patterns is given by the principal components (PCs), which describe the phase and the amplitude.

The resulting components are further checked to establish if they fulfil the requirements of the rule of North et al. (1982). This rule states that the pattern of the eigenvectors of one component is strongly contaminated by other EOFs that correspond to the closest eigenvalues (Storch and Zwiers, 1999). To determine whether two consecutive patterns can be interpreted as distinct patterns, it is necessary to calculate the standard error in the estimation of the eigenvalues; according to North et al. (1982), this is approximately

$$\Delta\lambda \sim \lambda\sqrt{2/n} \quad (3-1)$$

where  $\lambda$  is the eigenvalue, and  $n$  is the number of degrees of freedom of the dataset. In case that the eigenvalues of two EOFs are not more separated from each other than this standard error, it is unlikely that the two consecutive patterns can be interpreted as distinct from each other, as any linear combination of the two eigenvectors is equally significant. In this chapter, only the eigenvectors are considered where the successive eigenvalues are distinguishable.

The ISONET network consists of a multi-site and multi-species tree-ring network more or less covering the period from 1600 to 2003. However, some tree-ring series cover the whole period, whereas other series cover only a shorter period. In order to be able to have a long-term perspective, one needs to find a statistically meaningful way to extend the shorter records to make use of the whole 400 years of data. As most multilinear principal component analysis algorithms do not work with gaps in the initial matrix, the algorithm developed by Josse and Husson (2016) is used that is able to fill the temporal gaps without a change in the PC. In the first step, the mean is placed in the gap and execute a PCA with this dataset. Afterwards, the dataset is projected onto the new component axis so that the values are rotated and the value of the gap changes. The new value of the gap is placed into the initial dataset. With this new dataset, a PCA is again carried out. This process is repeated until convergence is reached. The result is a gap-free dataset that can be used for PCA. To quantify if the results are influenced by the gap-filling method, the correlation between PC1 based on the ISONET network and the first four PCs of the Old World Drought Atlas (OWDA; Cook et al., 2015) is tested for the period from 1850 to 2005 and from 1600 to 2005. If the filling algorithm altered the representation of climate signals over a longer time period, it is expected that the strength of correlation is changing.

Composite maps of average precipitation, air temperature, geopotential height 500 mbar (Z500), and SST are computed using years where the network's principal components are above or below a certain threshold. In this chapter, maxima events are chosen above ( $>\mu+\sigma$ ) and minima events below ( $<\mu-\sigma$ ) 1 standard deviation ( $\sigma$ ) with respect to the mean ( $\mu$ ). The composite maps allow us to analyse the general climate state occurring at times of minima (low) or maxima (high) separately. In addition, both composites of climate conditions can be combined under the assumption that the minima and maxima events show the opposite climate state. For this purpose, the minimum composite is subtracted from the maximum composite at each grid point (high-low). In addition to the composite maps, the values of PC1 are extracted for those years for which ENSO values are higher than the average plus 1 standard deviation and lower than the average minus 1 standard deviation. The difference from the former distribution for the values of minima and maxima years is tested with a t test. To better understand if El Niño or La Niña events co-evolve with extremes in the  $\delta^{18}\text{O}_{\text{cel}}$  time series, event coincidence analysis (ECA) (Donges et al., 2016; Siegmund et al., 2017) using PC1 and a December Niño 3.4 index is applied (HadISST1; Rayner, 2003). ECA quantifies the simultaneity of events contained in two series of observations that can be computed with the “CoinCalc” R package

(Siegmond et al., 2017). Furthermore, the CoinCalc package provides functions to test if the coincidences are significant. In this chapter, it is investigated if the years in which the Niño 3.4 index is above (below) the 75th (25th) percentile match the 75th (25th) percentile in PC1. In general, a significance level of  $\alpha=0.05$  was used in all analyses.

Finally, the relation between seasonally averaged  $\delta^{18}\text{O}_\text{P}$  and  $\delta^{18}\text{O}_\text{SW}$  from winter, spring, and summer is analysed, based on nudged ECHAM5-wiso simulations (Butzin et al., 2014), with PC1 based on the  $\delta^{18}\text{O}_\text{cel}$  values from the ISONET network. The goal is to test the correlation between  $\delta^{18}\text{O}_\text{cel}$  and modelled  $\delta^{18}\text{O}_\text{P}/\delta^{18}\text{O}_\text{SW}$  to identify if the water, which is used within the photosynthesis processes, has a multi-seasonal isotopic signature.

### 3.3 RESULTS OF THE $\delta^{18}\text{O}_\text{CEL}$ NETWORK ANALYSIS

#### 3.3.1 CHARACTERISTICS OF THE $\delta^{18}\text{O}_\text{CEL}$ NETWORK

The highest mean  $\delta^{18}\text{O}_\text{cel}$  values occur in the southern locations (i.e. in Turkey and Cazorla in Spain). For oaks and pines, the lowest mean values are found for the northern sites (Figure 3.2a). Moreover, generally lower  $\delta^{18}\text{O}_\text{cel}$  values are identified for *Quercus* compared with *Pinus*. Angiosperm wood tissue contains vessels (i.e. specialized water-conducting cells) that are generally larger in diameter and, therefore, more conductive to water than conifer wood cells (Sperry et al., 2006; Carnicer et al., 2013). The overall variance in the datasets is not dependent on the type of tree species. The  $\delta^{18}\text{O}_\text{cel}$  time series from Pöllau in Austria is characterized by the highest standard deviation, whereas the time series from Lochwood in Great Britain shows the lowest standard deviation.

As the  $\delta^{18}\text{O}_\text{cel}$  source values and the fractionation processes are temperature dependent, it is necessary to evaluate the influence of altitude and latitude on the oxygen isotope ratio. The relation of the  $\delta^{18}\text{O}_\text{cel}$  values with respect to the altitude and latitude of each site is shown in Figure 3.2b,c respectively. In Figure 3.2c, the linear relationship between the average  $\delta^{18}\text{O}_\text{cel}$  values of the locations and the corresponding latitudes are plotted. As shown by the boxplots in Figure 3.2a, the southern sample sites are characterized by the highest average  $\delta^{18}\text{O}_\text{cel}$  values, whereas the northern sites show the lowest average  $\delta^{18}\text{O}_\text{cel}$  values. The relation between the  $\delta^{18}\text{O}_\text{cel}$  values and latitude yields a significant linear regression.

In addition to the latitudinal effect, altitude also influences the oxygen isotope ratios (as shown in Figure 3.2b) which can likewise be described by a significant linear regression. It should be noted that the southern sites are found at higher altitudes than the northern sites; thus, the latitudinal and altitudinal gradients may have confounding effects on  $\delta^{18}\text{O}_\text{cel}$ . Therefore, it is shown that the  $\delta^{18}\text{O}_\text{cel}$  network is influenced by a latitudinal and an altitudinal effect.

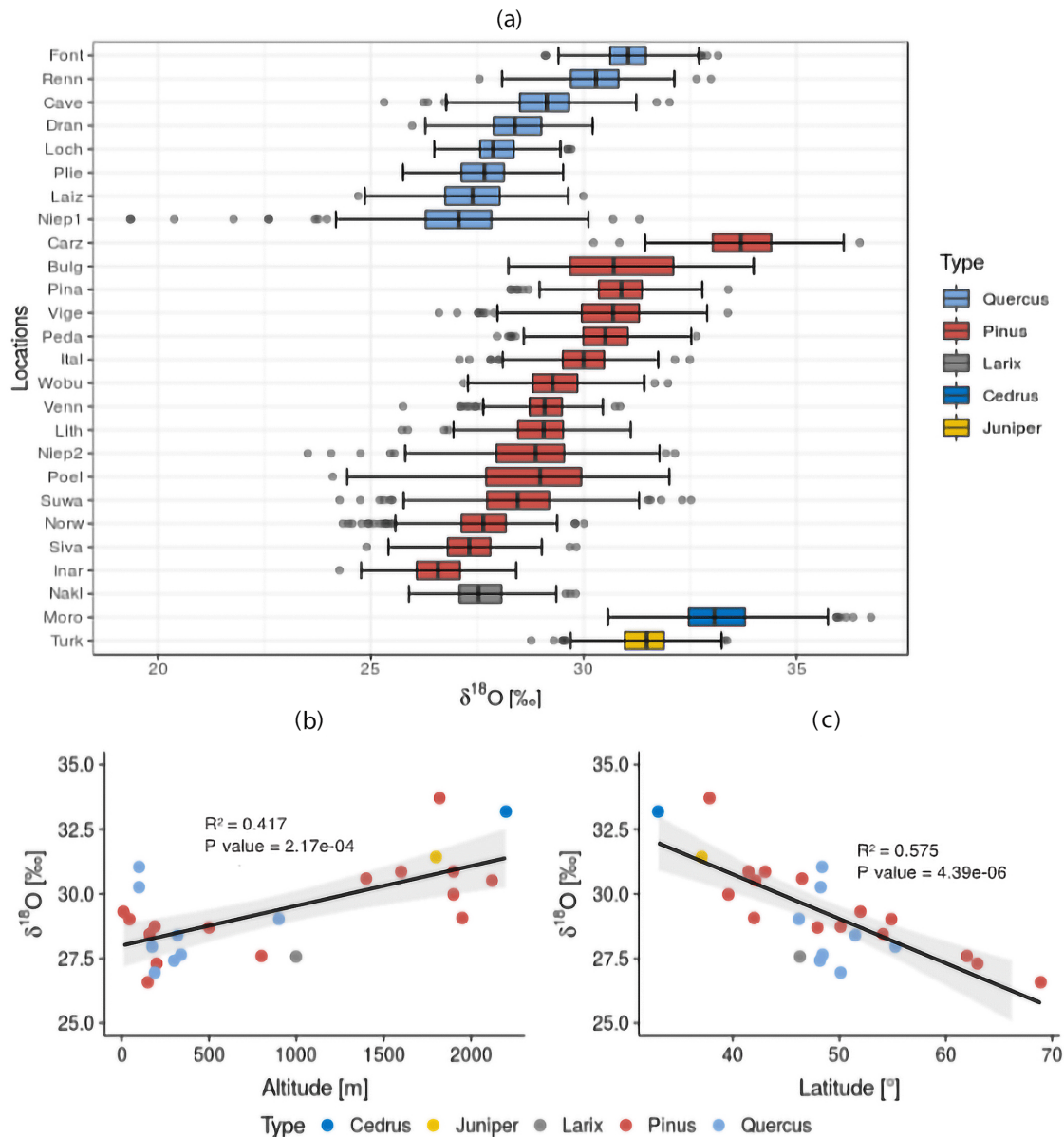


Figure 3.2: The characteristics of the European  $\delta^{18}\text{O}_{\text{cel}}$  time series. Panel (a) describes each time series using boxplots, which are firstly arranged by tree type and secondly by the average. Additionally, the relation between the average value of each time series is plotted against their latitudinal (b) and their altitudinal position (c).

### 3.3.2 CHARACTERISTICS OF THE PRINCIPAL COMPONENTS

Based on the EOF analysis, the first component of the isotope network explains 16.2% of the variance, the second explains 9.1%, the third explains 6.4%, the fourth explains 5.5%, and the fifth explains 5.2%. Therefore, the first five components explain a cumulative variability of around 43%. As the first two components also fulfilled the requirements of the rule of North et al. (1982), they are investigated with respect to their temporal and spatial characteristics.

The dominant pattern (EOF1), which describes 16.2% of the total variance, shows a spatially homogeneous structure (Figure 3.3a). The majority of time series in Europe are characterized by negative

eigenvector values. The pole of this EOF pattern is centred over France and Germany. In contrast, tree sites close to the Mediterranean Sea and the northernmost site in Finland are characterized by eigenvector values close to zero. Therefore, these locations contribute to a lesser extent to the first component's time series (PC1) shown in Figure 3.3c. The time series of PC1 is characterized by an underlying negative trend from the 17<sup>th</sup> to the 18<sup>th</sup> century. From the beginning of the 18<sup>th</sup> century, a positive trend is observed until the beginning of the 19<sup>th</sup> century, where the highest values are reached. For the last 150 years, no clear trend is visible.

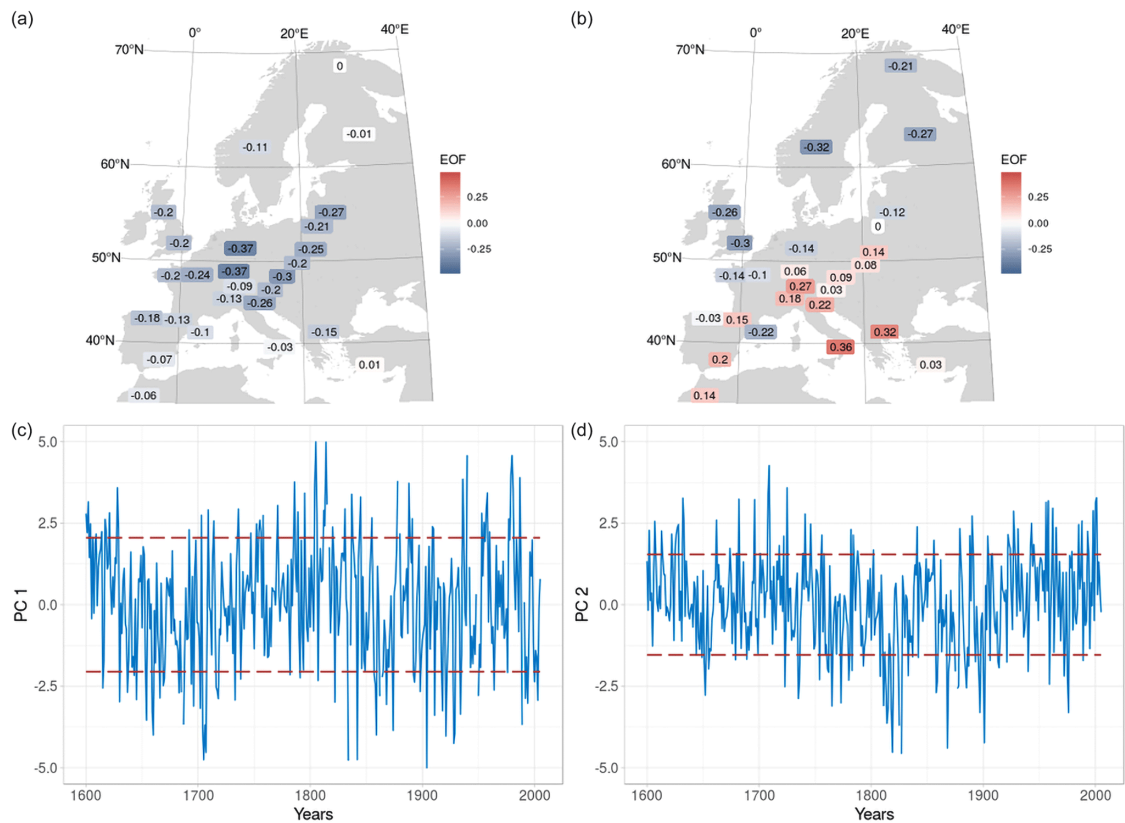


**Figure 3.3:** Spatial and temporal variability of the first two  $\delta^{18}\text{O}_{\text{cel}}$  components and EOFs: (a) EOF for the first  $\delta^{18}\text{O}_{\text{cel}}$  component (16.2% explained variance); (b) EOF for the second  $\delta^{18}\text{O}_{\text{cel}}$  component (9.5% explained variance). Panels (c) and (d) show the time series for the first and second  $\delta^{18}\text{O}_{\text{cel}}$  components. The dashed red lines indicate the standard deviation for the years 1600–2005.

The second EOF (EOF2) is characterized by a completely different spatial pattern (Figure 3.3b). Negative eigenvector values are found around the North and Baltic Sea, with the smallest eigenvector located in Norway, while positive eigenvector values are identified over the southern/south-eastern Europe and the Alpine region. The highest eigenvector values are recorded for the Italian site. In summary, this component highlights a dipole-like structure between northern and southern/south-eastern Europe. This dipole-like structure is a well-known feature of the European hydroclimate (Ionita et al., 2015). The time series of the second component (PC2) is characterized by an underlying positive trend from the middle of the 19<sup>th</sup> century onwards. Furthermore, the highest interannual

variability is found for the beginning of the 18<sup>th</sup> and 19<sup>th</sup> centuries. The highest values of the second component (PC2) are reached at the beginning of the 18<sup>th</sup> century, whereas the smallest values are identified for the beginning of the 19<sup>th</sup> century (Figure 3.3d).

Furthermore, the correlation between PC1 and the first four PCs for the summer drought reconstruction is tested based on the Old World Drought Atlas (OWDA; Cook et al., 2015) for the period from 1850 to 2005. The highest correlation ( $R=0.43$ ,  $p\text{-value}=3.1\times 10^{-08}$ ) is computed with PC2 of the OWDA, which explains 16.1% of the total variance of the OWDA (Supplement 2). If the filling algorithm altered the representation of climate signals over a longer time period, it is expected that the strength of the correlation would also change. However, the correlation changes only slightly to a Pearson's  $R=0.39$  ( $p\text{-value}=4.2\times 10^{-16}$ ) for the entire period from 1600 to 2005, which indicates that the filling algorithm does not impact the results. As a result, the climate signals obtained are robust and are presented in a similar manner as those for the period with a high sample coverage (i.e. 1850–2005). It is noted that, when using the gap-filling method, uncertainties might arise for the first century where the sample density is low. It is, therefore, important to mention that the interpretation for the first century needs to be handled with care, and statements should be regarded as less robust.

---

### 3.3.3 CLIMATE SIGNALS OF PC1

For the winter season, high values of PC1 are associated with significant warm SSTs in the equatorial Pacific and on the west coast of North and South America (Figure 3.4a), which indicates that the high values of PC1 are co-evolving with the occurrence of the El Niño conditions. The strong signal in the Pacific persists throughout spring (Figure 3.4c) and reduces in summer (Figure 3.4e). A significant warming of the tropical and North Atlantic is visible in spring and summer (Figure 3.4c, e). According to Latif and Grötzner (2000) the lagged warming of the equatorial Atlantic can be observed up to 6 months after an El Niño event. In contrast, the north-eastern Atlantic and the Mediterranean Sea are characterized by significantly colder SSTs in all three seasons. The low composite maps for PC1 and SST (Figure 3.4b, d, f) show features of La Niña conditions associated with colder than average SSTs. This pattern is particularly prominent in the tropical Pacific during winter and spring.

The related large-scale atmospheric circulation is shown in the composite map of Z500 (Figure 3.5). During high values of PC1 which are co-evolving with the occurrence of El Niño conditions, the atmospheric circulation over Europe is characterized by a low-pressure regime in winter, whereas high-pressure regimes can be identified over the north-western Atlantic as well as east of the low-pressure system (Figure 3.5a). This fits well with the composite map of air temperature in Figure 3.6b which shows significant cold conditions over northern Europe and significant warm conditions over south-eastern Europe. The described temperature pattern shows similarities to the effects of a negative phase of the winter NAO. The opposite climate state can be observed for low values of PC1 in

winter (Figure 3.5b Figure 3.6b). The atmospheric circulation remains in a similar configuration over Europe and the North Atlantic for low and high composite maps for spring (Figure 3.5c, d) compared with the winter season (Figure 3.5a, b). One important difference from the pre-season is that a pressure belt is visible between Europe and the Gulf of Maine in both maps.

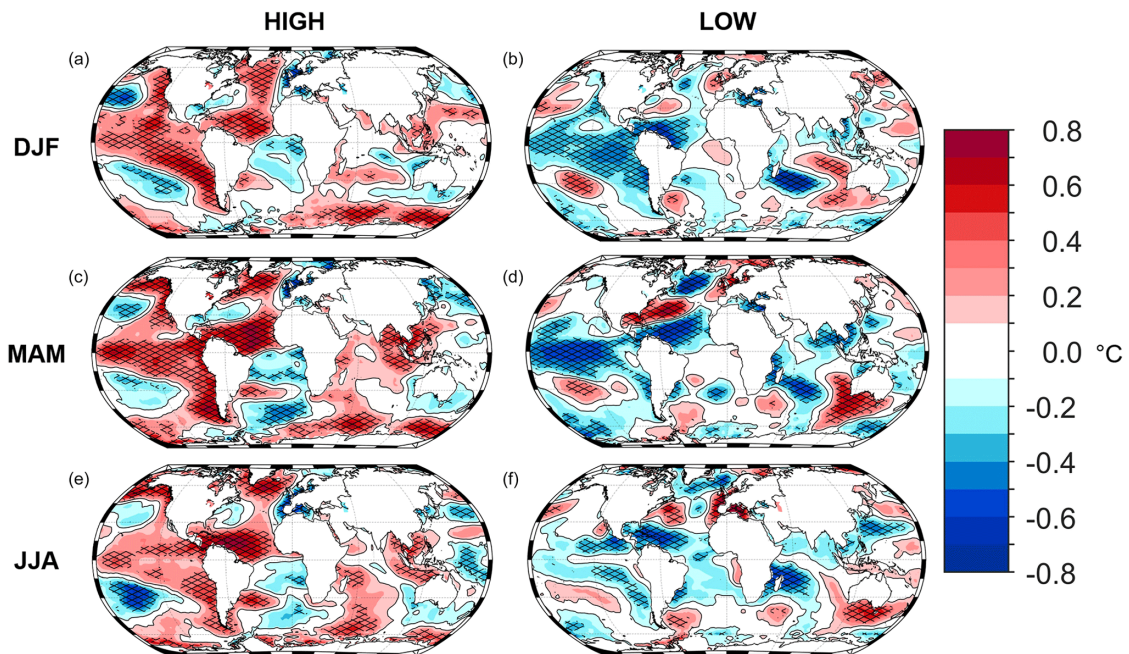


Figure 3.4: Composite maps (high and low) of SSTs related to the first  $\delta^{18}\text{O}_{\text{cel}}$  component for the DJF, MAM, and JJA seasons. Panels (a) and (b) show the characteristics of the climate in DJF, panels (c) and (d) show the characteristics of the climate in MAM, and panels (e) and (f) show the characteristics of the climate in JJA. The results for maxima (a, c, e) and minima (b, d, f) events of PC1 are also given. The SSTs in winter, spring, and summer are characterized by ENSO activity. Furthermore, the significance is shown using a black grid overlay. The SST dataset from ERSST (Huang et al., 2017) is included in this figure for the period from 1854 to 2005.

The composite maps of Z500 for summer are characterized by a pressure regime centred over France and Germany (Figure 3.5e, f). In both maps, it is visible that the low-/high-pressure regime in central and western Europe is surrounded by opposite pressure regimes. In case of a high-pressure system in the centre, it leads to a blocked zonal flow which is shown in Europe in Figure 3.5f. The composite maps of precipitation and temperature also support the analysis with the Z500 data. The climate of central and western Europe is characterized by significantly higher (lower) precipitation in central Europe as well as significantly lower (higher) surface air temperatures in summer corresponding to low (high)  $\delta^{18}\text{O}_{\text{cel}}$  values. The significant relation between PC1 and the summer hydroclimate is also resampled by the correlation between the SPEI3 index for JJA (Vicente-Serrano et al., 2010; longitude from  $-5^\circ$  to  $10^\circ$  and latitude from  $46^\circ$  to  $52^\circ$ ) and PC1. The correlation is significant ( $R=0.49$ ;  $p<0.01$ ) for the period from 1901 to 2005 which suggests that PC1 can capture the hydroclimate variability in summer.

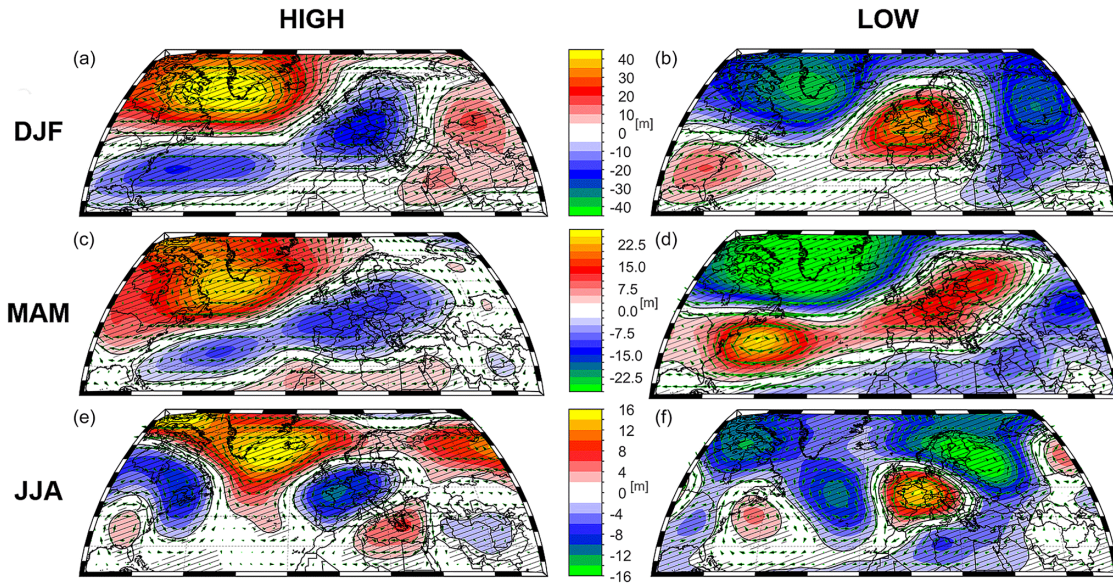


Figure 3.5: Composite maps (high and low) for Z500 related to the first  $\delta^{18}\text{O}_{\text{cel}}$  component for the DJF, MAM, and JJA seasons. Panels (a) and (b) show the characteristics of the climate in DJF, panels (c) and (d) show the characteristics of the climate in MAM, and panels (e) and (f) show the characteristics of the climate in JJA. The results for maxima (a, c, e) and minima (b, d, f) events of PC1 are also given. The Z500 maps show similar characteristics in winter and spring, whereas a pressure regime is directly located over central Europe in summer. The Z500 dataset from 20CRv2c (Compo et al., 2011) is used in this figure for the period from 1901 to 2005. Furthermore, the significance is shown using a black contour line.

To further investigate the relation between ENSO variability and the PC1, two different statistical approaches are used. The first approach is to analyse if El Niño and La Niña events are separated in the probability density plots of PC1. During El Niño years, the distribution of PC1 is shifted towards higher values, whereas the opposite occurs during La Niña years (Supplement 4). According to a t test, both shifts are significantly different compared with the distribution of PC1 ( $p < 0.05$ ). The second statistical approach investigates if extremes in  $\delta^{18}\text{O}_{\text{cel}}$  time series co-occur with El Niño or La Niña events. For this purpose, the event coincidence analysis (Siegmund et al., 2017; Donges et al., 2016) is applied using PC1 and the December Niño 3.4 index (HadISST1; Rayner et al., 2003). Over the period from 1871 to 2005, 41.2% of high and low extremes in the Niño 3.4 index coincided significantly during winter, with high and low extremes of PC1 ( $p < 0.01$ ). By extending the analysis period from 1750 to 1850, coincidence rates (28% of the NDJ Niño 3.4 (Li et al., 2013) high and low extremes coincided (not significantly;  $p > 0.1$ ) during winter with high and low extremes of PC1) and the correlations between PC1 and ENSO reconstructions Dätwyler et al. (2019) and Li et al. (2011, 2013) are shown to weaken.

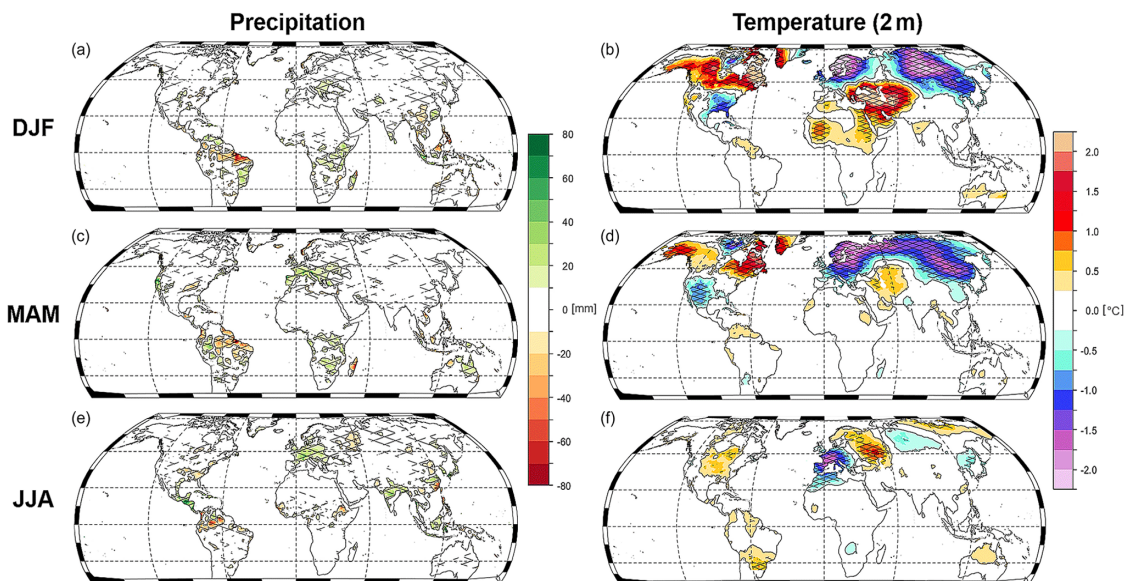


Figure 3.6: Composite maps (high–low) for precipitation and air temperature related to the first  $\delta^{18}\text{O}_{\text{cel}}$  component for the DJF, MAM, and JJA seasons. Panels (a) and (b) show the characteristics of the climate in DJF, panels (c) and (d) show the characteristics of the climate in MAM, and panels (e) and (f) show the characteristics of the climate in JJA. The results for precipitation (a, c, e) and air temperature (b, d, f) are also given. The precipitation and air temperature dataset from CRU TS (Harris et al., 2020) is included in this figure for the period from 1901 to 2005. The significance is shown using a black grid overlay.

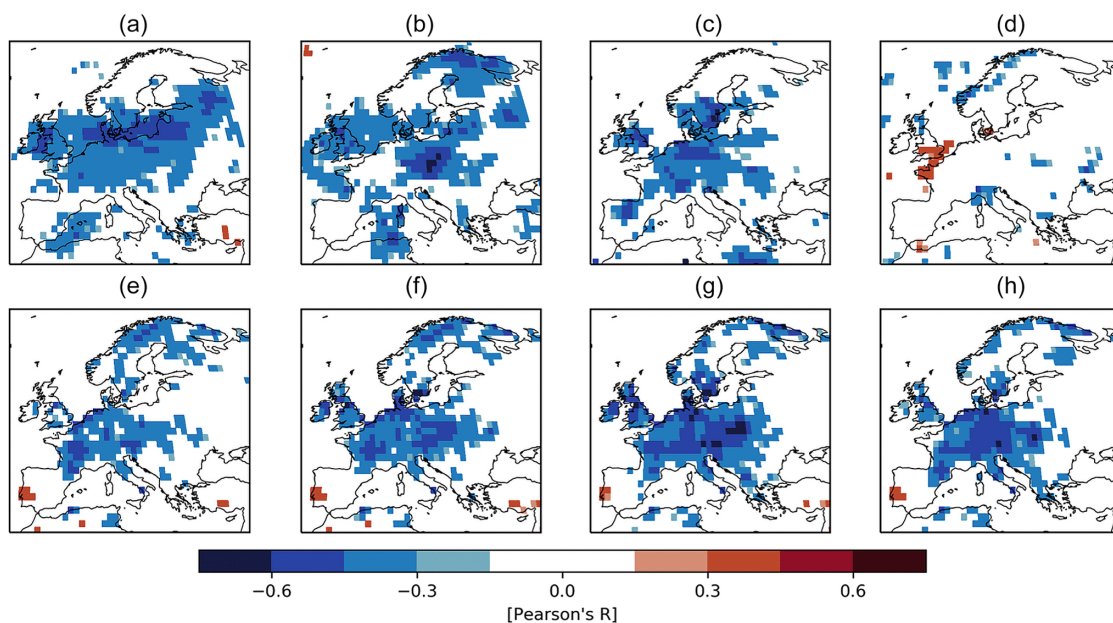


Figure 3.7: Links between the first  $\delta^{18}\text{O}_{\text{cel}}$  component and the modelled  $\delta^{18}\text{O}$  in soil water and precipitation from nudged climate simulations with ECHAM5-wiso (Butzin et al., 2014). Panels (a–d) show the correlation between the first  $\delta^{18}\text{O}_{\text{cel}}$  component (PC1) and  $\delta^{18}\text{O}$  in precipitation for winter (a), spring (b), summer (c), and autumn (d). Panels (e–h) are the correlation maps for PC1 and  $\delta^{18}\text{O}$  in soil water for winter, spring, summer, and autumn. For all maps, the significant grid cells are coloured.

### 3.3.4 COMPARISON WITH MODELLED $\delta^{18}\text{O}_{\text{CEL}}$ IN PRECIPITATION & SOIL WATER

By employing nudged climate simulations with ECHAM5-wiso (Butzin et al., 2014), it is evaluated how the  $\delta^{18}\text{O}_{\text{cel}}$  tree signature is related to the modelled  $\delta^{18}\text{O}_{\text{P}}$  and  $\delta^{18}\text{O}_{\text{SW}}$ . A significant correlation between PC1 and the modelled  $\delta^{18}\text{O}_{\text{P}}$  is shown in the correlation maps for winter, spring, and summer, where central Europe is characterized by a moderate correlation (Figure 3.7a–c). A similar pattern can be identified for the correlation between  $\delta^{18}\text{O}_{\text{SW}}$  and PC1. Compared with the previous analysis, the correlation between these quantities increases from winter to summer where it reaches the maximum correlation (Figure 3.7). As the  $\delta^{18}\text{O}_{\text{cel}}$  ratio is largely dependent on  $\delta^{18}\text{O}_{\text{SW}}$ , the relation with  $\delta^{18}\text{O}_{\text{SW}}$  is stronger compared with  $\delta^{18}\text{O}_{\text{P}}$ . Overall, the results indicate that significant correlations for both quantities can be computed for the entire European region except for the eastern parts.

### 3.3.5 FURTHER CLIMATE SIGNALS IN $\delta^{18}\text{O}_{\text{CEL}}$

In addition to the multi-seasonal signal, the second component of the  $\delta^{18}\text{O}_{\text{cel}}$  values significantly relates to the summer climate (Figure 3.8-9). A positive (negative) geopotential height anomaly in northern Europe with its centre over the North Sea co-occurs with a negative (positive) Z500 anomaly in south-eastern Europe (Figure 3.8). This coincides with low (high) temperature in central and north Europe, whereas north-eastern Europe is characterized by high (low) temperature (Figure 3.8a). The same pattern is also shown in the composite maps for precipitation where a similar pattern is presented (Figure 3.8b). Based on these patterns, the temporal distribution of extremes in the PC2 time series indicates that the 19<sup>th</sup> century has experienced increased dryness in northern Europe and enhanced precipitation in the Adriatic region (Figure 3.2d).

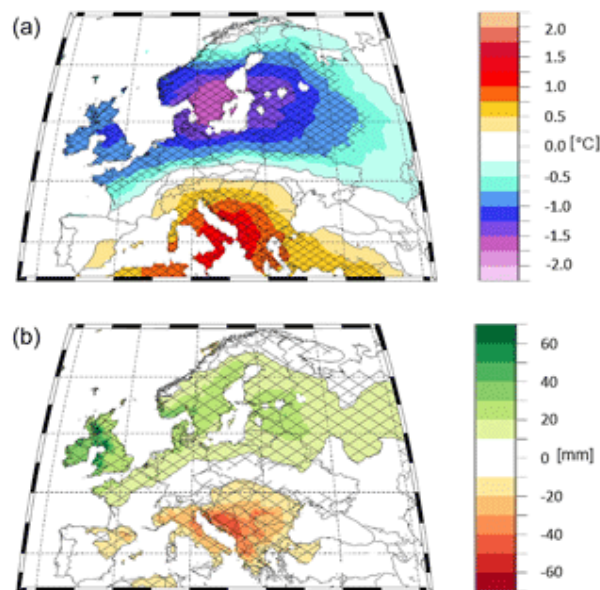


Figure 3.8: Composite maps (high–low) for the boreal summer related to the second  $\delta^{18}\text{O}_{\text{cel}}$  component. (a) surface temperature, JJA; (b) precipitation JJA. The datasets are the same as in Figure 3.6. Furthermore, the significance is shown using a black grid overlay.

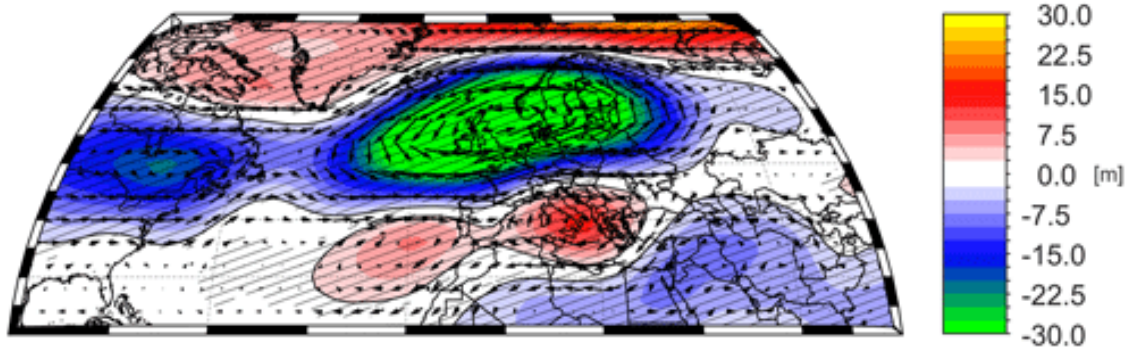


Figure 3.9: Composite map (high–low) for Z500 related to the second  $\delta^{18}\text{O}_{\text{cel}}$  component (PC2) for the boreal summer. The Z500 dataset from 20CRv2c (Compo et al., 2011) is used in this figure for the period from 1901 to 2005. Furthermore, the significance is shown using a black contour line.

### 3.4 DISCUSSION OF THE $\delta^{18}\text{O}_{\text{CEL}}$ NETWORK ANALYSIS

#### 3.4.1 LATITUDINAL AND ALTITUDINAL DEPENDENCE OF THE $\delta^{18}\text{O}_{\text{CEL}}$ NETWORK

The  $\delta^{18}\text{O}_{\text{cel}}$  ratio is affected by the isotopic composition of the source water ( $\delta^{18}\text{O}_{\text{p}}$ ,  $\delta^{18}\text{O}_{\text{sw}}$ ), which varies according to the latitude and altitude of the sample site (e.g. McCarroll and Loader, 2004). The latitudinal position has an influence on the  $\delta^{18}\text{O}$  in the atmosphere because of the strong correlation between the temperature and the  $\delta^{18}\text{O}$  composition of water vapour in the atmosphere (Dansgaard, 1964). In addition, Dansgaard (1964) suggested that the altitude also influences the  $\delta^{18}\text{O}$  ratio, primarily due to the cooling of air masses as they ascend a mountain which is accompanied by the rainout of the excess moisture (Gat, 2010).

The results from this subchapter show that there is a linear relationship between  $\delta^{18}\text{O}_{\text{cel}}$  and site altitude (Figure 3.2b) and latitude (Figure 3.2c), which re-enforces the commonly inferred effects of latitude and altitude on the  $\delta^{18}\text{O}_{\text{cel}}$  (McCarroll and Loader, 2004). Therefore, the results are in line with other studies that have presented such results in the past, e.g. Szejner et al. (2016).

The effects of altitude and latitude on the photosynthesis process are also visible for other tree-ring-based proxies. For example, according to the studies of Körner et al. (1991), Marshall and Zhang (1994), and Diefendorf et al. (2010), there is a highly significant altitude effect on the tree carbon isotope composition ( $\delta^{13}\text{C}$ ). As temperature decreases with increasing altitude and the partial air pressure is approximately 21% lower at 2000 m than at sea level, Körner (2007) argued that these environmental conditions lead to a faster molecular gas diffusion at any given temperature.

However, the distribution of the sample sites across Europe indicate that the isotope network is spatially limited (Figure 3.1). For instance, the time series from central and western Europe are overrepresented compared with those from south-eastern and northern Europe. In addition, it is

imperative to extend the isotope network by collecting more  $\delta^{18}\text{O}_{\text{cel}}$  records from eastern Europe to improve the validity of the results for this region. Furthermore, the samples were not taken from trees growing at the same altitude, which is critical for identifying a latitudinal effect. In fact, the sampled trees in southern Europe grew at higher altitudes ( $\geq 1600$  m) compared with the other sample sites, which could also bias the  $\delta^{18}\text{O}_{\text{cel}}$  ratio. It is, therefore, not viable to compare two adjacent sites located at different altitudes, and it is challenging to distinguish between latitudinal and altitudinal effects.

Another point that needs to be considered is that the  $\delta^{18}\text{O}_{\text{cel}}$  time series used were created using a pooling approach. Overall, the pooling approach has been tested and proven successful for climate analysis (Treydte et al., 2007b), but the approach also has some weaknesses and is strongly discussed in the literature (e.g. Foroozan et al., 2019). For example, Hangartner et al. (2012) recommend avoiding pooling, as an unsuitable tree cannot be omitted without resampling the whole period. They suggest measuring the trees individually instead and only using pooling when there is a strong correlation between the trees. Nevertheless, the pooling approach was adopted for all of the ISONET sites, allowing, for the first time, for the establishment of a tree-ring stable isotope network of more than 20 sites across Europe in collaboration with several laboratories within a reasonable time frame. Without pooling, the spatial dataset, analysis, and interpretation presented here would not be available to the community.

---

#### 3.4.2 LINKS BETWEEN ENSO AND PC1

The results presented in Chapter 3.3.3 are an indicator that ENSO activity influences the climate signal of PC1. The reason for this is the described warm and cold SST patterns in the equatorial Pacific and on the west coast of North and South America which are associated with El Niño and La Niña events (Allan et al., 1996). Furthermore, the clear and significant separation between El Niño and La Niña events in probability density functions and the coincidence of high and low values of Niño 3.4 and PC1 support the argumentation.

Moreover, the temperature pattern described in Figure 3.6b resembles the effects of the winter NAO. During the negative phase of the NAO, northern Europe experiences cold conditions and southeastern Europe experiences warm conditions in winter. Studies based on observations (Fraedrich and Müller, 1992; Fraedrich, 1994; Brönnimann et al., 2004; Pozo-Vázquez et al., 2005; Brönnimann et al., 2007) and models (Merkel and Latif, 2002; Mathieu et al., 2004) have shown that ENSO variability can influence the winter NAO. Their results showed that an El Niño event leads to a negative phase of the NAO. Based on the presented results, it is suggested that high values of PC1 co-evolve with the occurrence of El Niño conditions, and low values of PC1 co-evolve with the occurrence of La Niña conditions.

---

### 3.4.3 THE STABILITY OF THE ENSO SIGNAL IN THE ISOTOPE NETWORK

In this chapter, the correlation between ENSO and the PC1 of the  $\delta^{18}\text{O}_{\text{cel}}$  network with three different reconstructions (Li et al., 2011, 2013; Dätwyler et al., 2019) and for two different time periods (1750–1849, 1850–1949) is tested. Despite the fact that the sample density of the isotope network is relatively high in these two periods, the correlation between the PC1 and the ENSO reconstructions is weaker and non-significant for the period from 1750 to 1849. However, not only does the correlation get weaker, the correlation between a set of different ENSO reconstructions also becomes weaker in the 18<sup>th</sup> century, which was shown for specific periods in Dätwyler et al. (2019). Dätwyler et al. (2019) also found a consistent teleconnection pattern during the 18<sup>th</sup> century, which is different to the known teleconnection pattern of ENSO during the instrumental period. Moreover, the 1850s mark the end of Little Ice Age (LIA), when the atmospheric circulation over Europe (Felis et al., 2018b) and its teleconnections to ENSO changed significantly (Rimbu et al., 2003). In their study, Felis et al. (2018) found evidence of an abrupt reorganization of the atmospheric circulation over Europe at the end of the LIA, transitioning from predominantly negative phases of the NAO (weakening of westerly winds) to predominantly westerly flow patterns over central Europe. Furthermore, modelling studies (e.g. Henke et al., 2017) have also reported an increased frequency of El Niño during the LIA due to southern displacement of the Intertropical Convergence Zone.

A change in the ENSO characteristics would also have an influence on the teleconnection with the European climate. For instance, Rimbu et al. (2003) investigated coral time series from the northern Red Sea and identified a nonstationary relationship between the tropical Pacific and the European–Middle Eastern climate during the pre-instrumental period. They showed that a Pacific–North-American-teleconnection-like pattern in its negative phase, which is compatible with La Niña conditions, is associated with positive  $\delta^{18}\text{O}$  anomalies in the Red Sea coral record from the mid-1930s to late 1960s. After 1970, they detected a shift in the teleconnections that leads to the fact that positive anomalies in the Red Sea coral  $\delta^{18}\text{O}$  are related to El Niño conditions. An unstable relationship between ENSO variability and the climate of Europe is also found in studies based on instrumental data (e.g. Fraedrich and Müller, 1992; Fraedrich, 1994; Pozo-Vázquez et al., 2005) or ocean–atmosphere coupled models (e.g. Raible et al., 2004; Deser et al., 2006; Brönnimann, 2007). The temporally unstable relationship between climate variables and ENSO is not only restricted to Europe and is also present in other regions of the planet (e.g. Álvarez et al., 2015).

Weak or inconclusive correlations between PC1 and ENSO reconstructions could also arise from the fact that the quality of the ENSO reconstructions decreases, which could be based on an overly low number of samples (especially in first years of the reconstruction period) and a non-stationarity of the teleconnection used (Batehup et al., 2015). Furthermore, ENSO reconstructions are mostly trained within the last 150 years and are used for time periods characterized by an absence of instrumental data. Therefore, confident statements can only be made from 1850 onwards, as instrumental

measurements of different climate variables are available. Thus, the only possibility to test and analyse the teleconnection before 1850 is to use ENSO reconstructions. Another reason for the decrease in correlation could be the change in the climate signal of  $\delta^{18}\text{O}_{\text{cel}}$ . It is important to consider that the climate signal is directly coupled to the limiting factor for tree growth. It is possible that the limiting factor changes over time, which would result in different responses to climate. Esper et al. (2017) showed that the climate signals in  $\delta^{18}\text{O}_{\text{cel}}$  and  $\delta^{13}\text{O}_{\text{cel}}$  change during warm and cold periods for trees in Switzerland, and they proposed splitting the calibration between these two periods or using corresponding transfer models. Therefore, future research is required to investigate the climate signal during warm and cold periods, as well as the influence on the PCA results. However, the results suggest that the relationship between ENSO and the European climate may not be stable over time.

---

#### 3.4.4 THE WINTER CLIMATE SIGNAL IN $\delta^{18}\text{O}_{\text{CEL}}$

The exact mechanism through which the  $\delta^{18}\text{O}_{\text{cel}}$  captures a climate signal of the preseasons is still debated. For example, Heinrich et al. (2013) mentioned that winters with very low temperatures may damage the cambium more than usual, requiring a longer recovery period. Such winters may have a negative effect on the cambial activity and on the photosynthetic process. Furthermore, Vaganov et al. (1999) showed that precipitation during winter can sustainably affect tree growth in the following year. Their findings are similar to Treydte et al. (2006), who showed that  $\delta^{18}\text{O}_{\text{cel}}$  can contain a winter signal. Treydte et al. (2006) further argued that, depending on the root system, winter snow fall, and the characteristics of groundwater reservoirs, it is likely that trees use precipitation from the preseasons. Nevertheless, it is possible that winter climate conditions can also be memorized in  $\delta^{18}\text{O}_{\text{cel}}$  through different climate feedback processes. For example, Ogi et al. (2003) highlighted that a positive NAO is frequently followed by higher pressures and warmer temperatures in Europe during the next summer. The authors suggested that SST, sea ice extensions, and snow fall anomalies capture the winter climate conditions and influence the summer climate.

However, the oxygen isotope signal in cellulose depends primarily on the corresponding oxygen signal of the soil water and precipitation. According to Saurer et al. (2012),  $\delta^{18}\text{O}_{\text{SW}}$  constitutes the average  $\delta^{18}\text{O}$  input to the arboreal system over several precipitation events, and it is modified by partial evaporation from the soil (depending on soil texture and porosity) and by a potential time lag, depending on the rooting depth. Here, the strongest correlations with  $\delta^{18}\text{O}_{\text{P}}$  is obtained in winter, spring, and summer (Figure 3.7a, b, c). Because the correlations with  $\delta^{18}\text{O}_{\text{SW}}$  are strongest in summer and autumn (Figure 3.7g, h), and  $\delta^{18}\text{O}_{\text{SW}}$  is the input of the arboreal system, it is suggested that the isotopic signal of  $\delta^{18}\text{O}_{\text{cel}}$  corresponds to an average over  $\delta^{18}\text{O}_{\text{P}}$  events from winter, spring, and summer, transferred via the  $\delta^{18}\text{O}_{\text{SW}}$ . This may also explain the reason behind the strong ENSO signal that  $\delta^{18}\text{O}_{\text{cel}}$  is able to capture during winter. Moreover, it indicates the high potential of  $\delta^{18}\text{O}_{\text{cel}}$  to capture climate signals even outside of the growing season.

When considering the multi-seasonal signal, one has to account for the fact that this can lead to certain limitations in the analysis of  $\delta^{18}\text{O}_{\text{cel}}$ . This is because there is only one  $\delta^{18}\text{O}_{\text{cel}}$  value in the network used for each site and for each year; however, this value does not represent a clear seasonal signal referring to one season, instead representing a mix of signals referring to several seasons. Overall, the seasonal contributions to the climate signal can vary in strength. Due to the combinations of these influencing factors, the correlation with individual seasons is certainly weakened, as no clear seasonal signal can be represented by the  $\delta^{18}\text{O}_{\text{cel}}$  value. On the other hand, this enables the observation of several seasons and an understanding of which season has an influence on the biochemical processes in the tree.

---

#### 3.4.5 LINKS BETWEEN PC2 AND LARGE-SCALE ATMOSPHERIC MODES

In the composite maps for the PC2 (Figure 3.9), a dipole structure between northern Europe and the Mediterranean region is shown. The dipole is characterized by a pressure anomaly centred on the North Sea that expands from the north-eastern Atlantic to the Baltic Sea. Its counterpart is present in the northern Mediterranean region, especially in Italy, the northern parts of Greece, and the Adriatic region.

The described pattern shows similarities to the summer European blocking pattern (Barnston and Livezey, 1987; Cassou et al., 2005) which is often associated with the Summer North Atlantic Oscillation (SNAO; Hurrell and Van Loon, 1997). According to Cassou et al. (2005), 17.8% of the positive phase and 17.9% of the negative phase of the summer European blocking pattern influence the total summer weather regimes in Europe.

The summer European blocking pattern is a surrogate indicator for storm track activities. During the positive index phase, the storm track moves further northwards (Folland et al., 2009; Lehmann and Coumou, 2015). This results in a low storm activity over northern Europe that is characterized by dry conditions, less cloudiness, high temperatures, and a blocked cyclonic flow (Lehmann and Coumou, 2015). On the other hand, the Mediterranean region is affected by lower temperatures and more precipitation. The opposite phenomenon can be identified for the negative index phase. Northern Europe experiences an enhanced storm activity through the southward movement of the storm track over north-western Europe (Rolland et al., 2009; Lehmann and Coumou, 2015), which leads to higher precipitation, higher cloudiness, and lower temperatures. In contrast, the northern Mediterranean experiences dry and warm conditions. These predominant summer European blocking pattern features are well represented in the composite maps of precipitation and temperature for PC2 (Figure 3.8). Based on the temporal evolution of PC2, it is suggested that there is a tendency towards a negative index phase starting at the beginning of the 20<sup>th</sup> century.

In addition to the link to summer blocking activity in Europe, the geopotential height pattern is often used in another context. For example, Sillmann and Croci-Maspoli (2009) showed that a positive geopotential height anomaly over the North Sea describes an atmospheric-blocking-like pattern that relates to climate extremes like floods and droughts in the European mid-latitudes. Moreover, this circulation anomaly pattern has been identified as the main driver for extreme dry periods over the eastern Mediterranean (Oikonomou et al., 2010; Rimbu et al., 2014; Ionita and Nagavciuc, 2020) and for summer air temperature variability in Greece (Xoplaki et al., 2003a, b).

### 3.5 CONCLUSION OF THE $\delta^{18}\text{O}_{\text{CEL}}$ NETWORK STUDY

Here, a study of a  $\delta^{18}\text{O}_{\text{cel}}$  isotope network from tree rings for the last 400 years is presented that was used to investigate the large-scale climate teleconnections related to the European climate. According to the presented analysis, the climate signals of the network indicate that a link between the  $\delta^{18}\text{O}$  variability and ENSO exists in winter, spring, and summer. The investigation of the modelled  $\delta^{18}\text{O}_{\text{SW}}/\delta^{18}\text{O}_{\text{P}}$  suggests that the summer signal still dominates  $\delta^{18}\text{O}_{\text{cel}}$  but is partly influenced by lagged winter and spring precipitation signals. It is suggested that this is based on hydroclimatic feedback processes as well as characteristics of the water reservoirs of the different sample sites. The ENSO signal is detected for the last 130 years. However, no significant links can be deduced during the period from 1750 to 1850, indicating that the relationship between ENSO and the European climate could be unstable over time. The teleconnection changes between the tropical Pacific and Europe during the pre-instrumental period were also identified from coral data (Rimbu et al., 2003). Further knowledge about a change in teleconnections is essential because teleconnections have a remote climate impact on top of the current global warming.

Furthermore, the results show that the EOF2 is characterized by a dipole pattern between northern and south-eastern Europe which is comparable to the characteristics of the summer European blocking pattern. As this mode is highly relevant for the summer climate conditions on the entire European continent, the temporal perspective gives new insights into how the frequency of this mode changed through time. The findings suggest that there is a tendency towards a situation in which southeast Europe is predominantly characterized by a high-pressure system and northern Europe is predominantly characterized by a low-pressure system starting at the beginning of the 20<sup>th</sup> century. The described pressure pattern is relevant for society because it can influence the spatial and frequency characteristics of climate extremes.

In the context of the ongoing discussion about anthropogenic climate change, water isotope records can provide useful information about spatial and frequency changes in specific large-scale atmospheric circulation patterns. As the logical next step, more high-resolution paleoclimate data as well as comprehensive model simulations are required to provide additional insights into the stationarity of reconstructed European climate signals and their stationarity in teleconnections.

# 04

## A RECONSTRUCTION OF THE EUROPEAN SUMMER VPD

## 4.1 MOTIVATION FOR A RECONSTRUCTION

Evapotranspiration is a critical factor for understanding the links and feedbacks between atmospheric CO<sub>2</sub> and global climate (e.g. Good et al., 2015; IPCC, 2021). Within the terrestrial water fluxes, vegetation-produced transpiration represents the dominant factor (e.g. Jasechko et al., 2013; Good et al., 2015). One key driver for such vegetation resources and dynamics is vapor pressure deficit (VPD), which is defined by the difference between the water vapor pressure at saturation and the actual water vapor pressure (Lawrence, 2005). VPD is a key variable for vegetation resources and dynamics (Grossiord et al., 2020) representing the atmospheric evaporative demand which has an influence on the leaf-level transpiration of plants and the corresponding stomatal conductance. With increasing VPD, stomata close to minimize water loss (Running, 1976) due to the high atmospheric evaporative demand. As consequence, a minimal stomata opening decreases stomatal conductance and photosynthetic activity (Fletcher et al., 2007). Extremely high VPD may even lead to reduced growth, a higher risk of carbon starvation and hydraulic failure (Grossiord et al., 2020). In contrast, low VPD leads to reduced water transport into the leaves and thus a reduced supply of nutrients. This marks VPD as an important indicator for plant activity (Novick et al., 2016), which among other things notably affects plant growth (Restaino et al., 2016), forest mortality (Park Williams et al., 2013), drought occurrence (Dai, 2013), crop production (Zhao et al., 2017) and wildfire occurrence (Seager et al., 2015).

Since VPD is a function of temperature (Lawrence, 2005), the effects of climate change and the associated rise in temperature become evident for trends of VPD (Grossiord et al., 2020; IPCC, 2021). For instance, studies have shown that the water vapor pressure deficit has been increasing sharply at a global scale since the year 2000 (Simmons et al., 2010; Willett et al., 2014; Yuan et al., 2019). However, VPD records derived from remote sensing data cover only the last ~50 years and vary in quality, so that long-term perspectives of VPD are lacking. In addition, a long-term perspective can help to put recent observed trends of VPD in a long-term context and to estimate significance and robustness at local to continental scales. Furthermore, it is essential to investigate the independent physiological effects of VPD on large-scale vegetation dynamics, which are less explored (Grossiord et al., 2020). So far, first local reconstruction studies have shown the potential of a long-term perspective on VPD (e.g. Liu et al., 2017). For example, Churakova-Sidorova et al. (2020) have shown that the recent VPD increase does not yet exceed the maximum values reconstructed during the Medieval Warm Anomaly in Siberia. Nevertheless, most studies lack a wider spatial perspective as they only reconstruct VPD time series for a location.

To obtain the first long-term and large-scale perspective on VPD dynamics, the stable oxygen isotope ratio of tree-ring cellulose ( $\delta^{18}\text{O}_{\text{cel}}$ ) is used. The use of  $\delta^{18}\text{O}$  is motivated by the fact that the  $\delta^{18}\text{O}_{\text{cel}}$  ratio is controlled by only three main factors. The first factor is the  $\delta^{18}\text{O}$  signature of precipitation ( $\delta^{18}\text{O}_{\text{p}}$ ) supplying the trees with water through uptake by the roots from the soil. In middle and higher

latitudes a significant positive relationship between  $\delta^{18}\text{O}_\text{P}$  values and air temperature (commonly called the temperature effect) is observed (e.g. Rozanski et al., 2013). However,  $\delta^{18}\text{O}_\text{P}$  variability in these latitudes cannot be explained by air temperature alone (e.g. Welker, 2000).  $\delta^{18}\text{O}_\text{P}$  at any location is also the result of the previous rainout history and origin(s) of the moist air mass(es). That is controlled by atmospheric circulation patterns (e.g. Edwards et al., 1996) and the sum of (temperature-dependent) oxygen fractionations occurring during evaporation and condensation of water that is finally taken up by a tree. In the arboreal system,  $\delta^{18}\text{O}$  of soil water ( $\delta^{18}\text{O}_\text{SW}$ ) represents the  $\delta^{18}\text{O}_\text{cel}$  input, that usually reflects an average  $\delta^{18}\text{O}_\text{P}$  over several precipitation events. The average signal could be modified by fractionation due to partial evaporation of isotopically lighter water vapor from the soil (depending on soil texture and porosity; Saurer et al., 2012). Therefore,  $\delta^{18}\text{O}_\text{SW}$  in combination with  $\delta^{18}\text{O}_\text{P}$  and  $\delta^{18}\text{O}$  of the groundwater (depending on site and tree species) represents the baseline variability. The second factor is biochemical fractionation including partial isotopic exchange of cellulose precursors with stem water during cellulose biosynthesis (e.g. Saurer et al., 1997; Roden et al., 2000; Barbour, 2007), which is considered to be largely constant at  $27 \pm 4$  ‰ (Sternberg and Deniro, 1983).

The third factor, which is also the most important one, is the evaporative  $^{18}\text{O}$  enrichment of leaf or needle water via transpiration of water vapor to the atmosphere (e.g. Saurer et al., 1997; Roden et al., 2000; Barbour, 2007; Kahmen et al., 2011; Treydte et al., 2014 and citations therein). The transpiration process is controlled by leaf-to-air VPD modified by the aperture of stomata controlling the conductance for water vapor (Buckley, 2019). The  $\delta^{18}\text{O}$  values of leaf water are typically enriched in  $^{18}\text{O}$  compared to the plant's parent water because evaporative losses are greater for the lighter  $^{16}\text{O}$  than for  $^{18}\text{O}$  (Roden et al., 2000). However,  $\delta^{18}\text{O}_\text{cel}$  features the  $\delta^{18}\text{O}$  signature of chloroplast water which is not in isotopic equilibrium with leaf water at the actual sites of transpiration (stomata), i.e. the higher the transpiration rates the lower is the rate of enrichment of the chloroplast water (Péclet effect; Barbour et al., 2004). Nonetheless, since the variability of  $\delta^{18}\text{O}_\text{cel}$  results predominantly from a combination of the temperature-dependent  $\delta^{18}\text{O}$  of the water source and the evaporative  $^{18}\text{O}$  enrichment of leaf water controlled by leaf-to-air VPD,  $\delta^{18}\text{O}_\text{cel}$  can be used as a proxy for variations in VPD (Ferrio and Voltas, 2005; Kahmen et al., 2011).

To gain a spatial and temporal perspective on past VPD variability, multiple stable oxygen isotope records derived from tree-rings are used and a Random Forest (RandF; Breiman, 2001) regression method is applied, which is often considered as one of the core approaches for machine learning. According to Yang et al. (2020), RandF has become one of the most successful machine learning algorithms for practical applications over the last two decades due to its proven accuracy, stability, speed of processing, and ease of use (Rodríguez-Galiano et al., 2012; Belgiu and Drăguț, 2016; Maxwell et al., 2018; Bair et al., 2018; Qu et al., 2019; Reichstein et al., 2019; Tyrallis et al., 2019). The term RandF describes a non-linear and robust technique in which several decision trees are built and

aggregated at the end to make predictions or perform reconstructions (Breiman, 2001). The RandF approach is increasingly applied in climate and environmental sciences, and has been used for: the prediction of snow depth (Yang et al., 2020), solar radiation (Prasad et al., 2019), daily ozone (Zhan et al., 2018), precipitation (Ali et al., 2020); as well as reconstructions of last millennium North Atlantic Oscillation (Michel et al., 2020), streamflow since 1485 C.E. (Li et al., 2019) and vegetation cover during the mid-Holocene and the Last Glacial Maximum (Lindgren et al., 2021). Although RandF models have proved to be a useful method in geosciences, studies on the spatial-temporal reconstruction of climate variables based on  $\delta^{18}\text{O}_{\text{cel}}$  are relatively rare due to the low availability of time series.

In this chapter, a European  $\delta^{18}\text{O}_{\text{cel}}$  network from tree rings is used, consisting of 26 sites which cover the period 1600 – 1994 (Balting et al., 2021a) and a RandF approach (Breiman, 2001) to reconstruct gridded fields of European summer VPD from 1600 to 1994. The goal is to provide a spatial and long-term perspective on the past VPD variability. Therefore, the reconstruction is analysed from a spatio-temporal perspective for the regions Northern Europe, Central Europe and Mediterranean (Iturbide et al., 2020) as defined and used in the Sixth Assessment Report of the IPCC (IPCC, 2021). In this respect, the paper is structured as follows: in Subchapter 4.2 a detailed description of the data and methods employed throughout the paper are presented, while the main results are presented in Subchapter 4.3. The spatial variability of VPD is investigated for selected extreme years, for example the summer after the Tambora eruption (e.g. 1815-1816 A.D.). Afterwards, the reconstruction is compared to other studies and uncertainties are discussed. Furthermore, the VPD observations are compared with climate model projections of low (Shared Socioeconomic Pathways 1-2.6; SSP1-2.6), medium (SSP2-4.5) and high (SSP5-8.5) emission scenarios. In this way, the past and present VPD conditions are evaluated to assess the statistical significance of observed trends and which can be used to understand VPD variability on a local, regional and continental scale. The main conclusion is shown in Subchapter 4.4.

## 4.2 DATA & RECONSTRUCTION TECHNIQUE

### 4.2.1 THE STABLE ISOTOPE NETWORK

To reconstruct the European summer VPD, 26 timeseries of  $\delta^{18}\text{O}_{\text{cel}}$  (Figure 4.1) are used. 21 time series of the 26 were obtained from the dataset generated by the EU project ISONET (EVK2-CT-2002-00147) (e.g. Treydte et al., 2007b, a; Balting et al., 2021). In addition to ISONET dataset, five  $\delta^{18}\text{O}_{\text{cel}}$  time series from Bulgaria, Turkey, southwestern Germany, Romania, and Slovenia were added (Heinrich et al., 2013; Hafner et al., 2014; Nagavciuc et al., 2018).

The detailed measurement methodologies used within the ISONET project as well as for the other sites are described in Boettger et al. (2007), Treydte et al. (2007a, b), Heinrich et al. (2013), Hafner et

al. (2014) and Nagavciuc et al. (2018), respectively. At least four dominant trees were selected at each site and two increment cores were taken per tree for the ISONET project; 15 cores of five living trees were taken from the site in Turkey (Heinrich et al., 2013), 12 trees were sampled for the Slovenian time series (Hafner et al., 2014) and from nine trees, one core per tree was taken in Romania (Nagavciuc et al., 2018). Standard dendrochronological dating method was performed (Fritts, 1976), and subsequent individual growth rings were dissected from the cores. All tree rings from the same year were pooled for most sites prior to cellulose extraction for the ISONET sites (Treydte et al., 2007a, b) as well as for the Romanian site (Nagavciuc et al., 2018). The dissected tree rings from the Slovenian and Turkish sites were measured individually and not pooled (Heinrich et al., 2013; Hafner et al., 2014). For oak, only the latewood was used for the analyses, because this approach was assumed to use predominantly climate signals from the current year, as the earlywood of oaks usually contains climate information from the previous year (González-González et al., 2015; Davies and Loader, 2020). The results are expressed using the conventional  $\delta$  (delta) notation in per mil (‰) relative to the Vienna Standard Mean Ocean Water (Craig, 1957).

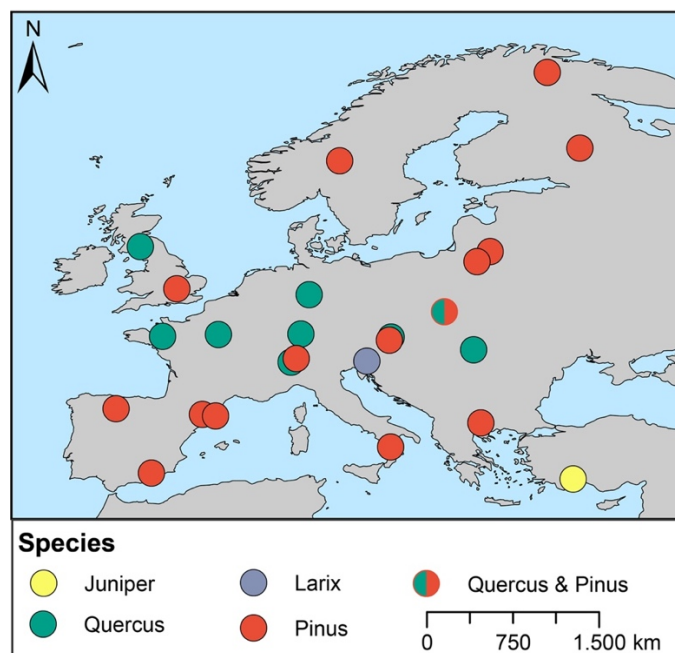
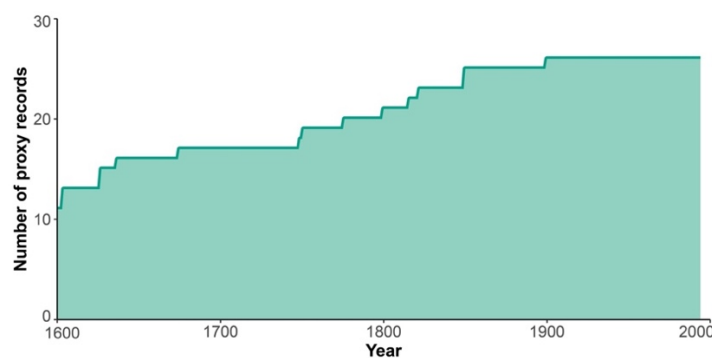


Figure 4.1: The site distribution of the used  $\delta^{18}\text{O}_{\text{cel}}$  network combined with the corresponding tree species.

The used isotope network consists of nine deciduous tree sites (*Quercus*) and 17 conifer sites (*Pinus*, *Juniper*, *Larix*; Table 4-1). The sample sites are well distributed over Europe (Figure 4.1). The elevation of the locations varies from 10 m a.s.l. (Woburn) to 2,120 m a.s.l. (Pedraforca). The longest chronologies cover a period from 1600 to 2005. The highest data density is available for the period 1900-1994 with 26 time series (Figure 4.2). For several sites or regional groups of sites from the ISONET datasets, the data is published within individual studies (Saurer et al., 2008; Vitas, 2008; Etien et al., 2008; Hiltunen et al., 2009; Haupt et al., 2011; Saurer et al., 2012; Rinne et al., 2013b; Helama et al., 2014; Labuhn et al., 2014; Saurer et al., 2014; Labuhn et al., 2016; Andreu-Hayles et al., 2017).

**Table 4-1: Characteristics of each sample site. 21 of the 26  $\delta^{18}\text{O}_{\text{cel}}$  records were obtained from the EU project ISONET (Treydte et al., 2007a, Balting et al., 2021a) and five additional sites from Bulgaria, Turkey, Southwest Germany, Romania and Slovenia were added (Hafner et al., 2014; Heinrich et al., 2013; Nagavciuc et al., 2018).**

Location	Country	Species	First year	Last year	Lon.	Lat.	Altitude
Cazorla	Spain	<i>Pinus nigra</i>	1600	2002	-2.57°	37.53°	1820 m
Cavergno	Switzerland	<i>Quercus petraea</i>	1637	2002	8.36°	46.21°	900 m
Dransfeld	Germany	<i>Quercus petraea</i>	1776	2002	9.78°	51.50°	320 m
Fontainebleau	France	<i>Quercus petraea</i>	1600	2000	2.67°	48.38°	100 m
Gutuli	Norway	<i>Pinus sylvestris</i>	1600	2003	12.18°	62.00°	800 m
Inari	Finland	<i>Pinus sylvestris</i>	1600	2002	28.42°	68.93°	150 m
Isibeli	Turkey	<i>Juniper excelsa</i>	1850	2005	30.45°	37.06°	1800 m
Lainzer Tiergarten	Austria	<i>Quercus petraea</i>	1600	2003	16.20°	48.18°	300 m
Lochwood	United Kingdom	<i>Quercus petraea</i>	1749	2003	-3.43°	55.27°	175 m
Monte Pollino	Italy	<i>Pinus leucodermis</i>	1604	2003	16.16°	39.58°	1900 m
Mount Vichren	Bulgaria	<i>Pinus heldreichii</i>	1800	2005	23.24°	41.46°	1900 m
Naklo	Slovenia	<i>Larix decidua</i>	1600	2005	14.30°	46.30°	440 m
Niepolomice	Poland	<i>Quercus robur</i> & <i>Pinus sylvestris</i>	1627	2003	20.38°	50.12°	190 m
Nusfalau	Romania	<i>Quercus robur</i>	1900	2016	22.66°	47.19°	270 m
Panemunės	Lithuania	<i>Pinus sylvestris</i>	1816	2002	23.97°	54.88°	45 m
Pedraforca	Spain	<i>Pinus uncinata</i>	1600	2003	1.42°	42.13°	2120 m
Pinar de Lillo	Spain	<i>Pinus sylvestris</i>	1600	2002	-5.34°	42.57°	1600 m
Plieningen	Germany	<i>Quercus petraea</i>	1822	1999	9.13°	48.42°	340 m
Poellau	Austria	<i>Pinus nigra</i>	1600	2002	16.06°	47.95°	500 m
Rennes	France	<i>Quercus robur</i>	1751	1998	-1.7°	48.25°	100 m
Sivakkovaara	Finland	<i>Pinus sylvestris</i>	1600	2002	30.98°	62.98°	200 m
Suwalki	Poland	<i>Pinus sylvestris</i>	1600	2004	22.93°	54.10°	160 m
Vigera	Switzerland	<i>Pinus sylvestris</i>	1675	2003	8.77°	46.50°	1400 m
Vinuesa	Spain	<i>Pinus uncinata</i>	1850	2002	2.45°	42.00°	720 m
Woburn	United Kingdom	<i>Pinus sylvestris</i>	1604	2003	-0.59°	51.98°	10 m



**Figure 4.1: The number of available  $\delta^{18}\text{O}_{\text{cel}}$  time series within the network.**

---

#### 4.2.2 OBSERVATIONAL DATA

Mean surface temperature in °C and near surface relative humidity in Vol. % are derived from the 20<sup>th</sup> Century Reanalysis Project (20CR) version V3 (Slivinski et al., 2019) at a monthly resolution. The 20CR reanalysis has a temporal resolution of three hours, 28 different pressure levels and a resolution of 1°x1°. The ensemble mean derived from an 80-member ensemble is used. The climate variables are available for the period from 1836 to 2015 and they are provided by NOAA/OAR/ESRL PSL, Boulder, Colorado, USA ([https://psl.noaa.gov/data/gridded/data.20thC\\_ReanV3.html](https://psl.noaa.gov/data/gridded/data.20thC_ReanV3.html)).

---

#### 4.2.3 GENERAL PROCEDURE OF THE EUROPEAN VPD RECONSTRUCTION

The Random Forest method (RandF; see Appendix A; Breiman, 2001) is applied to reconstruct European summer VPD spatially for the last 400 years. The VPD data derived from 20CRV3 (Slivinski et al., 2019) and the  $\delta^{18}\text{O}_{\text{cel}}$  network data are used as input. There is a small number of missing data (0.38% entries in total) which are infilled following Josse and Husson (2016). Before the reconstruction is started, a sensitivity study is done with  $\delta^{18}\text{O}_{\text{cel}}$  network to ensure the relation between  $\delta^{18}\text{O}_{\text{cel}}$  and observed VPD with correlations ( $\alpha < 0.05$ ).

The reconstruction is based on the methodology presented by Michel et al. (2020) and the corresponding scripts (ClimIndRec version 1.0), which were reprogrammed for a spatial reconstruction. In this chapter, the focus of the reconstruction is on the continental area of the European region (34.5°W to 49.5°E and 30.5°N to 74.5°N). The testing and validation period is set from 1900 to 1994 (Figure 4.2). The nesting approach is used which has the advantage that time series with different temporal coverage can be integrated in the reconstruction. With additional time series being available multiple reconstructions are derived. At the end of the calculations, the data sets are aggregated so that the RandF models with the highest data coverage represents the final VPD reconstruction. In addition to the reconstruction, validation parameters are calculated for each run of the RandF reconstruction using the Coefficient of Efficiency metric (CE; Appendix A; Nash and Sutcliffe, 1970).

Finally, the regional averages and running averages (30 years) of the reconstructed VPD are compared with temperature (Luterbacher et al., 2004), precipitation (Pauling et al., 2006) and Palmer Drought Severity Index (PDSI) reconstructions (Cook et al., 2015) for the three European AR6 regions: Northern Europe, Central Europe and Mediterranean (Iturbide et al., 2020). Furthermore, maps of the European summer VPD are presented for selected and highlighted wet (1737, 1814, 1815) and dry (1616, 1741, 1821) years to investigate the spatial variability of the reconstruction (Brooks and Glasspoole, 1922; Pauling et al., 2006; Trigo et al., 2009; Brázdil et al., 2013; Cook et al., 2015; Ionita et al., 2021). Prior to this mapping, all VPD grid cells are centred and standardized (z-transformation) to present z-anomalies for each grid cell.

---

#### 4.2.4 VPD COMPUTATION AND FURTHER PRE-PROCESSING

The calculation of the monthly VPD for Reanalysis, historical and future climate projections is based on the study of Barkhordarian et al. (2019) where the near surface air temperature ( $T$ ) and the dew point temperature ( $T_d$ ) both in °C are used. Since dew point temperature is not available for each of the datasets,  $T$  and relative humidity (RH) are used to compute  $T_d$  as follows:

$$T_d = \frac{a_1 * (\ln(\frac{RH}{100}) + \frac{a_2 * T}{a_1 + T})}{a_2 - (\ln(\frac{RH}{100}) + \frac{a_2 * T}{a_1 + T})} \quad (4-1)$$

Where  $a_1$  and  $a_2$  are defined as  $a_1 = 243.04$  °C and  $a_2 = 17.625$  hPa. This computation is reliable and is notably used in many climate models (Barkhordarian et al., 2019). The Clausius–Clapeyron relation is utilized in this chapter applying a term for the saturation vapor content of air and a term for the actual vapor pressure to calculate VPD as follows (Marengo et al., 2008; Seager et al., 2015; Barkhordarian et al., 2019; Behrangi et al., 2016):

$$VPD = c_1 \times e^{\frac{c_2 * T}{c_3 + T}} - c_1 \times e^{\frac{c_2 * T_d}{c_3 + T_d}} \quad (4-2)$$

where,  $c_1 = 0.611$  kPa,  $c_2 = 17.5$ ,  $c_3 = 240.978$  °C and VPD is in kPa (see WMO (2018) for further information). Seasonal averages are computed for DJF (December to February, winter), MAM (March to May, spring), JJA (June to August, summer) and SON (September to November, fall).

---

#### 4.2.5 FUTURE SCENARIOS

Monthly mean surface temperature and near surface relative humidity from the latest CMIP 6 models (Eyring et al., 2016) are used to compute VPD until the end of the 21<sup>st</sup> century. The historical simulations (1850 to 2014) are used in conjunction with the future simulations based on the shared socio-economic pathways (SSPs) projections (O'Neill et al., 2016) for the years 2015 to 2100. It was decided to focus on the SSP1-2.6, SSP2-4.5 and SSP5-8.5 scenarios. The criteria for the model selection is as follows (Seneviratne and Hauser, 2020): i) the selected models must provide the relevant variables, (ii) the models must have a temporal coverage from 1850 to 2100, and (iii) the selected models do not have duplicate or missing time steps. The presented regional means are calculated from the original grid resolution; for the maps, the data is regridded bilinear to a 1°x 1° grid. All models are listed in Supplement 6.

The regional averages of the reconstructed and observed VPD are compared with the projected VPD for three European AR6 regions (Iturbide et al., 2020). Beside the temporal perspective, anomaly maps are shown to investigate spatial trends in future scenarios.

## 4.3 RESULTS OF THE VPD RECONSTRUCTION

### 4.3.1 CLIMATE SENSITIVITY

The network of  $\delta^{18}\text{O}_{\text{cel}}$  time series is significantly correlated with the European Summer VPD over the observational period (i.e. 1900 – 1994). In Figure 4.3, the correlations of the individual  $\delta^{18}\text{O}_{\text{cel}}$  time series with the respective time series of the grid cell from the calculated VPD of 20CRV3 (Slivinski et al., 2019) are presented for summer and spring.

In total, 11 sites show a significant correlation with VPD in spring, with the maximum in Italy and Turkey ( $r=0.40$ ; Figure 4.3a). The sites with significant correlations are distributed across the continent without any spatial bias. There is no influence of the tree species used and no influence of the altitude of the sampled trees (Balting et al., 2021a). The high sensitivity of the time series from Turkey with spring climate has already been noted (Heinrich et al., 2013). 15 time series out of the 26 sites show no significant correlations with VPD during spring.

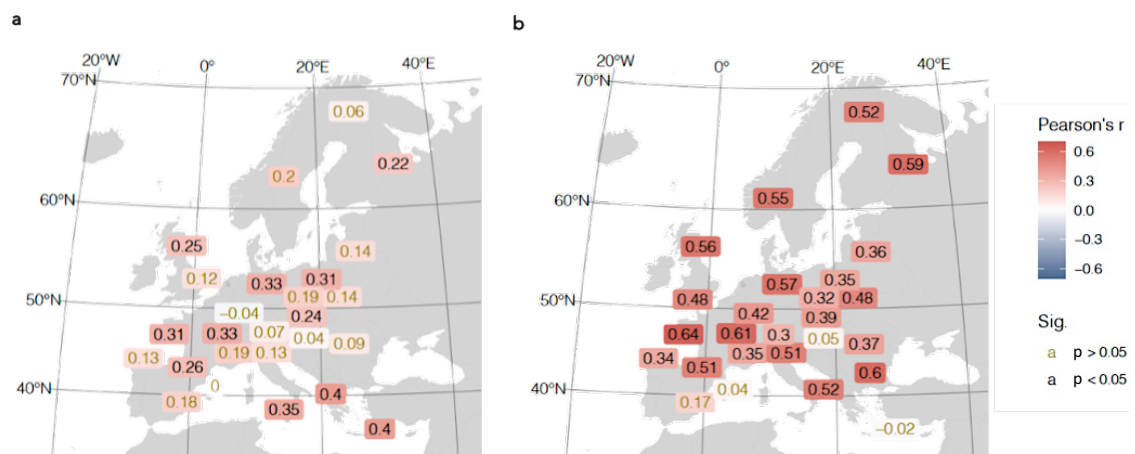


Figure 4.3: Correlation of the  $\delta^{18}\text{O}_{\text{cel}}$  time series with the European VPD for the period 1900 to 1994. a, for spring (MAM), b, for summer (JJA). The significant correlations are highlighted ( $p < 0.05$ ).

The most significant correlations as well as the highest seasonal correlation coefficients are reached with the summer VPD (Figure 4.3b). 22 of the 26 sites show a significant correlation, with most of these sites being located in France, Spain, Germany, Scandinavia and Great Britain. The highest correlation coefficient ( $r=0.64$ ) is calculated for the Rennes site (France). One time series from Turkey, two from Spain and one from Austria do not have a significant correlation with the summer VPD (Figure 3.4b). Based on these results and the shown sensitivity of the  $\delta^{18}\text{O}_{\text{cel}}$  for VPD variability, the reconstruction of VPD is performed for the summer months (JJA).

### 4.3.2 VALIDATION STATISTICS

Since the nesting approach is used, 13 RandF models in total were calculated and optimised by cross validation (see Michel et al., 2020), i.e. from each time when a new time series from the network is available. The quality of the reconstruction can be described with the CE (Appendix A), which is presented in Figure 4.4 for four selected time steps. For year 1600, CE scores indicate that a satisfactory quality for the reconstruction of VPD for Northeast Spain, Italy, Greece, France, Germany and large parts of Scandinavia (Figure 4.4). The described regions coincide with the locations of the eleven available time series for this time slice. Therefore, the reconstruction covers large parts of Europe from the beginning. For the time slice 1700 presented in Figure 4.4, an expansion of the significant regions is observed for the CE values. For this time slice, 16 of the 26 time series are available and the spatial coverage has improved towards Eastern Europe and isolated gaps, such as in parts of Norway, could be closed.

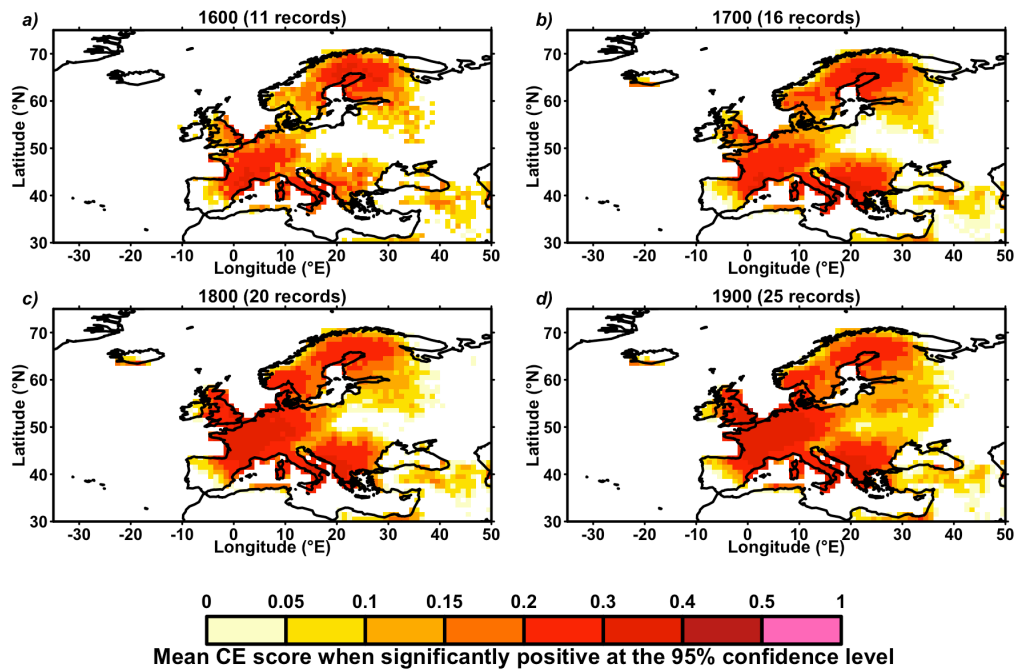


Figure 4.4: The Nash–Sutcliffe CE for four different time slices. The coloured areas show the regions where the model set up has a suitable quality, which was tested with a one-sided Student's t-test ( $p < 0.05$ ). No or lack of model efficiency largely relates to regions without  $^{18}\text{O}_{\text{ceI}}$  records (e.g. SW Spain, Belarus, Ukraine).

A further improvement of the CE values between 1700 and 1800 can also be observed (Figure 4.4), whereby it is most noticeable that Great Britain is now largely covered by grid points robustly reconstructed. This is because another time series from Scotland has been included for the 1700 time slice (Figure 4.4). Also, for the last time step an improvement of the spatial coverage of the reconstruction can be seen. In particular, a large gap in Eastern Europe has been closed, due to the time series from Romania, which is available for the reconstruction from 1900 onwards. It can also be noted that adjacent regions of Europe, such as parts of Turkey also have a suitable quality for reconstructing

past VPD variability changes. The overall spatial strength of the network is in Southern, Western and Northern Europe, whereas Eastern Europe can only be partly covered. Nevertheless, it must be mentioned that validation statistics for all time steps must be included in the consideration of the results. Therefore, only those grid cells with a satisfactory reconstruction performance will be included in the following analyses.

---

#### 4.3.3 TEMPORAL VARIABILITY OF THE EUROPEAN VPD RECONSTRUCTION

The average VPD of Northern Europe (Figure 4.5a) shows significant differences in variability as well as in the long-term mean. Northern Europe shows the lowest VPD of all three regions, which is due to the comparably low temperatures and high humidity in these broad areas. The increase of VPD between 1620 and 1660 is significant ( $m = 0.0017 \text{ kPa year}^{-1}$ ;  $p\text{-value} = 0.0026$ , where  $m$  is the linear regression slope), with the highest VPD value of the 400 years being reached in 1652 ( $\text{VPD} = 0.4619 \text{ kPa} > 2.7 \times \sigma$ , where  $\sigma$  is the standard deviation of the time series). After this peak, VPD drops until it starts to rise again in 1673. However, it is noted that this increase during Late Maunder Minimum (1675-1715; considered as the coldest phase of the Little Ice Age in Europe (Brönnimann, 2015)) is not as long-lasting as the former increase from 1620 to 1660. VPD starts to decrease again from the year 1700. The subsequent drop lasts until the 1720 to 1730 period, after which the time series shows further low frequency variability and a minor upward tendency in the 30-year rolling average that lasts until the end of the 20<sup>th</sup> century ( $m = 0.00002 \text{ kPa year}^{-1}$ ;  $p\text{-value} < 0.00001$ ). In total, the three years with lowest VPD in this region are 1674, 1782 and 1802 whereas the years with the highest VPD are 1652, 1735 and 1959.

The VPD reconstruction for Central Europe (Figure 4.5b) shows that VPD increases from 1600 up to the Late Maunder Minimum (i.e. early 1700s;  $m = 0.0007 \text{ kPa year}^{-1}$ ;  $p\text{-value} = 0.0003$ ). This increase is followed by a downward trend of VPD in Central Europe which ends in 1743 ( $m = -0.0014 \text{ kPa year}^{-1}$ ;  $p\text{-value} = 0.0286$ ). The period 1740 to 1760 is characterized by very low VPD values and the lowest 30-year rolling VPD. From this time on, the rolling average VPD is characterized by a rising trend ( $m = 0.0002 \text{ kPa year}^{-1}$ ;  $p\text{-value} = 0.0037$ ), but low values are reached during the Dalton Minimum (1790 to 1820). Furthermore, the VPD reconstruction is characterized by a significant 60 to 80 years oscillation (Supplement 5). The three years with lowest VPD are 1602, 1755 and 1786 whereas the years with the highest VPD are 1707, 1835 and 1921.

The VPD reconstruction for the Mediterranean region shows the largest VPD and higher variability compared to the other two regions (Figure 4.5c). It is noticeable that at the beginning of the reconstruction period (1610-1650) the VPD values decrease ( $m = -0.0017 \text{ kPa year}^{-1}$ ;  $p\text{-value} = 0.013$ ), which is followed by a VPD increase leading to an almost constant VPD level during the Late Maunder Minimum. From the end of the Maunder Minimum, the VPD falls steadily until 1761, where it remains at a similar level on average until 1773. This is followed by a short increase, which is stopped

at the beginning of the Dalton Minimum and leads to a decreasing VPD. The minimum of VPD value is also reached during this period (VPD=0.96 kPa for the year 1814). After the Dalton Minimum, the VPD rises again ( $m=0.0003$  kPa year<sup>-1</sup>;  $p$ -value= 0.0182). Furthermore, the VPD time series shows similar oscillations as for Central Europe, but most pronounced in the last 150 years. Low periods of the oscillation are shown for example between the end of the 19<sup>th</sup> century and the beginning of the 20<sup>th</sup> century as well as for the 1960s and 70s. In total, the three years with lowest VPD in this region are 1780, 1814 and 1815 whereas the years with the highest VPD are 1686, 1874 and 1945.

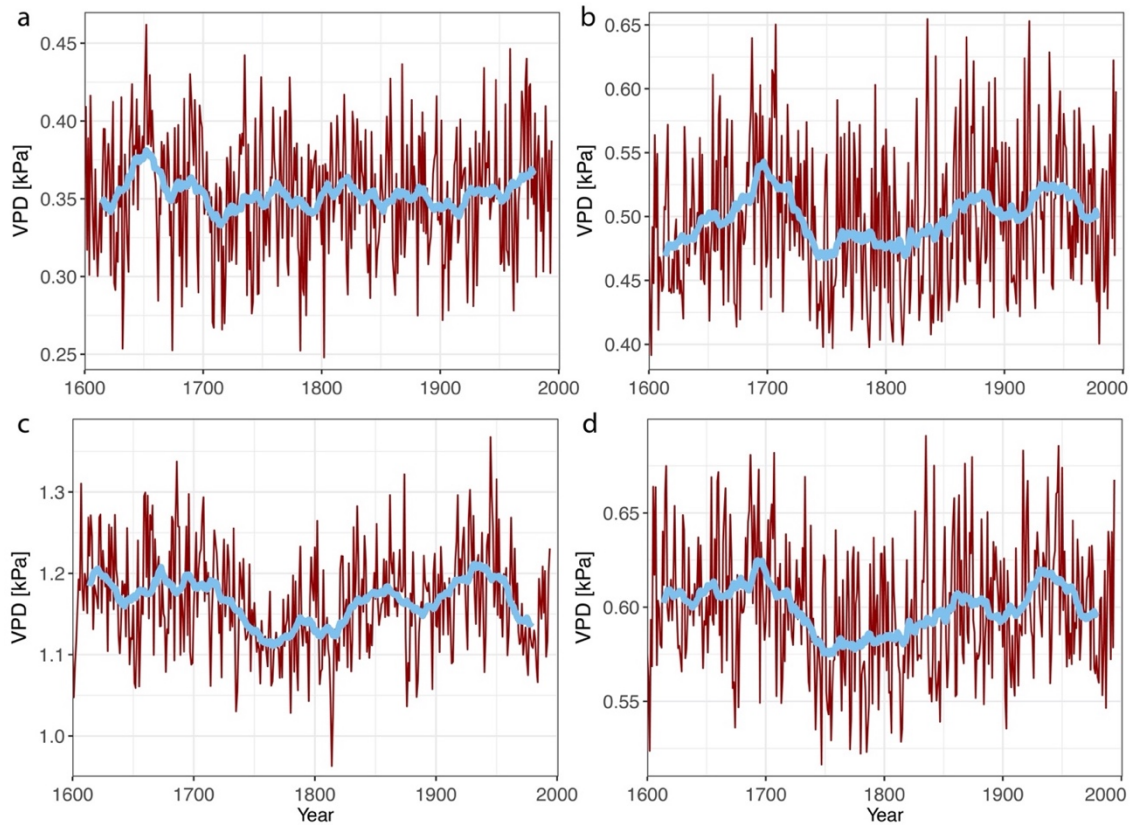


**Figure 4.5:** Temporal variability of the VPD reconstruction. a, Northern Europe, b, Central Europe, c, Mediterranean region, d, Europe. The red curve represents the annual summer values and the blue line the rolling mean for 30 years window. The average calculation included only those grid cells that had a sufficient CE in the validation statistics.

The mean VPD value for entire Europe increases until about 1690 (Figure 4.5d). However, the maximum VPD for Europe is reached before the Late Maunder Minimum. During the Late Maunder Minimum the trend starts to reverse and the average VPD decreases until the middle of the 18<sup>th</sup> century. From there on, the European mean VPD increases ( $m=0.0001$  kPa year<sup>-1</sup>;  $p$ -value= 0.00006), again due to the positive trends in Central Europe as well as changes in the Mediterranean.

## 4.3.4 COMPARISON OF THE TIME SERIES WITH OTHER RECONSTRUCTIONS

The VPD variability is compared with existing reconstructions of summer temperature (Luterbacher et al., 2004), precipitation (Pauling et al., 2006) and drought (PDSI) reconstruction (Cook et al., 2015) in Figure 4.6-8.

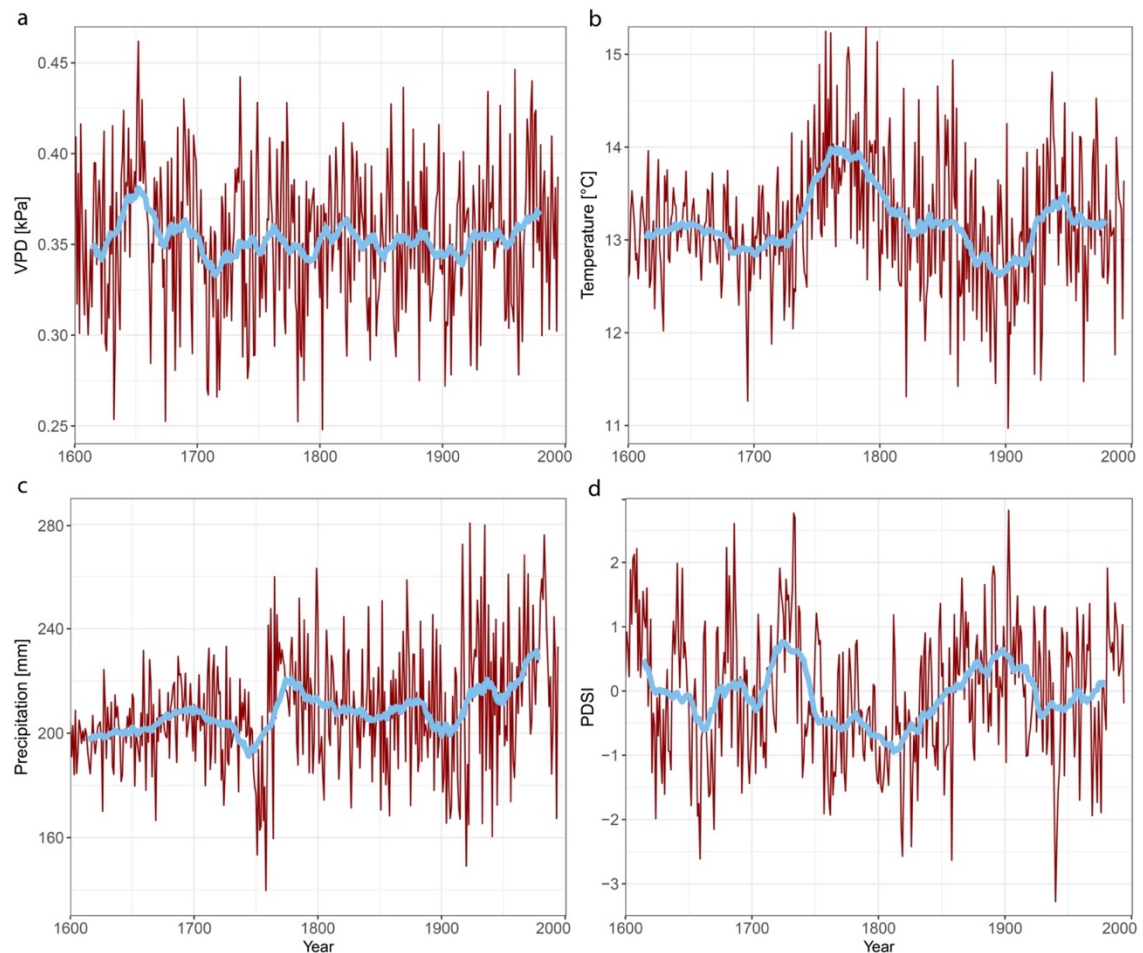


**Figure 4.6:** The reconstructed summer VPD for Northern Europe in comparison with reconstructed summer temperature, precipitation and PDSI. a, reconstructed VPD, b, surface temperature (Luterbacher et al., 2004), c, precipitation (Pauling et al., 2006), d, PDSI (Cook et al., 2015). The red line represents the annual summer values and the blue line the rolling mean for 30 years window. The average calculation included only those grid cells that had sufficient CE in the validation statistics.

For Northern Europe, the characteristics of VPD until 1700 shows little resemblance with the reconstructions of precipitation and temperature (Figure 4.6a,b,c). However, the PDSI indicates dry conditions for the time of the maximum VPD in 1652 (Figure 4.6d). Furthermore, the decrease of VPD between 1700 to 1730 is shown as a wet period in the drought reconstruction, which could be a possible explanation for these low values. From 1730 to 1800, the shown strong temperature increase is visible in VPD only partly. A possible reason for this could be the concurrent increase of precipitation. Since the temperature and precipitation changes in this region coincide, it is difficult to detect the characteristics of the two variables in the VPD time series.

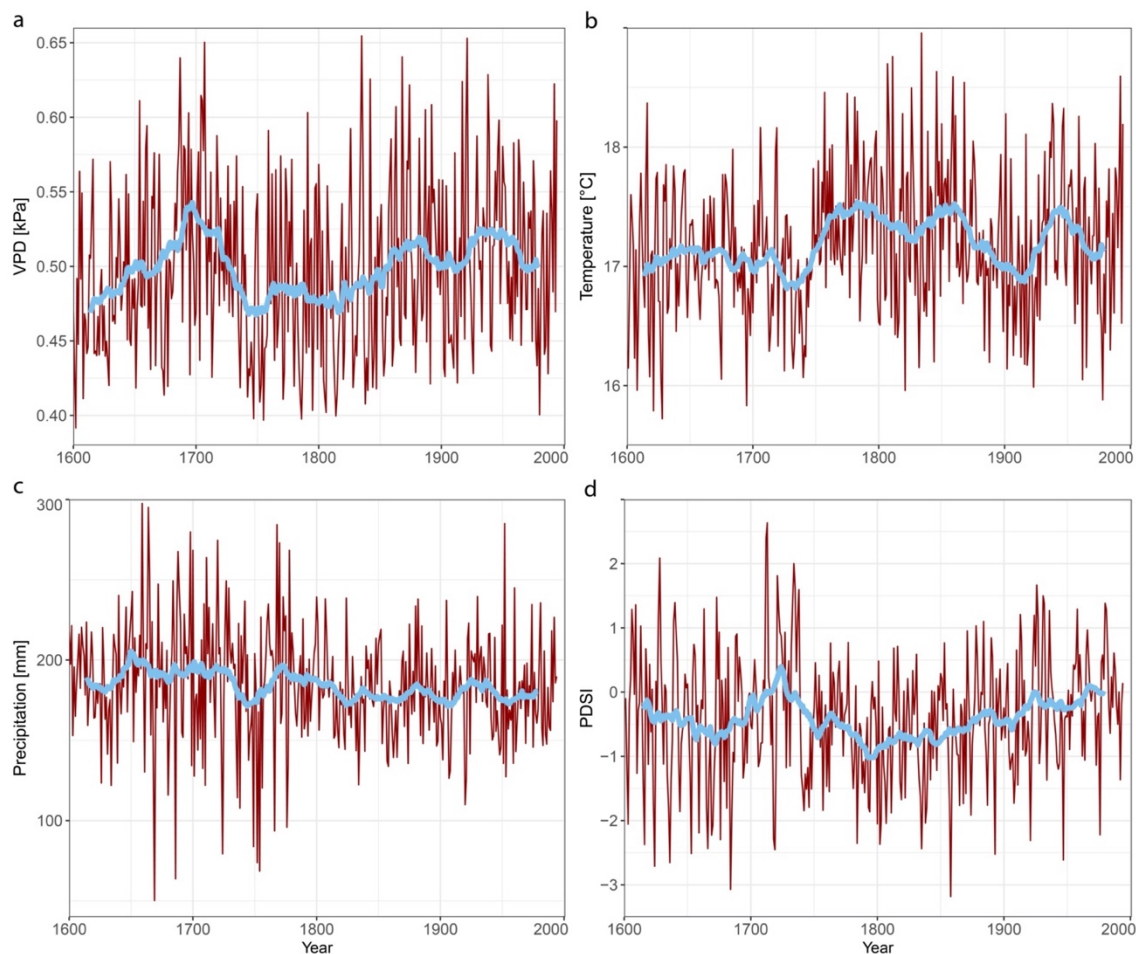


Figure 4.7: Same as Figure 4.6, but for Central Europe.

For Central Europe, the increase of the VPD until 1700 cannot be explained by the temperature or precipitation reconstruction (Figure 4.7a,b,c). The 30-year running mean of both time series show diverging trends. Nevertheless, the reconstruction of the PDSI also shows a trend towards drier conditions from 1670 to 1690 (Figure 4.7d). However, before the end of the 17<sup>th</sup> century, the data indicates a wetting trend again. Afterwards, the periods of high and low temperature and precipitation match very well with the corresponding periods of high and low VPD. For example, the decrease in precipitation and temperature between 1730 and 1745 is also present in the VPD time series. From 1800 onward, the VPD increases with a clear and significant oscillational behaviour which is closely related to the oscillational pattern of temperature (Supplement 5). However, the oscillation of the VPD time series is also influenced by the precipitation variability. The precipitation shows an oscillating behaviour from the second half of the 19<sup>th</sup> century, but the magnitude is represented weaker than in the VPD or the temperature time series. While the temperature, precipitation and VPD reconstruction show a consistent picture from 1800 onwards, meaning that it becomes warmer, there is less precipitation and the VPD increases in summer. The PDSI, on the other hand, shows a wetting trend from 1800 onwards. It is suggested that this could be based on accumulation processes of

precipitation in the preceding months which is represented by the PDSI. This could compensate the increasing temperature and the decreasing precipitation in summer.

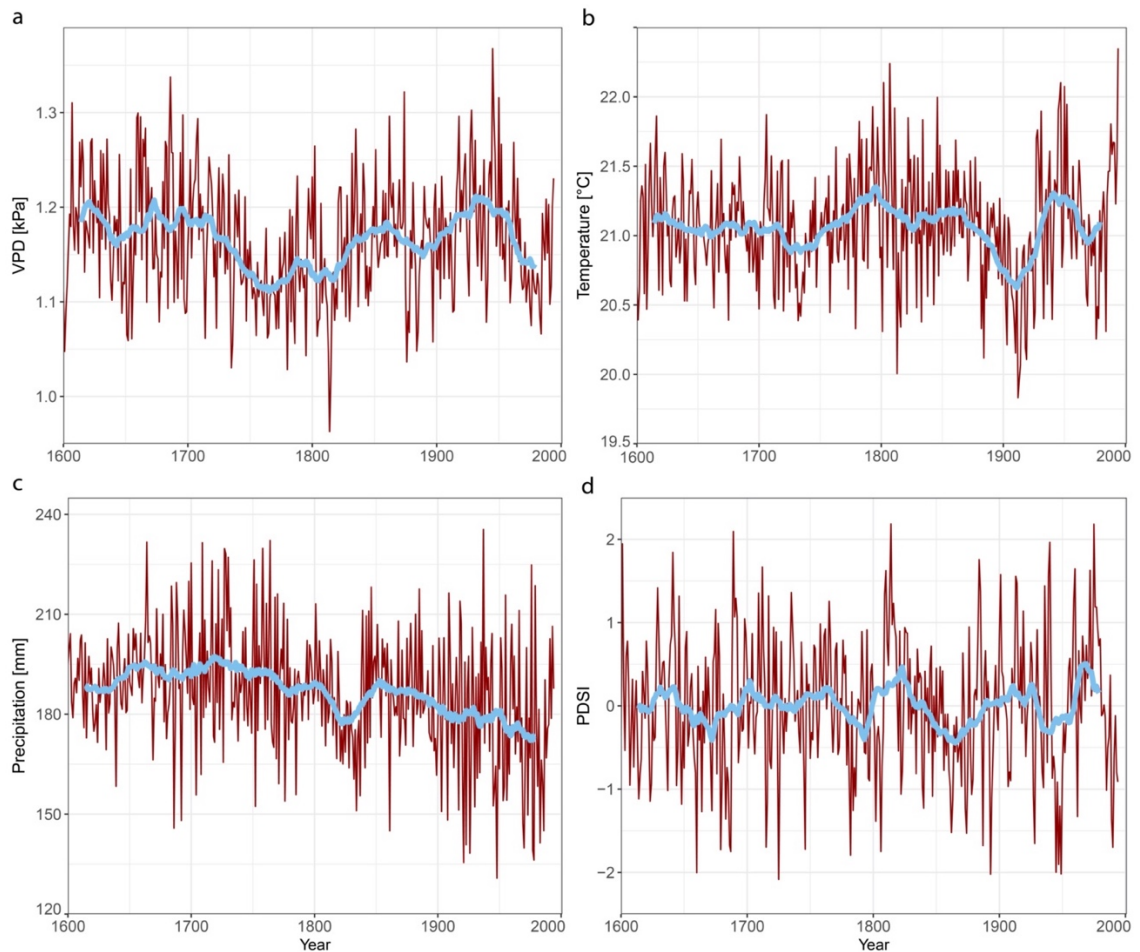


Figure 4.8: Same as Figure 4.6, but for the Mediterranean region.

For the Mediterranean area, the summer of 1814 is an extreme event in the temperature time series, as it shows the second coldest temperatures for this region in the last 400 years (Figure 4.8a,b,c). Furthermore, it is interesting that the precipitation increased during the Dalton Minimum (~1790) in this region and only decreases towards its end (1805-1810), which can also explain the behaviour of the VPD during this period. It is suggested that the comparable low temperatures and the high precipitation led to this extreme year in the VPD time series. After the Dalton Minimum, the temperature shows an increasing trend and the course of the curves is very similar to the oscillating behaviour already described for the VPD, even though the magnitude differs. Nevertheless, the periods with high and low values of temperature are almost identical to the corresponding periods of the VPD time series after the Dalton Minimum. Since the decrease in precipitation is almost linear in the 30-year mean from 1850, it is suggested that, comparatively, the oscillation of temperatures can be clearly seen in the VPD time series.

A similar situation is described by the drought reconstruction for the Mediterranean area (Figure 4.8d). Thus, the reconstructed PDSI shows wetter conditions towards the middle of the 18<sup>th</sup> century, which is complemented by the low VPD values for this period. Like the VPD and the temperature reconstruction, the PDSI shows drier conditions after the 1770s, intensifying until the beginning of the Dalton Minimum (~1790). Furthermore, the year 1814 is also the year with the wettest conditions in the PDSI time series. After the Dalton Minimum, the anti-correlation between temperature/VPD and the PDSI is again evident, so that an oscillatory behaviour is also visible.

---

#### 4.3.5 SPATIAL VARIABILITY OF THE VPD RECONSTRUCTION

To illustrate the spatial variability of the VPD reconstruction, selected extreme years are presented that represent either a particularly wet or dry period (see Figure 4.9). The first presented pattern of the spatial VPD variability is for the summer of the year 1616 (Figure 4.9 upper left). For this year, the VPD reconstruction represents positive VPD anomalies over the entire continent pattern where the high anomalies are reached in Germany, Austria, parts of Czech and Switzerland. The highest VPD anomaly is shown in Scotland ( $VPD_{z-anomaly} = -3.1$ ). Therefore, the spatial pattern of the VPD anomalies for the year 1616 shows similarities to a monopole pattern over Europe, since no negative VPD anomalies are shown. In contrast, the VPD reconstruction for the summer 1737 shows negative VPD anomalies for Central and Southern Europe (Figure 4.9 upper mid), where the lowest anomalies are shown for the Balkan area ( $VPD_{z-anomaly} = -2.16$ ). In contrast, Finland, northern Sweden, and northern Norway are characterized by high positive VPD anomalies (maximum  $VPD_{z-anomaly} = 2.92$ ). The pattern can be described as dipole pattern between northern Scandinavia and Central/South Europe.

The VPD anomaly for the summer of 1741 also presents a dipole pattern (Figure 4.9 upper right), but the centres are in this case Scandinavia and Southwest Europe. Low VPD anomalies are located in Scandinavia with the lowest values in southern Sweden and Denmark ( $VPD_{z-anomaly} = -2.73$ ). In contrast, Southwest Europe is characterized by high VPD anomalies with the highest values located in northeast Spain ( $VPD_{z-anomaly} = 2.47$ ). Also, Southeast Europe shows positive VPD anomalies, but with a lower magnitude compared to Northeast Spain.

The year 1814 is the year with the lowest VPD average in the Mediterranean region (Figure 4.5). The VPD anomaly map (Figure 4.9 lower left) shows a dipole between Northern and Southern Europe for this year. The highest VPD anomalies are shown in West Sweden, West Norway, Denmark and Great Britain with the highest values in southern Sweden and Denmark ( $VPD_{z-anomaly} = 2.09$ ). The opposite situation is presented for entire Southern Europe, where negative VPD anomalies characterize the entire area. The lowest VPD values are located in Southeast Europe ( $VPD_{z-anomaly} = -3.51$ ).

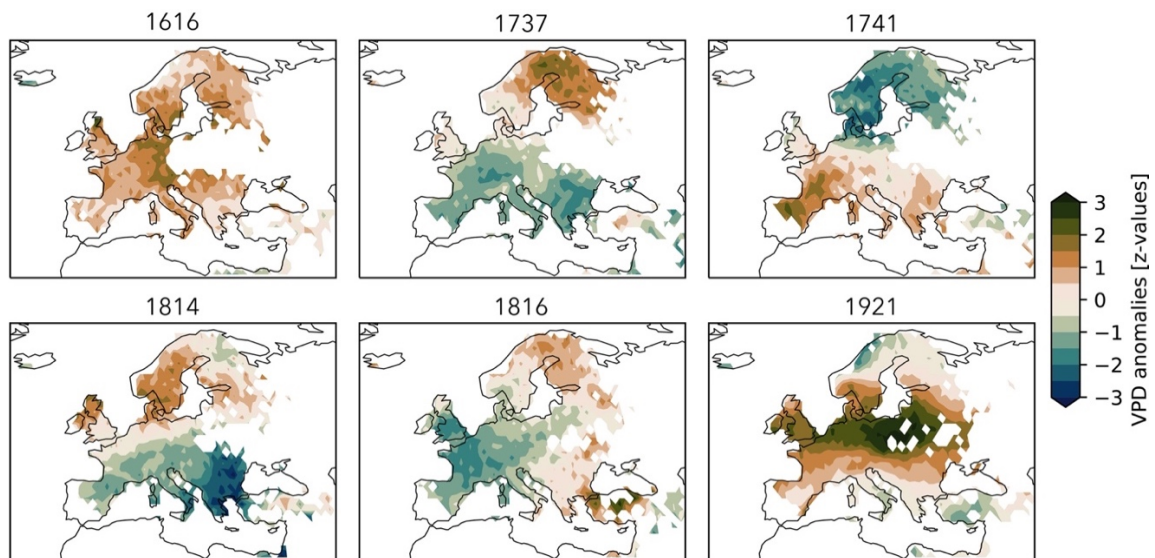


Figure 4.9: Spatial pattern of VPD anomalies for selected years. Values of each grid cell are standardised and centred. The anomalies were computed based on the subtraction of the average of the twelve preceding years as well as the twelve following years. Furthermore, only those grid cells with sufficient CE in the validation statistics are included in the plot.

The VPD anomaly map for 1816 illustrate a dipole between West/East (Figure 4.9 lower mid). Negative VPD anomalies are shown for West and Central Europe with the lowest values in Great Britain and France ( $VPD_{z-anomaly} = -2.06$ ). In contrast, positive values are represented in East Europe with highest values in Scandinavia and Southeast Europe especially Greece and Turkey ( $VPD_{z-anomaly} = 3.16$ ).

A tripolar pattern is shown in the VPD anomaly map for the year 1921 (Figure 4.9 lower right). High VPD values are observed for Central Europe which stretch in a band from North Spain/Great Britain to Poland. The highest VPD anomalies are located in eastern Germany, Poland and Lithuania ( $VPD_{z-anomaly} = 3.39$ ). In contrast, negative VPD anomalies are shown in southern Italy, Turkey and northern parts of Scandinavia. The lowest values are presented in Norway ( $VPD_{z-anomaly} = -2.15$ ). The presented spatial variations and varying VPD patterns underline the importance of a spatial field reconstruction.

#### 4.3.6 COMPARISON OF PAST/HISTORICAL SPATIAL VARIABILITY

According to a drought reconstruction for Czech, the drought of 1616 was one of five “outstanding drought events” since 1090 CE which began in the spring and continued throughout the summer with great heat and dried-up rivers (Brázdil et al., 2013). The dry conditions are also represented by the reconstruction, where positive VPD anomalies are shown for Europe with the highest values are reached in Germany, parts of Czech, Austria and Switzerland (Figure 4.9 upper left). In addition, the average time series for Europe in Figure 4.5 also indicate high VPD values during this time. A similar situation is also described by the PDSI (Cook et al., 2015) where severe to extreme drought are shown

over Central and Eastern Europe. Year 1616 was characterized by a long dry period which began in mid-April and lasted through the summer. The regional focus of this dry phase was in the East, but eventually spread to the rest of Central Europe. Overall, 1616 was a remarkably dry from April until November, characterized by a very hot and extremely dry summer (Glaser, 2013). The extreme dryness of this particular year, throughout whole Europe, is well captured by the VPD reconstruction.

The year 1737 is part of relatively wet period which is represented by the PDSI (Cook et al., 2015; Ionita et al., 2021) for Europe on average. The more humid conditions also fit with a comparatively low VPD in Central Europe as well as in the Mediterranean region as shown in Figure 4.9. However, relatively high VPD anomalies are shown over northern Scandinavia, which are also represented on average by the PDSI (Cook et al., 2015; Ionita et al., 2021). For example, August 1737 was too cold and too wet in Central Europe and almost continuous rainy weather was reported in Germany in the second decade of August (Glaser, 2013).

The year 1741 is often associated to the Irish famine, which according to documentary and early instrumental data was associated with low rainfall in spring and summer (Pauling et al., 2006). In the VPD reconstruction (Figure 4.9 upper right), parts of the UK and Germany are also represented by a high VPD anomaly, while the highest VPD anomalies are shown for France and northern parts of Spain. That agrees with the PDSI (Cook et al., 2015), precipitation (Pauling et al., 2006) and temperature reconstruction (Luterbacher et al., 2004). In contrast, low VPD values over Scandinavia are disagree with wet conditions in the PDSI (Cook et al., 2015). For example, in 1741 the northeast Germany experienced longer-lasting cooler phases, which were also very dry in some regions. In July, this pattern essentially remained intact. Overall, there was a prolonged period of rain in central Germany, that lasted until the winter. In August numerous downpours and thunderstorms have been reported (Glaser, 2013).

As already shown in the temporal perspective of VPD variability, the year 1814 shows the lowest VPD value for the Mediterranean region (Figure 4.9 lower left). However, there are high VPD anomalies in Scandinavia. The pattern resembles a dipole pattern which shows similarities to the summer European blocking pattern (Barnston and Livezey, 1987; Cassou et al., 2005) which is often associated with the Summer North Atlantic Oscillation (SNAO; Hurrell and Van Loon, 1997). According to Cassou et al. (2005), 17.8% of the positive phase and 17.9% of the negative phase of the summer European blocking pattern influence the total summer weather regimes in Europe. Furthermore, the summer European blocking pattern is a surrogate indicator for storm track activities (Folland et al., 2009; Lehmann and Coumou, 2015). The SNAO pattern is also evident in the OWDA for 1814.

The last selected year with humid conditions in Europe is 1816, which is related to the Tambora eruption in 1815 that caused a cooling of 2-3 °C in Central Europe (Trigo et al., 2009). Several studies refer to the year 1816 as the "year without a summer" due to a sharp drop in temperature revealed in

European reconstructions (e.g. Büntgen et al., 2006). 1816 was unusually cold and wet year, especially in Central Europe (Schurer et al., 2019). The largest temperature anomalies occurred in summer 1816, marking the coldest European mean summer temperature ever recorded over the last 235 years (Casty et al 2007). It was also associated with a Europe-wide famine and a sharp increase in food prices across Europe (Brönnimann and Krämer, 2016). Central and Western Europe show low VPD anomalies, while Southeast Europe and Scandinavia are interestingly not affected by a low VPD anomaly (Figure 4.9). The described pattern agrees well with the pattern resulting from reconstructed temperatures, precipitation and sea level pressure (e.g. Schurer et al., 2019).

Based on PDSI data (Cook et al., 2015), the conditions for 1921 are the driest of the last millennium, particularly for western and Central Europe. This drought was described as "a year of unprecedented low rainfall" across much of the British Isles, with the greatest deficit occurring in south-east England (Brooks and Glasspoole, 1922). 1921 was one of the driest years on record, over large areas in Europe, with a focus on Central Europe (Ionita and Nagavciuc, 2021) which is in agreement with the spatial pattern of the VPD reconstruction. This extreme dryness, was mainly driven by a long-lasting precipitation deficit throughout the year (Ionita and Nagavciuc, 2021). In addition, 1921 is also considered the driest year in the Rhine and Weser catchments based on observed runoff data (Ionita et al., 2021). This description fits the depicted conditions in Central and Western Europe, as large parts of Great Britain, Germany and Poland show high VPD anomalies in Figure 4.9 (lower right). Furthermore, it is evident from the time series that the VPD shows the second highest value within the last 400 years for Central Europe (Figure 4.5b). The less dry conditions in Italy are consistent with other studies (e.g. Bonacina, 1923).

---

#### 4.3.7 HISTORICAL AND FUTURE EUROPEAN VPD IN CMIP6

The reconstructed and observed VPD is compared with the ability of the CMIP6 models (Eyring et al., 2016) to simulate the VPD in the historical simulations and assess how the VPD variability is projected to change in the 21<sup>st</sup> century. In this respect, CMIP6 ensemble mean of VPD is used (see table S6 for a description of the used models) over the period 1851 – 2100 (merging ensemble averages from historical and future experiments). For Northern Europe, the model ensemble represents on average VPD in the historical run too weakly (Figure 4.10 up). Nevertheless, a large part of the observed and reconstructed VPD lies within the 75th percentiles of the model ensemble. From 1980 onwards, the model ensemble shows a positive trend of VPD until 2014 ( $m = 0.0014$  kPa;  $p\text{-value} < 0.0000001$ ), which cannot be represented by the reconstruction or observations. In the future scenarios, the strongest increase is shown by the scenario SSP5-8.5, whereas SSP1-2.6 and SSP2-4.5 show only a slight increase and small differences of VPD in Northern Europe (Table 4-2). For the last two scenarios, VPD does not increase beyond the observed values.

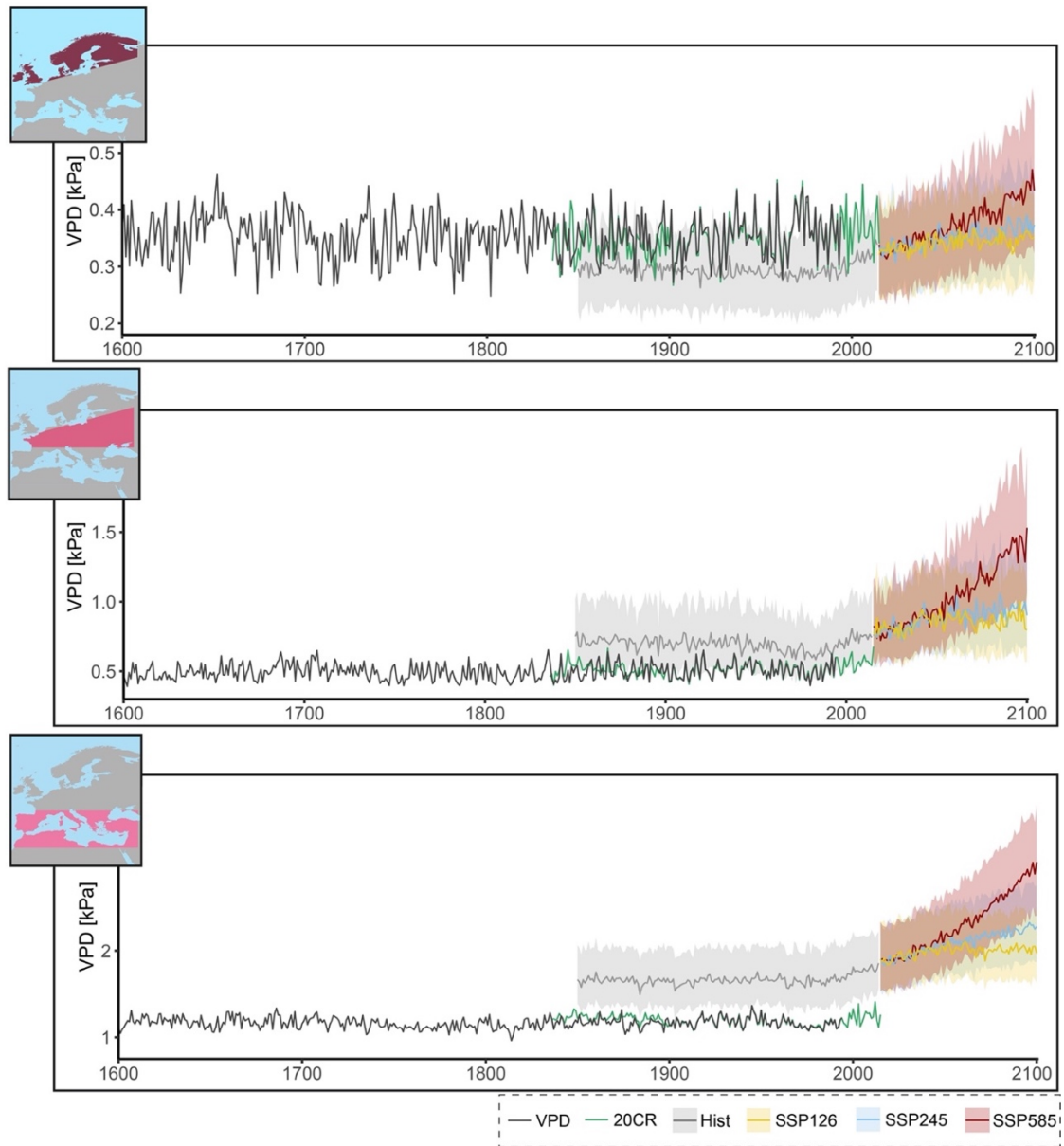


**Figure 4.10:** Five centuries of VPD variability for three different regions in Europe. The boundaries of the different regions are following the definitions of Iturbide et al. (2020). In this graph, the reconstructed and the observed VPD (20CR) are joined as well as the modelled VPD for the historical conditions (Hist) as well as for three different scenarios. (SSP1-2.6, SSP2-4.5, SSP5-8.5) The average of the model ensemble is shown with a bold line and the area between the 25<sup>th</sup> and 75<sup>th</sup> percentile with the corresponding slightly transparent colour.

There is significant offset between the historical run and the reconstructed as well as the observed VPD can be seen for Central Europe (Figure 4.10 mid). In contrast to Northern Europe, VPD in Central Europe is higher than the model ensemble. However, the observed VPD is close to the 25<sup>th</sup> percentile of the model ensemble. This is an interesting result which notably indicates that CMIP6 models are modestly able to simulate the observed VPD in those regions. From 1980 onwards, the model ensemble shows an increasing trend of VPD until 2014 ( $m = 0.0051$  kPa;  $p$ -value  $< 0.000000001$ ), which is also represented by the reconstruction and observations ( $m = 0.0028$  kPa;  $p$ -value  $< 0.01$ ). Furthermore, all three scenarios show a significantly stronger increase than for

Northern Europe (Table 4-2). It is noticeable that the SSP5-8.5 scenario provides the strongest VPD increase, and the other two scenarios behave very similarly despite a stronger increase compared to the projected changes of VPD in Northern Europe. SSP2-4.5 shows only minimal increased values compared to SSP1.2-6.

The strongest difference between observed and the modelled historical runs can be found for the Mediterranean region (Figure 4.10 down). Thus, the observed and model data differ by more than 0.5 kPa. Furthermore, the observed data also lie outside the interquartile range. However, the ensemble mean shows a trend from 1990 until 2014 ( $m = 0.006$  kPa;  $p\text{-value} < 0.000000001$ ) which is also represented in the reconstruction and observations ( $m = 0.004$  kPa;  $p\text{-value} < 0.01$ ). As for the Central Europe, the strongest VPD increase can be determined for the scenario SSP5-8.5 (Table 4-2). On average, an increase in VPD of more than 1 kPa is shown by the end of the 21<sup>st</sup> century. This is the largest increase of all regions considered. Furthermore, there is a clearer difference between the other two scenarios. In the scenario SSP1.2-6 there is only a comparatively weak increase which levels off again after a short time. A much larger increase can be observed for scenario SSP2.4-5, where the trend is increasing until the end of the century. This cannot be found in the other regions.

**Table 4.2: Characteristics of the linear trend of three different future scenarios for Northern Europe, Central Europe and Mediterranean.**

	SSP1.2-6	SSP2.4-5	SSP5-8.5
Northern Europe	$m = 0.0003$ kPa $p\text{-value} < 0.00001$	$m = 0.0005$ kPa $p\text{-value} < 0.000000001$	$m = 0.0014$ kPa $p\text{-value} < 0.000000001$
Central Europe	$m = 0.0008$ kPa $p\text{-value} < 0.001$	$m = 0.0022$ kPa $p\text{-value} < 0.000000001$	$m = 0.0083$ kPa $p\text{-value} < 0.000000001$
Mediterranean	$m = 0.0013$ kPa $p\text{-value} < 0.000001$	$m = 0.0051$ kPa $p\text{-value} < 0.000000001$	$m = 0.0134$ kPa $p\text{-value} < 0.000000001$

Thus, in order to clarify the question of how VPD will develop spatially in the future and what causes the behaviour in the scenarios, Figure 4.11 shows the change in VPD in the three scenarios for the European continent during summer. It is noticeable that especially the Mediterranean region is a hotspot for the increase of VPD as already shown in Figure 4.8. However, for the two regions of North and Central Europe, a different pattern is observed. For Central Europe, only a small and localized increase in VPD can be seen in SSP1.2-6 whereas Northern Europe shows even a smaller increase of VPD in this scenario. High VPD from the subtropics expand in these regions. This is detectable especially in Central Europe in the SSP2.4-5 scenario, where a stronger increase of VPD is observed. Nevertheless, a stronger and pronounced increase of VPD in Northern Europe can only be detected in scenario SSP5-8.5.

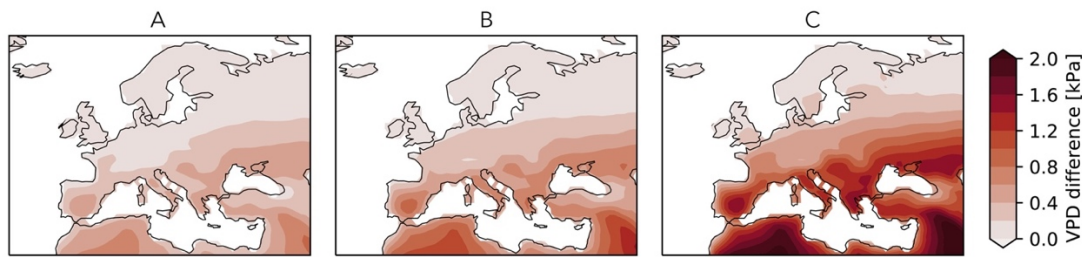


**Figure 4.11:** Spatial distribution of the summer VPD anomalies in Europe based on the projected changes (2071–2100) for SSP1-2.6 (A), SSP2-4.5 (B) and SSP5-8.5 (C) scenarios relative to the historical summer VPD during the 1971–2000 reference period. For the historical and projected changes, the average temperature of the CMIP6 model ensemble is used. All changes are significant according to the two-sided Student's t test ( $p < 0.05$ ).

#### 4.4. LIMITATIONS OF THE VPD RECONSTRUCTION

The used  $\delta^{18}\text{O}_{\text{cel}}$  network is characterized by specific limitations that influence the quality of the results. An over-representation of the sample sites in Central and Western Europe compared to the ones from Southeast, East and Northern Europe is shown in Figure 4.1. These characteristics of spatial distribution of sites are also represented in the validation statistics, where the regions with a good sample density show good validation scores (Subchapter 4.3.2). Therefore, further time series from uncovered regions are needed to enhance the quality and the spatial extent of the reconstruction. More time series from covered regions wouldn't improve much the RandF model because they are expected to be strongly correlated with the already used time series, which would have a very slight influence on the predictive performance of the RandF model (Boulesteix et al., 2012).

Beside the  $\delta^{18}\text{O}_{\text{cel}}$  climate signal, the observational data of VPD is given by the ensemble mean of 20CRV3 (Slivinski et al., 2019) for the period 1900 to 1994. Even though the quality and quantity of instrumental data available during this period is comparatively good, the ensemble mean can only represent the variability and diversity of the reanalysis with 80 ensemble members to a limited extent. Therefore, future studies are welcome to compare the quality of the reconstruction with other ensemble members.

The reconstruction is based on the application of the RandF algorithm calibrated and evaluated over the period 1900 to 1994. The model is therefore trained to represent exactly this period. Thus, when this model is applied to the years prior, stationarity between VPD variability and proxy records is assumed, as is generally the case for climate reconstructions (e.g. Cook et al., 2015). Since the climate system is not stationary, the assumption of stationarity must be included as a potential source of error. However, the RandF approach can represent non-linearities which is not possible with the classical approaches, for example PCR (e.g. Cook et al., 2015). Therefore, in order to eliminate errors when using the reconstruction, it is recommended a comparison with other available observational data, climate proxies, or reconstructions to quickly identify discrepancies.

Finally, even if the nested reconstruction approach is used by default for reconstructions (Luterbacher et al., 2004; Pauling et al., 2006; Cook et al., 2007, 2019; Freund et al., 2019) to cover the longest possible time range, it is important to check the quality of the model for the respective time range. Therefore, it is recommended to always consider the validation scores.

## 4.5 CONCLUSION OF THE LONG-TERM VPD VARIABILITY

Here, the first gridded reconstruction of the European summer VPD over the past 400 years is presented. Projected VPD conditions in the European summer are shown based on three different scenarios from the recent CMIP6 archive. The combination of reconstructed, observed and the projected variability allows conclusions about the past, present, and future VPD variability changes in Europe. Moreover, this is the first investigation that uses a  $\delta^{18}\text{O}_{\text{cel}}$  network and modern machine learning algorithm to perform a spatial reconstruction of a climate variable.

The past variability of VPD is different for the three investigated regions: North Europe, Central Europe and Mediterranean. The lowest VPD values as well as the lowest variability is shown for North Europe over the past 400 years. Also, in comparison to the other two regions, North Europe is showing the smallest increasing VPD trend in the reconstruction from the mid of the 18<sup>th</sup> century. The highest VPD values for this region are reached in the mid of the 17<sup>th</sup> century. Central Europe and the Mediterranean region reveal stronger trends of increasing VPD (highest VPD on average and highest VPD variability) which can be explained by a precipitation decrease and a temperature increase. The results underline that the European VPD has increased over the last decades. Based on the obtained long-term perspective, this increase in Europe has not started in 2000, but has already begun a few decades after the Late Maunder Minimum with a simultaneous increase in temperature in Europe in the mid 18<sup>th</sup> century.

The strong increase of the VPD at the end of the 20<sup>th</sup> and beginning of the 21<sup>st</sup> century is represented by the model ensemble used, although the magnitude of VPD increase partly differs. It is suggested that the differences are based on the differences in regional temperature between observation and models. However, when looking at the projected trends for the VPD, it is noticeable that the modelled trends for SSP1.2-6 and SSP2.4-5 are close to the trends between 1980 and 2014 of the observed VPD.

In the historical context, however, these trends are unique in magnitude and persistence, as comparable increases in VPD do not exist and, if they do, do not last longer than 30 years. The results imply that vegetation in Europe has been subject to an increase in VPD for a longer period of time, but that this increase has been significantly amplified by recent climate change, especially in Central Europe and the Mediterranean region. The association between high VPD and a decline in tree growth (Eamus et al., 2013), higher forest mortality (Park Williams et al., 2013), higher incidence of droughts

(Dai, 2013), a decline in crop production (Zhao et al., 2017) and a higher incidence of forest fires (Seager et al., 2015) suggests that the events will become more frequent as the average VPD continues to increase in the 21<sup>st</sup> century, with the magnitude being determined by the amount of greenhouse gas emissions.

The presented VPD reconstruction helps to visualize the local and regional impacts of the current climate change as well as to minimize statistical uncertainties of historical VPD variability. Furthermore, the interdisciplinary use of the data should be emphasized, as VPD is a crucial parameter for many climatological processes. As a logical next step, the regional and temporal boundaries of the reconstruction can be extended by using more and longer  $\delta^{18}\text{O}_{\text{cel}}$  time series from tree-ring cellulose. It is also possible to disentangle the influence of solar events on the VPD on the local, regional and continental scale.

# 05

## NORTHERN HEMISPHERE DROUGHT RISK IN A WARMING CLIMATE

## 5.1 FUTURE DROUGHT PROJECTIONS

In recent decades, historical climate observations have shown that many parts of the world are experiencing longer and more intense droughts as a consequence of observed atmospheric warming (Chiang et al., 2021). As a result, hydrological conditions are changing with potential regional climate change impacts on the society and ecosystems (Humphrey et al., 2018; Lu et al., 2019; Vicente-Serrano et al., 2020). Changing drought characteristics can lead not only to increased crop failures (Chal-linor et al., 2010), but also shifts in the entire ecosystem and vegetation zones (Loarie et al., 2009). Knowledge about the future drought occurrences, intensification and spatial distribution is therefore essential for developing adaptation policies and strategies.

In general, future drought projection is challenging since several relevant variables and complex processes contribute to the occurrence and severity of droughts. However, all drought-relevant variables are not necessary represented well in the general circulation models (GCMs). In particular, future changes in potential evapotranspiration ( $E_0$ ) and precipitation, which are integral parts of the hydrological cycle, are of major interest (Dai et al., 2018; Vicente-Serrano et al., 2019). Different multi-model efforts have explored climate change impacts on regional drought variability, e.g. the studies based on Fifth Phase of the Coupled Model Intercomparison Project (CMIP5; Taylor et al., 2012). Based on the CMIP5 simulations, hotspots of increased drought risk and severity have been identified (Seager et al., 2019), and the mechanisms behind the changes of the key drought related variables, e.g. precipitation,  $E_0$  and large-scale atmospheric circulation, have been investigated (Cook et al., 2014, 2015; Berg et al., 2017; Lemordant et al., 2018; Mankin et al., 2019). Nevertheless, it is important to revise the previous assessment based on the recently released state-of-the-art model simulations participating in Phase Six of the Coupled Model Intercomparison Project (CMIP6; Eyring et al., 2016). The main motivation is that the physical descriptions of the climate system in CMIP6 simulations, spatial resolution, and the climate forcing have improved substantially (Eyring et al., 2016). To investigate droughts several indices are available in the literature (Mishra and Singh, 2010). In this chapter, the Standardized Precipitation Evapotranspiration Index (SPEI; Vicente-Serrano et al., 2010a; Beguería et al., 2014), which represents a significant part of the atmospheric water balance, is used (Markonis et al., 2021). The advantage of the index is that it can be used for comparison across locations with different climatology because it is a standardized index for a given location relative to its long-term climatology (Stagge et al., 2015).

Using a multi-model ensemble mean drawn from CMIP6 database, changes in the key driving factors of droughts are evaluated and investigated, namely precipitation and  $E_0$  in the historical runs and the radiative forcing scenarios developed for ScenarioMIP (O'Neill et al., 2016). In this chapter, the conditions of low (Shared Socioeconomic Pathways 1-2.6; SSP1-2.6), medium (SSP2-4.5) and high (SSP5-8.5) emission scenario are investigated. Furthermore, the occurrence rate of dry periods is

computed for the updated regions of Sixth Assessment report (AR6) of the IPCC (Iturbide et al., 2020). The chapter focuses on the Northern Hemisphere during summer (June, July and August (JJA)), the season with the highest  $E_0$  and the highest spatial distribution of droughts (Lu et al., 2019). The overarching goal is to investigate the evolution of summer temperature and precipitation across different CMIP6 forcing scenarios, tendencies towards a wetter or drier climate and the occurrence of moderate to extreme droughts in three scenarios.

## 5.2 RISK STATISTICS & THE USED CLIMATE MODEL ENSEMBLE

### 5.2.1 CLIMATE MODEL ENSEMBLE

In this chapter, four climate variables from the CMIP6 (Eyring et al., 2016) simulations from historical simulations (1850 to 2014) and future projections (2015 to 2100) are analysed based on different shared socioeconomic pathways (SSPs; O'Neill et al., 2016). To present the analysis for a wide range of scenarios, SSPs including SSP1-2.6, SSP2-4.5 and SSP5-8.5 are used. The criteria for selecting climate models include (Seneviratne and Hauser, 2020): models must (i) provide the relevant variables, (ii) include simulations for the period 1850 to 2100, and (iii) not have duplicate time steps or missing time steps.

**Table 5-1: Description of the used climate model ensemble for the historical run and three future scenarios.**

Number of used realizations	Historical	SSP1-2.6	SSP2-4.5	SSP5-8.5	References
ACCESS-CM2	2	1	1	1	(Dix et al., 2019)
ACCESS-ESM1-5	3	3	3	3	(Ziehn et al., 2019)
AWI-CM-1-1-MR	2	1	1	1	(Semmler et al., 2018)
EC-Earth3	3	1	1	1	(EC-Earth Consortium, 2019a)
EC-Earth3-Veg	2	3	3	3	(EC-Earth Consortium, 2019b)
INM-CM4-8	1	1	1	1	(Volodin et al., 2019a)
INM-CM5-0	10	1	1	1	(Volodin et al., 2019b)
IPSL-CM6A-LR	32	6	6	6	(Boucher et al., 2018)
MIROC6	10	3	3	3	(Tatebe and Watanabe, 2018)
MPI-ESM1-2-HR	7	2	2	2	(Jungclaus et al., 2019)
MPI-ESM1-2-LR	10	10	10	10	(Wieners et al., 2019)
MRI-ESM2-0	5	1	1	1	(Yukimoto et al., 2019)

The maximum surface temperature ( $T_{max}$ ), minimum surface temperature ( $T_{min}$ ), mean surface temperature ( $T$ ), soil moisture, precipitation, wind speed, and cloud area fraction are downloaded with a monthly temporal resolution. The regional means are calculated from the original grid resolution, whereas for the maps the simulations are regridded onto a  $1^\circ \times 1^\circ$  grid using a bilinear interpolation approach. The names of models and their ensemble member counts are listed in Table 5-1.

### 5.2.2 COMPUTATION OF THE SPEI DROUGHT INDEX

To investigate the future drought conditions, the SPEI index (Vicente-Serrano et al., 2010a) is used. This index is a multiscalar drought index calculated from monthly precipitation ( $P$ ) and potential evapotranspiration ( $E_0$ ). The computation of SPEI index is based on the so-called climatic water balance defined as  $D_i = P_i - E_{0i}$ . One advantage of SPEI index is that it can be obtained for different accumulation periods, by aggregating the values of the climatic water balance over different time scales. This allows investigating different types of droughts by adjusting the accumulation period (Hayes et al., 2011; Vicente-Serrano et al., 2012). In this chapter, an accumulation period of 6 months (SPEI6) is used to capture the seasonal development of the drought and a WMO standard period from 1971 to 2000 as the reference period. A 6-month accumulation period is reasonable and widely used in the literature as it filters out short term anomalies, captures seasonal development of drought (e.g. from snow drought in winter to “classical rainfall deficit droughts” in summer) and correlates well with hydrological droughts (López-Moreno et al., 2013). The climatic water balance accumulations over six months periods are then standardized with a log-logistic distribution. Based on this distribution function, the SPEI values are standardized into a consistent scale and hence can be compared across space regardless of the climatology. Positive and negative SPEI values correspond to relatively wet and dry conditions, respectively whereas a SPEI of near 0 indicates near normal climatology (i.e.  $\sim 50^{\text{th}}$  percentile of the cumulative distribution function). For further details, the interested reader are referred to (Vicente-Serrano et al., 2010a).

Precipitation ( $P$ ) are used from the CMIP6 simulations. The monthly  $E_0$ , however, is computed with the FAO-56 Penman-Monteith equation (using a short reference crop with a height of 0.12 m; Allen et al., 1994):

$$E_0 = \frac{0.408 \times \Delta \times (R_n - G) + \gamma \frac{900}{T + 273} \times U \times (e_a - e_d)}{\Delta + \gamma(1 + 0.34U)} \quad (5-1)$$

where  $\Delta$  is the slope of the saturation vapour pressure function,  $\gamma$  is the psychrometric constant,  $T$  is the mean air temperature and  $U_2$  is the average near surface wind. Furthermore,  $e_a$  and  $e_s$  are mean saturation vapour pressure of the air and saturation vapour pressure at the kPa which are determined by minimum and maximum temperature.  $R_n$  and  $G$  are the net radiation and the soil heat flux (more details and the corresponding parametrization of  $R_n$ -FAO and  $G$  are presented in Allen et al. (1994)). The  $R_n$  is estimated by cloud cover, minimum, and maximum temperature, whereas  $G$  is determined by the average temperature. The required input datasets include the maximum and minimum temperature, wind speed, and cloud area fraction and a  $1^\circ$  elevation data from the Rand Corporation/Scripps Institution of Oceanography (accessed through the Cooperative Institute for Climate, Ocean, and Ecosystem Studies [http://research.jisao.washington.edu/data\\_sets/elevation/](http://research.jisao.washington.edu/data_sets/elevation/)).

SPEI6 and  $E_0$  were computed for the mean of the realizations of each model separately using the R package SPEI (Vicente-Serrano et al., 2010a; Beguería et al., 2014). Furthermore, the SPEI6 and the  $E_0$  dataset are averaged seasonally (December, January and February (DJF); March, April and May (MAM); June, July and August (JJA); September, October and November (SON)) to obtain a more comprehensive perspective about summer season droughts. Ensemble means of both SPEI6 and  $E_0$  are then computed for summer (JJA). To study droughts regionally, area averaged estimates are computed for the selected climate regions introduced in the IPCC (AR6) Assessment reports (Iturbide et al., 2020).

---

### 5.2.3 MODEL EVALUATION

To evaluate the consistency of the climate model simulations with observations, two different comparisons are performed. Data from CRU TS v. 4.05 (Harris et al., 2020) is used to evaluate temperature and precipitation simulations and data from SPEIbase v.2.6 (Vicente-Serrano et al., 2010a) to assess drought conditions. The former compares the average climate of WMO standard period 1971 to 2000 in summer considering three climate variables. To determine deviations between modelled and observed climate conditions, the ensemble mean from model simulations during 1971-2000 was subtracted from the average value of the observations. A positive (negative) value indicates that the ensemble mean of the models has a greater (smaller) value than the observations (overestimation).

For the model comparison, the differences between the means of two time periods are compared: 1975 to 1989 ( $t_1$ ) and 2000 to 2014 ( $t_2$ ) in model simulations (m) and observations (o). By comparing the change in the two periods one can compare change in model simulations relative to the observations ( $d=m-o$ ). A negative value indicates a stronger trend between the two time periods in the observations than the climate model ensemble (a positive value represents the opposite).

---

### 5.2.4 OCCURRENCE RATE STATISTICS

The initial data set for the computation of the extreme statistics consists of the SPEI time series for the AR6 regions from all models and their corresponding ensemble means. The advantage of using this drought index is that it is standardized on a given period and a predefined distribution. Therefore, each SPEI value corresponds to a predefined probability. Here, the threshold of -1.5 is chosen meaning that all occurrences of SPEI below the threshold would be considered as drought. This threshold generally corresponds to a moderate to extreme drought event. The probability that a value is below this threshold is predefined by the distribution function a 6.7% (approximately one event in 15 years). This or similar thresholds have been used in previous studies of extreme droughts (e.g. Vicente-Serrano et al., 2019; Haile et al., 2020). Then, time series of extreme droughts defined as SPEI value  $< -1.5$  are generate for analysis of occurrence probability.

Using the extreme drought time series, the occurrence probability is calculated. The occurrence can be considered as an indicator of risk over a time interval as follows (Mudelsee, 2020):

$$\hat{\lambda}(T) = h^{-1} \sum_{j=1}^m K\left(\frac{[T - T_{\text{ext}(j)}]}{h}\right) \quad (5-2)$$

The variable  $h$  is the bandwidth,  $T_{\text{ext}(j)}$  is an extreme year,  $m$  is the sample size of extremes and  $K$  is the Gaussian kernel. The size of the bandwidth defines how many data points contribute to the occurrence rate estimation. To find the most appropriate bandwidth for the dataset, the cross-validation bandwidth selector based on Brooks and Marron (1991) is used. Based on the cross validation analysis a bandwidth of  $h=9$  is used in this chapter which is consistent with the physical knowledge of underlying processes.

Sample size plays an important role in analysis of extremes. In methods that involve a window or bandwidth, some samples from the beginning or end of the record may not be used – an issue known as boundary effect/bias. Since the time series is temporally limited to the time frame of the SSPs, the entire period is used. Following Mudelsee (2020), an elegant way to deal with the boundary bias problem is the generation of pseudo data outside the observation period, which can be achieved through the reflection of the dataset at boundaries. The reflection technique is used to be able to ensure using the largest possible sample size. Note, the median of the occurrence rate is computed as the average of the occurrence rates of all models. Furthermore, it is also important to obtain a measure of uncertainty and to determine if it is significant. For this purpose, the 25<sup>th</sup> and 75<sup>th</sup> percentile of the occurrence rates is computed for all models. This technique provides more information about the ensemble spread.

It is also possible to use occurrence rate computation for hypothesis testing (Mudelsee, 2020). In this chapter, it is tested whether the occurrence rate is constant ( $H_0$ ) or increasing/decreasing ( $H_1$ ) using the following test statistics (Cox and Lewis, 1966):

$$U_{CL} = \frac{\sum_{j=1}^m \frac{T_{\text{ext}(j)}}{m} - [T(n) + T(1)]/2}{[T(n) - T(1)](12m)^{1/2}} \quad (5-3)$$

where  $n$  is the total sample size. Since the distribution of  $U_{cl}$  approaches a standard normal shape with increasing sample size ( $m$ ), a p-value can be calculated to reject or not reject  $H_0$  (Mudelsee, 2020).  $U_{CL}$  test statistics allows investigating the alternative hypothesis as changing, increasing or decreasing occurrences using the corresponding  $m$ .

## 5.3 FUTURE SUMMER WARMING & DROUGHT RISK

### 5.3.1 MODEL EVALUATION

In order to understand how drought is expected to change in the future using climate models, the quality of the simulations should be evaluated first. For this purpose, a comparison is performed between observed averages of summer temperature, precipitation and drought with modelled climate simulations for the period 1971 to 2000 (Figure 5.1). Positive (negative) values indicate that the ensemble mean of the models has a greater (lower) value than that of the observations.

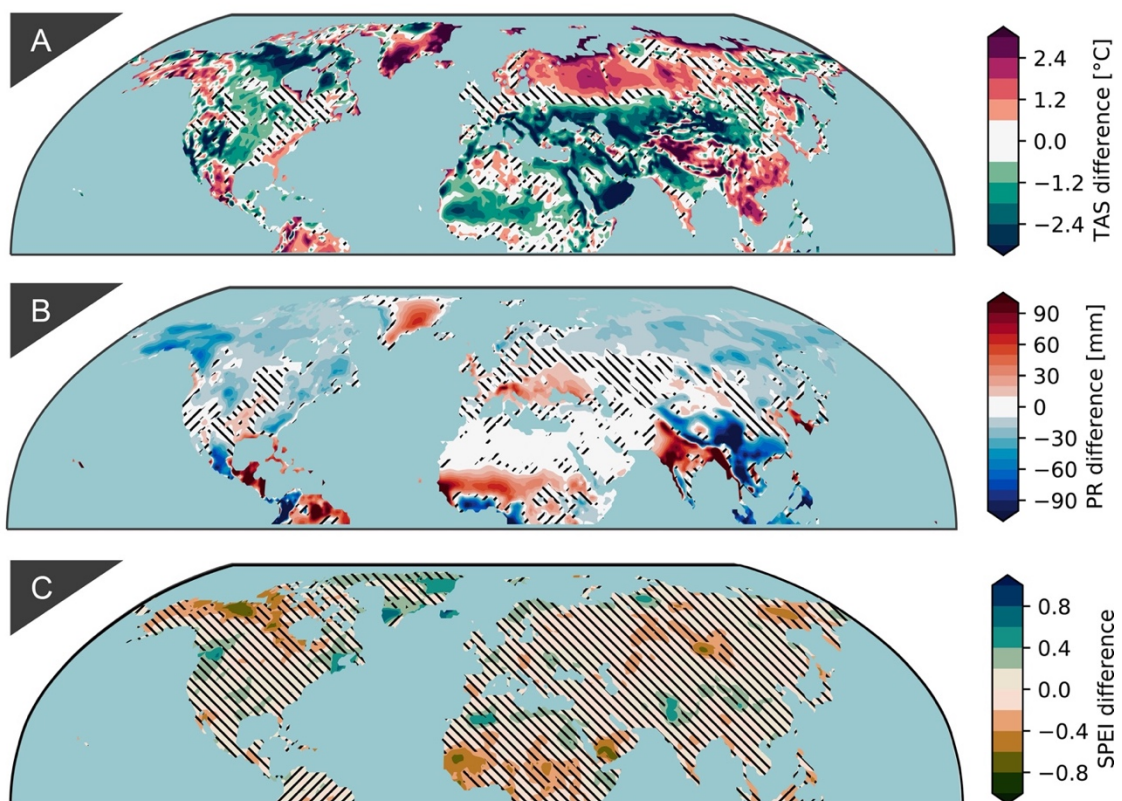
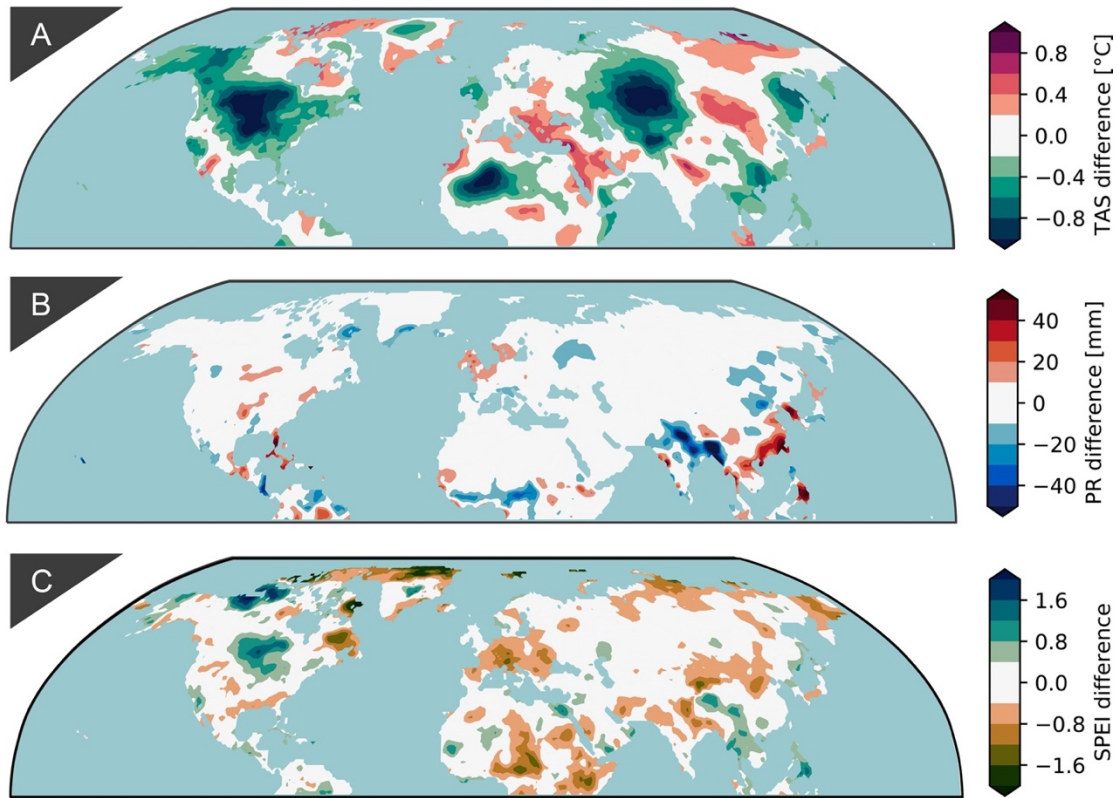


Figure 5.1: Comparison of the modelled and observed climate for the period 1971-2000 (JJA only). The climate simulations are averaged over the entire period and then subtracted from observations. a, surface air temperature, b, precipitation and c, SPEI. The hatched areas indicate areas with insignificant changes according to the two-sided Student's *t* test ( $p < 0.05$ ).

In Figure 5.1A, Greenland and western Russia, parts of the Himalayas and Southeast Asia are significantly colder in the multi-model ensemble than in reality. In contrast, northern Canada, parts of central North America, northern India, the Arabian Peninsula and a band from the Mediterranean to central Asia are significantly warmer in the modelled climate state than in reality. Another pattern is shown in the precipitation difference (Figure 5.1B) where large parts of North America, northern Central America, Southeast Asia and North Asia are characterised by significantly larger precipitation in the model ensemble mean. On the other hand, substantial underestimation of precipitation in the

multi-model ensemble is observed in the northern Mediterranean region, southern Sahara and northern part of India compared to the observations. Nonetheless, the difference map of SPEI shows no significant overall difference between the model simulations and observations except in some small regions (Figure 5.1C). Only small parts of northern North America, West Africa and the southern Arabian Peninsula and Greenland show a significant difference.



**Figure 5.2: Differences in trends in climate model simulations and observations. The differences are shown for the periods 1975-1989 and 2000 to 2014 (JJA only) in CMIP6 historical simulations relative to observations. A value of 0 represents that the trend in observations is the same as that of the model ensemble. Negative values indicate that trend in observations is stronger than in the model ensemble, whereas positive values show the opposite case. a, surface air temperature, b, precipitation and c, SPEI.**

To investigate the consistency of the observed and climate model ensemble trends, the differences of the temporal evolution of observed and modelled climate conditions are compared for the periods 1975 to 1989 and 2000 to 2014 (Figure 5.2). More specifically, the relative change based on observations and historical model simulations during two historical periods (2000-2014 vs. 1975-1989) is investigated. For all three variables, a negative value indicates a stronger trend between the two time periods in the observations than the climate model ensemble (a positive value represents the opposite). Comparison of temperature trends indicates that large parts of North America, Central Asia and Northwest Africa experience a higher temperature increase in observations than represented by the ensemble mean (Figure 5.2A). In contrast, the ensemble mean shows a more pronounced warming trend in the eastern and northern Mediterranean region, northern Russia and northern Canada

compared to observations. Considering precipitation (Figure 5.2B), the trend in the Indian monsoon region is noticeably stronger than that of the ensemble mean of simulations. In addition, the difference in simulated and observed SPEI between these two periods shows that Central Europe, Central Africa and North Greenland experience a much stronger trend in observations relative to the ensemble mean (Figure 5.2C). On the other hand, Central North America and Northern Canada are characterized by a stronger trend in the ensemble mean compared to the observations (Figure 5.2C).

---

### 5.3.2 PROJECTED SUMMER TEMPERATURE CHANGES

Future drought conditions, among others processes, depend on the temperature variability. Rising air temperature nonlinearly increases the saturated water vapour pressure at a rate of approximately 7%/K according to the Clausius-Clapeyron relationship (Yamada et al., 2020). The increasing water holding capacity of air can lead to a higher amount of water that can theoretically evaporate (increase of  $E_0$ ). Changes in the greenhouse gas concentration combined with other local geographical and biophysical features can change the spatial and temporal variability of the temperature heterogeneously. The heterogeneity of the temperature pattern is shown in Figure 5.3 for the Northern Hemisphere, where the temperature conditions for three different emissions are represented in terms of anomaly plots, i.e. the difference between the projected climate condition (2071-2100) and the historical (1971-2000) baseline.

An overall significant increase of the average summer temperature is shown in the Northern Hemisphere under all three future scenarios (Figure 5.3), but with substantial variability in the magnitude and spatial variability among them (compare Figures 5.3A, 5.3B and 5.3C). Under SSP1-2.6 (which represents a total anthropogenic forcing of  $2.6 \text{ W m}^{-2}$  (O'Neill et al., 2016)) the temperature increase is relatively homogenous over the whole Northern Hemisphere, with the magnitudes varying between 1 and 3 °C. A stronger warming is observed under SSP2-4.5 (which represents a total anthropogenic forcing of  $4.5 \text{ W m}^{-2}$  (O'Neill et al., 2016)) with summer temperature increases between 3 to 5 °C across the midlatitudes and the subtropics. The most affected areas, in terms of warming levels, are the Mediterranean region, Central North America, parts of Greenland and Siberia and Central Asia (Figure 5.3B) located in the subtropics, midlatitudes and the high latitudes.

Similar warming hotspots are also observed under SSP5-8.5 scenario (Figure 5.3C), which represents an anthropogenic forcing of  $8.5 \text{ W m}^{-2}$ . The spatial variability of the temperature anomalies under SSP5-8.5 is higher compared to the other two scenarios (SSP-2.6 and SSP-4.5). In the Northern Hemisphere, the average summer temperature increases between 3 to 8 °C, with the hotspots (the Mediterranean region, Central North America, parts of Greenland and Siberia and Central Asia) expected to experience between 7 and 8 °C of increase in temperature by the end of the century. Furthermore, it is noticeable that the tropics experience a weaker warming rate relative to the subtropics or mid-latitudes in all three scenarios. This is in agreement with the future warming distribution

projections from other studies based on CMIP5 (Feng et al., 2014) and CMIP6 (Fan et al., 2020) (to evaluate consistency across CMIP6 simulations see Supplement 7). In addition to the average summer temperature, the same results are also presented for the maximum temperature ( $T_{max}$ ) and minimum temperature ( $T_{min}$ ) in Supplement 8-11. The anomaly plots of both quantities share spatial characteristics similar to average temperature shown in Figure 5.3. Nevertheless, the magnitudes of  $T_{max}$  increases are more pronounced in the aforementioned hot spots relative to the  $T_{min}$ .

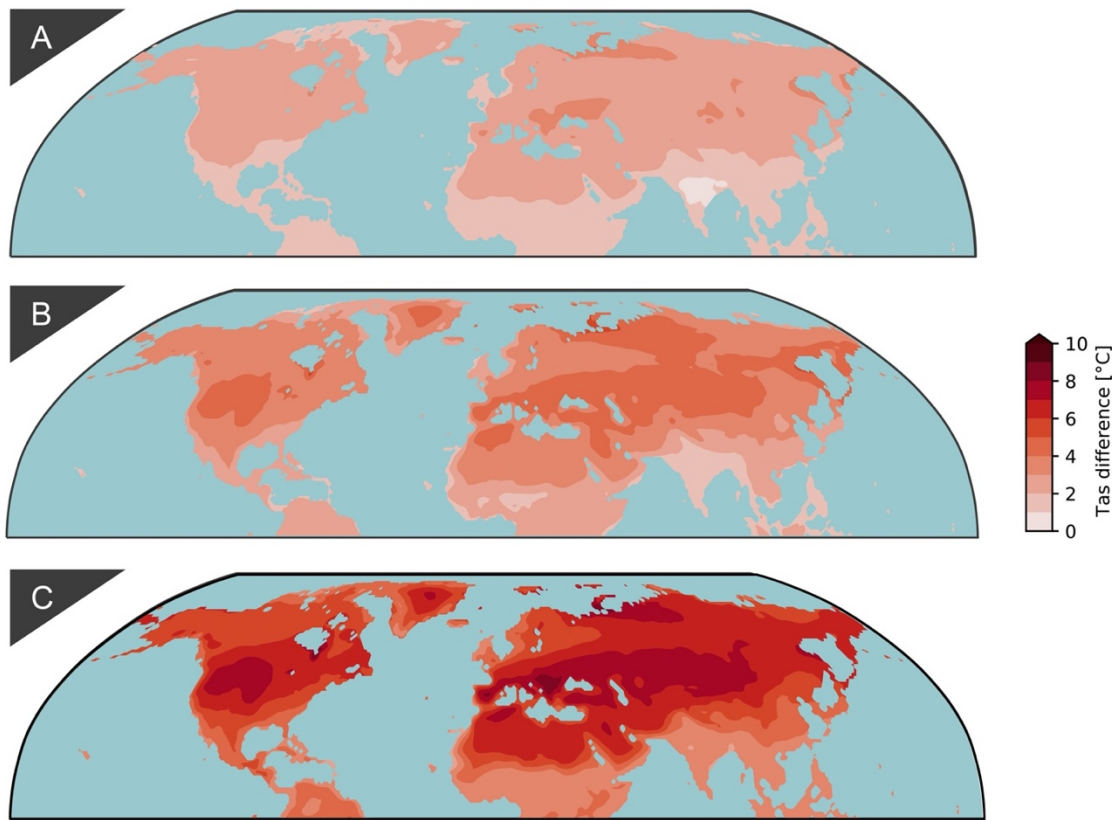


Figure 5.3: Projected changes to the Northern Hemisphere summer temperature. Spatial distribution of the summer temperature anomalies in the Northern Hemisphere based on the multi-model projected changes (2071-2100) based on SSP1-2.6 (a), SSP2-4.5 (b) and SSP5-8.5 (c) scenarios relative to the historical summer temperature during the 1971–2000 baseline period. All changes are significant according to the two-sided Student's t test ( $p < 0.05$ ).

### 5.3.3 PROJECTED PRECIPITATION AND POTENTIAL EVAPOTRANSPIRATION

The hydrological cycle is strongly dominated by the variability and amount of precipitation as the key driver of other variables such as runoff and soil moisture. Change in precipitation variability in the multi-model simulations and observations under the three scenario runs are shown in Figure 5.4. The smallest absolute changes are found under SSP1-2.6 (Figure 5.4A). Results show significantly more precipitation (20-40 mm) over a central band from East to West Africa and Southeast Asia. A smaller rate of precipitation increase is found in North Asia, Alaska and eastern coasts of North America. However, a significant precipitation deficit is shown in Central America and parts of the Mediterranean region. This is in agreement with previous studies based on CMIP5 (Lee and Wang, 2014) and

CMIP6 (Wang et al., 2020) that indicate strengthening of the future Asian–northern African monsoon leading to wetter conditions, and weakening of the North American monsoon causing a drying pattern. According to recent findings (e.g. Wang et al., 2020), the greenhouse gas forcing induces a stronger ‘land-warmer-than-ocean’ pattern, which enhances the Asian and West African monsoon low pressure system leading to increases in monsoon rainfall in these regions, and an El Niño–like warming, which reduces the North American monsoon rainfall.

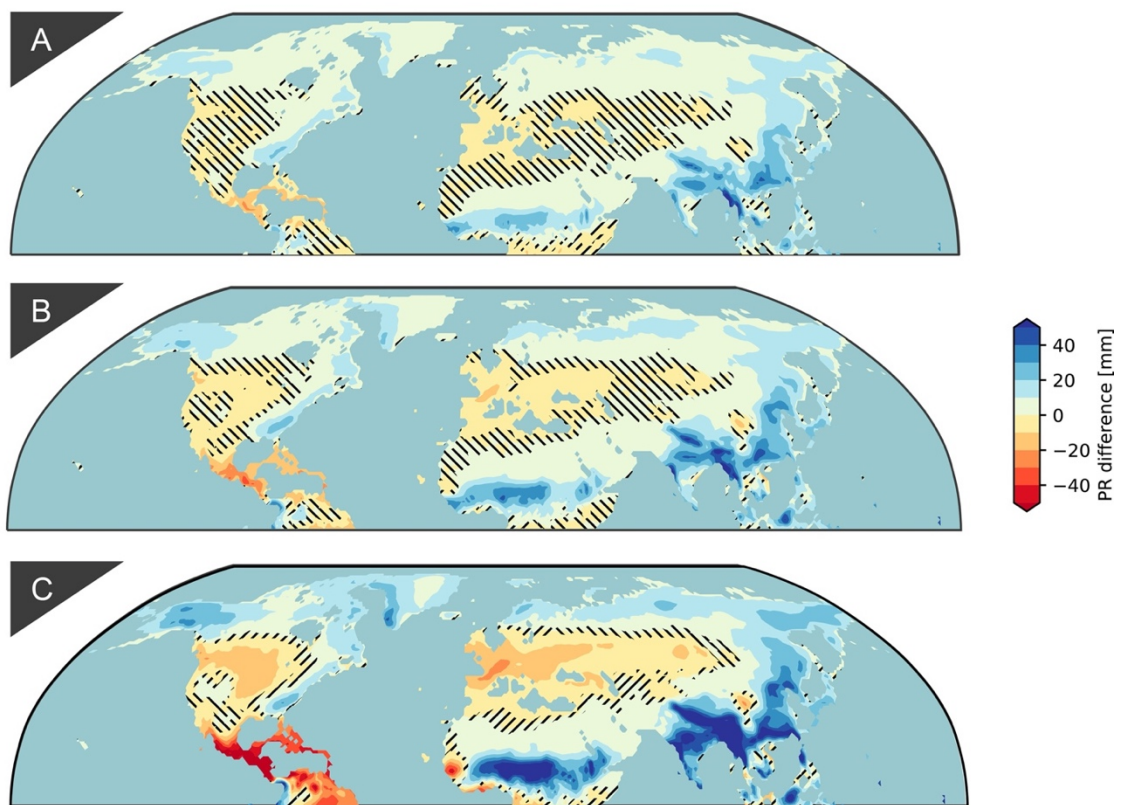


Figure 5.4: Changes to summer precipitation under SSP1-2.6, SSP2-4.5 and SSP5-8.5. Averaged anomalies of summer precipitation under SSP1-2.6 (a), SSP2-4.5 (b) and SSP5-8.5 (c) in the Northern Hemisphere. A reference period of 1971–2000 relative to the period 2071–2100 is used for deriving anomalies. The hatched areas indicate areas with insignificant changes according to the two-sided Student's *t* test ( $p < 0.05$ ).

The precipitation changes for the other two scenarios (Fig 5.4B and Fig 5.4C) look very similar to SSP1-2.6 from a spatial point of view. However, the precipitation anomalies are larger and more spread out spatially relative to the presented hotspots in Figure 5.4A. See for example the positive precipitation anomalies on the east and north coasts of Asia, North America and Europe in Figure 5.4C relative to 5.4A. The precipitation increase on the east shores of Asia and North America is likely because of higher water holding capacity of the atmosphere and warm water transport from ocean circulation. Figure 5.4C indicates that Central America, Europe (except Northern Europe), North Africa, Central Asia will likely experience a significant negative precipitation anomaly compared to the historical observations. To evaluate consistency of the multi-model CMIP6 ensemble members the interested reader is referred to Supplement 12.

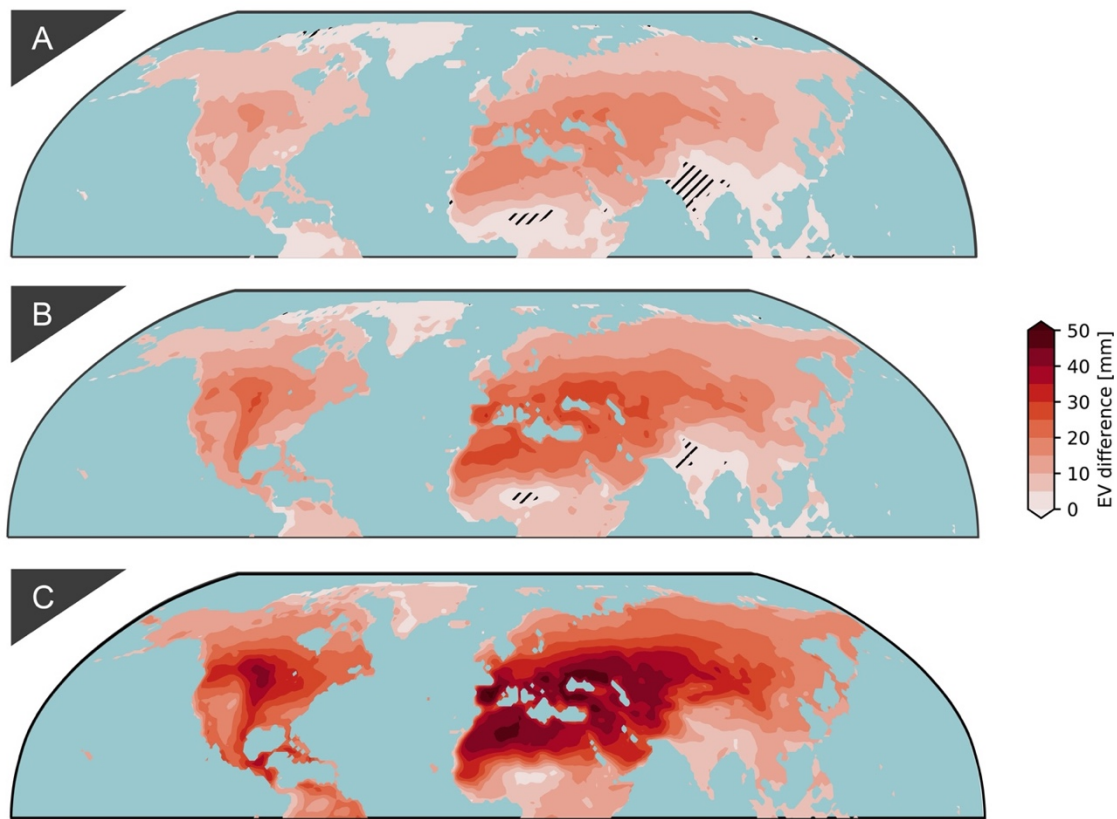


Figure 5.5: Changes to summer potential evapotranspiration under SSP1-2.6, SSP2-4.5 and SSP5-8.5. Averaged anomalies of summer potential evapotranspiration under SSP1-2.6 (a) and SSP2-4.5 (b) and SSP5-8.5 (c) in the Northern Hemisphere for the period 2071-2100 relative to the baseline period of 1971–2000. The hatched areas in all three subfigures indicate areas with insignificant changes according to the two-sided Student's t test ( $p < 0.05$ ).

The  $E_0$  is another essential component of the climatic and land surface water balance, because it represents the atmospheric demand for moisture. Recent studies indicate that the projected  $E_0$  in the CMIP6 multi-model simulations is higher than in CMIP5 under a comparable emission scenario, possibly because CMIP6 models simulate stronger warming for a given forcing or scenario (Liu et al., 2020). Due to the relation between  $E_0$  and temperature, the anomaly figures of  $E_0$  for the different SSPs show similar characteristics as the projected temperature changes in Figure 5.3. The strongest significant increase of  $E_0$  is found for the subtropics and the midlatitude under SSP1-2.6 (Figure 5.5A). The hotspots for the strongest increase of the  $E_0$  are Central North America, the Mediterranean region, Central Asia, the Arabian Peninsula and North Africa. However, no significant change of  $E_0$  is shown for parts of India and northern Nigeria. Similar insignificant changes in the same locations are also observed under SSP2-4.5, while significant increase of  $E_0$  in the hotspots is more pronounced in this scenario (Figure 5.5B).

Under SSP5-8.5 (Figure 5.5C), the highest positive anomalies are shown over Spain, around the Black Sea and parts of North Africa. A belt of strong  $E_0$  increase is shown from Spain and North Africa towards Central Asia. Also, an increase in  $E_0$  is shown over the central and southern parts of North America. It is noticeable that the increase in  $E_0$  is lower in the tropics compared to the subtropics

and mid-latitudes in all three scenarios. Evaluating consistency of the multi-model CMIP6 ensemble members indicates similar results with the exception of the African tropics, India and parts of Greenland (Supplement 13).

---

#### 5.3.4 DROUGHT CONDITIONS BY THE END OF 21<sup>ST</sup> CENTURY

Projected changes in drought characteristics are closely associated with the presented changes to temperature, precipitation and  $E_0$  (Figure 5.6). Under SSP1-2.6 (Figure 5.6A), significant drier conditions are projected over North Africa, Saudi Arabia, Central America, the Mediterranean region, Central America and the southwest of the USA, which are indicated by the negative SPEI values. The projected drying trend under SSP1-2.6 is primarily driven by the expected temperature increase (Figure 5.3A) leading to a higher  $E_0$  (Figure 5.5A). The higher  $E_0$  cannot be compensated by an increase in precipitation (Figure 5.4A, Supplement 14-15) leading to overall drier conditions in the summer. In contrast, significant wetter conditions are detected for parts of the coastal regions of Asia, parts of the east coast of North America, eastern parts of Greenland and Alaska. In these regions, the increase in precipitation is more pronounced relative to increase in  $E_0$ , resulting in overall wetter conditions (Figure 5.4A, 5.5A, 5.6A and Supplement 14-15).

SSP2-4.5 (Figure 5.6B) exhibits similar hotspots to those of SSP1-2.6 (e.g. significant negative SPEI anomalies over North Africa, Central Asia and Saudi Arabia). However, regions with a negative SPEI anomaly are more spread-out and drier mainly driven by projected reduction in precipitation (Figure 5.4B, Supplement 14-15) as well increase in  $E_0$  (Figure 5.5B). Over North America, significant drier conditions are found in Western North America and Central America. The drier conditions in Central America are also driven by a significant increase in  $E_0$  (Figure 5.5B) and a precipitation deficit (Figure 5.4B and Supplement 14-15). On the other hand, East Asia, Greenland and Alaska are characterized by a tendency towards wetter conditions.

An even stronger drying trend is visible under SSP5-8.5 (Figure 5.6C) with hotspots expanding over the Mediterranean region, Saudi Arabia, North Africa, Central Asia, Central Europe, Central America, Central North America, West North America and the Middle East. The drier conditions in these regions are driven by increases in  $E_0$  (Figure 5.5C) compared to SSP1-2.6 (Figure 5.5A) and SSP2-4.5 (Figure 5.5B) as well as decreases in precipitation (Figure 5.4C and Supplement 14-15). Comparing different scenarios, an expansion of dry conditions is noted from the subtropics towards the midlatitudes by the end of the 21<sup>st</sup> century. This is also shown for drought conditions in spring (Supplement 17-19). The drought hotspots identified in this chapter are broadly consistent with regional and global studies based on CMIP5 (Orlowsky and Seneviratne, 2012, 2013; Mariotti et al., 2015; Lu et al., 2019; Seager et al., 2019; Vicente-Serrano et al., 2019) and CMIP6 (Cook et al., 2020) simulations. However, parts of Greenland, East Asia, North East Asia, Alaska and Scandinavia show a positive SPEI anomaly indicating wetter conditions in the future (Figure 5.6C). The reason for that is the precipitation

increases in these regions and the corresponding small increase in  $E_0$  (Figure 5.4C and 5.5C). The majority individual members in the multi-model CMIP6 simulations confirm the presented results based on the ensemble mean (Supplement 20).

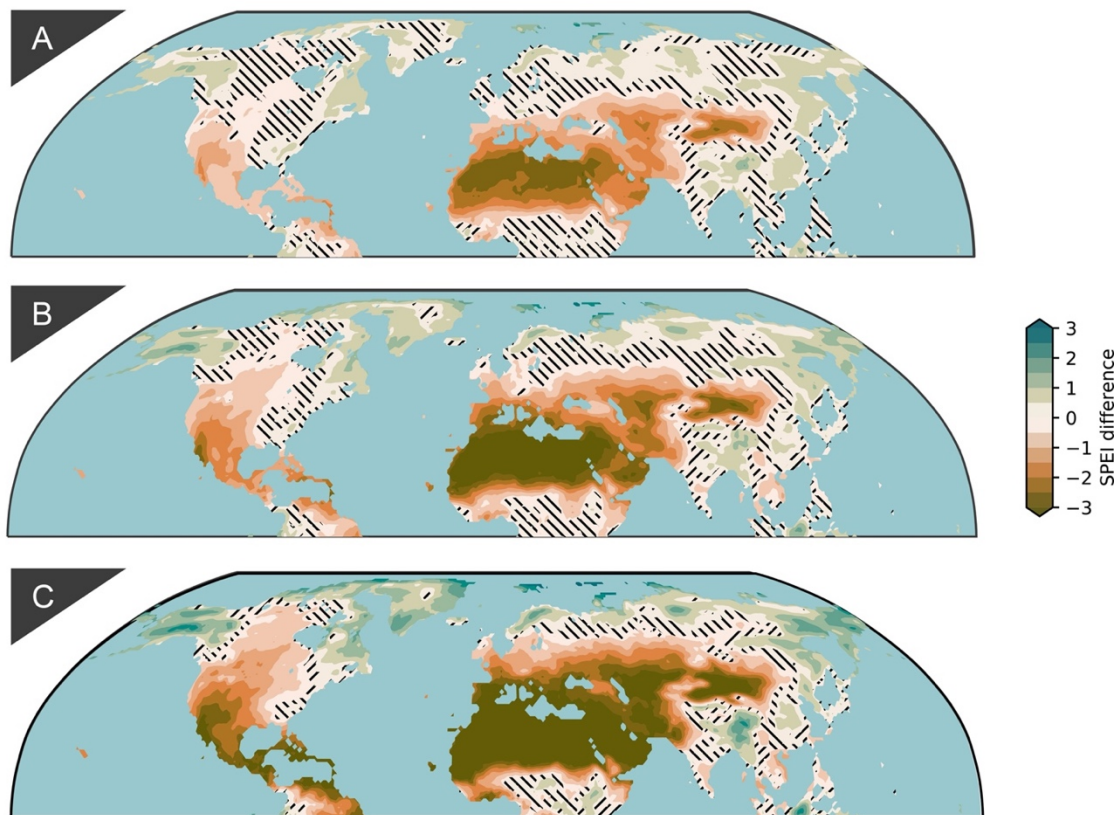


Figure 5.6: Changes to summer drought conditions under SSP1-2.6, SSP2-4.5 and SSP5-8.5. Averaged anomalies of summer droughts under SSP1-2.6 (a) and SSP2-4.5 (b) and SSP5-8.5 (c) in the Northern Hemisphere for the period 2071-2100 relative to the baseline period of 1971-2000. The hatched areas in all three subfigures indicate areas with insignificant changes according to the two-sided Student's t test ( $p < 0.05$ ).

### 5.3.5 OCCURRENCE OF DRY PERIODS AT THE END OF 21<sup>ST</sup> CENTURY

Based on the results presented in the previous subchapter, it is shown that the projected warming has an influence on the global distribution of dry regions and the severity of dryness based on the ensemble mean of CMIP6 simulations. However, anomaly plots of a 30 years period do not offer any insights on temporal variability of dry conditions. Therefore, the occurrence rate (see Subchapter 5.2 for the definition) of  $\text{SPEI} < -1.5$  for the updated AR6 regions (Iturbide et al., 2020) are computed to investigate the risk of moderate to extreme droughts under the same three future scenarios. Since the SPEI is a standardized index based on a reference period (here, 1971 to 2000), each standardized value corresponds to an occurrence probability. The selected  $\text{SPEI} < -1.5$  refers to 6.7% occurrence probability (approximately one drought event in 15 years).

In Figure 5.7, the occurrence rate is shown for selected regions in Europe and Asia (Supplement 22-26). The occurrence rate  $\lambda$  is the probability of SPEI falling below -1.5 during one year. If  $\lambda(a)^{-1}=1$ , it means that a SPEI value below -1.5 can be observed every year whereas  $\lambda(a)^{-1}=0.5$  would mean that this SPEI threshold is reached every two years. For the Mediterranean region (MED), it is shown that the risk of a SPEI below -1.5 is projected to change over time and is highly dependent on the choice of scenario (Figure 5.7A). Under SSP1-2.6, a significant positive trend is shown until 2030 whereas a small negative trend can be found thereafter. From 2038 onwards, the occurrence rate decreases. It is noted that the median stabilizes at  $\lambda(a)^{-1}=0.45$  from 2064 onwards.

Under SSP2-4.5 and SSP5-8.5, an entirely different pattern is projected. Under SSP5-8.5, the ensemble median is characterized by a significantly increasing ( $p<0.01$ ) occurrence rate reaching the maximum of  $\lambda(a)^{-1}=1$  in 2081. The 75<sup>th</sup> percentile is characterized by a steep trend towards a  $\lambda_{75}(a)^{-1}=1$  and remains at this high level from 2029 onwards. This indicates that a drought event which is characterized by a SPEI < -1.5 in today's climate is projected to occur every year by the end of the 21<sup>st</sup> century. The strong increase in the drought risk is driven by the projected increase to  $E_0$  and decrease to precipitation (Figure 5.4C and 5.5C), associated with a projected widening of the Hadley Circulation that shifts downwelling and inhibits precipitation (IPCC, 2013). The occurrence rates under SSP2-4.5 also show significant increases ( $p<0.01$ ), reaching a median occurrence rate of  $\lambda(a)^{-1}=0.91$  by the end of the 21<sup>st</sup> century. The 75<sup>th</sup> percentile, however, reaches the upper bound of  $\lambda_{75}(a)^{-1}=1$ . This shows that despite the lower warming compared to SSP5-8.5, the drought risk under SSP2-4.5 is projected to enhance by the end of the 21<sup>st</sup> century. The weaker occurrence rate in SSP2-4.5, in comparison to SSP5-8.5, is related to the lower total and input rate of greenhouse gas emissions in SSP2-4.5 (O'Neill et al., 2016). Results show that the MED region will be one of the hotspots for dryer conditions by the end of the 21<sup>st</sup> century. In contrast to SSP1-2.6, no decrease of the occurrence rate is shown for the MED region under SSP2-4.5 and SSP5-8.5.

The northern bordering region of Central Europe (CEU) is characterized by totally different occurrence rates for the three different SSPs. Under SSP1-2.6, the occurrence rate of the median, 75<sup>th</sup> percentile and 25<sup>th</sup> percentile do not exhibit significantly increasing trends ( $p>0.01$ ). While the median of the occurrence rate under SSP2-4.5 does not show a significantly increasing ( $p>0.01$ ), the 75<sup>th</sup> percentile does and reaches  $\lambda_{75}(a)^{-1}=0.52$  by the end of the 21<sup>st</sup> century. In contrast to the occurrence rates under SSP1-2.6 and SSP2-4.5, the occurrence rate under SSP5-8.5 exhibits a significantly increasing trend ( $p<0.01$ ). From around 2050 the median increases and reached  $\lambda(a)^{-1}=0.55$ . Based on the results, it can be concluded that the drought risk in Central Europe is main projected to increase significantly under the SSP5-8.5 scenario.

In East Europe (EEU) and West Siberia (WS), one can see a similar behaviour as in the CEU. For both regions, no significant increasing trend ( $p>0.01$ ) of the occurrence rate can be found under SSP1-2.6 and SSP2-4.5, whereas a significant increasing trend ( $p<0.01$ ) appears under SSP5-8.5 which

starts around 2050. The median, 25<sup>th</sup> and 75<sup>th</sup> percentiles in EEU and WS by the end of 21<sup>st</sup> century can be summarized as follows: EEU  $\lambda(a)^{-1}=0.41$  ( $\lambda_{25}(a)^{-1}=0.31$ ,  $\lambda_{75}(a)^{-1}=0.78$ ); WS  $\lambda(a)^{-1}=0.46$  ( $\lambda_{25}(a)^{-1}=0.22$ ,  $\lambda_{75}(a)^{-1}=0.79$ ).

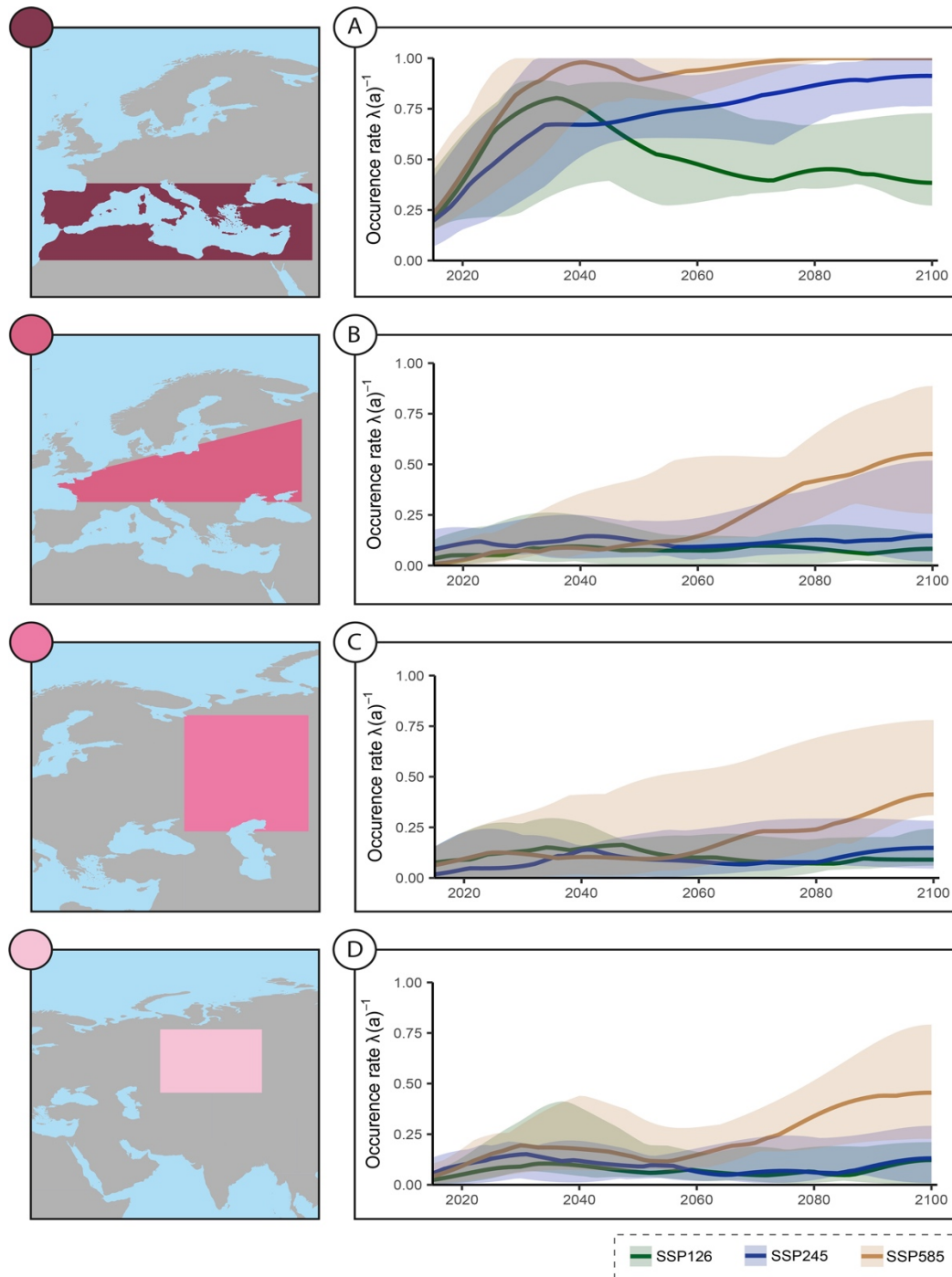


Figure 5.7: Projected drought conditions for selected AR6 regions (Iturbide et al., 2020) in Europe and Asia. Temporal evolution of occurrence rate of SPEI below -1.5 under different future climate scenarios (SSP1-2.6, SSP2-4.5, SSP5-8.5).  $\lambda(a)^{-1}=1$  indicates a SPEI value below -1.5 can be observed every year. The SPEI is derived based on the baseline period of 1971 to 2100. The medians of the model ensemble from CMIP6 are highlighted. The 25<sup>th</sup> and 75<sup>th</sup> percentiles of the model ensemble for each scenario are indicated with shaded colour around the median.

The occurrence rate of SPEI below -1.5 during one year is also investigated over the North America (Figure 5.8). The West North America (WNA) region is characterized by a clear separation of the different occurrence rates under the three analysed SSPs. From 2050, a significant increase ( $p < 0.01$ ) of the drought occurrence rate is shown under SSP5-8.5. The occurrence is significantly increasing with the median and lower and upper bounds reaching  $\lambda(a)^{-1} = 0.78$  ( $\lambda_{25}(a)^{-1} = 0.49$ ,  $\lambda_{75}(a)^{-1} = 1$ ), respectively. In contrast, no significant trend in the occurrence rate is shown under SSP1-2.6 and SSP2-4.5, where the occurrence rates are  $\lambda(a)^{-1} = 0.22$  ( $\lambda_{25}(a)^{-1} = 0.03$ ,  $\lambda_{75}(a)^{-1} = 0.32$ ) and  $\lambda(a)^{-1} = 0.36$  ( $\lambda_{25}(a)^{-1} = 0.25$ ,  $\lambda_{75}(a)^{-1} = 0.46$ ) by the end of the 21<sup>st</sup> century, respectively.

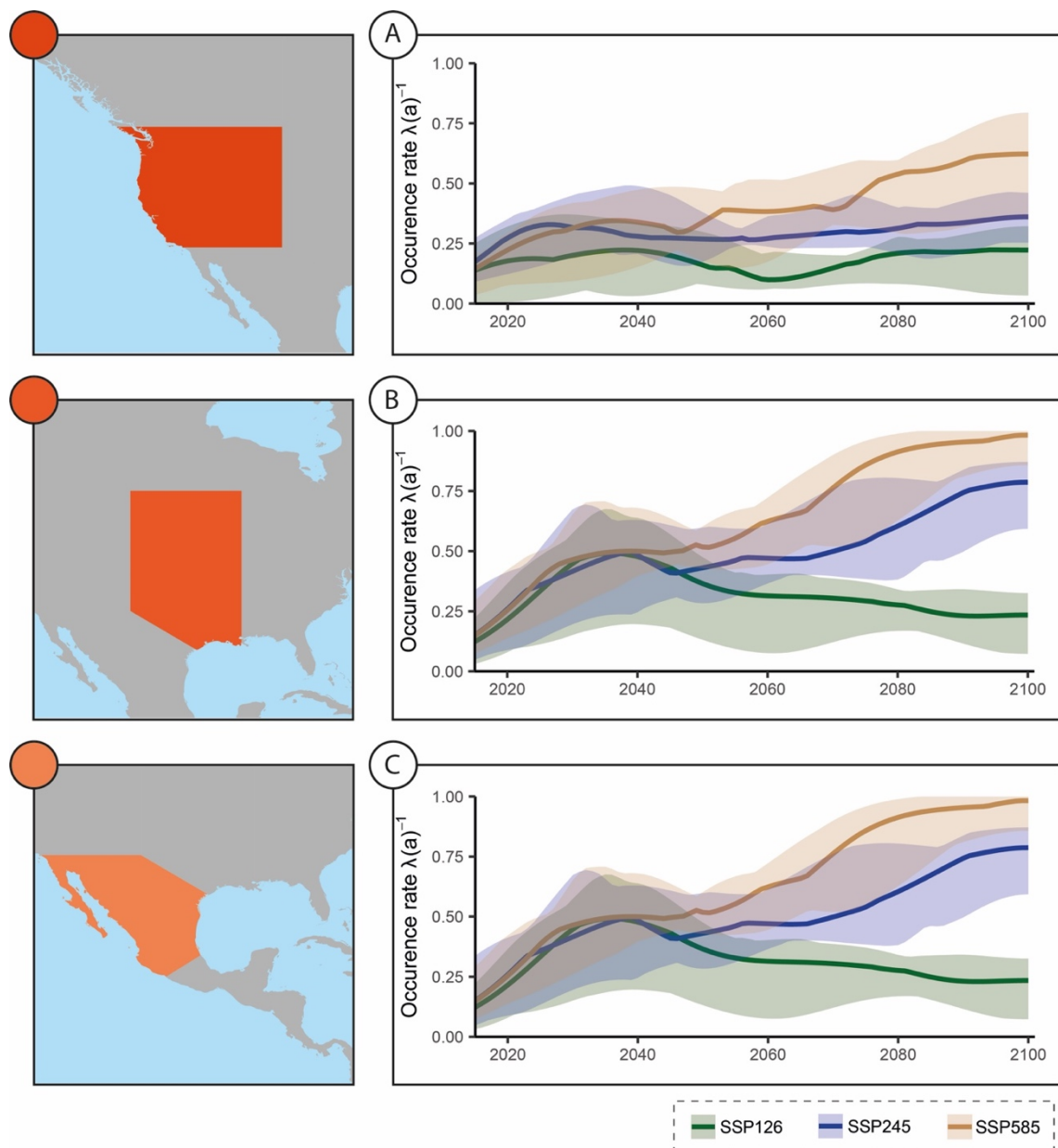


Figure 5.8: Projected drought conditions for selected AR6 regions (Iturbide et al., 2020) in North America. Temporal evolution of the occurrence rate of SPEI below -1.5 under different future climate scenarios (SSP1-2.6, SSP2-4.5, SSP5-8.5).  $\lambda(a)^{-1} = 1$  indicates a SPEI value below -1.5 can be observed every year. The medians, the 25<sup>th</sup> and 75<sup>th</sup> percentiles are highlighted as in Figure 5.7.

Similar to CEU, WS and EEU, Central North America (CNA) does not show a significant trend in the occurrence rate of dry conditions under SSP1-2.6 and SSP2-4.5. Another similarity is that the occurrence rate under SSP5-8.5 shows a significant increasing trend ( $p < 0.01$ ). The positive trend starts around 2050 with the occurrence rates reaching  $\lambda(a)^{-1} = 0.45$  ( $\lambda_{25}(a)^{-1} = 0.35$ ,  $\lambda_{75}(a)^{-1} = 0.85$ ) by the end of the 21<sup>st</sup> century.

The region of North Central America (NCA) shows a similar occurrence rate that of the MED region. The strongest and significant increase ( $p < 0.01$ ) of the occurrence rate is observed under SSP5-8.5 with  $\lambda(a)^{-1} = 0.98$  ( $\lambda_{25}(a)^{-1} = 0.85$ ,  $\lambda_{75}(a)^{-1} = 1$ ). Figure 5.8C displays that 75<sup>th</sup> percentile reaches an occurrence of  $\lambda_{75}(a)^{-1} = 1$  around 2082 and remains thereafter. A not as pronounced yet significant increasing trend ( $p < 0.01$ ) is projected under SSP2-4.5 with  $\lambda(a)^{-1} = 0.79$  ( $\lambda_{25}(a)^{-1} = 0.59$ ,  $\lambda_{75}(a)^{-1} = 0.87$ ) by 2100. Despite the weaker warming in SSP2-4.5, the risk of drought is still projected to increase without levelling off. Furthermore, the occurrence rate under SSP1-2.6 is projected to increase until 2050 and decrease then after with  $\lambda(a)^{-1} = 0.23$  ( $\lambda_{25}(a)^{-1} = 0.07$ ,  $\lambda_{75}(a)^{-1} = 0.32$ ) by the end of the 21<sup>st</sup> century without showing a statistically significant trend ( $p < 0.01$ ).

## 5.4 DISCUSSION & CONCLUSION OF DROUGHT PROJECTIONS

In this chapter, changes in the drought occurrence based on the newly published CMIP6 simulations (Eyring et al., 2016) have been quantified. The presented results based on the anomaly and frequency analysis indicate an increase in the occurrence of summer droughts and an intensification of droughts in the majority of the subtropics and parts of the midlatitudes, mainly due to an increase of greenhouse gases. In addition, hotspots for drought occurrence, such as the Mediterranean region, can experience more widespread events depending on the magnitude of greenhouse gas emissions of the SSP. Some of the hotspots identified in this chapter have also been identified in studies based on the CMIP5 (Orlowsky and Seneviratne, 2012, 2013; Mariotti et al., 2015; Zhao and Dai, 2015; Lu et al., 2019; Seager et al., 2019; Vicente-Serrano et al., 2019) and CMIP6 (Cook et al., 2020) which gives additional confidence to the presented results. For this reason, the presented results confirm previous findings that the projected droughts and drought risk in CMIP5 and CMIP6 are broadly consistent.

One reason for intensification of droughts in the Northern Hemisphere subtropics is that the summer temperature is projected to rise leading an increase in  $E_0$  and sometimes a decrease in precipitation (Orlowsky and Seneviratne, 2012, 2013; Mariotti et al., 2015). The increase in  $E_0$  is suggested to double the percentage of the global land area projected to experience significant drying based on CMIP5 simulations by the end of 21<sup>st</sup> century (Cook et al., 2020) and is a key variable to understand drought variability (Dai et al., 2018). Recent studies indicate that the projected  $E_0$  is more pronounced in CMIP6 multi-model simulations than in CMIP5 (Liu et al., 2020), mainly because of the changes in the total anthropogenic forcing (O'Neill et al., 2016). As a result, more intense droughts are projected based on CMIP6 simulations in comparison to studies based on CMIP 5 (Cook et al., 2014).

Previous studies addressing changes in hydrological conditions based on CMIP6 (Cook et al., 2020) have projected declines in soil moisture and runoff as a consequence of continued greenhouse gas emissions. Although the SPEI index does not include soil parameters in the calculation, many of the predicted trends in soil moisture across the soil column match the drought hotspots presented the result subchapters (Figure 5.9A-C and Supplement 16). For example, soil moisture projections indicate robust and significant decreases in soil moisture in large parts of the Mediterranean, Central America, North Central America and North South America (Figure 5.9 and Supplement 16). This is consistent with the projected of precipitation and temperature (Figure 5.3 and 5.4). Nevertheless, there are differences too. For example, the SPEI indicates that large parts of Central Asia, parts of Northwest India and the Middle East are at greater risk of drought depending on the strength of emissions (Figure 5.6), whereas soil moisture is projected to increase in the same regions (Figure 5.9) that require future investigation.

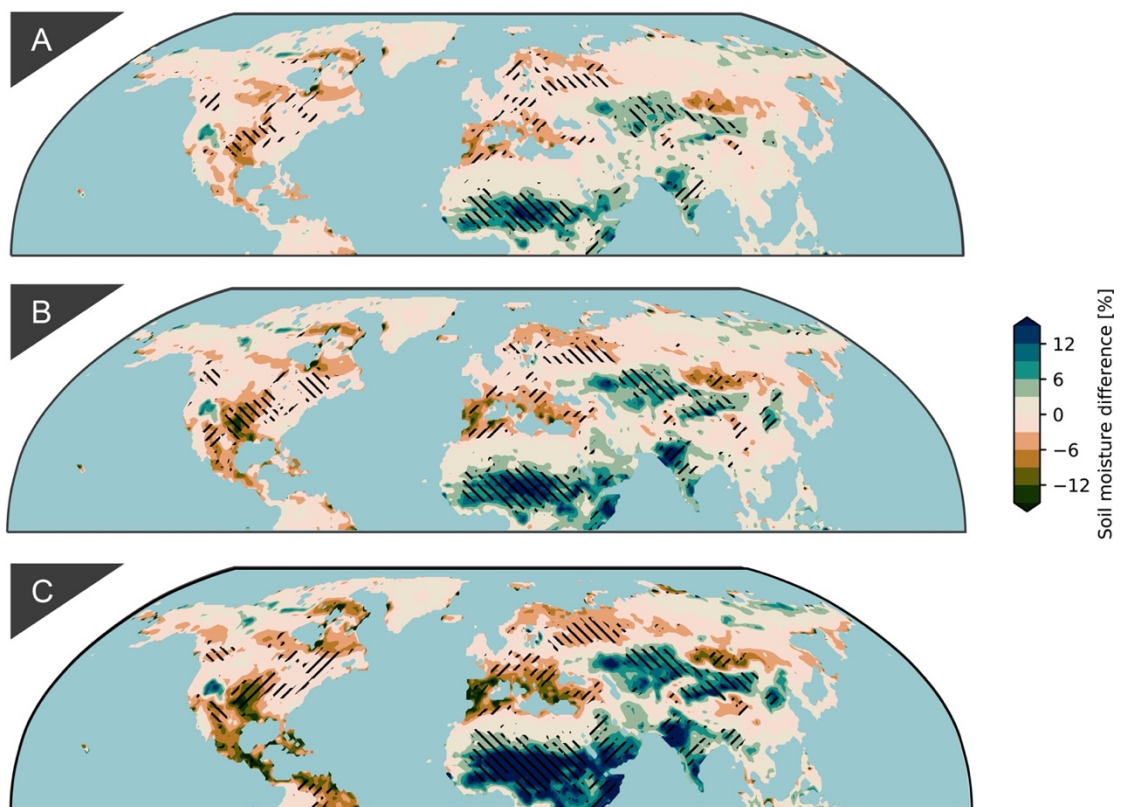


**Figure 5.9:** Averaged anomalies of summer soil moisture (entire column) under SSP1-2.6, SSP2-4.5, and SSP5-8.5. Averaged anomalies of summer soil moisture under SSP1-2.6 (a) and SSP2-4.5 (b) and SSP5-8.5 (c) in the Northern Hemisphere for the period 2071-2100 relative to the baseline period of 1971-2000. The hatched areas indicate areas where 10 of the 11 CMIP6 models show the same sign of change (data from the AWI-CM-1-1-MR model are not used in this figure because the required variable does not exist.).

The projected increase in occurrence rate of droughts over the selected AR6 regions indicates a significant stress on economy (Tian et al., 2018), agriculture (Zhao et al., 2017), migration (Grolle, 2015), and ecosystems (Barnosky et al., 2012) of the regions in the future. Northward shifts in forests and

vegetation (Loarie et al., 2009) leading to shifts in the habitat distributions (Davis and Shaw, 2001) is among major ecosystem impacts. Changes to habitats can also contribute to significant alteration of the carbon cycle (Koven, 2013). Furthermore, the projected climate conditions are likely to increase vegetation mortality due to droughts and other relevant drivers such as fires and infestation (Anderegg et al., 2013).

It should be noted that the model simulations and SSPs are uncertain and characterized by different limitations that have been evaluated in different studies (Cook et al., 2018). Some challenges include limitations associated with physical representation of clouds and uncertainty in precipitation projections in GCMs (Knutti and Sedláček, 2013). Furthermore, current land surface models do not simulate all the hydrological subsurface processes well contributing to uncertain projections (Lu et al., 2019). Also, dynamical phenomena like atmospheric blocking, which are relevant for climate extremes, are generally poorly represented by climate models or are subject to biases (Davini and D'Andrea, 2020). In addition, PET estimation is also subject to high uncertainty which leads to biases in drought projections. Other challenges include uncertain and complex role of vegetation processes (Lemordant et al., 2018; Trugman et al., 2018) in a warming climate, different climate sensitivity of GCMs (Seneviratne and Hauser, 2020) or uncertainties in future radiative forcing (Lu et al., 2019) all of which contribute to uncertainties in drought projection.

Despite the uncertainties of the GCMs, they can reasonably simulate the general tendencies of regional drought trends and patterns in the future. As shown in this chapter, the shown historical evaluation exhibits reasonable consistency between spatial patterns in climate model simulations and observations (Figure 5.1). However, there are differences in how well the models represent trends in drought conditions – e.g. multi-model ensemble underestimating the drying trend in Central Europe (Figure 5.2). The presented results are consistent with drought hotspots identified in prior studies. The presented findings indicate that projected droughts are sensitive to the greenhouse gas emissions and Shared Socioeconomic Pathways. The warmer the future climate, the more intense are the projected droughts spreading from the subtropics to the mid-latitudes. In a relative sense, droughts under SSP1-2.6 are less intense compared to more unfavourable scenarios which highlights the need to reduce greenhouse emissions to reduce future drought impacts.

# 06

## FINAL CONSIDERATION OF THE RESEARCH QUESTIONS

## 6.1 CONCLUSION

In this work, the European summer climate is investigated from different spatio-temporal perspectives, over the time period from A.D. 1600 until A.D. 2100. For this purpose, large-scale influences on the summer climate were investigated by using a  $\delta^{18}\text{O}_{\text{cel}}$  network in order to subsequently reconstruct past climate states. In addition to the "past climate" perspective, one low (SSP1-2.6), medium (SSP2-4.5) and high emission scenario (SSP5-8.5) were analysed with regard to drought conditions and drought probabilities. The elaborated chapters of the thesis were always inspired by the four defined strategy points of documenting, understanding, modelling and attributing (Alexander et al., 2016). The main conclusions in response to the specific questions of the chapters are as follows (Balting et al., 2021a, b, in preparation):

1. What large-scale patterns can be captured by a  $\delta^{18}\text{O}_{\text{cel}}$  tree-ring network and is there a link to the El Niño-Southern Oscillation (ENSO)?

Based on the EOF analysis in Chapter 3, two meaningful climatological patterns of the  $\delta^{18}\text{O}_{\text{cel}}$  network can be derived. The first mode of the  $\delta^{18}\text{O}_{\text{cel}}$  network is a monopole pattern for whole Europe with the centre in Germany. The pattern can also be represented by correlations of PC1 with e.g. global surface air temperature or SST and is further linked to anomaly patterns pointing to ENSO. The ENSO coupling is pronounced for the last 130 years, but weak for the period from 1600 to 1850, suggesting that the relationship between ENSO and European climate may not be stable over time. Hence, the analyses confirm that the link between European climate is non-linear and non-stationary (e.g. Fraedrich and Müller, 1992). Furthermore, it is shown that even with missing instrumental data (Van Oldenborgh and Burgers, 2005; Brönnimann, 2007), it is possible to describe the range of ENSO variability and its consequences for the climate of the European continent using a European  $\delta^{18}\text{O}_{\text{cel}}$  network. The second mode of  $\delta^{18}\text{O}_{\text{cel}}$  variability, which captures a north-south dipole, is associated with a regional summer atmospheric circulation pattern that has a distinct centre over the North Sea. Locally, the  $\delta^{18}\text{O}_{\text{cel}}$  anomalies associated with this mode show the same (opposite) sign as the temperature (precipitation) patterns. The described pattern shows similarities to the summer European blocking pattern (Barnston and Livezey, 1987; Cassou et al., 2005) and relevant for e.g. storm track activity or droughts (Lehmann and Coumou, 2015).

Thus, the presented results have shown that two meaningful climatological patterns can be derived from the  $\delta^{18}\text{O}_{\text{cel}}$  network and that there is not always a stable link to the ENSO variability. Moreover, it has been successfully demonstrated that it is possible to reconstruct changes in the large-scale atmospheric circulation based on the  $\delta^{18}\text{O}_{\text{cel}}$  network beyond the instrumental period. This is a significant improvement, as until now mainly local atmospheric variability or the interplay of two locations was reconstructed (e.g. Trouet et al. (2018)), which did not allow for a reliable large-scale evaluation. The use of a European  $\delta^{18}\text{O}_{\text{cel}}$  network is unique in this context.

2. What trends in the summer VPD have occurred in Europe over the last 400 years and how do they look like in future scenarios?

To answer this research question, the first grid-based reconstruction of the European summer VPD is made based on 26  $\delta^{18}\text{O}_{\text{cel}}$  tree ring records. The reconstruction covers the last 400 years and was produced using the RandF algorithm. From the mid-17<sup>th</sup> century until now, the VPD in Central Europe and Mediterranean is characterized by an increasing trend, due to a simultaneous increase in temperature and decrease in precipitation. Additionally, the presented ensemble means for three climate model projections (SSP1-2.6, SSP2-4.5, SSP5-8.5) show that this increase in VPD in the Mediterranean region will continue until the end of the 21<sup>st</sup> century. In contrast, the projected VPD in Northern and Central Europe shows a trend towards a higher VPD only in the scenario with the highest emissions (SSP5-8.5).

Hence, the newly gained long-term and large-scale perspective shows that the increase of the VPD is not a phenomenon of the last decades as suggested in the literature (e.g. Simmons et al., 2010; Willett et al., 2014; Yuan et al., 2019), but already starts some decades after the Late Maunder Minimum. Nevertheless, the VPD increase, especially in Central Europe and the Mediterranean, has been significantly amplified by recent climate change. For vegetation dynamics, this means that vegetation has been stressed by the VPD increase (e.g. through the correlation between VPD and plant activity (Novick et al., 2016) and forest mortality (Park Williams et al., 2013) for much longer as previously known. The complex technical and scientific combination of the three scientific fields of climate models, climate proxies and climate observations in Chapter 4 as well as the use of a state-of-the-art machine learning algorithm for the reconstruction should be emphasised.

3. Can historical simulations of a climate model reproduce historical summer drought observations, and how do the greenhouse gas concentration affect the probability of summer droughts?

To answer the first part of the research question, state-of-the-art multi-model simulations of the historical climate are used from CMIP6. The presented evaluation of the historical climate in Chapter 5 shows that the observed summer drought conditions in the Northern Hemisphere match simulated conditions almost 100% in the climatological mean for the period 1971 to 2000. Thus, the first research question can in principle be answered in the affirmative. However, there are differences in how well the models reproduce the trends in drought conditions - e.g. the multi-model ensemble underestimates the drying trend in Central Europe.

For the second part of the question, the state-of-the-art multi-model simulations for SSP1-2.6, SSP2-4.5 and SSP5-8.5 are investigated. This reveals that droughts are expected to worsen significantly in arid regions, with the severity depending on greenhouse gas emissions and development pathways. The drought hotspots are located in subtropical regions, where moderate to extreme summer droughts are expected to persist under the current climate until the end of the 21<sup>st</sup> century.

Furthermore, for those regions that are currently less affected by prolonged droughts, such as Central Europe, the climate model ensemble shows that the probability of drought occurrence increases significantly under the warmest future scenario. Hence, the used model ensemble shows that the warmer the future climate and the higher the greenhouse gas concentration, the more intense the projected droughts, which spread from the subtropics to the mid-latitudes. Furthermore, it should be emphasized that the technically complex computations of the drought occurrence rate for state-of-the-art multi-model simulations provide entirely new temporal perspectives on drought variability and severity (e.g. the decrease in drought occurrence in the Mediterranean region in SSP1-2.6 from 2050). These findings are highly relevant for societal mitigation and adaptation strategies.

## 6.2 OUTLOOK

As a logical next step, more high-resolution paleoclimate data as well as comprehensive model simulations are needed to gain additional insights into the stationarity of the reconstructed European climate signals and their relationship with the large-scale atmospheric and oceanic circulation. Furthermore, the influence of solar events on the VPD can be disentangled at local, regional and continental scales. The VPD time series indicate that there is a clear pattern of lower VPD values for Central Europe and the Mediterranean during solar minima, such as the Dalton Minimum. These results can in turn be useful for monthly, seasonal and annual forecasts, as well as for the quality of the scenarios in CMIP6.

In order to further strengthen the validity of the drought probabilities in future scenarios, it is necessary to examine the performance of each individual model and to understand which processes are better or worse represented in terms of temperature, potential evapotranspiration, soil moisture and precipitation. One of the most important tasks is to minimise the spatial differences between historical simulations and observations. For example, it must be investigated why parts of the Mediterranean region, Greenland and northern Canada are more than 2 °C too warm on average in summer compared to observations (Figure 5.1).

## REFERENCES

- Alexander, L., Zhang, X., Hegerl, G., Seneviratne, S., Behrangi, A., Fischer, E., Martius, O., Otto, F., Sillmann, J., and Vautard, R.: Implementation Plan for WCRP Grand Challenge on Understanding and Predicting Weather and Climate Extremes—the “Extremes Grand Challenge,” World Clim. Reseach Programme, Version June, 2016.
- Ali, M., Prasad, R., Xiang, Y., and Yaseen, Z. M.: Complete ensemble empirical mode decomposition hybridized with random forest and kernel ridge regression model for monthly rainfall forecasts, *J. Hydrol.*, 584, 124647, <https://doi.org/10.1016/j.jhydrol.2020.124647>, 2020.
- Allan, R. J., Lindesay, J., and Parker, D. E.: El Niño, southern oscillation & climatic variability, CSIRO, Collingwood, Vic., Australia, 405 pp., 1996.
- Allen, R. G., Smith, M., Perrier, A., and Pereira, L. S.: An update for the definition of reference evapotranspiration, *ICID Bull.*, 43, 1994.
- Álvarez, C., Veblen, T. T., Christie, D. A., and González-Reyes, Á.: Relationships between climate variability and radial growth of *Nothofagus pumilio* near altitudinal treeline in the Andes of northern Patagonia, Chile, *For. Ecol. Manag.*, 10, 2015.
- Anderegg, W. R. L., Kane, J. M., and Anderegg, L. D. L.: Consequences of widespread tree mortality triggered by drought and temperature stress, *Nat. Clim. Change*, 3, 30–36, <https://doi.org/10.1038/nclimate1635>, 2013.
- Andreu-Hayles, L., Ummenhofer, C. C., Barriendos, M., Schleser, G. H., Helle, G., Leuenberger, M., Gutiérrez, E., and Cook, E. R.: 400 Years of summer hydroclimate from stable isotopes in Iberian trees, *Clim. Dyn.*, 49, 143–161, <https://doi.org/10.1007/s00382-016-3332-z>, 2017.
- Aono, Y. and Saito, S.: Clarifying springtime temperature reconstructions of the medieval period by gap-filling the cherry blossom phenological data series at Kyoto, Japan, *Int. J. Biometeorol.*, 54, 211–219, <https://doi.org/10.1007/s00484-009-0272-x>, 2010.
- Audi, G., Kondev, F. G., Wang, M., Huang, W. J., and Naimi, S.: The NUBASE2016 evaluation of nuclear properties, *Chin. Phys. C*, 41, 030001, <https://doi.org/10.1088/1674-1137/41/3/030001>, 2017.
- Bair, E. H., Abreu Calfa, A., Rittger, K., and Dozier, J.: Using machine learning for real-time estimates of snow water equivalent in the watersheds of Afghanistan, *The Cryosphere*, 12, 1579–1594, <https://doi.org/10.5194/tc-12-1579-2018>, 2018.
- Balting, D. F., Ionita, M., Wegmann, M., Helle, G., Schleser, G. H., Rimbu, N., Freund, M. B., Heinrich, I., Caldarescu, D., and Lohmann, G.: Large-scale climate signals of a European oxygen isotope network from tree rings, *Clim. Past*, 17, 1005–1023, <https://doi.org/10.5194/cp-17-1005-2021>, 2021a.
- Balting, D. F., AghaKouchak, A., Lohmann, G., and Ionita, M.: Northern Hemisphere drought risk in a warming climate, *Npj Clim. Atmospheric Sci.*, 4, 1–13, <https://doi.org/10.1038/s41612-021-00218-2>, 2021b.
- Balting, D. F., Michel, S., Nagavciuc, V., Helle, G., Schleser, G. H., Steger, D., Lohmann, G., and Ionita, M.: A past, present and future perspective on the European summer vapour pressure deficit, *Nat. Sci. Data*, in preparation.
- Barbour, M. M.: Stable oxygen isotope composition of plant tissue: a review, *Funct. Plant Biol.*, 34, 83–94, <https://doi.org/10.1071/FP06228>, 2007.
- Barbour, M. M., Roden, J. S., Farquhar, G. D., and Ehleringer, J. R.: Expressing leaf water and cellulose oxygen isotope ratios as enrichment above source water reveals evidence of a Pelet effect, *Oecologia*, 138, 426–435, <https://doi.org/10.1007/s00442-003-1449-3>, 2004.

- Barkhordarian, A., Saatchi, S. S., Behrang, A., Loikith, P. C., and Mechoso, C. R.: A Recent Systematic Increase in Vapor Pressure Deficit over Tropical South America, *Sci. Rep.*, 9, 15331, <https://doi.org/10.1038/s41598-019-51857-8>, 2019.
- Barnosky, A. D., Hadly, E. A., Bascompte, J., Berlow, E. L., Brown, J. H., Fortelius, M., Getz, W. M., Harte, J., Hastings, A., Marquet, P. A., Martinez, N. D., Mooers, A., Roopnarine, P., Vermeij, G., Williams, J. W., Gillespie, R., Kitzes, J., Marshall, C., Matzke, N., Mindell, D. P., Revilla, E., and Smith, A. B.: Approaching a state shift in Earth's biosphere, *Nature*, 486, 52–58, <https://doi.org/10.1038/nature11018>, 2012.
- Barnston, A. G. and Livezey, R. E.: Classification, Seasonality and Persistence of Low-Frequency Atmospheric Circulation Patterns, *Mon. Weather Rev.*, 115, 1083–1126, [https://doi.org/10.1175/1520-0493\(1987\)115<1083:CSAPOL>2.0.CO;2](https://doi.org/10.1175/1520-0493(1987)115<1083:CSAPOL>2.0.CO;2), 1987.
- Batehup, R., McGregor, S., and Gallant, A. J. E.: The influence of non-stationary teleconnections on palaeoclimate reconstructions of ENSO variance using a pseudoproxy framework, *Clim. Past*, 11, 1733–1749, <https://doi.org/10.5194/cp-11-1733-2015>, 2015.
- Beguéría, S., Vicente-Serrano, S. M., Reig, F., and Latorre, B.: Standardized precipitation evapotranspiration index (SPEI) revisited: parameter fitting, evapotranspiration models, tools, datasets and drought monitoring, *Int. J. Climatol.*, 34, 3001–3023, <https://doi.org/10.1002/joc.3887>, 2014.
- Behrang, A., Fetzer, E. J., and Granger, S. L.: Early detection of drought onset using near surface temperature and humidity observed from space, *Int. J. Remote Sens.*, 37, 3911–3923, <https://doi.org/10.1080/01431161.2016.1204478>, 2016.
- Belgiu, M. and Drăguț, L.: Random forest in remote sensing: A review of applications and future directions, *ISPRS J. Photogramm. Remote Sens.*, 114, 24–31, <https://doi.org/10.1016/j.isprsjprs.2016.01.011>, 2016.
- Berg, A., Sheffield, J., and Milly, P. C. D.: Divergent surface and total soil moisture projections under global warming, *Geophys. Res. Lett.*, 44, 236–244, <https://doi.org/10.1002/2016GL071921>, 2017.
- Berrisford, P., Källberg, P., Kobayashi, S., Dee, D., Uppala, S., Simmons, A. J., Poli, P., and Sato, H.: Atmospheric conservation properties in ERA-Interim, *Q. J. R. Meteorol. Soc.*, 137, 1381–1399, <https://doi.org/10.1002/qj.864>, 2011.
- Boettger, T., Haupt, M., Knöller, K., Weise, S. M., Waterhouse, J. S., Rinne, K. T., Loader, N. J., Sonninen, E., Jungner, H., Masson-Delmotte, V., Stievenard, M., Guillemin, M.-T., Pierre, M., Pazdur, A., Leuenberger, M., Filot, M., Saurer, M., Reynolds, C. E., Helle, G., and Schleser, G. H.: Wood Cellulose Preparation Methods and Mass Spectrometric Analyses of  $\delta^{13}\text{C}$ ,  $\delta^{18}\text{O}$ , and Nonexchangeable  $\delta^2\text{H}$  Values in Cellulose, Sugar, and Starch: An Interlaboratory Comparison, *Anal. Chem.*, 79, 4603–4612, <https://doi.org/10.1021/ac0700023>, 2007.
- Bonacina, L. C. W.: The European Drought of 1921, *Nature*, 112, 488–489, <https://doi.org/10.1038/112488b0>, 1923.
- Boucher, O., Denvil, S., Caubel, A., and Foujols, M. A.: IPSL IPSL-CM6A-LR model output prepared for CMIP6 CMIP (20201102), <https://doi.org/10.22033/ESGF/CMIP6.1534>, 2018.
- Boulesteix, A.-L., Janitza, S., Kruppa, J., and König, I. R.: Overview of random forest methodology and practical guidance with emphasis on computational biology and bioinformatics, *WIREs Data Min. Knowl. Discov.*, 2, 493–507, <https://doi.org/10.1002/widm.1072>, 2012.
- Brasseur, G. and Carlson, D.: Future Directions for the World Climate Research Programme, *Eos*, 43, <https://doi.org/10.1029/2015EO033577>, 2015.

- Brázdil, R., Dobrovolný, P., Trnka, M., Kotyza, O., Řezníčková, L., Valášek, H., Zahradníček, P., and Štěpánek, P.: Droughts in the Czech Lands, 1090–2012 AD, *Clim. Past*, 9, 1985–2002, <https://doi.org/10.5194/cp-9-1985-2013>, 2013.
- Breiman, L.: Random Forests, *Mach. Learn.*, 45, 5–32, <https://doi.org/10.1023/A:1010933404324>, 2001.
- Brienen, R. J. W., Helle, G., Pons, T. L., Guyot, J.-L., and Gloor, M.: Oxygen isotopes in tree rings are a good proxy for Amazon precipitation and El Niño–Southern Oscillation variability, *Proc. Natl. Acad. Sci.*, 109, 16957–16962, <https://doi.org/10.1073/pnas.1205977109>, 2012.
- Brönnimann, S.: Impact of El Niño–Southern Oscillation on European climate, *Rev. Geophys.*, 45, <https://doi.org/10.1029/2006RG000199>, 2007.
- Brönnimann, S.: *Climatic Changes Since 1700*, Springer, Switzerland, 373 pp., 2015.
- Brönnimann, S. and Krämer, D.: Tambora and the “year without a summer” of 1816 a perspective on earth and human systems science, 2016.
- Brönnimann, S., Luterbacher, J., Staehelin, J., Svendby, T. M., Hansen, G., and Svenøe, T.: Extreme climate of the global troposphere and stratosphere in 1940–42 related to El Niño, *Nature*, 431, 971, <https://doi.org/10.1038/nature02982>, 2004.
- Brönnimann, S., Xoplaki, E., Casty, C., Pauling, A., and Luterbacher, J.: ENSO influence on Europe during the last centuries, *Clim. Dyn.*, 28, 181–197, <https://doi.org/10.1007/s00382-006-0175-z>, 2007.
- Brooks, C. E. P. and Glasspoole, J.: The drought of 1921, *Q. J. R. Meteorol. Soc.*, 48, 139–168, <https://doi.org/10.1002/qj.49704820205>, 1922.
- Brooks, M. M. and Marron, J. S.: Asymptotic optimality of the least-squares cross-validation bandwidth for kernel estimates of intensity functions, *Stoch. Process. Their Appl.*, 38, 157–165, [https://doi.org/10.1016/0304-4149\(91\)90076-O](https://doi.org/10.1016/0304-4149(91)90076-O), 1991.
- Buckley, T. N.: How do stomata respond to water status?, *New Phytol.*, 224, 21–36, <https://doi.org/10.1111/nph.15899>, 2019.
- Büntgen, U., Frank, D. C., Nievergelt, D., and Esper, J.: Summer Temperature Variations in the European Alps, a.d. 755–2004, *J. Clim.*, 19, 5606–5623, <https://doi.org/10.1175/JCLI3917.1>, 2006.
- Butzin, M., Werner, M., Masson-Delmotte, V., Risi, C., Frankenberger, C., Griбанov, K., Jouzel, J., and Zakharov, V. I.: Variations of oxygen-18 in West Siberian precipitation during the last 50 years, *Atmospheric Chem. Phys.*, 14, 5853–5869, <https://doi.org/10.5194/acp-14-5853-2014>, 2014.
- Carnicer, J., Barbeta, A., Sperlich, D., Coll, M., and Penuelas, J.: Contrasting trait syndromes in angiosperms and conifers are associated with different responses of tree growth to temperature on a large scale, *Front. Plant Sci.*, 4, <https://doi.org/10.3389/fpls.2013.00409>, 2013.
- Cassou, C., Terray, L., and Phillips, A. S.: Tropical Atlantic Influence on European Heat Waves, *J. Clim.*, 18, 2805–2811, <https://doi.org/10.1175/JCLI3506.1>, 2005.
- Challinor, A. J., Simelton, E. S., Fraser, E. D. G., Hemming, D., and Collins, M.: Increased crop failure due to climate change: assessing adaptation options using models and socio-economic data for wheat in China, *Environ. Res. Lett.*, 5, 034012, <https://doi.org/10.1088/1748-9326/5/3/034012>, 2010.
- Chiang, F., Mazdizyarni, O., and AghaKouchak, A.: Evidence of anthropogenic impacts on global drought frequency, duration, and intensity, *Nat. Commun.*, 12, 2754, <https://doi.org/10.1038/s41467-021-22314-w>, 2021.

- Churakova Sidorova, O. V., Corona, C., Fonti, M. V., Guillet, S., Saurer, M., Siegwolf, R. T. W., Stoffel, M., and Vaganov, E. A.: Recent atmospheric drying in Siberia is not unprecedented over the last 1,500 years, *Sci. Rep.*, 10, 15024, <https://doi.org/10.1038/s41598-020-71656-w>, 2020.
- Compo, G. P., Whitaker, J. S., Sardeshmukh, P. D., Matsui, N., Allan, R. J., Yin, X., Gleason, B. E., Vose, R. S., Rutledge, G., Bessemoulin, P., Brönnimann, S., Brunet, M., Crouthamel, R. I., Grant, A. N., Groisman, P. Y., Jones, P. D., Kruk, M. C., Kruger, A. C., Marshall, G. J., Mauger, M., Mok, H. Y., Nordli, ø., Ross, T. F., Trigo, R. M., Wang, X. L., Woodruff, S. D., and Worley, S. J.: The Twentieth Century Reanalysis Project, *Q. J. R. Meteorol. Soc.*, 137, 1–28, <https://doi.org/10.1002/qj.776>, 2011.
- Cook, B. I., Smerdon, J. E., Seager, R., and Coats, S.: Global warming and 21st century drying, *Clim. Dyn.*, 43, 2607–2627, <https://doi.org/10.1007/s00382-014-2075-y>, 2014.
- Cook, B. I., Mankin, J. S., and Anchukaitis, K. J.: Climate Change and Drought: From Past to Future, *Curr. Clim. Change Rep.*, 4, 164–179, <https://doi.org/10.1007/s40641-018-0093-2>, 2018.
- Cook, B. I., Mankin, J. S., Marvel, K., Williams, A. P., Smerdon, J. E., and Anchukaitis, K. J.: Twenty-First Century Drought Projections in the CMIP6 Forcing Scenarios, *Earths Future*, 8, e2019EF001461, <https://doi.org/10.1029/2019EF001461>, 2020.
- Cook, E. R., Woodhouse, C. A., Eakin, C. M., Meko, D. M., and Stahle, D. W.: Long-Term Aridity Changes in the Western United States, *Science*, 306, 1015–1018, <https://doi.org/10.1126/science.1102586>, 2004.
- Cook, E. R., Seager, R., Cane, M. A., and Stahle, D. W.: North American drought: Reconstructions, causes, and consequences, *Earth-Sci. Rev.*, 81, 93–134, <https://doi.org/10.1016/j.earscirev.2006.12.002>, 2007.
- Cook, E. R., Seager, R., Kushnir, Y., Briffa, K. R., Büntgen, U., Frank, D., Krusic, P. J., Tegel, W., Schrier, G. van der, Andreu-Hayles, L., Baillic, M., Baittinger, C., Bleicher, N., Bonde, N., Brown, D., Carrer, M., Cooper, R., Čufar, K., Dittmar, C., Esper, J., Griggs, C., Gunnarson, B., Günther, B., Gutierrez, E., Haneca, K., Helama, S., Herzig, F., Heussner, K.-U., Hofmann, J., Janda, P., Kontic, R., Köse, N., Kyncl, T., Levanić, T., Linderholm, H., Manning, S., Melvin, T. M., Miles, D., Neuwirth, B., Nicolussi, K., Nola, P., Panayotov, M., Popa, I., Rothe, A., Seftigen, K., Seim, A., Svarva, H., Svoboda, M., Thun, T., Timonen, M., Touchan, R., Trotsiuk, V., Trouet, V., Walder, F., Ważny, T., Wilson, R., and Zang, C.: Old World megadroughts and pluvials during the Common Era, *Sci. Adv.*, 1, 1–9, <https://doi.org/10.1126/sciadv.1500561>, 2015.
- Cook, E. R., Kushnir, Y., Smerdon, J. E., Williams, A. P., Anchukaitis, K. J., and Wahl, E. R.: A Euro-Mediterranean tree-ring reconstruction of the winter NAO index since 910 C.E., *Clim. Dyn.*, <https://doi.org/10.1007/s00382-019-04696-2>, 2019.
- Cox, D. R. and Lewis, P. A. W.: *The Statistical Analysis of Series of Events*, Springer Netherlands, Dordrecht, <https://doi.org/10.1007/978-94-011-7801-3>, 1966.
- Craig, H.: Isotopic standards for carbon and oxygen and correction factors for mass-spectrometric analysis of carbon dioxide, *Geochim. Cosmochim. Acta*, 12, 133–149, [https://doi.org/10.1016/0016-7037\(57\)90024-8](https://doi.org/10.1016/0016-7037(57)90024-8), 1957.
- Dai, A.: Increasing drought under global warming in observations and models, *Nat. Clim. Change*, 3, 52–58, <https://doi.org/10.1038/nclimate1633>, 2013.
- Dai, A., Zhao, T., and Chen, J.: Climate Change and Drought: a Precipitation and Evaporation Perspective, *Curr. Clim. Change Rep.*, 4, 301–312, <https://doi.org/10.1007/s40641-018-0101-6>, 2018.
- Dansgaard, W.: Stable isotopes in precipitation, *Tellus*, 16, 436–468, <https://doi.org/10.1111/j.2153-3490.1964.tb00181.x>, 1964.

- Dätwyler, C., Abram, N. J., Grosjean, M., Wahl, E. R., and Neukom, R.: El Niño–Southern Oscillation variability, teleconnection changes and responses to large volcanic eruptions since AD 1000, *Int. J. Climatol.*, 39, 2711–2724, <https://doi.org/10.1002/joc.5983>, 2019.
- Davies, D. and Loader, N. J.: An evaluation of english oak earlywood vessel area as a climate proxy in the UK, *Dendrochronologia*, 64, 1–8, <https://doi.org/10.1016/j.dendro.2020.125777>, 2020.
- Davini, P. and D’Andrea, F.: From CMIP3 to CMIP6: Northern Hemisphere Atmospheric Blocking Simulation in Present and Future Climate, *J. Clim.*, 33, 10021–10038, <https://doi.org/10.1175/JCLI-D-19-0862.1>, 2020.
- Davis, M. B. and Shaw, R. G.: Range Shifts and Adaptive Responses to Quaternary Climate Change, *Science*, 292, 673–679, <https://doi.org/10.1126/science.292.5517.673>, 2001.
- Dee, D. P., Uppala, S. M., Simmons, A. J., Berrisford, P., Poli, P., Kobayashi, S., Andrae, U., Balmaseda, M. A., Balsamo, G., Bauer, P., Bechtold, P., Beljaars, A. C. M., van de Berg, L., Bidlot, J., Bormann, N., Delsol, C., Dragani, R., Fuentes, M., Geer, A. J., Haimberger, L., Healy, S. B., Hersbach, H., Hólm, E. V., Isaksen, L., Kållberg, P., Köhler, M., Matricardi, M., McNally, A. P., Monge-Sanz, B. M., Morcrette, J.-J., Park, B.-K., Peubey, C., de Rosnay, P., Tavolato, C., Thépaut, J.-N., and Vitart, F.: The ERA-Interim reanalysis: configuration and performance of the data assimilation system, *Q. J. R. Meteorol. Soc.*, 137, 553–597, <https://doi.org/10.1002/qj.828>, 2011.
- Deser, C., Capotondi, A., Saravanan, R., and Phillips, A. S.: Tropical Pacific and Atlantic Climate Variability in CCSM3, *J. Clim.*, 19, 2451–2481, <https://doi.org/10.1175/JCLI3759.1>, 2006.
- Diefendorf, A. F., Mueller, K. E., Wing, S. L., Koch, P. L., and Freeman, K. H.: Global patterns in leaf  $^{13}\text{C}$  discrimination and implications for studies of past and future climate, *Proc. Natl. Acad. Sci.*, 107, 5738–5743, <https://doi.org/10.1073/pnas.0910513107>, 2010.
- Dix, M., Bi, D., Dobrotoff, P., Fiedler, R., Harman, I., Law, R., Mackallah, C., Marsland, S., O’Farrell, S., Rashid, H., Srbinovsky, J., Sullivan, A., Trenham, C., Vohralik, P., Watterson, I., Williams, G., Woodhouse, M., Bodman, R., Dias, F. B., Domingues, C., Hannah, N., Heerdegen, A., Savita, A., Wales, S., Allen, C., Druken, K., Evans, B., Richards, C., Ridzwan, S. M., Roberts, D., Smillie, J., Snow, K., Ward, M., and Yang, R.: CSIRO-ARCCSS ACCESS-CM2 model output prepared for CMIP6 CMIP (20200715), <https://doi.org/10.22033/ESGF/CMIP6.2281>, 2019.
- Domeisen, D. I. V., Garfinkel, C. I., and Butler, A. H.: The Teleconnection of El Niño Southern Oscillation to the Stratosphere, *Rev. Geophys.*, 57, 5–47, <https://doi.org/10.1029/2018RG000596>, 2019.
- Donges, J. F., Schleussner, C.-F., Siegmund, J. F., and Donner, R. V.: Event coincidence analysis for quantifying statistical interrelationships between event time series, *Eur. Phys. J. Spec. Top.*, 225, 471–487, <https://doi.org/10.1140/epjst/e2015-50233-y>, 2016.
- Eamus, D., Boulain, N., Cleverly, J., and Breshears, D. D.: Global change-type drought-induced tree mortality: vapor pressure deficit is more important than temperature per se in causing decline in tree health, *Ecol. Evol.*, 3, 2711–2729, <https://doi.org/10.1002/ece3.664>, 2013.
- EC-Earth Consortium: EC-Earth-Consortium EC-Earth3 model output prepared for CMIP6 CMIP (20200715), <https://doi.org/10.22033/ESGF/CMIP6.181>, 2019a.
- EC-Earth Consortium: EC-Earth-Consortium EC-Earth3-Veg model output prepared for CMIP6 CMIP (20200715), <https://doi.org/10.22033/ESGF/CMIP6.642>, 2019b.
- EC-Earth Consortium: EC-Earth-Consortium EC-Earth3-Veg-LR model output prepared for CMIP6 CMIP (20210201), <https://doi.org/10.22033/ESGF/CMIP6.643>, 2020.

- Edwards, T. W. D., Wolfe, B. B., and Macdonald, G. M.: Influence of Changing Atmospheric Circulation on Precipitation  $\delta^{18}\text{O}$ -Temperature Relations in Canada during the Holocene, *Quat. Res.*, 46, 211–218, <https://doi.org/10.1006/qres.1996.0061>, 1996.
- Epstein, S., Thompson, P., and Yapp, C. J.: Oxygen and Hydrogen Isotopic Ratios in Plant Cellulose, *Science*, 198, 1209–1215, <https://doi.org/10.1126/science.198.4323.1209>, 1977.
- Esper, J., Carnelli, A. L., Kamenik, C., Filot, M., Leuenberger, M., and Treydte, K.: Spruce tree-ring proxy signals during cold and warm periods, *Dendrobiology*, 77, 3–18, <https://doi.org/10.12657/denbio.077.001>, 2017.
- Etien, N., Daux, V., Masson-Delmotte, V., Stievenard, M., Bernard, V., Durost, S., Guillemin, M. T., Mestre, O., and Pierre, M.: A bi-proxy reconstruction of Fontainebleau (France) growing season temperature from A.D. 1596 to 2000, *Clim. Past*, 4, 91–106, 2008.
- Etien, N., Daux, V., Masson-Delmotte, V., Mestre, O., Stievenard, M., Guillemin, M. T., Boettger, T., Breda, N., Haupt, M., and Perraud, P. P.: Summer maximum temperature in northern France over the past century: instrumental data versus multiple proxies (tree-ring isotopes, grape harvest dates and forest fires), *Clim. Change*, 94, 429–456, <https://doi.org/10.1007/s10584-008-9516-8>, 2009.
- Eyring, V., Bony, S., Meehl, G. A., Senior, C. A., Stevens, B., Stouffer, R. J., and Taylor, K. E.: Overview of the Coupled Model Intercomparison Project Phase 6 (CMIP6) experimental design and organization, *Geosci. Model Dev.*, 9, 1937–1958, <https://doi.org/10.5194/gmd-9-1937-2016>, 2016.
- Fan, X., Duan, Q., Shen, C., Wu, Y., and Xing, C.: Global surface air temperatures in CMIP6: historical performance and future changes, *Environ. Res. Lett.*, 15, 104056, <https://doi.org/10.1088/1748-9326/abb051>, 2020.
- Farquhar, G. D. and Lloyd, J.: 5 - Carbon and Oxygen Isotope Effects in the Exchange of Carbon Dioxide between Terrestrial Plants and the Atmosphere, in: *Stable Isotopes and Plant Carbon-water Relations*, edited by: Ehleringer, J. R., Hall, A. E., and Farquhar, G. D., Academic Press, San Diego, 47–70, <https://doi.org/10.1016/B978-0-08-091801-3.50011-8>, 1993.
- Fekete, A. and Sandholz, S.: Here Comes the Flood, but Not Failure? Lessons to Learn after the Heavy Rain and Pluvial Floods in Germany 2021, *Water*, 13, 3016, <https://doi.org/10.3390/w13213016>, 2021.
- Felis, T., Ionita, M., Rimbu, N., Lohmann, G., and Kölling, M.: Mild and Arid Climate in the Eastern Sahara-Arabian Desert During the Late Little Ice Age, *Geophys. Res. Lett.*, 45, 7112–7119, <https://doi.org/10.1029/2018GL078617>, 2018a.
- Felis, T., Ionita, M., Rimbu, N., Lohmann, G., and Kölling, M.: Mild and Arid Climate in the Eastern Sahara-Arabian Desert During the Late Little Ice Age, *Geophys. Res. Lett.*, 45, 7112–7119, <https://doi.org/10.1029/2018GL078617>, 2018b.
- Feng, S., Hu, Q., Huang, W., Ho, C.-H., Li, R., and Tang, Z.: Projected climate regime shift under future global warming from multi-model, multi-scenario CMIP5 simulations, *Glob. Planet. Change*, 112, 41–52, <https://doi.org/10.1016/j.gloplacha.2013.11.002>, 2014.
- Ferrio, J. P. and Voltas, J.: Carbon and oxygen isotope ratios in wood constituents of *Pinus halepensis* as indicators of precipitation, temperature and vapour pressure deficit, *Tellus B Chem. Phys. Meteorol.*, 57, 164–173, <https://doi.org/10.3402/tellusb.v57i2.16780>, 2005.
- Flato, G. M.: Earth system models: an overview, *WIREs Clim. Change*, 2, 783–800, <https://doi.org/10.1002/wcc.148>, 2011.

- Fletcher, A. L., Sinclair, T. R., and Allen, L. H.: Transpiration responses to vapor pressure deficit in well watered 'slow-wilting' and commercial soybean, *Environ. Exp. Bot.*, 61, 145–151, <https://doi.org/10.1016/j.envexpbot.2007.05.004>, 2007.
- Folland, C. K., Knight, J., Linderholm, H. W., Fereday, D., Ineson, S., and Hurrell, J. W.: The Summer North Atlantic Oscillation: Past, Present, and Future, *J. Clim.*, 22, 1082–1103, <https://doi.org/10.1175/2008JCLI2459.1>, 2009.
- Foroozan, Z., Griesinger, J., Pourtahmasi, K., and Bräuning, A.: Evaluation of Different Pooling Methods to Establish a Multi-Century  $\delta^{18}\text{O}$  Chronology for Paleoclimate Reconstruction, *Geosciences*, 9, 270, <https://doi.org/10.3390/geosciences9060270>, 2019.
- Fraedrich, K.: An ENSO impact on Europe?, *Tellus A*, 46, 541–552, <https://doi.org/10.1034/j.1600-0870.1994.00015.x>, 1994.
- Fraedrich, K. and Müller, K.: Climate anomalies in Europe associated with ENSO extremes, *Int. J. Climatol.*, 12, 25–31, <https://doi.org/10.1002/joc.3370120104>, 1992.
- Freund, M. B., Henley, B. J., Karoly, D. J., McGregor, H. V., Abram, N. J., and Dommenget, D.: Higher frequency of Central Pacific El Niño events in recent decades relative to past centuries, *Nat. Geosci.*, 12, 450–455, <https://doi.org/10.1038/s41561-019-0353-3>, 2019.
- Fritts, H. C.: *Tree rings and climate*, Academic Press, London ; New York, 567 pp., 1976.
- Fry, B.: *Stable Isotope Ecology*, Springer Science & Business Media, New York, 318 pp., 2007.
- Gat, J.: *Isotope Hydrology: A Study of the Water Cycle*, World Scientific, London, 198 pp., 2010.
- Geisser, S.: The Predictive Sample Reuse Method with Applications, *J. Am. Stat. Assoc.*, 70, 320–328, <https://doi.org/10.2307/2285815>, 1975.
- Gleckler, P. J., Taylor, K. E., and Doutriaux, C.: Performance metrics for climate models, *J. Geophys. Res.*, 113, 1–20, <https://doi.org/10.1029/2007JD008972>, 2008.
- González-González, B. D., Vázquez-Ruiz, R. A., and García-González, I.: Effects of climate on earlywood vessel formation of *Quercus robur* and *Q. pyrenaica* at a site in the northwestern Iberian Peninsula, *Can. J. For. Res.*, 45, 698–709, <https://doi.org/10.1139/cjfr-2014-0436>, 2015.
- Good, S. P., Noone, D., and Bowen, G.: Hydrologic connectivity constrains partitioning of global terrestrial water fluxes, *Science*, 349, 175–177, <https://doi.org/10.1126/science.aaa5931>, 2015.
- Grolle, J.: Historical case studies of famines and migrations in the West African Sahel and their possible relevance now and in the future, *Popul. Environ.*, 37, 181–206, <https://doi.org/10.1007/s11111-015-0237-4>, 2015.
- Grossiord, C., Buckley, T. N., Cernusak, L. A., Novick, K. A., Poulter, B., Siegwolf, R. T. W., Sperry, J. S., and McDowell, N. G.: Plant responses to rising vapor pressure deficit, *New Phytol.*, 226, 1550–1566, <https://doi.org/10.1111/nph.16485>, 2020.
- Hafner, P., McCarroll, D., Robertson, I., Loader, N. J., Gagen, M., Young, G. H., Bale, R. J., Sonninen, E., and Levanič, T.: A 520 year record of summer sunshine for the eastern European Alps based on stable carbon isotopes in larch tree rings, *Clim. Dyn.*, 43, 971–980, <https://doi.org/10.1007/s00382-013-1864-z>, 2014.
- Hagemann, S., Arpe, K., and Roeckner, E.: Evaluation of the Hydrological Cycle in the ECHAM5 Model, *J. Clim.*, 19, 3810–3827, <https://doi.org/10.1175/JCLI3831.1>, 2006.

- Haile, G. G., Tang, Q., Hosseini-Moghari, S.-M., Liu, X., Gebremicael, T. G., Leng, G., Kebede, A., Xu, X., and Yun, X.: Projected Impacts of Climate Change on Drought Patterns Over East Africa, *Earths Future*, 8, 1–23, <https://doi.org/10.1029/2020EF001502>, 2020.
- Hangartner, S., Kress, A., Saurer, M., Frank, D., and Leuenberger, M.: Methods to merge overlapping tree-ring isotope series to generate multi-centennial chronologies, *Chem. Geol.*, 294–295, 127–134, <https://doi.org/10.1016/j.chemgeo.2011.11.032>, 2012.
- Hansen, J., Johnson, D., Lacis, A., Lebedeff, S., Lee, P., Rind, D., and Russell, G.: Climate Impact of Increasing Atmospheric Carbon Dioxide, *Science*, 213, 957–966, <https://doi.org/10.1126/science.213.4511.957>, 1981.
- Harris, I., Osborn, T. J., Jones, P., and Lister, D.: Version 4 of the CRU TS monthly high-resolution gridded multivariate climate dataset, *Sci. Data*, 7, 1–18, <https://doi.org/10.1038/s41597-020-0453-3>, 2020.
- Haupt, M., Weigl, M., Grabner, M., and Boettger, T.: A 400-year reconstruction of July relative air humidity for the Vienna region (eastern Austria) based on carbon and oxygen stable isotope ratios in tree-ring latewood cellulose of oaks (*Quercus petraea* Matt. Liebl.), *Clim. Change*, 105, 243–262, <https://doi.org/10.1007/s10584-010-9862-1>, 2011.
- Hayes, M., Svoboda, M., Wall, N., and Widhalm, M.: The Lincoln Declaration on Drought Indices: Universal Meteorological Drought Index Recommended, *Bull. Am. Meteorol. Soc.*, 92, 485–488, <https://doi.org/10.1175/2010BAMS3103.1>, 2011.
- Heinrich, I., Touchan, R., Dorado Liñán, I., Vos, H., and Helle, G.: Winter-to-spring temperature dynamics in Turkey derived from tree rings since AD 1125, *Clim. Dyn.*, 41, 1685–1701, <https://doi.org/10.1007/s00382-013-1702-3>, 2013.
- Helama, S., Meriläinen, J., and Tuomenvirta, H.: Multicentennial megadrought in northern Europe coincided with a global El Niño–Southern Oscillation drought pattern during the Medieval Climate Anomaly, *Geology*, 37, 175–178, <https://doi.org/10.1130/G25329A.1>, 2009.
- Helama, S., Läänelaid, A., Raisio, J., Mäkelä, H. M., Hilasvuori, E., Jungner, H., and Sonninen, E.: Oak decline analyzed using intraannual radial growth indices,  $\delta^{13}\text{C}$  series and climate data from a rural hemiboreal landscape in southwesternmost Finland, *Environ. Monit. Assess.*, 186, 4697–4708, <https://doi.org/10.1007/s10661-014-3731-8>, 2014.
- Helle, G. and Schleser, G. H.: Beyond CO<sub>2</sub>-fixation by Rubisco - an interpretation of  $^{13}\text{C}/^{12}\text{C}$  variations in tree rings from novel intra-seasonal studies on broad-leaf trees, *Plant Cell Environ.*, 27, 367–380, <https://doi.org/10.1111/j.0016-8025.2003.01159.x>, 2004.
- Helliker, B. R. and Griffiths, H.: Toward a plant-based proxy for the isotope ratio of atmospheric water vapor, *Glob. Change Biol.*, 13, 723–733, <https://doi.org/10.1111/j.1365-2486.2007.01325.x>, 2007.
- Henke, L. M. K., Lambert, F. H., and Charman, D. J.: Was the Little Ice Age more or less El Niño-like than the Medieval Climate Anomaly? Evidence from hydrological and temperature proxy data, *Clim. Past*, 13, 267–301, <https://doi.org/10.5194/cp-13-267-2017>, 2017.
- Hilasvuori, E., Berninger, F., Sonninen, E., Tuomenvirta, H., and Jungner, H.: Stability of climate signal in carbon and oxygen isotope records and ring width from Scots pine (*Pinus sylvestris* L.) in Finland, *J. Quat. Sci.*, 24, 469–480, <https://doi.org/10.1002/jqs.1260>, 2009.
- Hill, S. A., Waterhouse, J. S., Field, E. M., Switsur, V. R., and Rees, T. A.: Rapid recycling of triose phosphates in oak stem tissue, *Plant Cell Environ.*, 18, 931–936, <https://doi.org/10.1111/j.1365-3040.1995.tb00603.x>, 1995.
- Hotelling, H.: The most predictable criterion, *J. Educ. Psychol.*, 26, 139–142, <https://doi.org/10.1037/h0058165>, 1935.

- Huang, B., Thorne, P. W., Banzon, V. F., Boyer, T., Chepurin, G., Lawrimore, J. H., Menne, M. J., Smith, T. M., Vose, R. S., and Zhang, H.-M.: Extended Reconstructed Sea Surface Temperature, Version 5 (ERSSTv5): Upgrades, Validations, and Intercomparisons, *J. Clim.*, 30, 8179–8205, <https://doi.org/10.1175/JCLI-D-16-0836.1>, 2017.
- Humphrey, V., Zscheischler, J., Ciais, P., Gudmundsson, L., Sitch, S., and Seneviratne, S. I.: Sensitivity of atmospheric CO<sub>2</sub> growth rate to observed changes in terrestrial water storage, *Nature*, 560, 628–631, <https://doi.org/10.1038/s41586-018-0424-4>, 2018.
- Hurrell, J. and Van Loon, H.: Decadal variations in climate associated with the North Atlantic Oscillation, *Clim. Change*, 36, 301–326, <https://doi.org/10.1023/A:1005314315270>, 1997.
- Ionita, M. and Nagavciuc, V.: Forecasting low flow conditions months in advance through teleconnection patterns, with a special focus on summer 2018, *Sci. Rep.*, 10, 1–12, <https://doi.org/10.1038/s41598-020-70060-8>, 2020.
- Ionita, M. and Nagavciuc, V.: Changes in drought features at the European level over the last 120 years, *Nat. Hazards Earth Syst. Sci.*, 21, 1685–1701, <https://doi.org/10.5194/nhess-21-1685-2021>, 2021.
- Ionita, M., Boroneanț, C., and Chelcea, S.: Seasonal modes of dryness and wetness variability over Europe and their connections with large scale atmospheric circulation and global sea surface temperature, *Clim. Dyn.*, 45, 2803–2829, <https://doi.org/10.1007/s00382-015-2508-2>, 2015.
- Ionita, M., Dima, M., Nagavciuc, V., Scholz, P., and Lohmann, G.: Past megadroughts in central Europe were longer, more severe and less warm than modern droughts, *Commun. Earth Environ.*, 2, 1–9, <https://doi.org/10.1038/s43247-021-00130-w>, 2021.
- IPCC: Special report on emissions scenarios: a special report of Working Group III of the Intergovernmental Panel on Climate Change, Cambridge University Press, Cambridge ; New York, 599 pp., 2000.
- IPCC: Climate Change 2007: Synthesis Report. Contribution of Working Groups I, II and III to the Fourth Assessment Report of the Intergovernmental Panel on Climate Change, IPCC, Geneva, 103 pp., 2008.
- IPCC: Climate Change 2013 - The Physical Science Basis: Working Group I Contribution to the Fifth Assessment Report of the Intergovernmental Panel on Climate Change, Cambridge University Press, Cambridge, 1535 pp., <https://doi.org/10.1017/CBO9781107415324>, 2013.
- IPCC: Climate Change 2021: The Physical Science Basis. Contribution of Working Group I to the Sixth Assessment Report of the Intergovernmental Panel on Climate Change, Cambridge University Press, in Press pp., 2021.
- Iturbide, M., Gutiérrez, J. M., Alves, L. M., Bedia, J., Cerezo-Mota, R., Gimeno, E., Gochis, A. S., Di Luca, A., Faria, S. H., Gorodetskaya, I. V., Hauser, M., Herrera, S., Hennessy, K., Hewitt, H. T., Jones, R. G., Kravik, S., Manzananas, R., Martínez-Castro, D., Narisma, G. T., Nurhati, I. S., Pinto, I., Seneviratne, S. I., van den Hurk, B., and Vera, C. S.: An update of IPCC climate reference regions for subcontinental analysis of climate model data: definition and aggregated datasets, *Earth Syst. Sci. Data*, 12, 2959–2970, <https://doi.org/10.5194/essd-12-2959-2020>, 2020.
- Jasechko, S., Sharp, Z. D., Gibson, J. J., Birks, S. J., Yi, Y., and Fawcett, P. J.: Terrestrial water fluxes dominated by transpiration, *Nature*, 496, 347–350, <https://doi.org/10.1038/nature11983>, 2013.
- Josse, J. and Husson, F.: missMDA: A Package for Handling Missing Values in Multivariate Data Analysis, *J. Stat. Softw.*, 70, 1–31, <https://doi.org/10.18637/jss.v070.i01>, 2016.
- Jungclaus, J., Bittner, M., Wieners, K.-H., Wachsmann, F., Schupfner, M., Legutke, S., Giorgetta, M., Reick, C., Gayler, V., Haak, H., de Vrese, P., Raddatz, T., Esch, M., Mauritsen, T., von Storch, J.-S., Behrens, J., Brovkin, V., Claussen, M., Crueger, T., Fast, I., Fiedler, S., Hagemann, S., Hohenegger, C., Jahns, T., Kloster, S., Kinne,

S., Lasslop, G., Kornbluh, L., Marotzke, J., Matei, D., Meraner, K., Mikolajewicz, U., Modali, K., Müller, W., Nabel, J., Notz, D., Peters, K., Pincus, R., Pohlmann, H., Pongratz, J., Rast, S., Schmidt, H., Schnur, R., Schulzweida, U., Six, K., Stevens, B., Voigt, A., and Roeckner, E.: MPI-M MPIESM1.2-HR model output prepared for CMIP6 CMIP (20200715), <https://doi.org/10.22033/ESGF/CMIP6.741>, 2019.

Kaennel, M. and Schweingruber, F. H. (Eds.): Multilingual glossary of dendrochronology: terms and definitions in English, German, French, Spanish, Italian, Portuguese and Russian, Haupt, Bern, 467 pp., 1995.

Kahmen, A., Sachse, D., Arndt, S. K., Tu, K. P., Farrington, H., Vitousek, P. M., and Dawson, T. E.: Cellulose  $\delta^{18}\text{O}$  is an index of leaf-to-air vapor pressure difference (VPD) in tropical plants, *Proc. Natl. Acad. Sci.*, 108, 1981–1986, <https://doi.org/10.1073/pnas.1018906108>, 2011.

Keith, L., Meerow, S., Hondula, D. M., Turner, V. K., and Arnott, J. C.: Deploy heat officers, policies and metrics, *Nature*, 598, 29–31, <https://doi.org/10.1038/d41586-021-02677-2>, 2021.

King, M. P., Yu, E., and Sillmann, J.: Impact of strong and extreme El Niños on European hydroclimate, *Tellus Dyn. Meteorol. Oceanogr.*, 72, 1–10, <https://doi.org/10.1080/16000870.2019.1704342>, 2020.

Knutti, R. and Sedláček, J.: Robustness and uncertainties in the new CMIP5 climate model projections, *Nat. Clim. Change*, 3, 369–373, <https://doi.org/10.1038/nclimate1716>, 2013.

Körner, C.: The use of ‘altitude’ in ecological research, *Trends Ecol. Evol.*, 22, 569–574, <https://doi.org/10.1016/j.tree.2007.09.006>, 2007.

Körner, Ch., Farquhar, G. D., and Wong, S. C.: Carbon isotope discrimination by plants follows latitudinal and altitudinal trends, *Oecologia*, 88, 30–40, <https://doi.org/10.1007/BF00328400>, 1991.

Koven, C. D.: Boreal carbon loss due to poleward shift in low-carbon ecosystems, *Nat. Geosci.*, 6, 452–456, <https://doi.org/10.1038/ngeo1801>, 2013.

Krasting, J. P., John, J. G., Blanton, C., McHugh, C., Nikonov, S., Radhakrishnan, A., Rand, K., Zadeh, N. T., Balaji, V., Durachta, J., Dupuis, C., Menzel, R., Robinson, T., Underwood, S., Vahlenkamp, H., Dunne, K. A., Gauthier, P. P., Ginoux, P., Griffies, S. M., Hallberg, R., Harrison, M., Hurlin, W., Malyshev, S., Naik, V., Paulot, F., Paynter, D. J., Ploshay, J., Schwarzkopf, D. M., Seman, C. J., Silvers, L., Wyman, B., Zeng, Y., Adcroft, A., Dunne, J. P., Dussin, R., Guo, H., He, J., Held, I. M., Horowitz, L. W., Lin, P., Milly, P. C. D., Shevliakova, E., Stock, C., Winton, M., Xie, Y., and Zhao, M.: NOAA-GFDL GFDL-ESM4 model output prepared for CMIP6 CMIP (20200715), <https://doi.org/10.22033/ESGF/CMIP6.1407>, 2018.

Kriegler, E., O’Neill, B. C., Hallegatte, S., Kram, T., Lempert, R. J., Moss, R. H., and Wilbanks, T.: The need for and use of socio-economic scenarios for climate change analysis: A new approach based on shared socio-economic pathways, *Glob. Environ. Change*, 22, 807–822, <https://doi.org/10.1016/j.gloenvcha.2012.05.005>, 2012.

Krishnamurti, T. N., Xue, J., Bedi, H. S., Ingles, K., and Oosterhof, D.: Physical initialization for numerical weather prediction over the tropics, *Tellus B*, 43, 53–81, <https://doi.org/10.1034/j.1600-0889.1991.t01-2-00007.x>, 1991.

Labuhn, I., Daux, V., Pierre, M., Stievenard, M., Girardclos, O., Féron, A., Genty, D., Masson-Delmotte, V., and Mestre, O.: Tree age, site and climate controls on tree ring cellulose  $\delta^{18}\text{O}$ : A case study on oak trees from south-western France, *Dendrochronologia*, 32, 78–89, <https://doi.org/10.1016/j.dendro.2013.11.001>, 2014.

Labuhn, I., Daux, V., Girardclos, O., Stievenard, M., Pierre, M., and Masson-Delmotte, V.: French summer droughts since 1326 CE: a reconstruction based on tree ring cellulose delta O-18, *Clim. Past*, 12, 1101–1117, <https://doi.org/10.5194/cp-12-1101-2016>, 2016.

Latif, M. and Grötzner, A.: The equatorial Atlantic oscillation and its response to ENSO, *Clim. Dyn.*, 16, 213–218, <https://doi.org/10.1007/s003820050014>, 2000.

- Lavergne, A., Daux, V., Villalba, R., Pierre, M., Stievenard, M., Vimeux, F., and Srur, A. M.: Are the oxygen isotopic compositions of *Fitzroya cupressoides* and *Nothofagus pumilio* cellulose promising proxies for climate reconstructions in northern Patagonia?, *J. Geophys. Res. Biogeosciences*, 121, 767–776, <https://doi.org/10.1002/2015JG003260>, 2016.
- Lawrence, M. G.: The Relationship between Relative Humidity and the Dewpoint Temperature in Moist Air: A Simple Conversion and Applications, *Bull. Am. Meteorol. Soc.*, 86, 225–234, <https://doi.org/10.1175/BAMS-86-2-225>, 2005.
- Lee, J.-Y. and Wang, B.: Future change of global monsoon in the CMIP5, *Clim. Dyn.*, 42, 101–119, <https://doi.org/10.1007/s00382-012-1564-0>, 2014.
- Lehmann, J. and Coumou, D.: The influence of mid-latitude storm tracks on hot, cold, dry and wet extremes, *Sci. Rep.*, 5, 1–9, <https://doi.org/10.1038/srep17491>, 2015.
- Lemordant, L., Gentine, P., Swann, A. S., Cook, B. I., and Scheff, J.: Critical impact of vegetation physiology on the continental hydrologic cycle in response to increasing CO<sub>2</sub>, *Proc. Natl. Acad. Sci.*, 115, 4093–4098, <https://doi.org/10.1073/pnas.1720712115>, 2018.
- Li, J., Xie, S.-P., Cook, E. R., Huang, G., D'Arrigo, R., Liu, F., Ma, J., and Zheng, X.-T.: Interdecadal modulation of El Niño amplitude during the past millennium, *Nat. Clim. Change*, 1, 114–118, <https://doi.org/10.1038/nclimate1086>, 2011.
- Li, J., Xie, S.-P., Cook, E. R., Morales, M. S., Christie, D. A., Johnson, N. C., Chen, F., D'Arrigo, R., Fowler, A. M., Gou, X., and Fang, K.: El Niño modulations over the past seven centuries, *Nat. Clim. Change*, 3, 822–826, <https://doi.org/10.1038/nclimate1936>, 2013.
- Li, J., Wang, Z., Lai, C., and Zhang, Z.: Tree-ring-width based streamflow reconstruction based on the random forest algorithm for the source region of the Yangtze River, China, *CATENA*, 183, 1–15, <https://doi.org/10.1016/j.catena.2019.104216>, 2019.
- Lindgren, A., Lu, Z., Zhang, Q., and Hugelius, G.: Reconstructing Past Global Vegetation With Random Forest Machine Learning, Sacrificing the Dynamic Response for Robust Results, *J. Adv. Model. Earth Syst.*, 13, 1–16, <https://doi.org/10.1029/2020MS002200>, 2021.
- Liu, X., Zhang, X., Zhao, L., Xu, G., Wang, L., Sun, W., Zhang, Q., Wang, W., Zeng, X., and Wu, G.: Tree ring  $\delta^{18}\text{O}$  reveals no long-term change of atmospheric water demand since 1800 in the northern Great Hinggan Mountains, China: 200 Year Vapor-Pressure Deficit Record, *J. Geophys. Res. Atmospheres*, 122, 6697–6712, <https://doi.org/10.1002/2017JD026660>, 2017.
- Liu, X., Li, C., Zhao, T., and Han, L.: Future changes of global potential evapotranspiration simulated from CMIP5 to CMIP6 models, *Atmospheric Ocean. Sci. Lett.*, 13, 568–575, <https://doi.org/10.1080/16742834.2020.1824983>, 2020.
- Lloyd-Hughes, B. and Saunders, M. A.: Seasonal prediction of European spring precipitation from El Niño–Southern Oscillation and Local sea-surface temperatures, *Int. J. Climatol.*, 22, 1–14, <https://doi.org/10.1002/joc.723>, 2002.
- Loader, N. J., Street-Perrott, F. A., Daley, T. J., Hughes, P. D. M., Kimak, A., Levanič, T., Mallon, G., Mauquoy, D., Robertson, I., Roland, T. P., van Bellen, S., Ziehmer, M. M., and Leuenberger, M.: Simultaneous Determination of Stable Carbon, Oxygen, and Hydrogen Isotopes in Cellulose, *Anal. Chem.*, 87, 376–380, <https://doi.org/10.1021/ac502557x>, 2015.
- Loarie, S. R., Duffy, P. B., Hamilton, H., Asner, G. P., Field, C. B., and Ackerly, D. D.: The velocity of climate change, *Nature*, 462, 1052–1055, <https://doi.org/10.1038/nature08649>, 2009.

- López-Moreno, J. I., Vicente-Serrano, S. M., Zabalza, J., Beguería, S., Lorenzo-Lacruz, J., Azorin-Molina, C., and Morán-Tejeda, E.: Hydrological response to climate variability at different time scales: A study in the Ebro basin, *J. Hydrol.*, 477, 175–188, <https://doi.org/10.1016/j.jhydrol.2012.11.028>, 2013.
- Lorenz, E. N.: *Empirical Orthogonal Functions and Statistical Weather Prediction*, Massachusetts Institute of Technology, Department of Meteorology, Massachusetts, 112 pp., 1956.
- Lu, J., Carbone, G. J., and Grego, J. M.: Uncertainty and hotspots in 21st century projections of agricultural drought from CMIP5 models, *Sci. Rep.*, 9, 1–12, <https://doi.org/10.1038/s41598-019-41196-z>, 2019.
- Luterbacher, J., Dietrich, D., Xoplaki, E., Grosjean, M., and Wanner, H.: European Seasonal and Annual Temperature Variability, Trends, and Extremes Since 1500, *Science*, 303, 1499–1503, <https://doi.org/10.1126/science.1093877>, 2004.
- Mankin, J. S., Seager, R., Smerdon, J. E., Cook, B. I., and Williams, A. P.: Mid-latitude freshwater availability reduced by projected vegetation responses to climate change, *Nat. Geosci.*, 12, 983–988, <https://doi.org/10.1038/s41561-019-0480-x>, 2019.
- Marengo, J. A., Nobre, C. A., Tomasella, J., Oyama, M. D., Sampaio de Oliveira, G., de Oliveira, R., Camargo, H., Alves, L. M., and Brown, I. F.: The Drought of Amazonia in 2005, *J. Clim.*, 21, 495–516, <https://doi.org/10.1175/2007JCLI1600.1>, 2008.
- Mariotti, A., Pan, Y., Zeng, N., and Alessandri, A.: Long-term climate change in the Mediterranean region in the midst of decadal variability, *Clim. Dyn.*, 44, <https://doi.org/10.1007/s00382-015-2487-3>, 2015.
- Markonis, Y., Kumar, R., Hanel, M., Rakovec, O., Máca, P., and AghaKouchak, A.: The rise of compound warm-season droughts in Europe, *Sci. Adv.*, 7, 1–7, <https://doi.org/10.1126/sciadv.abb9668>, 2021.
- Marshall, J. D. and Zhang, J.: Carbon Isotope Discrimination and Water-Use Efficiency in Native Plants of the North-Central Rockies, *Ecology*, 75, 1887–1895, <https://doi.org/10.2307/1941593>, 1994.
- Mathieu, P.-P., Sutton, R. T., Dong, B., and Collins, M.: Predictability of Winter Climate over the North Atlantic European Region during ENSO Events, *J. Clim.*, 17, 1953–1974, [https://doi.org/10.1175/1520-0442\(2004\)017<1953:POWCOT>2.0.CO;2](https://doi.org/10.1175/1520-0442(2004)017<1953:POWCOT>2.0.CO;2), 2004.
- Maxwell, A. E., Warner, T. A., and Fang, F.: Implementation of machine-learning classification in remote sensing: an applied review, *Int. J. Remote Sens.*, 39, 2784–2817, <https://doi.org/10.1080/01431161.2018.1433343>, 2018.
- McCarroll, D. and Loader, N. J.: Stable isotopes in tree rings, *Quat. Sci. Rev.*, 23, 771–801, <https://doi.org/10.1016/j.quascirev.2003.06.017>, 2004.
- Meehl, G. A., Boer, G. J., Covey, C., Latif, M., and Stouffer, R. J.: Intercomparison makes for a better climate model, *Eos Trans. Am. Geophys. Union*, 78, 445–446, <https://doi.org/10.1029/97EO00276>, 1997.
- Meehl, G. A., Boer, G. J., Covey, C., Latif, M., and Stouffer, R. J.: The Coupled Model Intercomparison Project (CMIP), *Bull. Am. Meteorol. Soc.*, 81, 313–318, 2000.
- Meehl, G. A., Covey, C., McAvaney, B., Latif, M., and Stouffer, R. J.: Overview of the Coupled Model Intercomparison Project, *Bull. Am. Meteorol. Soc.*, 86, 89–93, 2005.
- Meehl, G. A., Covey, C., Delworth, T., Latif, M., McAvaney, B., Mitchell, J. F. B., Stouffer, R. J., and Taylor, K. E.: THE WCRP CMIP3 Multimodel Dataset: A New Era in Climate Change Research, *Bull. Am. Meteorol. Soc.*, 88, 1383–1394, <https://doi.org/10.1175/BAMS-88-9-1383>, 2007.

- Meehl, G. A., Moss, R., Taylor, K. E., Eyring, V., Stouffer, R. J., Bony, S., and Stevens, B.: Climate Model Intercomparisons: Preparing for the Next Phase, *Eos Trans. Am. Geophys. Union*, 95, 77–78, <https://doi.org/10.1002/2014EO090001>, 2014.
- Merkel, U. and Latif, M.: A high resolution AGCM study of the El Niño impact on the North Atlantic/Euro-pean sector, *Geophys. Res. Lett.*, 29, 5-1-5–4, <https://doi.org/10.1029/2001GL013726>, 2002.
- Michel, S., Swingedouw, D., Chavent, M., Ortega, P., Mignot, J., and Khodri, M.: Reconstructing climatic modes of variability from proxy records using ClimIndRec version 1.0, *Geosci. Model Dev.*, 13, 841–858, <https://doi.org/10.5194/gmd-13-841-2020>, 2020.
- Mishra, A. K. and Singh, V. P.: A review of drought concepts, *J. Hydrol.*, 391, 202–216, <https://doi.org/10.1016/j.jhydrol.2010.07.012>, 2010.
- Moss, R. H., Edmonds, J. A., Hibbard, K. A., Manning, M. R., Rose, S. K., van Vuuren, D. P., Carter, T. R., Emori, S., Kainuma, M., Kram, T., Meehl, G. A., Mitchell, J. F. B., Nakicenovic, N., Riahi, K., Smith, S. J., Stouffer, R. J., Thomson, A. M., Weyant, J. P., and Wilbanks, T. J.: The next generation of scenarios for climate change research and assessment, *Nature*, 463, 747–756, <https://doi.org/10.1038/nature08823>, 2010.
- Mudelsee, M.: *Statistical Analysis of Climate Extremes*, 1st ed., Cambridge University Press, 200 pp., <https://doi.org/10.1017/9781139519441>, 2020.
- Nagavciuc, V., Ionita, M., Perşoiu, A., Popa, I., Loader, N. J., and McCarroll, D.: Stable oxygen isotopes in Romanian oak tree rings record summer droughts and associated large-scale circulation patterns over Europe, *Clim. Dyn.*, 52, 6557–6568, <https://doi.org/10.1007/s00382-018-4530-7>, 2018.
- Nakićenović, N., Alcamo, J., and IPCC (Eds.): *Special report on emissions scenarios: a special report of Working Group III of the Intergovernmental Panel on Climate Change*, Cambridge University Press, Cambridge ; New York, 599 pp., 2000.
- Nash, J. E. and Sutcliffe, J. V.: River flow forecasting through conceptual models part I - A discussion of principles, *J. Hydrol.*, 10, 282–290, [https://doi.org/10.1016/0022-1694\(70\)90255-6](https://doi.org/10.1016/0022-1694(70)90255-6), 1970.
- North, G. R., Bell, T. L., Cahalan, R. F., and Moeng, F. J.: Sampling Errors in the Estimation of Empirical Orthogonal Functions, *Mon. Weather Rev.*, 110, 699–706, [https://doi.org/10.1175/1520-0493\(1982\)110<0699:SEITEO>2.0.CO;2](https://doi.org/10.1175/1520-0493(1982)110<0699:SEITEO>2.0.CO;2), 1982.
- Novick, K. A., Ficklin, D. L., Stoy, P. C., Williams, C. A., Bohrer, G., Oishi, A. C., Papuga, S. A., Blanken, P. D., Noormets, A., Sulman, B. N., Scott, R. L., Wang, L., and Phillips, R. P.: The increasing importance of atmospheric demand for ecosystem water and carbon fluxes, *Nat. Clim. Change*, 6, 1023–1027, <https://doi.org/10.1038/nclimate3114>, 2016.
- Nowaczyk, N. R., Liu, J., Plessen, B., Wegwerth, A., and Arz, H. W.: A High-Resolution Paleosecular Variation Record for Marine Isotope Stage 6 From Southeastern Black Sea Sediments, *J. Geophys. Res. Solid Earth*, 126, <https://doi.org/10.1029/2020JB021350>, 2021.
- Nultsch, W.: *Allgemeine Botanik*, Thieme, Stuttgart, 684 pp., 2001.
- Ogi, M., Tachibana, Y., and Yamazaki, K.: Impact of the wintertime North Atlantic Oscillation (NAO) on the summertime atmospheric circulation, *Geophys. Res. Lett.*, 30, <https://doi.org/10.1029/2003GL017280>, 2003.
- Oikonomou, C., Flocas, H. A., Hatzaki, M., Nisantzi, A., and Asimakopoulos, D. N.: Relationship of extreme dry spells in Eastern Mediterranean with large-scale circulation, *Theor. Appl. Climatol.*, 100, 137–151, <https://doi.org/10.1007/s00704-009-0171-4>, 2010.
- O’Leary, M. H.: Carbon isotope fractionation in plants, *Phytochemistry*, 20, 553–567, 1981.

O'Neill, B. C., Tebaldi, C., van Vuuren, D. P., Eyring, V., Friedlingstein, P., Hurtt, G., Knutti, R., Kriegler, E., Lamarque, J.-F., Lowe, J., Meehl, G. A., Moss, R., Riahi, K., and Sanderson, B. M.: The Scenario Model Inter-comparison Project (ScenarioMIP) for CMIP6, *Geosci. Model Dev.*, 9, 3461–3482, <https://doi.org/10.5194/gmd-9-3461-2016>, 2016.

O'Neill, B. C., Kriegler, E., Ebi, K. L., Kemp-Benedict, E., Riahi, K., Rothman, D. S., van Ruijven, B. J., van Vuuren, D. P., Birkmann, J., Kok, K., Levy, M., and Solecki, W.: The roads ahead: Narratives for shared socio-economic pathways describing world futures in the 21st century, *Glob. Environ. Change*, 42, 169–180, <https://doi.org/10.1016/j.gloenvcha.2015.01.004>, 2017.

Orlowsky, B. and Seneviratne, S. I.: Global changes in extreme events: regional and seasonal dimension, *Clim. Change*, 110, 669–696, <https://doi.org/10.1007/s10584-011-0122-9>, 2012.

Orlowsky, B. and Seneviratne, S. I.: Elusive drought: uncertainty in observed trends and short- and long-term CMIP5 projections, *Hydrol. Earth Syst. Sci.*, 17, 1765–1781, <https://doi.org/10.5194/hess-17-1765-2013>, 2013.

Oshiro, T. M., Perez, P. S., and Baranauskas, J. A.: How Many Trees in a Random Forest?, in: *Machine Learning and Data Mining in Pattern Recognition*, Berlin, Heidelberg, 154–168, [https://doi.org/10.1007/978-3-642-31537-4\\_13](https://doi.org/10.1007/978-3-642-31537-4_13), 2012.

Park Williams, A., Allen, C. D., Macalady, A. K., Griffin, D., Woodhouse, C. A., Meko, D. M., Swetnam, T. W., Rauscher, S. A., Seager, R., Grissino-Mayer, H. D., Dean, J. S., Cook, E. R., Gangodagamage, C., Cai, M., and McDowell, N. G.: Temperature as a potent driver of regional forest drought stress and tree mortality, *Nat. Clim. Change*, 3, 292–297, <https://doi.org/10.1038/nclimate1693>, 2013.

Pauling, A., Luterbacher, J., Casty, C., and Wanner, H.: Five hundred years of gridded high-resolution precipitation reconstructions over Europe and the connection to large-scale circulation, *Clim. Dyn.*, 26, 387–405, <https://doi.org/10.1007/s00382-005-0090-8>, 2006.

Pearson, K.: On lines and planes of closest fit to systems of points in space, *Lond. Edinb. Dublin Philos. Mag. J. Sci.*, 2, 559–572, <https://doi.org/10.1080/14786440109462720>, 1902.

Peterson, B. J. and Fry, B.: Stable Isotopes in Ecosystem Studies, *Ann Rev Col Syst*, 18, 293–320, 1987.

Philip, S. Y., Kew, S. F., van Oldenborgh, G. J., Anslow, F. S., Seneviratne, S. I., Vautard, R., Coumou, D., Ebi, K. L., Arrighi, J., Singh, R., van Aalst, M., Pereira Marghidan, C., Wehner, M., Yang, W., Li, S., Schumacher, D. L., Hauser, M., Bonnet, R., Luu, L. N., Lehner, F., Gillett, N., Tradowsky, J., Vecchi, G. A., Rodell, C., Stull, R. B., Howard, R., and Otto, F. E. L.: Rapid attribution analysis of the extraordinary heatwave on the Pacific Coast of the US and Canada June 2021, *Earth system change: climate scenarios*, <https://doi.org/10.5194/esd-2021-90>, 2021.

Porter, T. J., Pisaric, M. F. J., Field, R. D., Kokelj, S. V., Edwards, T. W. D., deMontigny, P., Healy, R., and LeGrande, A. N.: Spring-summer temperatures since AD 1780 reconstructed from stable oxygen isotope ratios in white spruce tree-rings from the Mackenzie Delta, northwestern Canada, *Clim. Dyn.*, 42, 771–785, <https://doi.org/10.1007/s00382-013-1674-3>, 2014.

Pozo-Vázquez, D., Gámiz-Fortis, S. R., Tovar-Pescador, J., Esteban-Parra, M. J., and Castro-Díez, Y.: El Niño–southern oscillation events and associated European winter precipitation anomalies, *Int. J. Climatol.*, 25, 17–31, <https://doi.org/10.1002/joc.1097>, 2005.

Prasad, R., Ali, M., Kwan, P., and Khan, H.: Designing a multi-stage multivariate empirical mode decomposition coupled with ant colony optimization and random forest model to forecast monthly solar radiation, *Appl. Energy*, 236, 778–792, <https://doi.org/10.1016/j.apenergy.2018.12.034>, 2019.

- Qu, Y., Zhu, Z., Chai, L., Liu, S., Montzka, C., Liu, J., Yang, X., Lu, Z., Jin, R., Li, X., Guo, Z., and Zheng, J.: Rebuilding a Microwave Soil Moisture Product Using Random Forest Adopting AMSR-E/AMSR2 Brightness Temperature and SMAP over the Qinghai–Tibet Plateau, China, *Remote Sens.*, 11, 1–28, <https://doi.org/10.3390/rs11060683>, 2019.
- Raible, C. C., Luksch, U., and Fraedrich, K.: Precipitation and Northern Hemisphere regimes, *Atmospheric Sci. Lett.*, 5, 43–55, <https://doi.org/10.1016/j.atmoscilet.2003.12.001>, 2004.
- Rast, S., Brokopf, R., Cheedela, S.-K., Esch, M., Gayler, V., Kirchner, I., Kornblueh, L., Rhodin, A., Schmidt, H., Schulzweida, U., and Wieners, K.-H.: User manual for ECHAM6 - June 21, 2013 - version echam-6.1.06p3-guide-1.3, *Berichte Zur Erdsystemforschung*, 136, 1–220, <https://doi.org/10.17617/2.1810486>, 2013.
- Rathgeber, C. B. K., Cuny, H. E., and Fonti, P.: Biological Basis of Tree-Ring Formation: A Crash Course, *Front. Plant Sci.*, 7, 1–7, <https://doi.org/10.3389/fpls.2016.00734>, 2016.
- Rayner, N. A., Parker, D. E., Horton, E. B., Folland, C. K., Alexander, L. V., Rowell, D. P., Kent, E. C., and Kaplan, A.: Global analyses of sea surface temperature, sea ice, and night marine air temperature since the late nineteenth century, *J. Geophys. Res.*, 108, 1–37, <https://doi.org/10.1029/2002JD002670>, 2003.
- Reichstein, M., Camps-Valls, G., Stevens, B., Jung, M., Denzler, J., Carvalhais, N., and Prabhat: Deep learning and process understanding for data-driven Earth system science, *Nature*, 566, 195–204, <https://doi.org/10.1038/s41586-019-0912-1>, 2019.
- Restaino, C. M., Peterson, D. L., and Littell, J.: Increased water deficit decreases Douglas fir growth throughout western US forests, *Proc. Natl. Acad. Sci.*, 113, 9557–9562, <https://doi.org/10.1073/pnas.1602384113>, 2016.
- Riahi, K., van Vuuren, D. P., Kriegler, E., Edmonds, J., O’Neill, B. C., Fujimori, S., Bauer, N., Calvin, K., Dellink, R., Fricko, O., Lutz, W., Popp, A., Cuaserna, J. C., Kc, S., Leimbach, M., Jiang, L., Kram, T., Rao, S., Emmerling, J., Ebi, K., Hasegawa, T., Havlik, P., Humpenöder, F., Da Silva, L. A., Smith, S., Stehfest, E., Bosetti, V., Eom, J., Gernaat, D., Masui, T., Rogelj, J., Strefler, J., Drouet, L., Krey, V., Luderer, G., Harmsen, M., Takahashi, K., Baumstark, L., Doelman, J. C., Kainuma, M., Klimont, Z., Marangoni, G., Lotze-Campen, H., Obersteiner, M., Tabeau, A., and Tavoni, M.: The Shared Socioeconomic Pathways and their energy, land use, and greenhouse gas emissions implications: An overview, *Glob. Environ. Change*, 42, 153–168, <https://doi.org/10.1016/j.gloenvcha.2016.05.009>, 2017.
- Rimbu, N., Lohmann, G., Felis, T., and Tzold, J. P.: Shift in ENSO Teleconnections Recorded by a Northern Red Sea Coral, *J. Clim.*, 16, 1414–1422, [https://doi.org/10.1175/1520-0442\(2003\)16<1414:SI-ETRB>2.0.CO;2](https://doi.org/10.1175/1520-0442(2003)16<1414:SI-ETRB>2.0.CO;2), 2003.
- Rimbu, N., Lohmann, G., and Ionita, M.: Interannual to multidecadal Euro-Atlantic blocking variability during winter and its relationship with extreme low temperatures in Europe, *J. Geophys. Res. Atmospheres*, 119, 13,621–13,636, <https://doi.org/10.1002/2014JD021983>, 2014.
- Rinne, K. T., Loader, N. J., Switsur, V. R., and Waterhouse, J. S.: 400-year May–August precipitation reconstruction for Southern England using oxygen isotopes in tree rings, *Quat. Sci. Rev.*, 60, 13–25, <https://doi.org/10.1016/j.quascirev.2012.10.048>, 2013a.
- Rinne, K. T., Loader, N. J., Switsur, V. R., and Waterhouse, J. S.: 400-year May–August precipitation reconstruction for Southern England using oxygen isotopes in tree rings, *Quat. Sci. Rev.*, 60, 13–25, <https://doi.org/10.1016/j.quascirev.2012.10.048>, 2013b.
- Roden, J. S., Lin, G., and Ehleringer, J. R.: A mechanistic model for interpretation of hydrogen and oxygen isotope ratios in tree-ring cellulose, *Geochim. Cosmochim. Acta*, 64, 21–35, [https://doi.org/10.1016/S0016-7037\(99\)00195-7](https://doi.org/10.1016/S0016-7037(99)00195-7), 2000.

- Rodriguez-Galiano, V. F., Ghimire, B., Rogan, J., Chica-Olmo, M., and Rigol-Sanchez, J. P.: An assessment of the effectiveness of a random forest classifier for land-cover classification, *ISPRS J. Photogramm. Remote Sens.*, 67, 93–104, <https://doi.org/10.1016/j.isprsjprs.2011.11.002>, 2012.
- Roeckner, E., Bäuml, G., Bonaventura, L., Brokopf, R., Esch, M., Giorgetta, M., Hagemann, S., Kirchner, I., Kornbluch, L., Manzini, E., Rhodin, A., Schlese, U., Schulzweida, U., and Tompkins, A.: The atmospheric general circulation model ECHAM 5. PART I: Model description, Rep. Max-Planck-Inst. Für Meteorol., 349, 1–127, <https://doi.org/10.17617/2.995269>, 2003.
- Roeckner, E., Brokopf, R., Esch, M., Giorgetta, M., Hagemann, S., Kornbluch, L., Manzini, E., Schlese, U., and Schulzweida, U.: Sensitivity of Simulated Climate to Horizontal and Vertical Resolution in the ECHAM5 Atmosphere Model, *J. Clim.*, 19, 3771–3791, <https://doi.org/10.1175/JCLI3824.1>, 2006.
- Rosch, A. and Schmidbauer, H.: *WaveletComp 1.1: A guided tour through the R package*, 58 pp., 2018.
- Rozanski, K., Araguás-Araguás, L., and Gonfiantini, R.: Isotopic Patterns in Modern Global Precipitation, in: *Climate Change in Continental Isotopic Records*, American Geophysical Union (AGU), 1–36, <https://doi.org/10.1029/GM078p0001>, 2013.
- Running, S. W.: Environmental control of leaf water conductance in conifers, *Can. J. For. Res.*, 6, 104–112, <https://doi.org/10.1139/x76-013>, 1976.
- Saurer, M., Borella, S., Schweingruber, F., and Siegwolf, R.: Stable carbon isotopes in tree rings of beech: climatic versus site-related influences, *Trees*, 11, 291–297, <https://doi.org/10.1007/s004680050087>, 1997.
- Saurer, M., Cherubini, P., Reynolds-Henne, C. E., Treydte, K. S., Anderson, W. T., and Siegwolf, R. T. W.: An investigation of the common signal in tree ring stable isotope chronologies at temperate sites, *J. Geophys. Res. Biogeosciences*, 113, 1–11, <https://doi.org/10.1029/2008JG000689>, 2008.
- Saurer, M., Kress, A., Leuenberger, M., Rinne, K. T., Treydte, K. S., and Siegwolf, R. T. W.: Influence of atmospheric circulation patterns on the oxygen isotope ratio of tree rings in the Alpine region, *J. Geophys. Res. Atmospheres*, 117, 1–12, <https://doi.org/10.1029/2011JD016861>, 2012.
- Saurer, M., Spahni, R., Frank, D. C., Joos, F., Leuenberger, M., Loader, N. J., McCarroll, D., Gagen, M., Poulter, B., Siegwolf, R. T. W., Andreu-Hayles, L., Boettger, T., Liñán, I. D., Fairchild, I. J., Friedrich, M., Gutierrez, E., Haupt, M., Hiltunen, E., Heinrich, I., Helle, G., Grudd, H., Jalkanen, R., Levanič, T., Linderholm, H. W., Robertson, I., Sonninen, E., Treydte, K., Waterhouse, J. S., Woodley, E. J., Wynn, P. M., and Young, G. H. F.: Spatial variability and temporal trends in water-use efficiency of European forests, *Glob. Change Biol.*, 20, 3700–3712, <https://doi.org/10.1111/gcb.12717>, 2014.
- Schleser, G. H., Frenzel, B., Stauffer, B., and Weiss, M. M.: Parameters determining carbon isotope ratios in plants, *Probl. Stable Isot. Tree Rings Lake Sediments Peat Bogs Clim. Evid. Holocene*, Paläoklimaforschung 15, 71–95, 1995.
- Schneider, U., Becker, A., Finger, P., Meyer-Christoffer, A., and Ziese, M.: GPCP Full Data Monthly Version 2018.0 at 1.0°: Monthly Land-Surface Precipitation from Rain-Gauges built on GTS-based and Historic Data, [https://doi.org/10.5676/DWD\\_GPCC/FD\\_M\\_V2018\\_100](https://doi.org/10.5676/DWD_GPCC/FD_M_V2018_100), 2018.
- Schollaen, K., Baschek, H., Heinrich, I., Slotta, F., Pauly, M., and Helle, G.: A guideline for sample preparation in modern tree-ring stable isotope research, *Dendrochronologia*, 44, 133–145, <https://doi.org/10.1016/j.dendro.2017.05.002>, 2017.
- Schönwiese, C.-D.: *Klimatologie*, UTB GmbH, Stuttgart, 495 pp., 2013a.
- Schönwiese, C.-D.: *Praktische Statistik für Meteorologen und Geowissenschaftler*, Borntraeger, Berlin, 319 pp., 2013b.

- Schurer, A. P., Hegerl, G. C., Luterbacher, J., Brönnimann, S., Cowan, T., Tett, S. F. B., Zanchettin, D., and Timmreck, C.: Disentangling the causes of the 1816 European year without a summer, *Environ. Res. Lett.*, 14, 1–10, <https://doi.org/10.1088/1748-9326/ab3a10>, 2019.
- Schweingruber, F. H.: *Der Jahrring: Standort, Methodik, Zeit und Klima in der Dendrochronologie*, P. Haupt, Bern, 244 pp., 1983.
- Schweingruber, F. H.: *Tree Rings and Environment Dendroecology*, Paul Haupt, Bern, 626 pp., 1996.
- Seager, R., Hooks, A., Williams, A. P., Cook, B., Nakamura, J., and Henderson, N.: Climatology, Variability, and Trends in the U.S. Vapor Pressure Deficit, an Important Fire-Related Meteorological Quantity, *J. Appl. Meteorol. Climatol.*, 54, 1121–1141, <https://doi.org/10.1175/JAMC-D-14-0321.1>, 2015.
- Seager, R., Osborn, T. J., Kushnir, Y., Simpson, I. R., Nakamura, J., and Liu, H.: Climate Variability and Change of Mediterranean-Type Climates, *J. Clim.*, 32, 2887–2915, <https://doi.org/10.1175/JCLI-D-18-0472.1>, 2019.
- Semmler, T., Danilov, S., Rackow, T., Sidorenko, D., Barbi, D., Hegewald, J., Sein, D., Wang, Q., and Jung, T.: AWI AWI-CM1.1MR model output prepared for CMIP6 CMIP (20200908), <https://doi.org/10.22033/ESGF/CMIP6.359>, 2018.
- Seneviratne, S. I. and Hauser, M.: Regional Climate Sensitivity of Climate Extremes in CMIP6 Versus CMIP5 Multimodel Ensembles, *Earths Future*, 8, 1–12, <https://doi.org/10.1029/2019EF001474>, 2020.
- Sharp, Z.: *Principles of stable isotope geochemistry*, Pearson/Prentice Hall, New Mexico, 368 pp., 2007.
- Siegmund, J. F., Siegmund, N., and Donner, R. V.: CoinCalc—A new R package for quantifying simultaneities of event series, *Comput. Geosci.*, 98, 64–72, <https://doi.org/10.1016/j.cageo.2016.10.004>, 2017.
- Sillmann, J. and Croci-Maspoli, M.: Present and future atmospheric blocking and its impact on European mean and extreme climate, *Geophys. Res. Lett.*, 36, 1–6, <https://doi.org/10.1029/2009GL038259>, 2009.
- Sillmann, J., Thorarinsdottir, T., Keenlyside, N., Schaller, N., Alexander, L. V., Hegerl, G., Seneviratne, S. I., Vautard, R., Zhang, X., and Zwiers, F. W.: Understanding, modeling and predicting weather and climate extremes: Challenges and opportunities, *Weather Clim. Extrem.*, 18, 65–74, <https://doi.org/10.1016/j.wace.2017.10.003>, 2017.
- Simmons, A. J., Willett, K. M., Jones, P. D., Thorne, P. W., and Dee, D. P.: Low-frequency variations in surface atmospheric humidity, temperature, and precipitation: Inferences from reanalyses and monthly gridded observational data sets, *J. Geophys. Res. Atmospheres*, 115, 1–21, <https://doi.org/10.1029/2009JD012442>, 2010.
- Slivinski, L. C., Compo, G. P., Whitaker, J. S., Sardeshmukh, P. D., Giese, B. S., McColl, C., Allan, R., Yin, X., Vose, R., Titchner, H., Kennedy, J., Spencer, L. J., Ashcroft, L., Brönnimann, S., Brunet, M., Camuffo, D., Cornes, R., Cram, T. A., Crouthamel, R., Domínguez-Castro, F., Freeman, J. E., Gergis, J., Hawkins, E., Jones, P. D., Jourdain, S., Kaplan, A., Kubota, H., Blancq, F. L., Lee, T.-C., Lorrey, A., Luterbacher, J., Maugeri, M., Mock, C. J., Moore, G. W. K., Przybylak, R., Pudmenzky, C., Reason, C., Slonosky, V. C., Smith, C. A., Tinz, B., Trewin, B., Valente, M. A., Wang, X. L., Wilkinson, C., Wood, K., and Wyszzyński, P.: Towards a more reliable historical reanalysis: Improvements for version 3 of the Twentieth Century Reanalysis system, *Q. J. R. Meteorol. Soc.*, 145, 2876–2908, <https://doi.org/10.1002/qj.3598>, 2019.
- Sperry, J. S., Hacke, U. G., and Pittermann, J.: Size and function in conifer tracheids and angiosperm vessels, *Am. J. Bot.*, 93, 1490–1500, <https://doi.org/10.3732/ajb.93.10.1490>, 2006.
- Stagge, J. H., Tallaksen, L. M., Gudmundsson, L., Loon, A. F. V., and Stahl, K.: Candidate Distributions for Climatological Drought Indices (SPI and SPEI), *Int. J. Climatol.*, 35, 4027–4040, <https://doi.org/10.1002/joc.4267>, 2015.

- Sternberg, L. and Deniro, M. J.: Isotopic Composition of Cellulose from C3, C4, and CAM Plants Growing Near One Another, *Science*, 220, 947–949, <https://doi.org/10.1126/science.220.4600.947>, 1983.
- Stocker, T.: Introduction to climate modelling, Springer, New York, 179 pp., 2011.
- Stone, M.: Cross-validation and multinomial prediction, *Biometrika*, 61, 509–515, <https://doi.org/10.1093/biomet/61.3.509>, 1974.
- Storch, H. v and Zwiers, F. W.: Statistical analysis in climate research, Cambridge University Press, Cambridge ; New York, 484 pp., 1999.
- Szejner, P., Wright, W. E., Babst, F., Belmecheri, S., Trouet, V., Leavitt, S. W., Ehleringer, J. R., and Monson, R. K.: Latitudinal gradients in tree ring stable carbon and oxygen isotopes reveal differential climate influences of the North American Monsoon System, *J. Geophys. Res. Biogeosciences*, 121, 1978–1991, <https://doi.org/10.1002/2016JG003460>, 2016.
- Tatebe, H. and Watanabe, M.: MIROC MIROC6 model output prepared for CMIP6 CMIP (20201102), <https://doi.org/10.22033/ESGF/CMIP6.881>, 2018.
- Taylor, K. E., Stouffer, R. J., and Meehl, G. A.: An Overview of CMIP5 and the Experiment Design, *Bull. Am. Meteorol. Soc.*, 93, 485–498, <https://doi.org/10.1175/BAMS-D-11-00094.1>, 2012.
- Tebaldi, C. and Knutti, R.: The use of the multi-model ensemble in probabilistic climate projections, *Philos. Trans. R. Soc. Math. Phys. Eng. Sci.*, 365, 2053–2075, <https://doi.org/10.1098/rsta.2007.2076>, 2007.
- Tian, L., Yuan, S., and Quiring, S. M.: Evaluation of six indices for monitoring agricultural drought in the south-central United States, *Agric. For. Meteorol.*, 249, 107–119, <https://doi.org/10.1016/j.agrformet.2017.11.024>, 2018.
- Treydte, K., Schleser, G. H., Helle, G., Frank, D. C., Winiger, M., Haug, G. H., and Esper, J.: The twentieth century was the wettest period in northern Pakistan over the past millennium, *Nature*, 440, 1179–1182, <https://doi.org/10.1038/nature04743>, 2006.
- Treydte, K., Schleser, G. H., Esper, J., Andreu, L., Bednarz, Z., and Berninger, F.: Climate signals in the European isotope network ISONET, TRACE, 5, 138–147, 2007a.
- Treydte, K., Frank, D., Esper, J., Andreu, L., Bednarz, Z., Berninger, F., Boettger, T., D'Alessandro, C. M., Etien, N., Filot, M., Grabner, M., Guillemin, M. T., Gutierrez, E., Haupt, M., Helle, G., Hilasvuori, E., Jungner, H., Kalela-Brundin, M., Krapiec, M., Leuenberger, M., Loader, N. J., Masson-Delmotte, V., Pazdur, A., Pawelczyk, S., Pierre, M., Planells, O., Pukiene, R., Reynolds-Henne, C. E., Rinne, K. T., Saracino, A., Saurer, M., Sonninen, E., Stievenard, M., Switsur, V. R., Szczepanek, M., Szychowska-Krapiec, E., Todaro, L., Waterhouse, J. S., Weigl, M., and Schleser, G. H.: Signal strength and climate calibration of a European tree-ring isotope network, *Geophys. Res. Lett.*, 34, 1–6, <https://doi.org/10.1029/2007GL031106>, 2007b.
- Treydte, K., Boda, S., Graf Pannatier, E., Fonti, P., Frank, D., Ullrich, B., Saurer, M., Siegwolf, R., Battipaglia, G., Werner, W., and Gessler, A.: Seasonal transfer of oxygen isotopes from precipitation and soil to the tree ring: source water versus needle water enrichment, *New Phytol.*, 202, 772–783, <https://doi.org/10.1111/nph.12741>, 2014.
- Trigo, R. M., Vaquero, J. M., Alcoforado, M.-J., Barriendos, M., Taborda, J., García-Herrera, R., and Luterbacher, J.: Iberia in 1816, the year without a summer, *Int. J. Climatol.*, 29, 99–115, <https://doi.org/10.1002/joc.1693>, 2009.
- Trouet, V., Babst, F., and Meko, M.: Recent enhanced high-summer North Atlantic Jet variability emerges from three-century context, *Nat. Commun.*, 9, 1–9, <https://doi.org/10.1038/s41467-017-02699-3>, 2018.

- Trugman, A. T., Medvigy, D., Mankin, J. S., and Anderegg, W. R. L.: Soil Moisture Stress as a Major Driver of Carbon Cycle Uncertainty, *Geophys. Res. Lett.*, 45, 6495–6503, <https://doi.org/10.1029/2018GL078131>, 2018.
- Tyrallis, H., Papacharalampous, G., and Langousis, A.: A Brief Review of Random Forests for Water Scientists and Practitioners and Their Recent History in Water Resources, *Water*, 11, 1–37, <https://doi.org/10.3390/w11050910>, 2019.
- Uppala, S. M., KÅllberg, P. W., Simmons, A. J., Andrae, U., Bechtold, V. D. C., Fiorino, M., Gibson, J. K., Haseler, J., Hernandez, A., Kelly, G. A., Li, X., Onogi, K., Saarinen, S., Sokka, N., Allan, R. P., Andersson, E., Arpe, K., Balmaseda, M. A., Beljaars, A. C. M., Berg, L. V. D., Bidlot, J., Bormann, N., Caires, S., Chevallier, F., Dethof, A., Dragosavac, M., Fisher, M., Fuentes, M., Hagemann, S., Hólm, E., Hoskins, B. J., Isaksen, I., Janssen, P. A. E. M., Jenne, R., McNally, A. P., Mahfouf, J.-F., Morcrette, J.-J., Rayner, N. A., Saunders, R. W., Simon, P., Sterl, A., Trenberth, K. E., Untch, A., Vasiljevic, D., Viterbo, P., and Woollen, J.: The ERA-40 re-analysis, *Q. J. R. Meteorol. Soc.*, 131, 2961–3012, <https://doi.org/10.1256/qj.04.176>, 2005.
- Urry, L. A., Cain, M. L., and Wasserman, S. A.: *Campbell Biology*, 11th ed., Pearson Education, New York, NY, 1488 pp., 2016.
- Vaganov, E. A., Hughes, M. K., Kirilyanov, A. V., Schweingruber, F. H., and Silkin, P. P.: Influence of snowfall and melt timing on tree growth in subarctic Eurasia, *Nature*, 400, 149–151, <https://doi.org/10.1038/22087>, 1999.
- Van Oldenborgh, G. J., Burgers, G., and Tank, A. K.: On the El Niño teleconnection to spring precipitation in Europe, *Int. J. Climatol.*, 20, 565–574, [https://doi.org/10.1002/\(SICI\)1097-0088\(200004\)20:5<565::AID-JOC488>3.0.CO;2-5](https://doi.org/10.1002/(SICI)1097-0088(200004)20:5<565::AID-JOC488>3.0.CO;2-5), 2000.
- Van Oldenborgh, J. and Burgers, G.: Searching for decadal variations in ENSO precipitation teleconnections, *Geophys. Res. Lett.*, 32, 1–5, <https://doi.org/10.1029/2005GL023110>, 2005.
- Vicente-Serrano, S. M., Beguería, S., and López-Moreno, J. I.: A Multiscalar Drought Index Sensitive to Global Warming: The Standardized Precipitation Evapotranspiration Index, *J. Clim.*, 23, 1696–1718, <https://doi.org/10.1175/2009JCLI2909.1>, 2010a.
- Vicente-Serrano, S. M., Beguería, S., López-Moreno, J. I., Angulo, M., and El Kenawy, A.: A New Global 0.5° Gridded Dataset (1901–2006) of a Multiscalar Drought Index: Comparison with Current Drought Index Datasets Based on the Palmer Drought Severity Index, *J. Hydrometeorol.*, 11, 1033–1043, <https://doi.org/10.1175/2010JHM1224.1>, 2010b.
- Vicente-Serrano, S. M., Beguería, S., Lorenzo-Lacruz, J., Camarero, J. J., López-Moreno, J. I., Azorin-Molina, C., Revuelto, J., Morán-Tejeda, E., and Sanchez-Lorenzo, A.: Performance of Drought Indices for Ecological, Agricultural, and Hydrological Applications, *Earth Interact.*, 16, 1–27, <https://doi.org/10.1175/2012EI000434.1>, 2012.
- Vicente-Serrano, S. M., Domínguez-Castro, F., McVicar, T. R., Tomas-Burguera, M., Peña-Gallardo, M., Noguera, I., López-Moreno, J. I., Peña, D., and Kenawy, A. E.: Global characterization of hydrological and meteorological droughts under future climate change: The importance of timescales, vegetation-CO<sub>2</sub> feedbacks and changes to distribution functions, *Int. J. Climatol.*, 40, 2557–2567, <https://doi.org/10.1002/joc.6350>, 2019.
- Vicente-Serrano, S. M., Quiring, S. M., Peña-Gallardo, M., Yuan, S., and Domínguez-Castro, F.: A review of environmental droughts: Increased risk under global warming?, *Earth-Sci. Rev.*, 201, <https://doi.org/10.1016/j.earscirev.2019.102953>, 2020.
- Vitas, A.: Tree-Ring Chronology of Scots Pine (*Pinus sylvestris* L.) for Lithuania, *Balt. For.*, 14, 110–115, 2008.

- Volodin, E., Mortikov, E., Gritsun, A., Lykossov, V., Galin, V., Diansky, N., Gusev, A., Kostykin, S., Iakovlev, N., Shestakova, A., and Emelina, S.: INM INM-CM4-8 model output prepared for CMIP6 CMIP (20200715), <https://doi.org/10.22033/ESGF/CMIP6.1422>, 2019a.
- Volodin, E., Mortikov, E., Gritsun, A., Lykossov, V., Galin, V., Diansky, N., Gusev, A., Kostykin, S., Iakovlev, N., Shestakova, A., and Emelina, S.: INM INM-CM5-0 model output prepared for CMIP6 CMIP (20200715), <https://doi.org/10.22033/ESGF/CMIP6.1423>, 2019b.
- van Vuuren, D. P., Edmonds, J., Kainuma, M., Riahi, K., Thomson, A., Hibbard, K., Hurtt, G. C., Kram, T., Krey, V., Lamarque, J.-F., Masui, T., Meinshausen, M., Nakicenovic, N., Smith, S. J., and Rose, S. K.: The representative concentration pathways: an overview, *Clim. Change*, 109, 5–31, <https://doi.org/10.1007/s10584-011-0148-z>, 2011.
- van Vuuren, D. P., Kriegler, E., O'Neill, B. C., Ebi, K. L., Riahi, K., Carter, T. R., Edmonds, J., Hallegatte, S., Kram, T., Mathur, R., and Winkler, H.: A new scenario framework for Climate Change Research: scenario matrix architecture, *Clim. Change*, 122, 373–386, <https://doi.org/10.1007/s10584-013-0906-1>, 2014.
- Wang, B., Jin, C., and Liu, J.: Understanding Future Change of Global Monsoons Projected by CMIP6 Models, *J. Clim.*, 33, 6471–6489, <https://doi.org/10.1175/JCLI-D-19-0993.1>, 2020.
- Welker, J. M.: Isotopic ( $\delta^{18}\text{O}$ ) characteristics of weekly precipitation collected across the USA: an initial analysis with application to water source studies, *Hydrol. Process.*, 14, 1449–1464, [https://doi.org/10.1002/1099-1085\(20000615\)14:8<1449::AID-HYP993>3.0.CO;2-7](https://doi.org/10.1002/1099-1085(20000615)14:8<1449::AID-HYP993>3.0.CO;2-7), 2000.
- Werner, M., Langebroek, P. M., Carlsen, T., Herold, M., and Lohmann, G.: Stable water isotopes in the ECHAM5 general circulation model: Toward high-resolution isotope modeling on a global scale, *J. Geophys. Res. Atmospheres*, 116, 1–14, <https://doi.org/10.1029/2011JD015681>, 2011.
- Wieners, K.-H., Giorgetta, M., Jungclaus, J., Reick, C., Esch, M., Bittner, M., Legutke, S., Schupfner, M., Wachsmann, F., Gayler, V., Haak, H., de Vrese, P., Raddatz, T., Mauritsen, T., von Storch, J.-S., Behrens, J., Brovkin, V., Claussen, M., Crueger, T., Fast, I., Fiedler, S., Hagemann, S., Hohenegger, C., Jahns, T., Kloster, S., Kinne, S., Lasslop, G., Kornbluh, L., Marotzke, J., Matei, D., Meraner, K., Mikolajewicz, U., Modali, K., Müller, W., Nabel, J., Notz, D., Peters, K., Pincus, R., Pohlmann, H., Pongratz, J., Rast, S., Schmidt, H., Schnur, R., Schulzweida, U., Six, K., Stevens, B., Voigt, A., and Roeckner, E.: MPI-M MPIESM1.2-LR model output prepared for CMIP6 CMIP (20200715), <https://doi.org/10.22033/ESGF/CMIP6.742>, 2019.
- Willett, K. M., Dunn, R. J. H., Thorne, P. W., Bell, S., de Podesta, M., Parker, D. E., Jones, P. D., and Williams Jr., C. N.: HadISDH land surface multi-variable humidity and temperature record for climate monitoring, *Clim. Past*, 10, 1983–2006, <https://doi.org/10.5194/cp-10-1983-2014>, 2014.
- WMO: State of the Global Climate 2021 : WMO Provisional report, WMO, Geneva, 47 pp., 2021.
- Wu, A. and Hsieh, W. W.: The nonlinear Northern Hemisphere winter atmospheric response to ENSO, *Geophys. Res. Lett.*, 31, 1–4, <https://doi.org/10.1029/2003GL018885>, 2004.
- Xoplaki, E., González-Rouco, J., Gyalistras, D., Luterbacher, J., Rickli, R., and Wanner, H.: Interannual summer air temperature variability over Greece and its connection to the large-scale atmospheric circulation and Mediterranean SSTs 1950–1999, *Clim. Dyn.*, 20, 537–554, <https://doi.org/10.1007/s00382-002-0291-3>, 2003a.
- Xoplaki, E., González-Rouco, J. F., Luterbacher, J., and Wanner, H.: Mediterranean summer air temperature variability and its connection to the large-scale atmospheric circulation and SSTs, *Clim. Dyn.*, 20, 723–739, <https://doi.org/10.1007/s00382-003-0304-x>, 2003b.
- Yamada, T. J., Seang, C. N., and Hoshino, T.: Influence of the Long-Term Temperature Trend on the Number of New Records for Annual Maximum Daily Precipitation in Japan, *Atmosphere*, 11, 1–7, <https://doi.org/10.3390/atmos11040371>, 2020.

- Yang, J., Jiang, L., Luo, K., Pan, J., Lemmetyinen, J., Takala, M., and Wu, S.: Snow depth estimation and historical data reconstruction over China based on a random forest machine learning approach, *The Cryosphere*, 14, 1763–1778, <https://doi.org/10.5194/tc-14-1763-2020>, 2020.
- Yuan, W., Zheng, Y., Piao, S., Ciais, P., Lombardozzi, D., Wang, Y., Ryu, Y., Chen, G., Dong, W., Hu, Z., Jain, A. K., Jiang, C., Kato, E., Li, S., Lienert, S., Liu, S., Nabel, J. E. M. S., Qin, Z., Quine, T., Sitch, S., Smith, W. K., Wang, F., Wu, C., Xiao, Z., and Yang, S.: Increased atmospheric vapor pressure deficit reduces global vegetation growth, *Sci. Adv.*, 5, 1–12, <https://doi.org/10.1126/sciadv.aax1396>, 2019.
- Yukimoto, S., Koshiro, T., Kawai, H., Oshima, N., Yoshida, K., Urakawa, S., Tsujino, H., Deushi, M., Tanaka, T., Hosaka, M., Yoshimura, H., Shindo, E., Mizuta, R., Ishii, M., Obata, A., and Adachi, Y.: MRI MRI-ESM2.0 model output prepared for CMIP6 CMIP (20201217), <https://doi.org/10.22033/ESGF/CMIP6.621>, 2019.
- Zhan, Y., Luo, Y., Deng, X., Grieneisen, M. L., Zhang, M., and Di, B.: Spatiotemporal prediction of daily ambient ozone levels across China using random forest for human exposure assessment, *Environ. Pollut.*, 233, 464–473, <https://doi.org/10.1016/j.envpol.2017.10.029>, 2018.
- Zhang, X., Hegerl, G., Seneviratne, S., Steward, R., Zwiers, F., and Alexander, L.: WCRP Grand Challenge Science Underpinning the Prediction and Attribution of Extreme Events, World Climate Research Program, 2014.
- Zhao, C., Liu, B., Piao, S., Wang, X., Lobell, D. B., Huang, Y., Huang, M., Yao, Y., Bassu, S., Ciais, P., Durand, J.-L., Elliott, J., Ewert, F., Janssens, I. A., Li, T., Lin, E., Liu, Q., Martre, P., Müller, C., Peng, S., Peñuelas, J., Ruane, A. C., Wallach, D., Wang, T., Wu, D., Liu, Z., Zhu, Y., Zhu, Z., and Asseng, S.: Temperature increase reduces global yields of major crops in four independent estimates, *Proc. Natl. Acad. Sci.*, 114, 9326–9331, <https://doi.org/10.1073/pnas.1701762114>, 2017.
- Zhao, T. and Dai, A.: The Magnitude and Causes of Global Drought Changes in the Twenty-First Century under a Low–Moderate Emissions Scenario, *J. Clim.*, 28, 4490–4512, <https://doi.org/10.1175/JCLI-D-14-00363.1>, 2015.
- Ziehn, T., Chamberlain, M., Lenton, A., Law, R., Bodman, R., Dix, M., Wang, Y., Dobrohotoff, P., Srbinovsky, J., Stevens, L., Vohralik, P., Mackallah, C., Sullivan, A., O’Farrell, S., and Druken, K.: CSIRO ACCESS-ESM1.5 model output prepared for CMIP6 CMIP (20200715), <https://doi.org/10.22033/ESGF/CMIP6.2288>, 2019.

## APPENDIX A

### 1 RANDOM FOREST RECONSTRUCTION

We use a Random Forest approach (simplified illustration is shown in Supplement 1) to reconstruct VPD at each grid point. RandF is a machine learning method, which was introduced by Breiman (2001). Since RandF encompass a large variety of regression and classification methods, we use the random forest regression known as random-input random forests (Breiman, 2001). This approach is used among others within the publication of Michel et al. (2020) and is performed using a model evaluation and optimization framework by adding hold-out sampling and cross validation techniques to the initial RandF algorithm. In this section, we first detail the general workflow with which a reconstructed timeseries is evaluated within the reconstruction framework. In a second step, we give details on how a RandF model is built and optimized for a given pair of VPD and proxy data. The following subchapters are part of Balting et al. (in preparation).

---

#### 1.1 WORKFLOW FOR THE RECONSTRUCTION AND EVALUATION

We here consider as predictands the observed fields of the climate quantity which we want to reconstruct. In our case, we independently reconstruct each of the observation time series from the VPD fields over the period 1900-1994 as predictand  $Y$  (applied to each grid point of the initial VPD data). The predictors which are needed to reconstruct  $Y$  are the  $\delta^{18}\text{O}_{\text{cel}}$  time series from our  $\delta^{18}\text{O}_{\text{cel}}$  network (denoted  $X_1, \dots, X_{26}$ ). No proxy selection is made prior to the RandF models fittings, since we use a relatively modest number of predictors (26) well geographically constrained to the area of interest (Europe). Nevertheless, it is worth noting that for the RandF-based reconstruction of a given grid point, the RandF method naturally attribute largest weights to  $\delta^{18}\text{O}_{\text{cel}}$  time series with the closest variations with the target VPD time series.

To evaluate the reconstruction of each grid point, the common period of observational data and proxy data is randomly divided (i.e. a bootstrap sample)  $R=30$  times into two distinct groups (i.e. hold-out sampling: Michel et al., 2020). RandF models will then be set up using the first groups of each pair of bootstrap splits (called training or calibration periods), each covering 75% of the data. The remaining 25% of the data for each bootstrap split (called the validation periods) will allow evaluating the quality of the RandF models. The ratio between the validation and the training window is a compromise to have enough years to train the model as well as to calculate meaningful validation statistics. A too small time window for the validation period would make robust statements impossible, as a too short training period may result in the model not being built well due to missing or overlooked data. In other studies, the size of the training period varies between two-thirds and three-quarters of the total test period.

To quantify the RandF model efficiency, the actual values of VPD are compared with the reconstructed VPD over the testing periods, that are given by RandF models trained over the corresponding training periods from the same bootstrap split. In our study, we use the Nash–Sutcliffe model efficiency coefficient (CE; Nash and Sutcliffe, 1970) which is primary used in hydrological modelling and is an adapted version of the common  $R^2$ . The CE is defined as:

$$CE=1-\frac{\sum_{t=1}^T (Q_m^t - Q_o^t)^2}{\sum_{t=1}^T (Q_o^t - \overline{Q_o})^2} \quad (A-1)$$

where  $\overline{Q_o}$  is the average of the observed VPD,  $Q_o^t$  is the RandF modelled VPD and  $Q_o^t$  is the observed VPD at time  $t$ .

It represents the following cases which are presented in the publication (Nash and Sutcliffe, 1970). If  $CE=1$ , the RandF model fits perfectly which is characterized by an error variance equal to zero; if  $CE=0$ , it indicates that the RandF model has the same predictive skill as the mean of the time-series in terms of the sum of the squared error; if  $CE<0$ , it indicates that the observed mean is a better predictor than the model. Therefore, a  $CE=1$  suggest a model with more predictive skill it is useful and meaningful to use. In our study, the hypothesis, if CE is significantly greater than 0 at the 95% confidence level, is tested with a one sided t-test.

The final gridded reconstruction is obtained by reapplying the RandF model over the whole period 1900-1994 for a given window (nest), and its final score is obtained as the averaged CE scores over the 30 training/testing splits. In our study, a given grid point will be considered as robustly reconstructed if its CE scores over the 30 training/testing splits are significantly greater than 0 at the 95% confidence, based on a one sided Student t-test.

---

## 1.2 REGRESSION TREE AND RANDOM FOREST

For all RandF models either based on training samples or complete timeseries over the historical period, we here denote  $Y$  the VPD time series for a given grid point,  $X=(X_j)_{1 \leq j \leq p}$  are the  $p$  proxy records over the same period than  $Y$  (either a training period or the full 1900-1994 period), and  $X'=(X'_j)_{1 \leq j \leq p}$  are the same  $p$  proxy records, but for the period over which  $Y$  is reconstructed (either a testing period or a period prior to 1900).

The RandF is an aggregate of the outputs given by different regression trees (Supplement 1), which are based on randomly drawn subsample of the initial  $p$  predictors. To build a single regression tree the  $X$  and  $Y$  data are gathered at the root of the tree as an initial node. This node is then cut into two child nodes. Any cut can be written as:

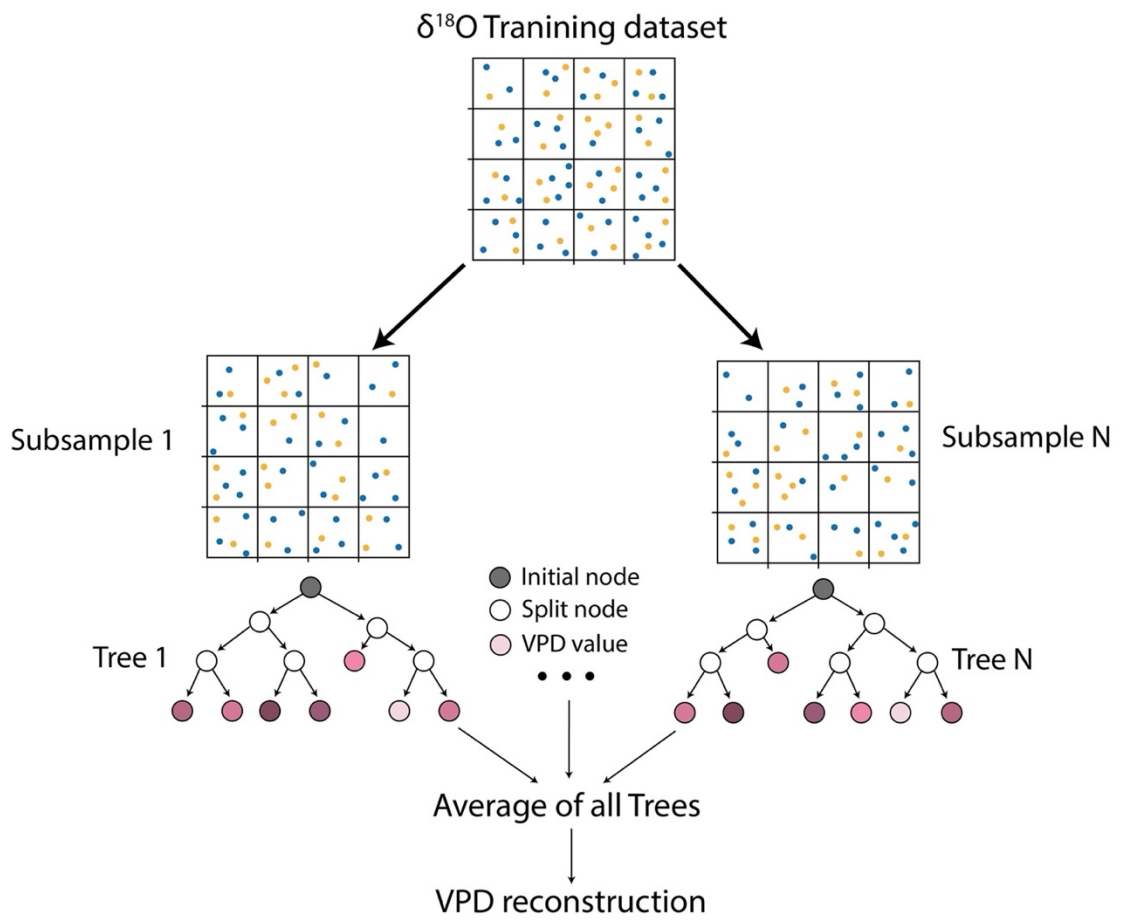
$$\{X^j \leq d\} \cup \{X^j \geq d\} \quad (A-2)$$

where  $j = \{1, \dots, p\}$  is the proxy (variable) index and  $d \in \mathbb{R}$  is the value of the cut. As a consequence, all observations with a  $j^{\text{th}}$  variable greater than  $d$  are placed in one child node and all observations with a  $j^{\text{th}}$  variable lesser than  $d$  are placed in another child node. The optimal  $(j,d)$  pair is determined by minimizing the sum of the intra-nodes variance of  $Y$  within the two the child nodes (Michel et al., 2020). Therefore,  $(j,d)$  is found by minimizing the following convex problem:

$$(j,d) = \arg \min_{\substack{d \in \mathbb{R} \\ 1 \leq j \leq p}} \sum_{i: X_j^i < d} \left( Y_i - \frac{\sum_{i: X_j^i < d} Y_i}{\#\{i: X_j^i < d\}} \right)^2 + \sum_{i: X_j^i > d} \left( Y_i - \frac{\sum_{i: X_j^i > d} Y_i}{\#\{i: X_j^i > d\}} \right)^2 \quad (\text{A-3})$$

Where  $p$  is the number of proxy records used which varies with the inferior boundary of the nested time frame (section 2.1),  $X_j^i$  denotes the  $i^{\text{th}}$  value of the  $j^{\text{th}}$  proxy, and  $\#$  is the cardinal operator. We then recursively apply the same procedure to the next child nodes with the same variables until one node contains less than  $s=5$  observations. Based on this method, a decision or regression tree is created. Hence, the RandF model is obtained by building a number of  $N$  such trees, but each are based on  $m$  randomly picked variables from the  $p$  initial ones, with  $m < p$ . The proxy records values over the reconstruction period of interest (i.e.  $X^*$ ) are then used to browse each of the RandF trees according to the cuts previously made during the model fitting. The RandF reconstruction is then given as the average of the outputs given by the  $N$  trees.

It is worth noting that there are inherent parameters to the RandF method (i.e. control parameters). These parameters are the number of randomly used proxies in each tree ( $m$ ), the number of trees ( $N$ ) and the amount of data required in a node to stop the construction of regression trees ( $s$ ). The optimization of three parameters is very consuming in terms of time and energy, but a very large advantage of the RandF method is that it only needs one to be effectively optimized (Breiman, 2001; Oshiro et al., 2012). Indeed, for a large suite of simulated datasets, Oshiro et al. (2012) have shown that using more than  $N=128$  trees have a very low likelihood to gain in robustness, which they then recommended to use whatever the source of modelled data. In the same way, Breiman (2001) has shown that  $s=5$  always give very satisfying results, while the gain of robustness by its optimisation does not worth the time it takes to. Therefore, we here further optimise  $m$ , for each RandF model built in this study. To estimate the optimal  $m$  for each of the RandF models, we use the  $K$ -fold cross-validation approach (Stone, 1974; Geisser, 1975) with  $K=5$  similarly to Michel et al. (2020). It consists in building RandF models for every possible value of  $m$  ( $0 < m < p$ ,  $m \in \mathbb{N}$ ) over 5 further training/testing samples determined with each of the  $K$  folds being used as the testing sample (see Michel et al. 2020 for more details on the cross validation procedure). The resulting optimised RandF model is then applied to the entire data of  $X$  and  $Y$ .

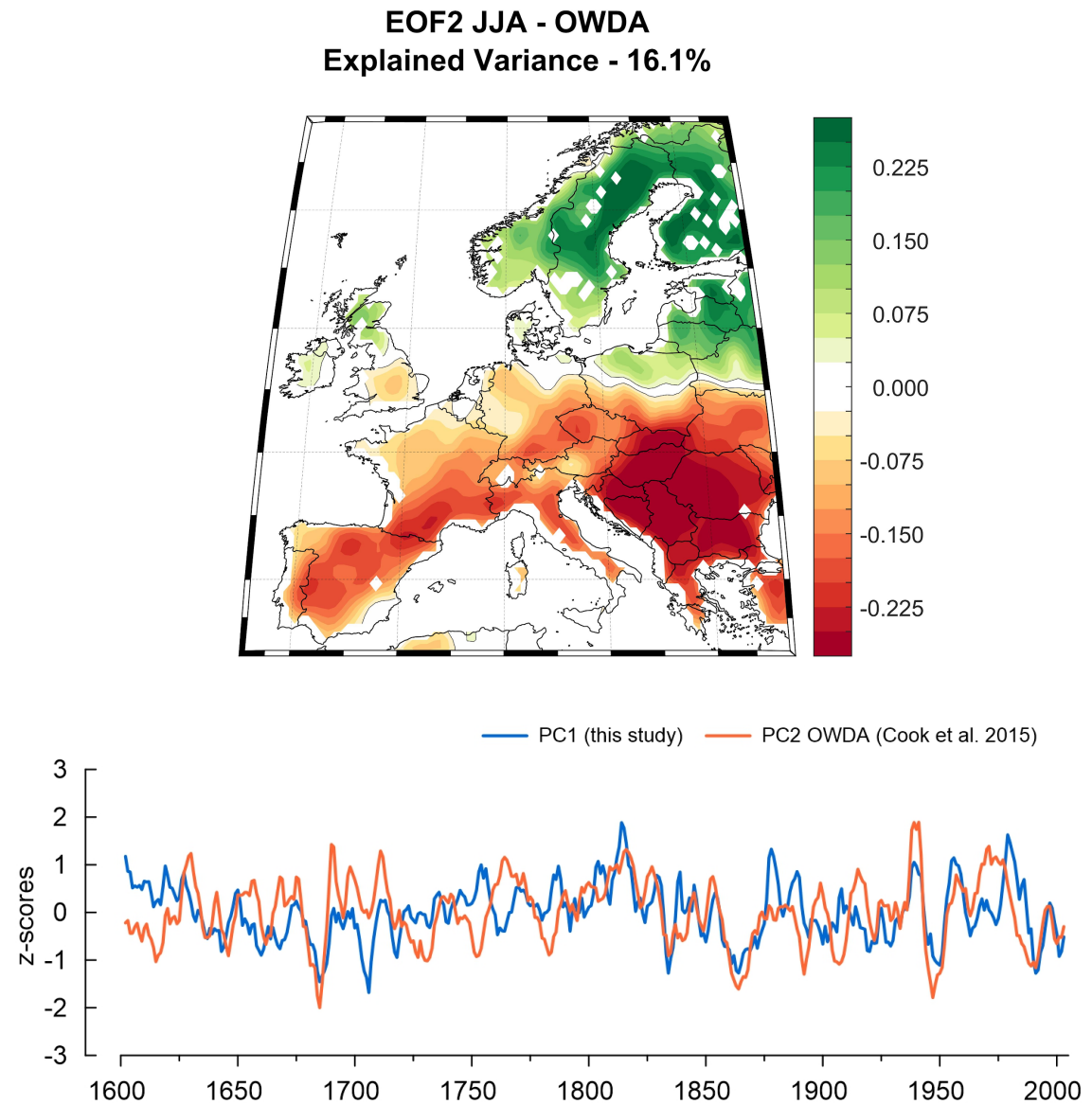


Supplement 1: Simplified illustration of the RandF approach for our VPD reconstruction.

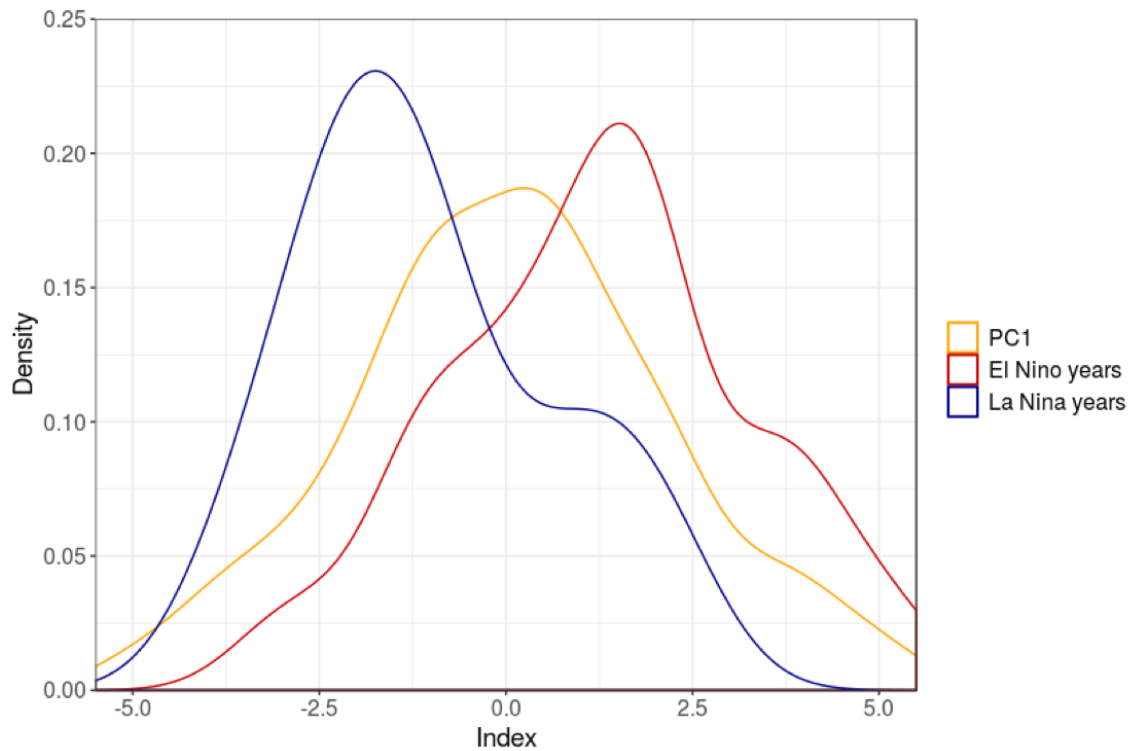
## APPENDIX B

Location	Country	Species	First year	Last year	Lon.	Lat.	Altitude
Cazorla	Spain	<i>Pinus nigra</i>	1600	2002	-2.57°	37.53°	1820 m
Cavergno	Switzerland	<i>Quercus petraea</i>	1637	2002	8.36°	46.21°	900 m
Col Du Zad	Morocco	<i>Cedrus atlantica</i>	2200 m	32.59°	-5.14°	1600	2000
Fontainebleau	France	<i>Quercus petraea</i>	1600	2000	2.67°	48.38°	100 m
Gutuli	Norway	<i>Pinus sylvestris</i>	1600	2003	12.18°	62.00°	800 m
Inari	Finland	<i>Pinus sylvestris</i>	1600	2002	28.42°	68.93°	150 m
Isibeli	Turkey	<i>Juniper excelsa</i>	1850	2005	30.45°	37.06°	1800 m
Lainzer Tiergarten	Austria	<i>Quercus petraea</i>	1600	2003	16.20°	48.18°	300 m
Lochwood	United Kingdom	<i>Quercus petraea</i>	1749	2003	-3.43°	55.27°	175 m
Monte Pollino	Italy	<i>Pinus leucodermis</i>	1604	2003	16.16°	39.58°	1900 m
Mount Vichren	Bulgaria	<i>Pinus heldreichii</i>	1800	2005	23.24°	41.46°	1900 m
Naklo	Slovenia	<i>Larix decidua</i>	1600	2005	14.30°	46.30°	440 m
Niepolomice	Poland	<i>Quercus robur</i> & <i>Pinus sylvestris</i>	1627	2003	20.38°	50.12°	190 m
Nusfalau	Romania	<i>Quercus robur</i>	1900	2016	22.66°	47.19°	270 m
Panemunės	Lithuania	<i>Pinus sylvestris</i>	1816	2002	23.97°	54.88°	45 m
Pedraforca	Spain	<i>Pinus uncinata</i>	1600	2003	1.42°	42.13°	2120 m
Pinar de Lillo	Spain	<i>Pinus sylvestris</i>	1600	2002	-5.34°	42.57°	1600 m
Plieningen	Germany	<i>Quercus petraea</i>	1822	1999	9.13°	48.42°	340 m
Poellau	Austria	<i>Pinus nigra</i>	1600	2002	16.06°	47.95°	500 m
Rennes	France	<i>Quercus robur</i>	1751	1998	-1.7°	48.25°	100 m
Sivakkovaara	Finland	<i>Pinus sylvestris</i>	1600	2002	30.98°	62.98°	200 m
Suwalki	Poland	<i>Pinus sylvestris</i>	1600	2004	22.93°	54.10°	160 m
Vigera	Switzerland	<i>Pinus sylvestris</i>	1675	2003	8.77°	46.50°	1400 m
Vinuesa	Spain	<i>Pinus uncinata</i>	1850	2002	2.45°	42.00°	720 m
Woburn	United Kingdom	<i>Pinus sylvestris</i>	1604	2003	-0.59°	51.98°	10 m

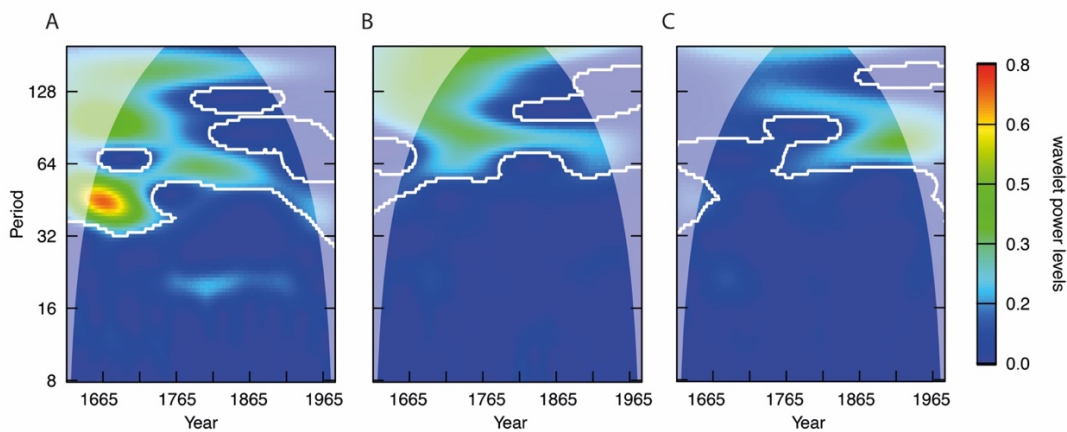
**Supplement 2: The characteristics of each sample site which is used within our study. 22 of the 26  $\delta^{18}\text{O}_{\text{cell}}$  records were created within the EU project ISONET (Treydte et al., 2007a, b) and four additional sites from Bulgaria, Turkey, Southwest Germany and Slovenia were added (Hafner et al., 2014; Heinrich et al., 2013).**



Supplement 3: Upper panel: The second EOF of the OWDA (Cook et al., 2015) for JJA (explaining 16.1% of the variance). Lower panel: The associated PC2 of the OWDA for JJA and PC1 of our study. The correlation between the two time series is  $R=0.39$  ( $p\text{-value}=4.2e-16$ ).



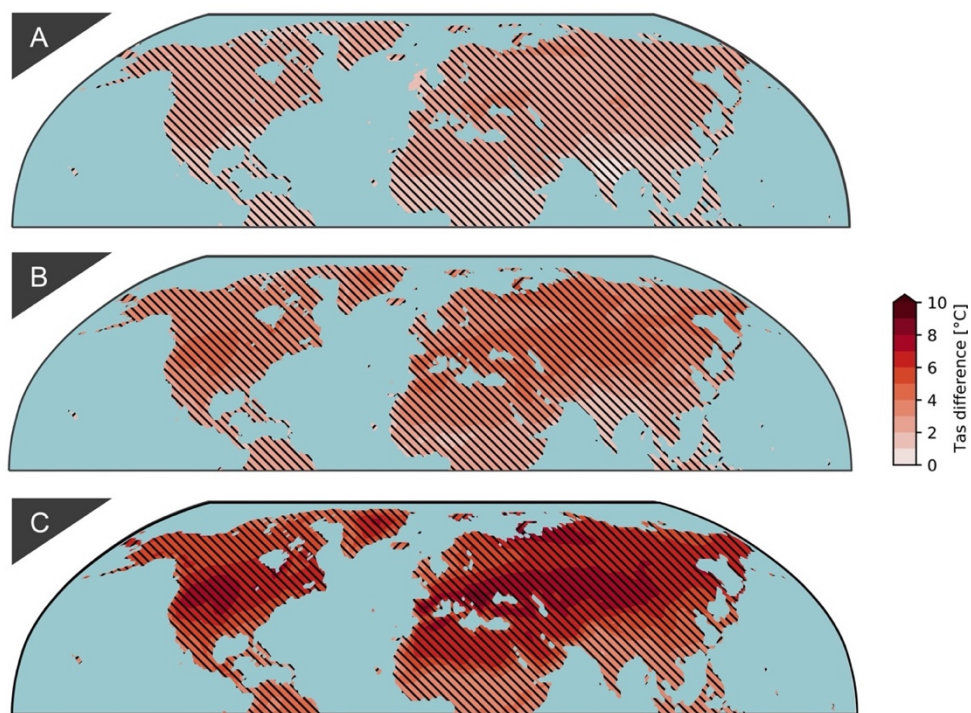
Supplement 4: The probability density function of PC1 with two additional functions for El Niño and La Niña years. The El Niño and La Niña years have been extracted out of a Niño 3.4 DJF index (HadISST1; Rayner et al., 2003) for the period from 1870 to 2000.



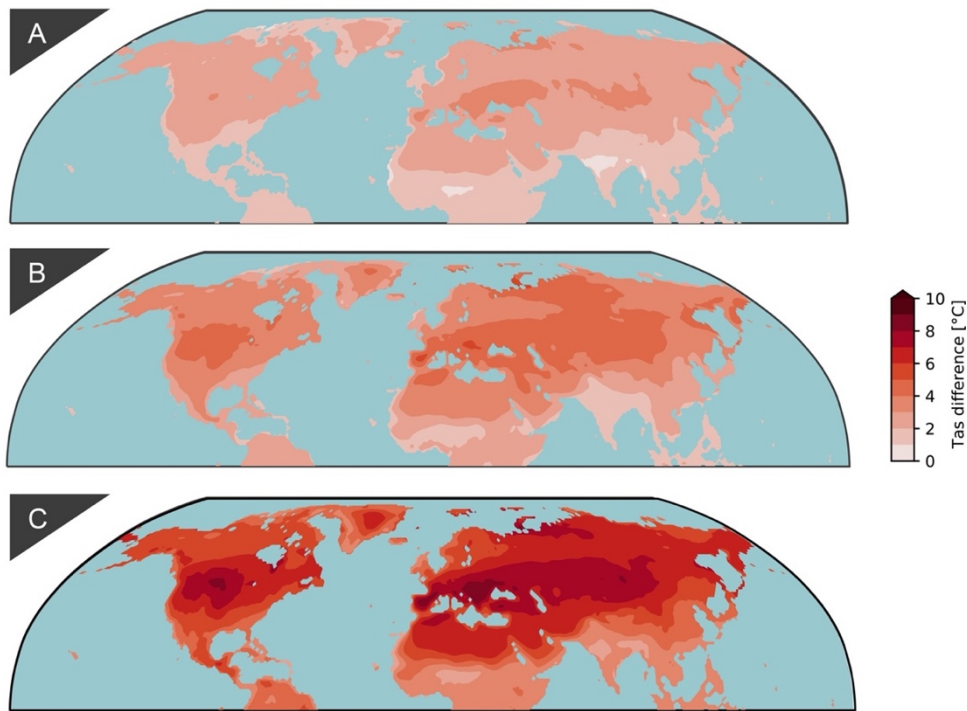
Supplement 5: Investigation of the different spectra of the rolling mean time series of the three reconstructed areas. A, North Europe, B, Central Europe and C, Mediterranean region. The white contour lines indicate significant frequencies ( $p < 0.01$ ). All the plots are done with the WaveletComp package in R (Rosch and Schmidbauer, 2018).

Number of used realizations	Historical	SSP1-2.6	SSP2-4.5	SSP5-8.5	References
ACCESS-CM2	1	1	1	1	(Dix et al., 2019)
ACCESS-ESM1-5	1	1	1	1	(Ziehn et al., 2019)
EC-Earth3	1	1	1	1	(EC-Earth Consortium, 2019a)
EC-Earth3-Veg	1	1	1	1	(EC-Earth Consortium, 2019b)
EC-Earth3-Veg-LR	1	1	1	1	(EC-Earth Consortium, 2020)
GFDL-ESM4	1	1	1	1	(Krasting et al., 2018)
INM-CM4-8	1	1	1	1	(Volodin et al., 2019a)
INM-CM5-0	1	1	1	1	(Volodin et al., 2019b)
MIROC6	1	1	1	1	(Tatebe and Watanabe, 2018)
MPI-ESM1-2-HR	1	1	1	1	(Jungclaus et al., 2019)
MPI-ESM1-2-LR	1	1	1	1	(Wieners et al., 2019)
MRI-ESM2-0	1	1	1	1	(Yukimoto et al., 2019)

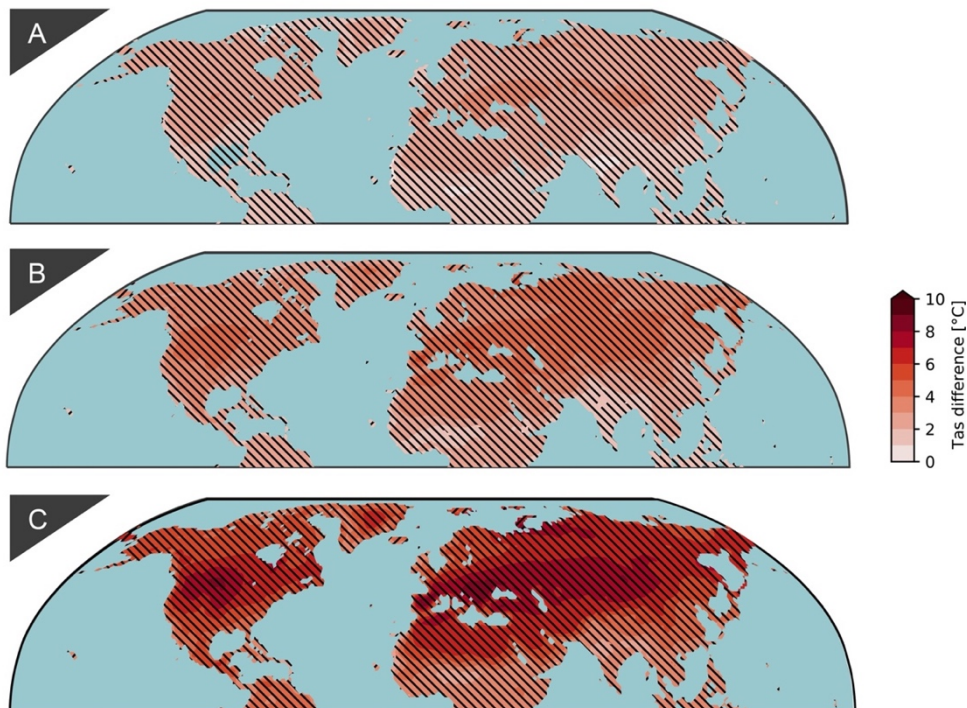
Supplement 6: Description of the used climate model ensemble for the historical run and three future scenarios. In the entire analysis, the first realization (r1i1p1f1) has been used.



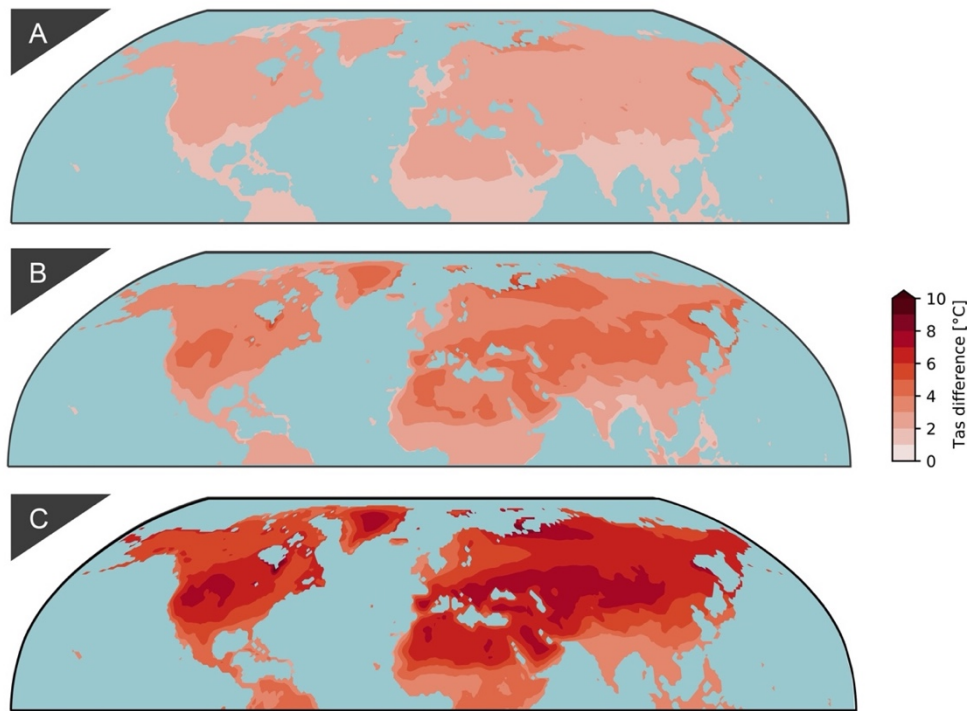
Supplement 7: A-C Averaged anomalies of summer temperature under SSP1-2.6 (A) and SSP2-4.5 (B) and SSP5-8.5 (C) in the Northern Hemisphere for the period 2071-2100 relative to the baseline period of 1971-2000. The hatched areas indicate areas where at least 10 of the 12 used models show the same sign of change.



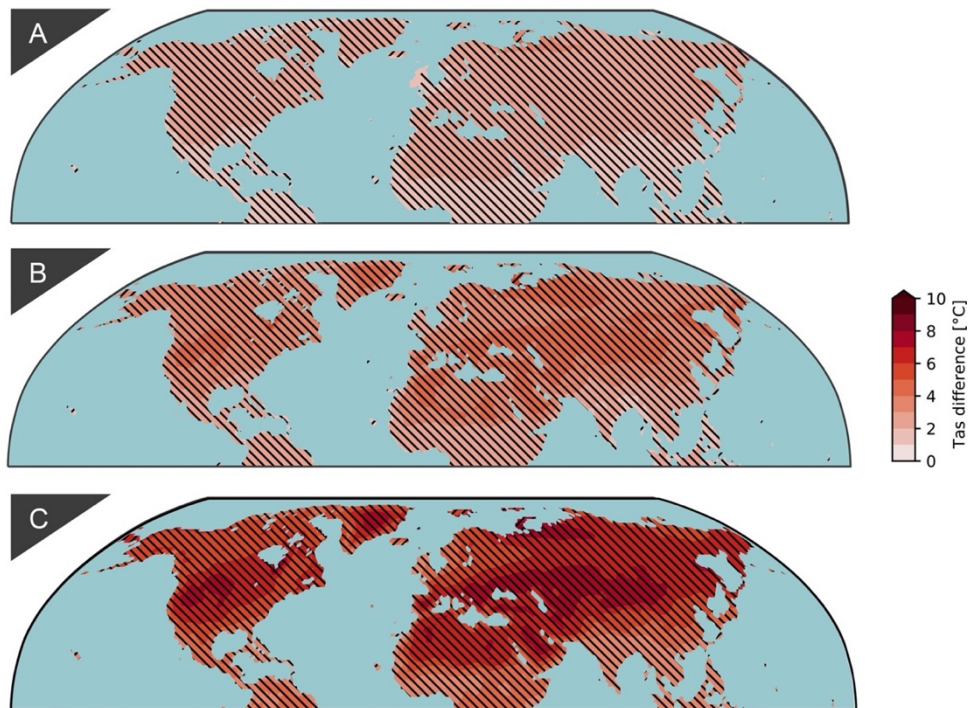
Supplement 8: A-C Averaged anomalies of summer maximum temperature under SSP1-2.6 (A) and SSP2-4.5 (B) and SSP5-8.5 (C) in the Northern Hemisphere for the period 2071-2100 relative to the base-line period of 1971-2000. Furthermore, the presented changes in all three subfigures are significant according to the two-sided Student's t test ( $p < 0.05$ ).



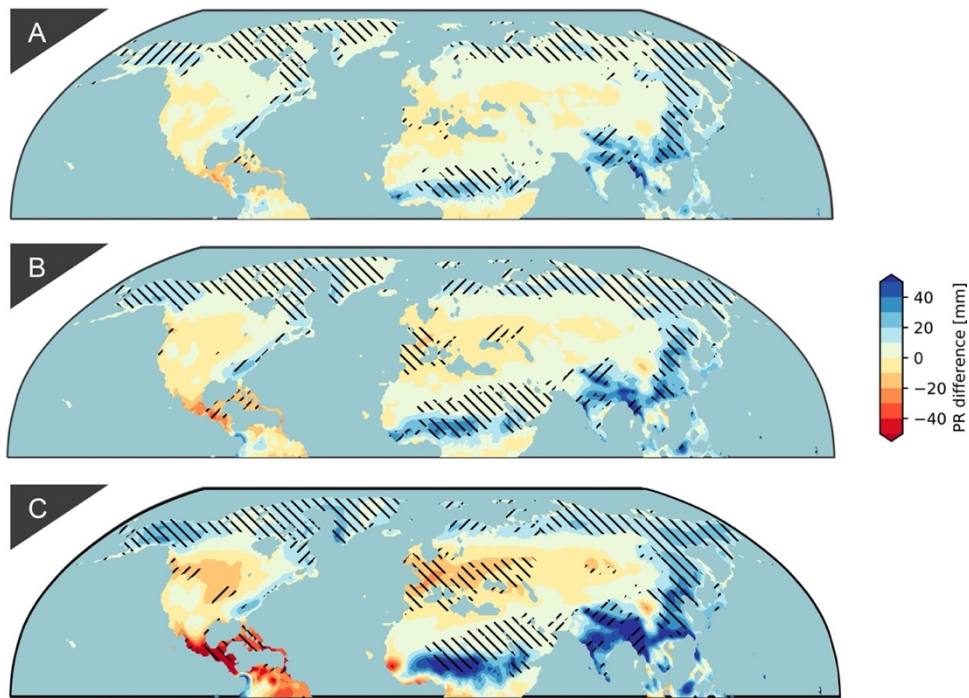
Supplement 9: A-C Averaged anomalies of summer maximum temperature under SSP1-2.6 (A) and SSP2-4.5 (B) and SSP5-8.5 (C) in the Northern Hemisphere for the period 2071-2100 relative to the baseline period of 1971-2000. The hatched areas indicate areas where at least 10 of the 12 used models show the same sign of change.



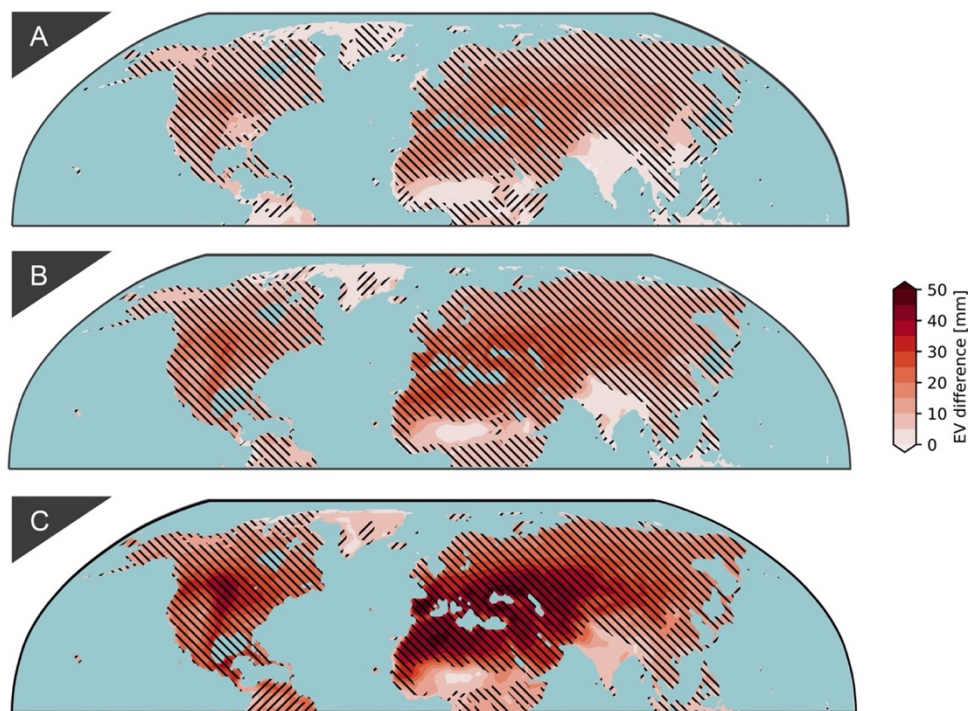
Supplement 10: A-C Averaged anomalies of summer minimum temperature under SSP1-2.6 (A) and SSP2-4.5 (B) and SSP5-8.5 (C) in the Northern Hemisphere for the period 2071-2100 relative to the baseline period of 1971-2000. Furthermore, the presented changes in all three subfigures are significant according to the two-sided Student's t test ( $p < 0.05$ ).



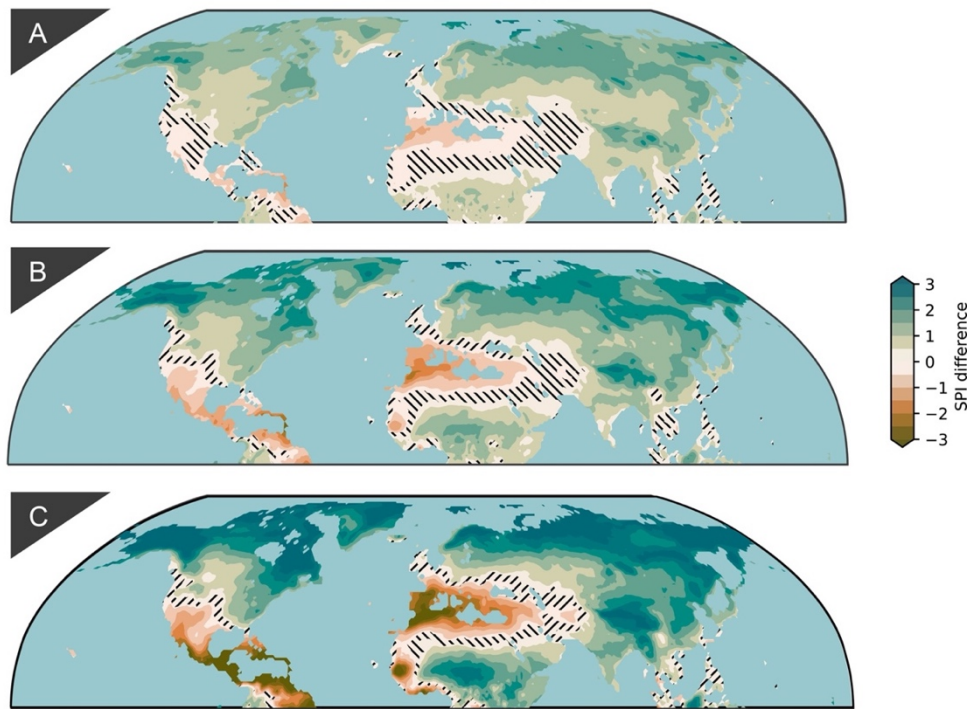
Supplement 11: A-C Averaged anomalies of summer minimum temperature under SSP1-2.6 (A) and SSP2-4.5 (B) and SSP5-8.5 (C) in the Northern Hemisphere for the period 2071-2100 relative to the baseline period of 1971-2000. The hatched areas indicate areas where at least 10 of the 12 used models show the same sign of change.



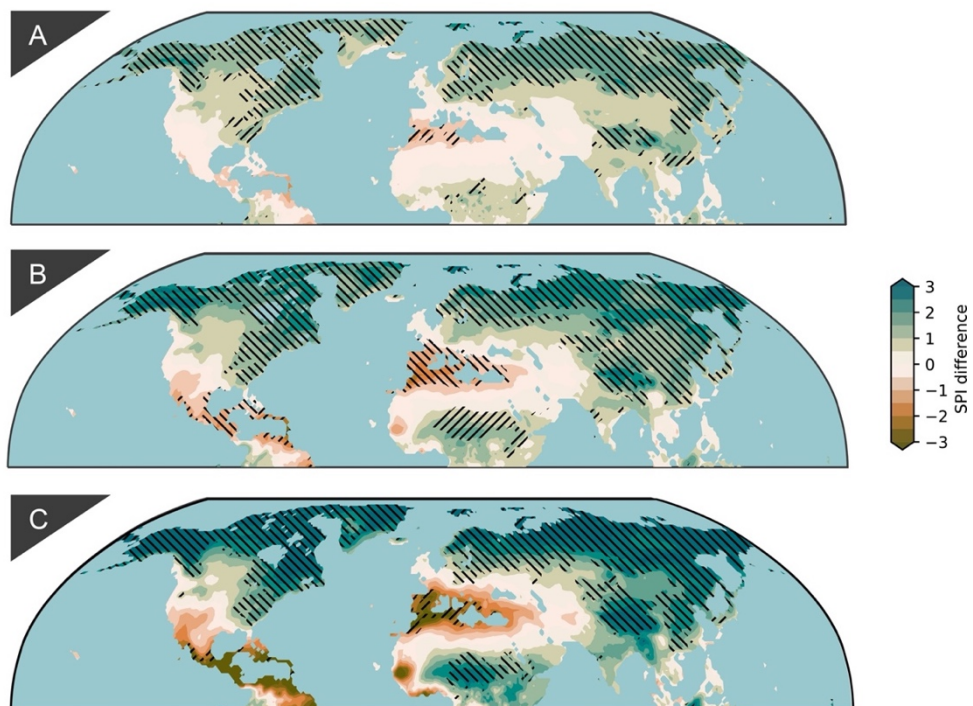
Supplement 12: A-C Averaged anomalies of summer precipitation under SSP1-2.6 (A) and SSP2-4.5 (B) and SSP5-8.5 (C) in the Northern Hemisphere for the period 2071-2100 relative to the baseline period of 1971–2000. The hatched areas indicate areas where at least 10 of the 12 used models show the same sign of change.



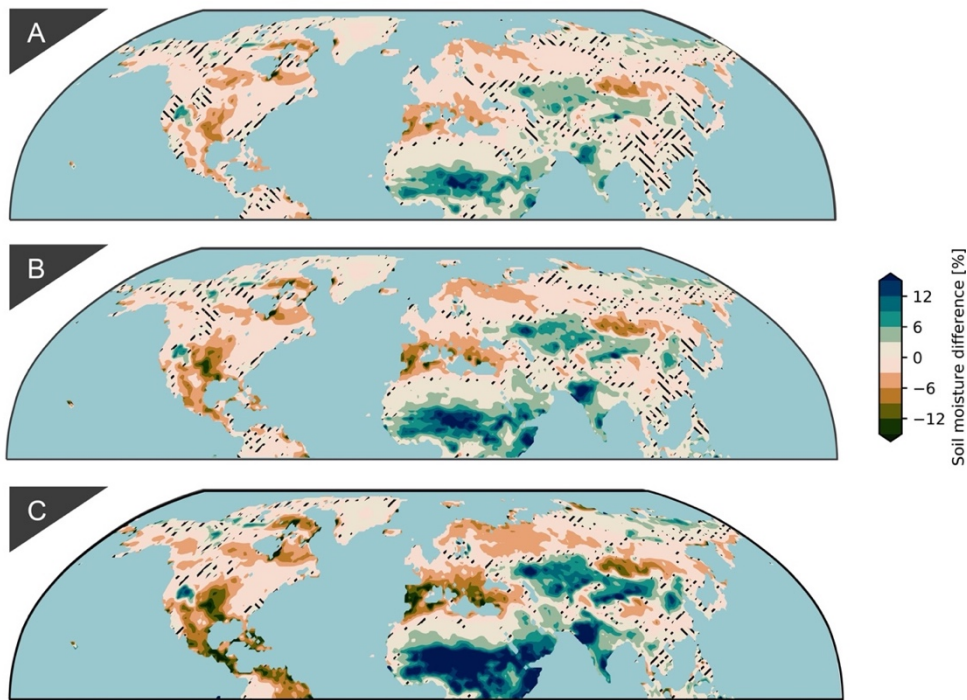
Supplement 13: A-C Averaged anomalies of summer potential evapotranspiration under SSP1-2.6 (A) and SSP2-4.5 (B) and SSP5-8.5 (C) in the Northern Hemisphere for the period 2071-2100 relative to the baseline period of 1971–2000. The hatched areas indicate areas where at least 10 of the 12 used models show the same sign of change.



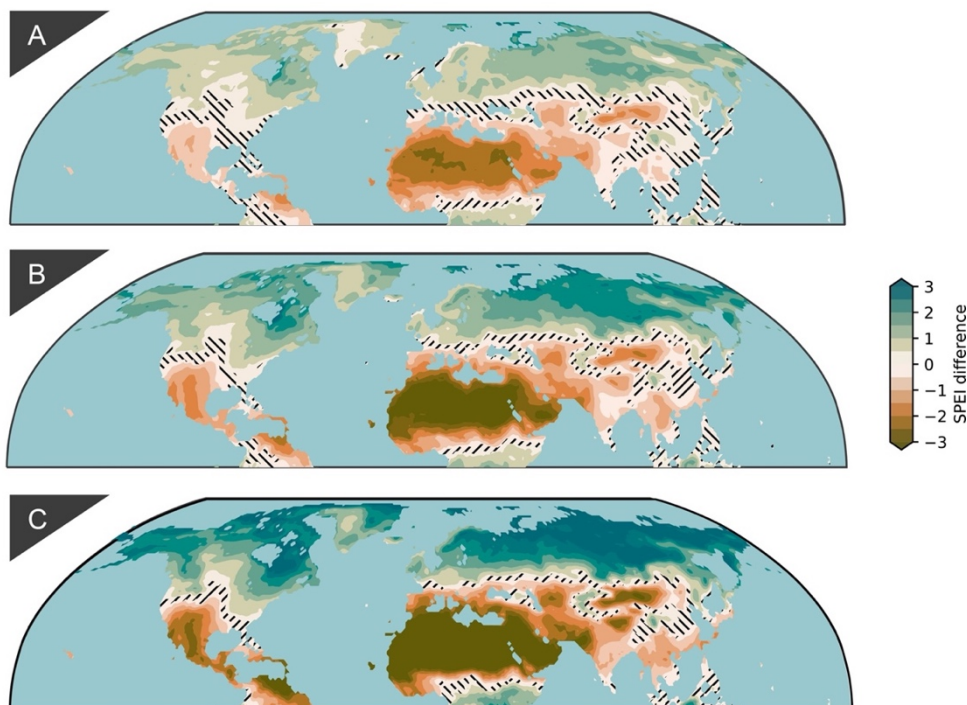
Supplement 14: A-C Averaged anomalies of summer SPI6 under SSP1-2.6 (A) and SSP2-4.5 (B) and SSP5-8.5 (C) in the Northern Hemisphere for the period 2071-2100 relative to the baseline period of 1971-2000. The SPI6 is calibrated from 1971 to 2000. The hatched areas indicate areas with insignificant changes according to the two-sided Student's *t* test ( $p < 0.05$ ).



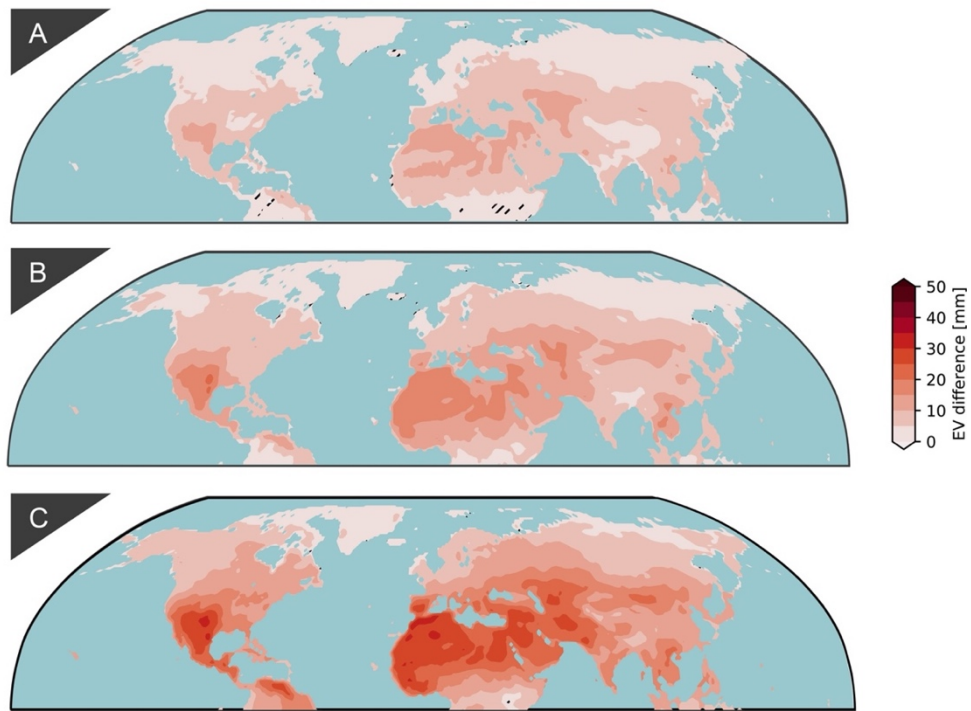
Supplement 15: A-C Averaged anomalies of summer SPI6 under SSP1-2.6 (A) and SSP2-4.5 (B) and SSP5-8.5 (C) in the Northern Hemisphere for the period 2071-2100 relative to the base-line period of 1971-2000. The SPI6 is calibrated from 1971 to 2000. The hatched areas indicate areas where at least 10 of the 12 used models show the same sign of change.



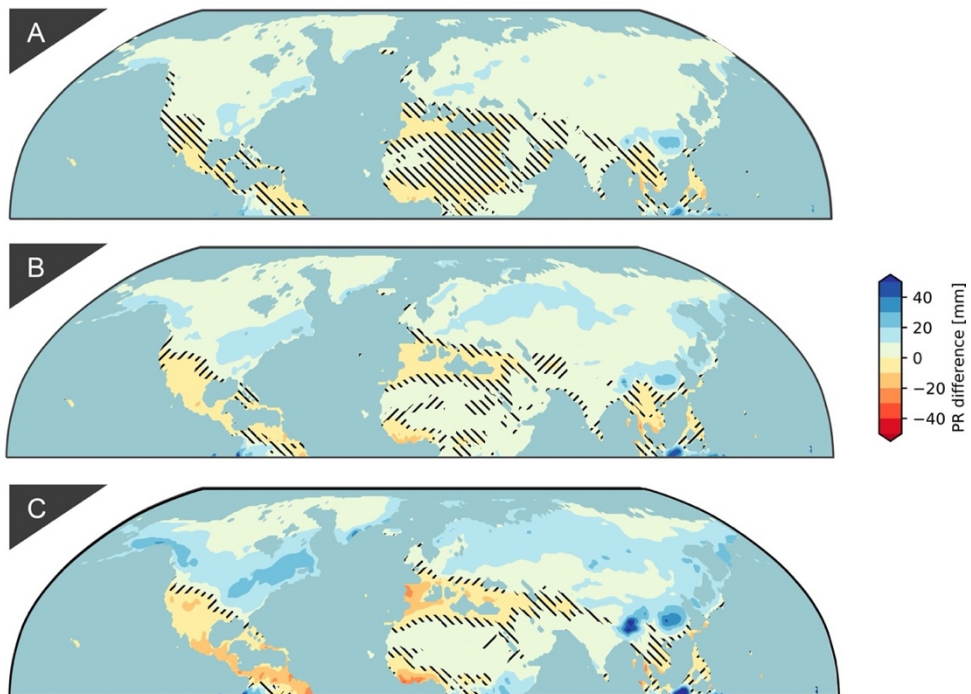
Supplement 16: A-C Averaged anomalies of summer soil moisture under SSP1-2.6 (A) and SSP2-4.5 (B) and SSP5-8.5 (C) in the Northern Hemisphere for the period 2071-2100 relative to the baseline period of 1971-2000. The hatched areas indicate areas with insignificant changes according to the two-sided Student's  $t$  test ( $p < 0.05$ ) (data from AWI-CM-1-1-MR model is not used in this figure because the required variables are not provided).



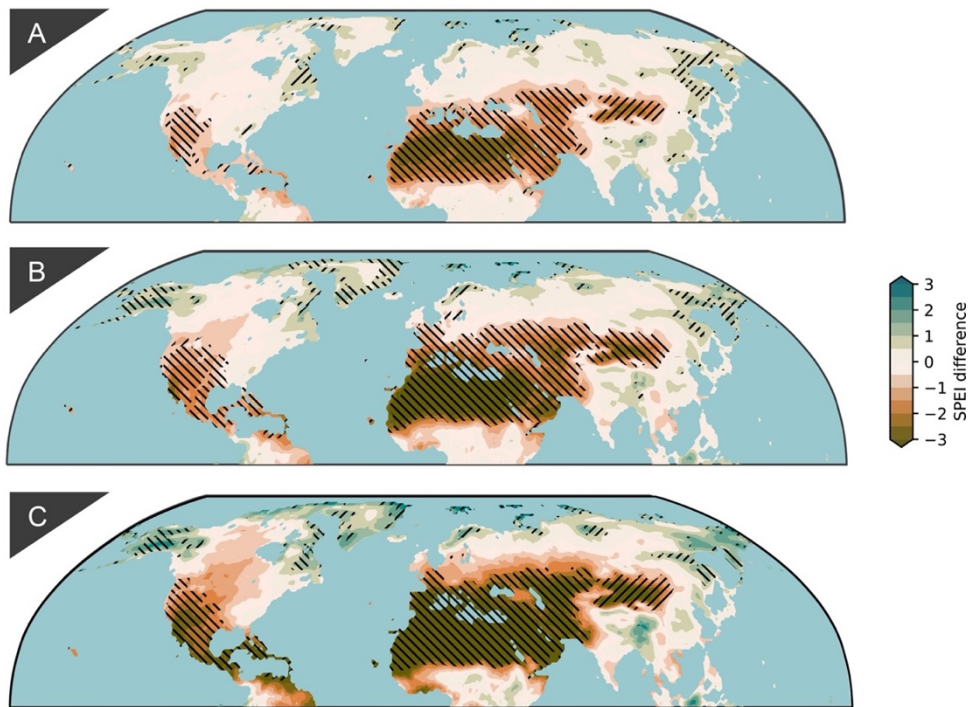
Supplement 17: A-C Averaged anomalies of spring droughts under SSP1-2.6 (A) and SSP2-4.5 (B) and SSP5-8.5 (C) in the Northern Hemisphere for the period 2071-2100 relative to the baseline period of 1971-2000. The hatched areas in all three subfigures indicate areas with insignificant changes according to the two-sided Student's  $t$  test ( $p < 0.05$ ).



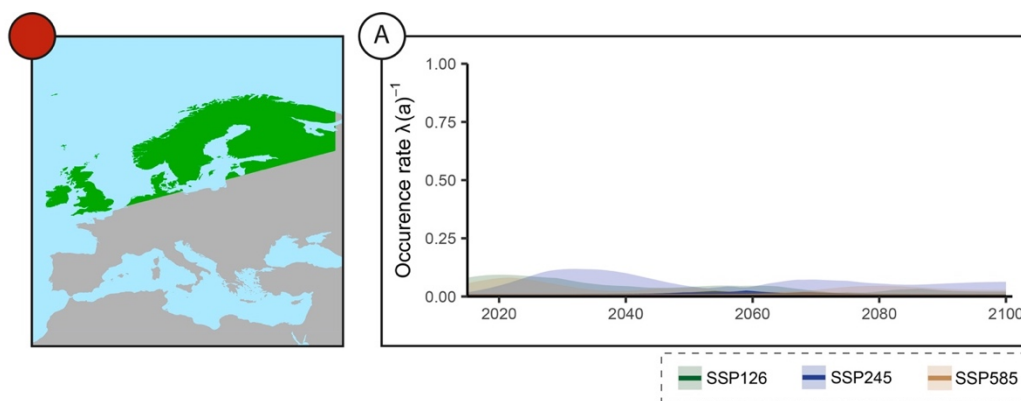
Supplement 18: A-C Averaged anomalies of spring potential evapotranspiration under SSP1-2.6 (A) and SSP2-4.5 (B) and SSP5-8.5 (C) in the Northern Hemisphere for the period 2071-2100 relative to the baseline period of 1971-2000. The hatched areas in all three subfigures indicate areas with insignificant changes according to the two-sided Student's *t* test ( $p < 0.05$ ).



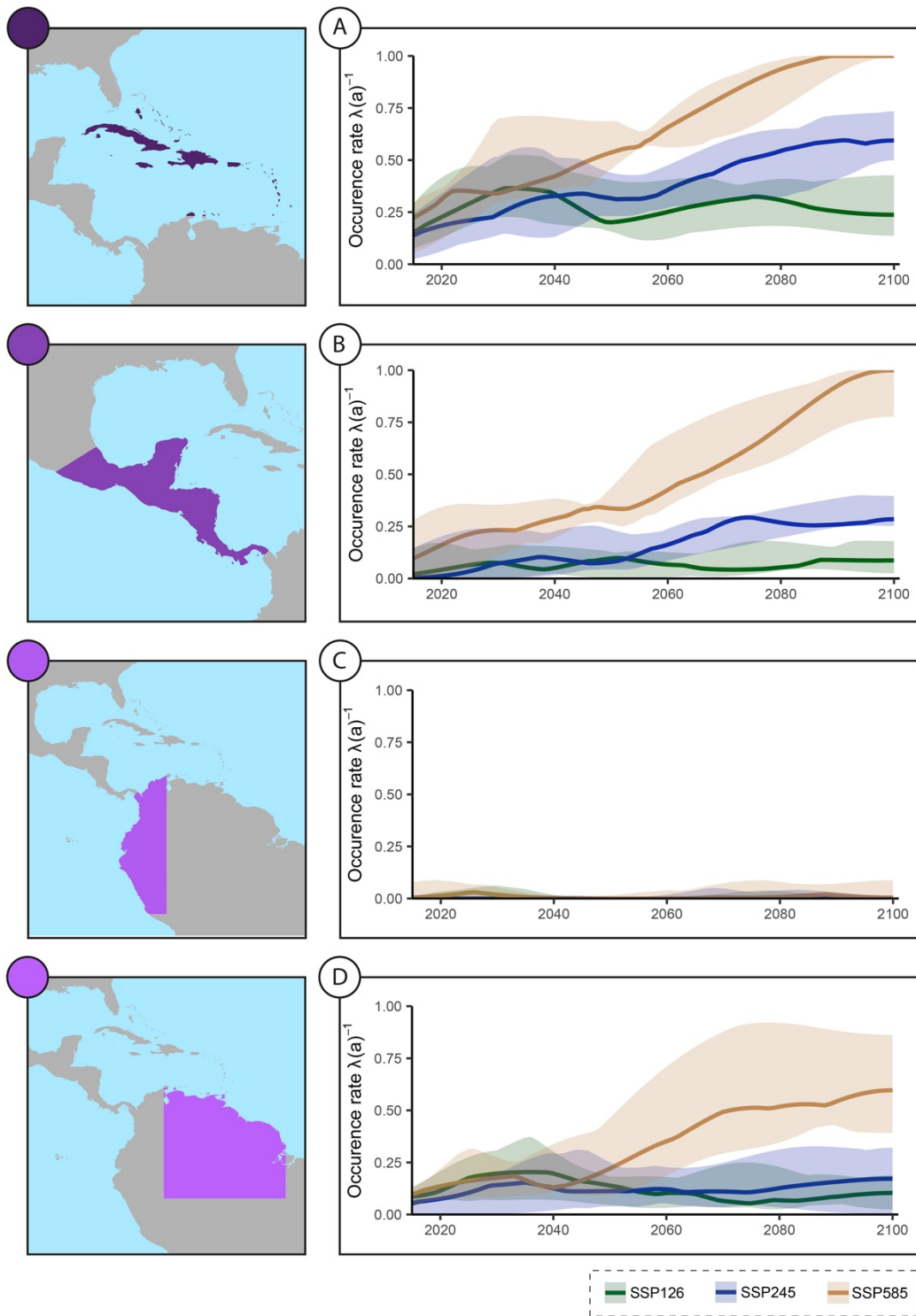
Supplement 19: A-C Averaged anomalies of spring precipitation under SSP1-2.6 (A) and SSP2-4.5 (B) and SSP5-8.5 (C) in the Northern Hemisphere for the period 2071-2100 relative to the baseline period of 1971-2000. The hatched areas in all three subfigures indicate areas with insignificant changes according to the two-sided Student's *t* test ( $p < 0.05$ ).



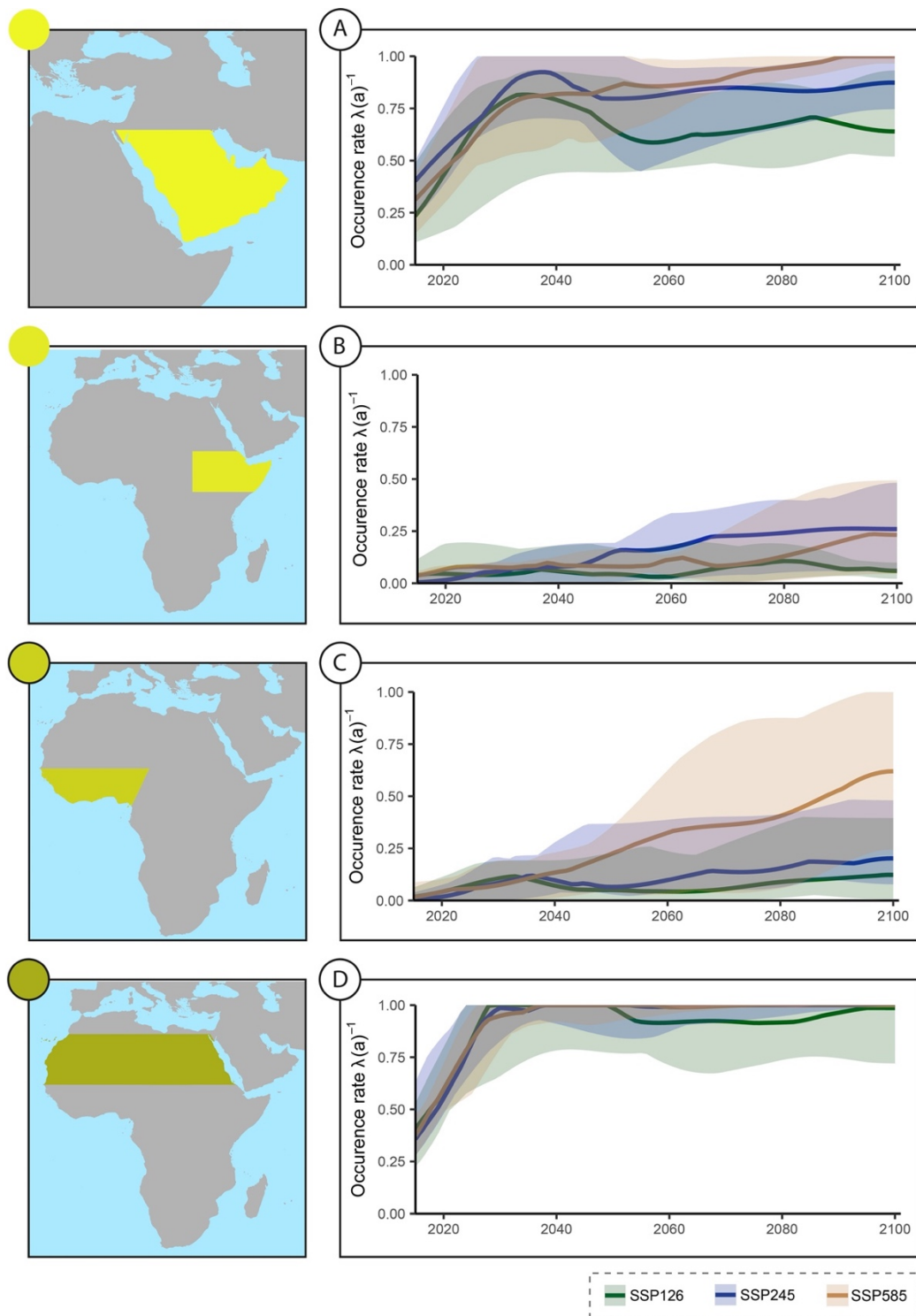
Supplement 20: A-C Averaged anomalies of summer droughts under SSP1-2.6 (A) and SSP2-4.5 (B) and SSP5-8.5 (C) in the Northern Hemisphere for the period 2071-2100 relative to the baseline period of 1971–2000. The hatched areas indicate areas where at least 10 of the 12 used models show the same sign of change.



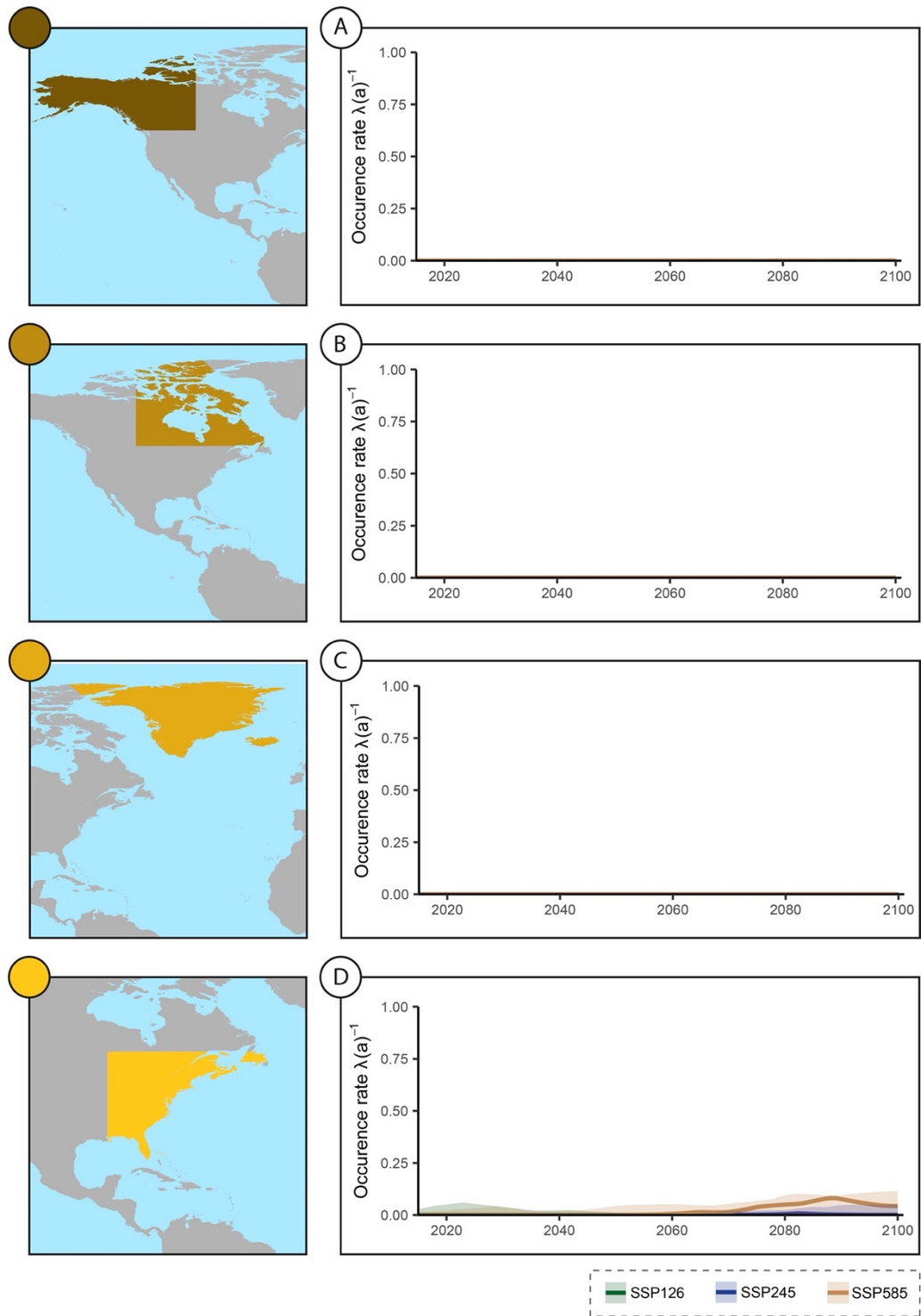
Supplement 21: A Temporal evolution of occurrence rate of SPEI below -1.5 for North Europe under different future climate scenarios (SSP1-2.6, SSP2-4.5, SSP5-8.5).  $\lambda(a)^{-1}=1$  indicates a SPEI value below -1.5 can be observed every year. The SPEI is derived based on the baseline period of 1971 to 2100. The medians of the model ensemble from CMIP6 are highlighted. The 25th and 75th percentiles of the model ensemble for each scenario are indicated with shaded colour around the median



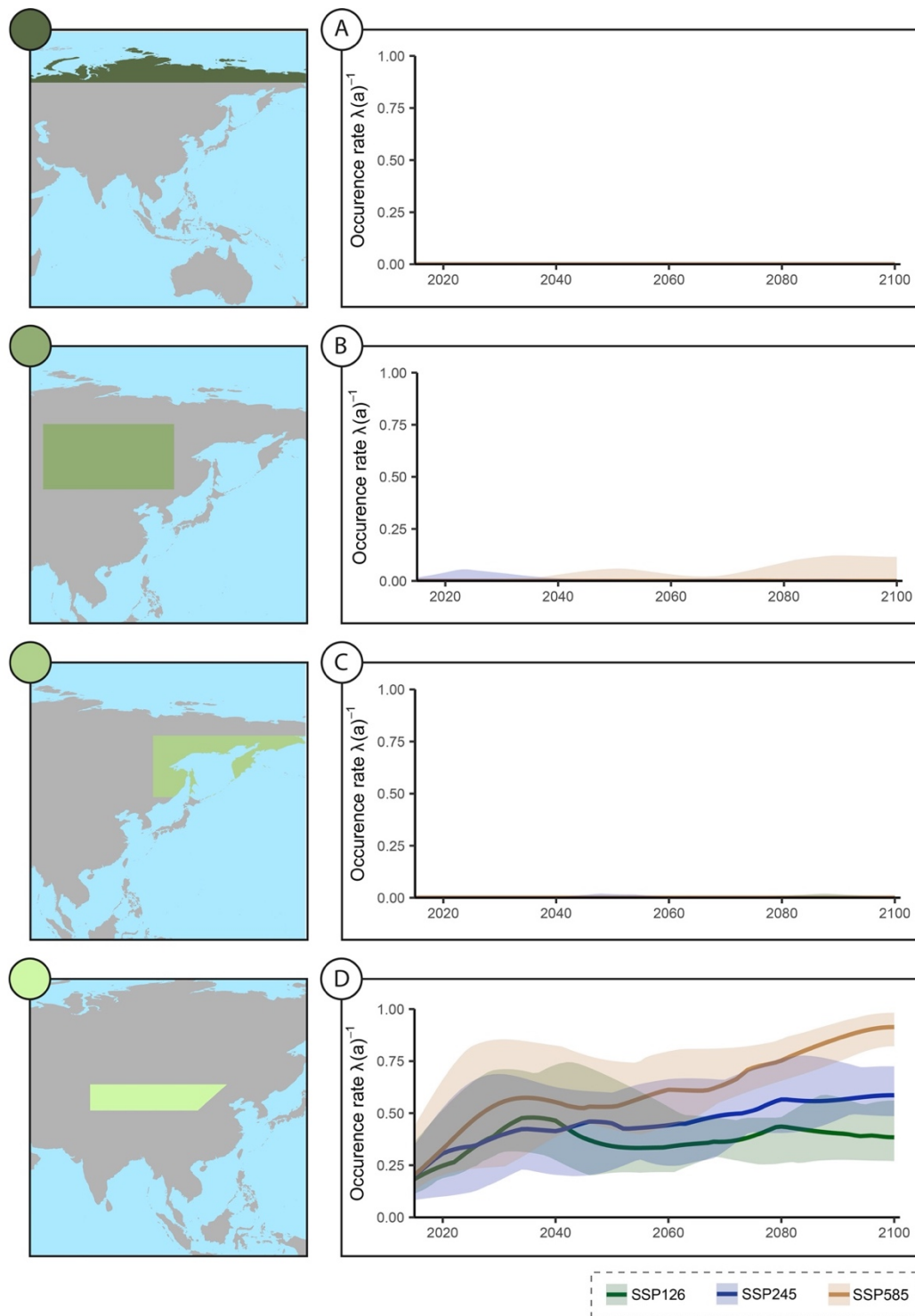
Supplement 22: A-D Temporal evolution of occurrence rate of SPEI below -1.5 for regions in Central and South America under different future climate scenarios (SSP1-2.6, SSP2-4.5, SSP5-8.5).  $\lambda(a)^{-1}=1$  indicates a SPEI value below -1.5 can be observed every year. The SPEI is derived based on the baseline period of 1971 to 2100. The medians of the model ensemble from CMIP6 are highlighted. The 25th and 75th percentiles of the model ensemble for each scenario are indicated with shaded colour around the median.



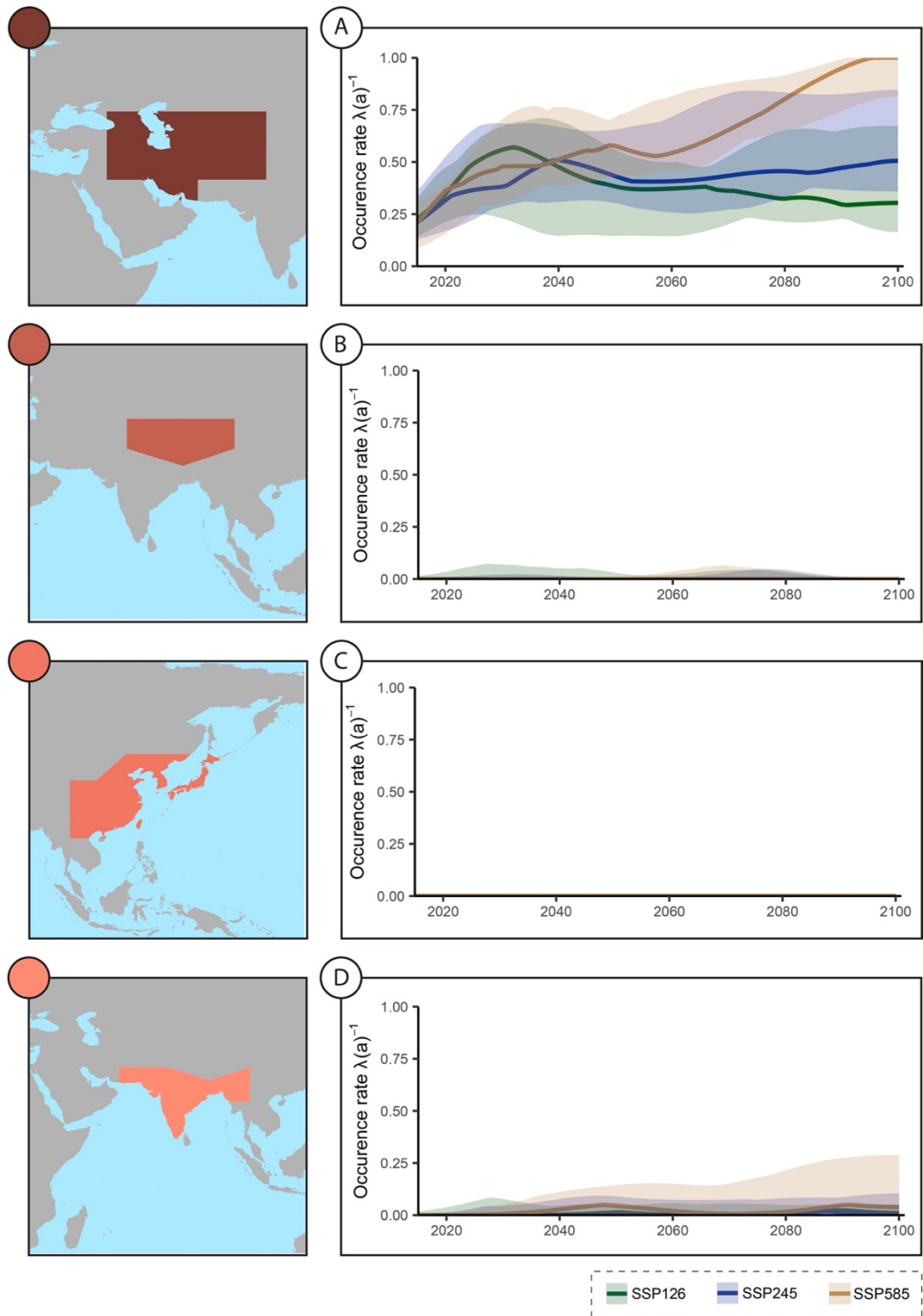
Supplement 23: A-D Temporal evolution of occurrence rate of SPEI below -1.5 for regions in Africa and Middle East under different future climate scenarios (SSP1-2.6, SSP2-4.5, SSP5-8.5).  $\lambda(a)^{-1}=1$  indicates a SPEI value below -1.5 can be observed every year. The SPEI is derived based on the baseline period of 1971 to 2100. The medians of the model ensemble from CMIP6 are highlighted. The 25th and 75th percentiles of the model ensemble for each scenario are indicated with shaded colour around the median.



Supplement 24: A-D Temporal evolution of occurrence rate of SPEI below -1.5 for regions in North America and Greenland under different future climate scenarios (SSP1-2.6, SSP2-4.5, SSP5-8.5).  $\lambda(a)^{-1}=1$  indicates a SPEI value below -1.5 can be observed every year. The SPEI is derived based on the baseline period of 1971 to 2100. The medians of the model ensemble from CMIP6 are highlighted. The 25th and 75th percentiles of the model ensemble for each scenario are indicated with shaded colour around the median.



Supplement 25: A-D Temporal evolution of occurrence rate of SPEI below -1.5 for regions in North Asia under different future climate scenarios (SSP1-2.6, SSP2-4.5, SSP5-8.5).  $\lambda(a)^{-1}=1$  indicates a SPEI value below -1.5 can be observed every year. The SPEI is derived based on the baseline period of 1971 to 2100. The medians of the model ensemble from CMIP6 are highlighted. The 25th and 75th percentiles of the model ensemble for each scenario are indicated with shaded colour around the median.



Supplement 26: A-D Temporal evolution of occurrence rate of SPEI below -1.5 for regions in South Asia under different future climate scenarios (SSP1-2.6, SSP2-4.5, SSP5-8.5).  $\lambda(a)^{-1}=1$  indicates a SPEI value below -1.5 can be observed every year. The SPEI is derived based on the baseline period of 1971 to 2100. The medians of the model ensemble from CMIP6 are highlighted. The 25th and 75th percentiles of the model ensemble for each scenario are indicated with shaded colour around the median.

## ACKNOWLEDGMENT

First of all, I would like to thank my doctoral supervisor Prof. Dr. Gerrit Lohmann for his scientific supervision and guidance. He was very helpful with all specialist questions and, in addition to the actual work, he always supported me in my role as PhD student spokesperson at the AWI. Only in this way, it was possible to arrange COVID-19-related contract extensions for all doctoral students at the AWI.

I would like to thank my supervisor, Dr. Monica Ionita, who was always there for me with help and valuable advice, even in stressful times. She is in charge of the PALEX project (Climate extremes from a paleo perspective), within the framework of which this thesis was written. Besides her many responsibilities, she never got tired of reading my drafts and commenting on them diligently.

Without a whole team of friends and colleagues behind me, this work would not have been possible. Therefore, I would like to particularly thank Dr. Gerd Helle, who has accompanied my path since 2014, enthused me for the subject, and always supported me. I will not forget that! In addition, I would like to thank Prof. Dr. Amir AghaKouchak, Dr. Martin Wegmann, Dr. Norel Rimbu, Dr. Martin Werner, Dr. Paul Gierz, Dr. Christian Stepanek, Dr. Christopher Danek, Dr. Mandy Freund, Dr. Simon Michel, Franziska Slotta, Maren Pauly, Prof. Dr. Gerhard Schleser, Dr. Maria Josefa Verdugo, Dr. Klaus Grosfeld, Nadine Hillenbrand, Dr. Eduardo Queiroz Alves, Prof. Dr. Ronny Schomacker, Stephan Krätschmer, Diana Caldarescu, Dr. Viorica Nagavciuc, Katharina Kirchhoff, Prof. Dr. Olaf Eisen, POLMAR, Jenna Balaguer, Miriam Seifert, Nadezhda Sokolova, Vanessa Teske, Maximilian Jochmann, Julia Nixdorf, Lukas Minnemann, Justus Contzen, Lars Ackermann, Tilmann Ranft, Jonas Schulz, Jonathan Guba, Jennifer Hörstel, Jonas Kuhl, Richard Herbst, Ludwig Wiegank, Richard Dehne, Konrad Röder, Joseph Birke and many more. The World Climate Research Programme, the Climate Model Intercomparison Project, and the technical and administrative infrastructure at the Alfred-Wegener-Institute are greatly acknowledged.

I would like to thank my family, who have always supported me in my goals, no matter how difficult they seemed at the beginning. Furthermore, I would like to acknowledge my uncle Prof. Dr. Tjark Siefkes for proofreading my doctoral thesis and providing helpful comments. Finally, I would like to express my gratitude to my girlfriend Julia Schmitz, who has always pushed me, always had advice for me, got me out of scientific crises and always made me something to eat when I needed it most. For that, I thank you with all my heart.